Final Report:
Cathode Catalysis in Hydrogen/Oxygen Fuel Cells:
New Catalysts, Mechanism, and Characterization

Andrew A. Gewirth, Paul J. A. Kenis, Ralph G. Nuzzo, and Thomas B. Rauchfuss
Department of Chemistry, Department of Chemical and Biomolecular Engineering, and
the Fredrick Seitz Materials Research Laboratory
University of Illinois at Urbana-Champaign
Urbana, IL 61801

Grant Number:	DE-FG02-05ER46260
Date of report:	Jan 14, 2016
Research period:	September 1, 2005 – July 14, 2015

Applicant/Institution: Board of Trustees of the University of Illinois
Address: Grants and Contracts
109 Coble Hall
801 S. Wright St
Champaign IL 61820-6242

Principal Investigator: Prof. Andrew A. Gewirth
Address: Department of Chemistry
University of Illinois
600 S. Mathews Avenue
Urbana, IL 61801

Telephone: 217-333-8329
Email: agewirth@illinois.edu

DOE/Office of Science Program Office: BES
DOE/office of Science Program Technical Program Manager Contact: Michael Sennett

One Paragraph Project Summary

In this research, we prosecuted a comprehensive plan of research directed at developing new catalysts and new understandings relevant to the operation of low temperature hydrogen-oxygen fuel cells. The focal point of this work was one centered on the Oxygen Reduction Reaction (ORR), the electrochemical process that most fundamentally limits the technological utility of these environmentally benign energy conversion devices. Over the period of grant support, we developed new ORR catalysts, based on Cu dimers and multimers. In this area, we developed substantial new insight into design rules required to establish better ORR materials, inspired by the three-Cu active site in laccase which has the highest ORR onset potential of any material known. We also developed new methods of characterization for the ORR on conventional (metal-based) catalysts. Finally, we developed a new platform to study the rate of proton transfer relevant to proton coupled electron transfer (PCET) reactions, of which the ORR is an exemplar. Other aspects of work involved theory and prototype catalyst testing.

1. The Development of New Metal Catalysts for ORR

1.1. Non-precious Metal Catalysts based on Cu Scaffolds

Utilizing support from this project, we developed new classes of ORR catalysts based on Cu dimers and multimers.[1] These new materials exhibit ORR onsets at potentials higher than any other Cu-based material in neutral and basic environments[2] and are inspired by the three-Cu active site in laccase which has the highest ORR onset potential of any material known.[3-4]

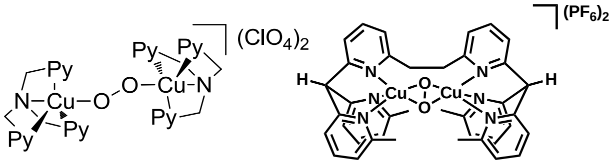

Figure 1. μ-η^1:η^1 (left) and μ-η^2:η^2 (right) coordination of O_2 in binuclear Cu complexes. Only complexes with μ-η^1:η^1 coordination of O_2 exhibit enhanced ORR activity.

The design of new ORR catalysts could benefit from more accurate mimicry of biological catalysts for the same reaction. To further understand laccase reactivity, we interrogated the rate determining step (RDS) of the ORR using laccase as the cathode catalyst. We developed a novel method of immobilizing laccase on a Au surface, using an anthracene thiol, backfilled with a short chain thiol to allow space for the laccase to adsorb with the correct orientation on the Au surface.[5] The stabilized laccase enables direct electron transfer between the enzyme and the Au surface, and direct determination that the Tafel slope is 140 mV/decade. Such a Tafel slope can only be consistent with the first electron transfer between the substrate and the electron transfer associated type 1 Cu center being the rate determining step. Consequently, this implies that the tri-Cu active site is in fact kinetically competent and that the ORR occurs quickly there.

The focus on coordination of Cu with ligands containing N to form competent ORR catalysts possibly mimicking laccase has led to the examination of the activity of ORR toward two different classes of binuclear Cu complexes. The first of the molecular laccase mimics are related to the structurally defined μ-η^2:η^2 Cu complexes developed by Kitajima [6] and then further refined by Kodera and coworkers. [7-8] Although these complexes exhibit well defined O_2 coordination between the Cu centers as shown in Fig. 1 (right), μ-η^2:η^2 Cu complexes do not exhibit catalytic activity for ORR due to the apparent electrophilic reactivity rather than the nucleophilic reactivity required for the ORR. [9-10] The second class of binuclear Cu complexes evaluated exhibit μ-η^1:η^1 coordination to O_2, shown in Fig. 1 (left). These complexes, based on the tris(2-pyridylmethyl)amine (TPA) ligand, have a long history as hemocyanin mimics[11] and were used to examine the ORR in a nonaqueous context.[12] We have shown that TPA, complexed with Cu, yields the most positive potential onset for the ORR in aqueous acidic solution relative to any Cu-containing complex thus far examined. [13] Derivatives of TPA exhibit even higher onset potentials at the cost of some stability. A chart showing ORR onset potentials as a function of pH for a variety of Cu complexes is shown in Fig. 2.[14] The chart shows that while activity is low at low pH values, it becomes much more active at higher pH values.

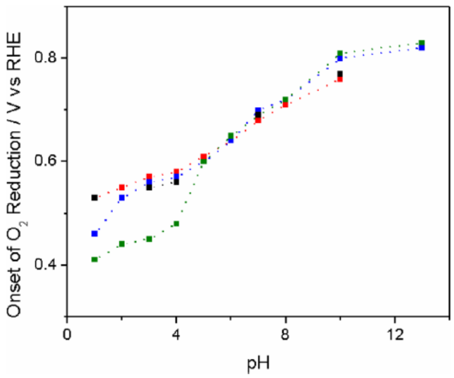

Figure 2. Plot of onset potential for O_2 reduction vs the solution pH for $[Cu(TPA)(L)]^{2+}$ (black), $[Cu(PMEA)(L)]^{2+}$ (red), $[Cu(PMAP)\text{-}(L)]^{2+}$ (blue), and $[Cu(TEPA)(L)]^{2+}$ (green).

An interesting observation from these studies is shown in Fig. 3. The initial ORR activity of the TPA Cu complex is shown in blue. Following pyrolysis the activity decreases—shown by the red curve—as expected. However, when the TPA ligand is added to the surface of the pyrolyzed material, the initial onset is recovered, as shown by the black curve. This is the first evidence that direct ligand participation in a complex is required for ORR activity.[14]

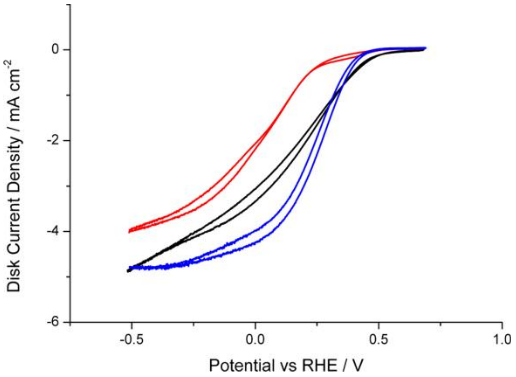

Figure 3. RRDE voltammograms of $[Cu(TPA)(L)](BPh_4)_2$ (black), pyrolyzed $Cu(TPA)(L)](BPh_4)_2$ (red), and pyrolyzed $Cu(TPA)(L)](BPh_4)_2$ reconstituted with TPA (blue) all supported on Vulcan XC-72.

We sought to more generally examine features important for facile ORR activity in binuclear Cu complexes. We tested a series of binuclear Cu complexes for both ORR onset and peroxide production by varying the Cu-Cu distance, as well as the ligand coordinated between the Cu centers. Only the triamino Cu complex and the 3,5-diamino-1,2,4-triazole (DAT) Cu complex [15] reduce oxygen by 4 electrons. The inactive complexes contain either a bridging hydroxide, or a Cu-Cu spacing of the bis (pyridyl) complex that is too large.[16] In addition, the effect of DAT substituents on ORR activity was also examined. Both DAT and the 4-methoxybezylidene diamino triazole exhibit four-electron reduction of oxygen. However, the very similar 4-ethanone diamino triazole, which exhibiting an identical onset potential, shows only a two-electron reduction. [16]

As part of the effort to synthesize new Cu-containing ORR catalysts, we designed new polypyridyl ligands and developed new methodology that produces such tripodal species. We published a report on the new ligand design which includes a study of the effects of the second coordination sphere on the ORR. We demonstrate that pendant OH groups do not enhance the activation of O_2, but that their deprotonation greatly accelerates the reduction process.[14] Extending the theme of polypyridyl polytopic ligands, we are investigating bis[di(2-picolyl)amine] derivatives as scaffolds for Cu-based ORR catalysts to mimic the three-Cu active site in laccase as closely as possible. To start, we constructed a series of complexes featuring dipicolylamino (DPA) coordination to Cu including $[LCu_2Cl_4]$ (L is defined as 1,6-bis[di(2-picolyl)amino]hexane), which is a precatalyst for the ORR. Reflecting the reactivity of dicopper species, the dicopper(I) species $[LCu_2(MeCN)_2]^{2+}$ undergoes oxygenation to afford a dimeric (i.e. tetranuclear) cluster in which formal reduction of O_2 affords OH^- ligands bound to Cu(II) centers. The intermolecular oxygenation means that these materials will not be good ORR catalysts, and indeed the ORR behavior is no better than that found with dinuclear Cu complexes previously. A focus of future work then is to prevent intermolecular oxygenation by using bulkier ligands.

1.2. Coordination Polymers with Cu Sites as ORR Catalysts

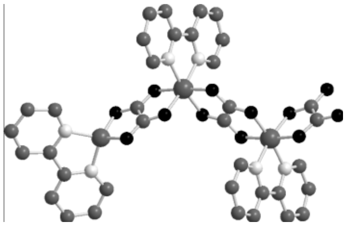

Figure 4. Model of poly[(2,2'-bipyridine)copper(II)-μ4-oxalato].

In a related effort, we have initiated the development of new molecular systems to reduce oxygen to water. While surface, nanoparticle, and decomposition systems remain popular, there is relatively little progress reported to date in the development of well-defined molecule based systems for oxygen reduction. In a first attempt, we examined the oxygen reduction capability of poly[(2,2'-bipyridine)copper(II)-μ4-oxalato] (pBpCuOx) (Fig. 4) coated on a glassy carbon electrode. The molecule was chosen because of its ability to polymerize and impart some stability to the electrode surface in addition to the similar metal-metal distance calculated for the polymer, which is close to that found in known ORR catalyst: the (2×2) Bi underdeposited on Au(111) system.[17] The electroreduction of O_2 on pBpCuOx-coated GCE occurs as a four-electron reduction at a potential 450 mV more positive than that found at a bare GCE. Intriguingly, studies of related monomeric systems exhibit only two-electron reduction activity, confirming both the synergy and need for two metal atoms to exhibit four electron activity. Other coordination polymer systems including those based on 1,2,3-triazole, for example, exhibited substantially increased activity relative to glassy carbon, while other triazole-based coordination polymers did not exhibit this activity. Recently, we showed that other substituted triazoles exhibit even better activity, and this is now a focus of intensive research efforts.

1.3. Multi-Copper O_2 Complexes as ORR Catalysts

A related focus of activity examines the possible catalytic properties of well-defined, thermally stable multi-copper O_2 complexes, motivated by the high catalytic efficiency of laccase. The premier examples of thermally stable complexes are those of Kodera and coworkers, which exhibit O_2-carrying properties akin to the behavior of hemerythrin. In these systems, a pair of CuN_3 sites cooperate in the binding of O_2 in a μ-η^2:η^2-O_2 binding mode. We investigated the following hypothesis: that hydrogen-bond donors and acceptors proximal to the O_2 binding site would strongly affect O_2 reduction. This hypothesis was tested both using solution methods and via electrochemical analysis of complexes absorbed on carbon.

Highly-organized ligand superstructures were prepared via multistep processes.[18-19] Key methods include double deprotonation of 6-methyl-2-pyridone and the reversible demethylation of methoxypyridines. The resulting hexadentate ligands are capable of hosting two copper(I) centers whereas the tridentate (tricyclic) ligands form monocuprous derivatives. Replacement of four flanking Me groups by four OMe groups decreases the affinity of the Cu_2^{2+} center for O_2. In contrast, replacement of four flanking OMe groups with four OH groups brings about a complete change in reactivity attributable to proton-induced reduction of O_2. Equally dramatic effects are seen for monomeric Cu centers of the tris-pyridyl ligands. Simple $[HC(2\text{-}C_5H_3N\text{-}6\text{-}Me)_3Cu]^+$ displays *no* measureable affinity for O_2. Changing of one flanking Me group to OH allows the Cu(I) center to rapidly reduce O_2. The Cu-containing product is the novel mixed valence Cu_2^{3+} complex, as established by single crystal X-ray diffraction.

When supported on carbon, this hemocyanin model was found to exhibit good activity for the ORR. Comparison of the di-Cu model system to the mono-Cu analogue reveals similar activities at high pH, likely due to the catalysis by copper hydroxide species. Both catalysts exhibit high activity for H_2O_2 reduction at pH 10. Interestingly, at low pH the di-Cu system is more active. The onset for the di-Cu catalyst at pH 2 was 60 mV more positive than the mono-Cu catalyst, and also produced less H_2O_2 (Fig. 5). The reaction mechanism is likely a two-electron reduction of oxygen to hydrogen peroxide, followed by further a further two-electron reduction of H_2O_2 to water.

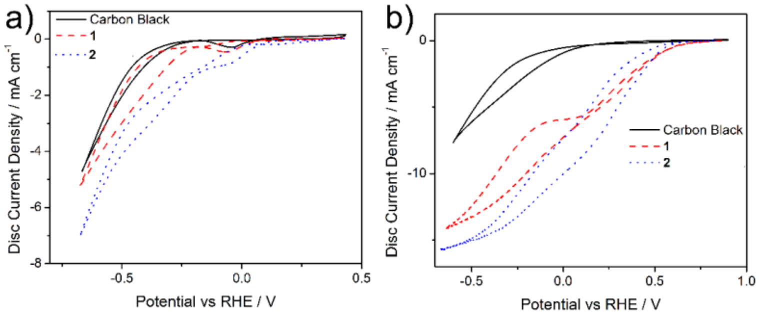

Figure 5. RDE of monocopper (labeled **1**, dashed line), dicopper (labeled **2**, dotted line), and XC-72 carbon black in Britton-Robinson buffer with 10 mM H_2O_2 under 1 atm. of Ar at 1600 rpm at (a) pH 2 and (b) pH 10.

1.4. Homogeneous ORR Catalysts based on Ir Scaffolds

Our specific goal for this part of the project was to develop new, homogeneous catalysts for the Knall Gas reaction, ($2H_2 + O_2 \rightarrow 2H_2O$) that would be amenable to mechanistic analysis relevant to the design of new cathode catalysts. We discovered that transfer hydrogenation catalysts are excellent catalysts for the hydrogenation of O_2.[20] Scheme 1 depicts the key mechanistic concept.

The transfer hydrogenation catalyst Cp*Ir(H)(TsDPEN) reacts rapidly at room temperature with O_2 (TsDPEN = tosylated diphenylethyene-diamine monoanion), resulting in the catalytic hydrogenation to give water. Reduction of O_2 by Cp*Ir(H)(TsDPEN) vs. Cp*Ir(D)(TsDPEN) exhibits an isotope effect of ~12, consistent with insertion and the participation of Ir-H/D bond breaking in a rate limiting step. We showed that a variety of other hydrogen-rich substrates could serve in place of H_2 including borane amines and even alcohols, and other electron acceptors could be used in place of O_2, including nitrosobenzene (PhNO, an analogue of singlet O_2). This project has also resulted in new insights into the activation of H_2, also relevant to DOE's hydrogen initiative. In particular we discovered that protons strongly enhance the rate of addition of H_2 to the unsaturated complex Cp*Ir(TsDPEN).

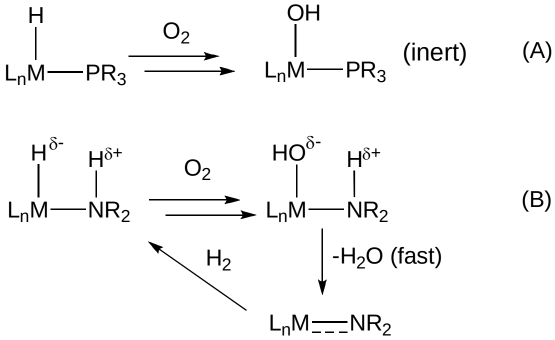

Scheme 1. Differing reactivity patterns anticipated for oxygen toward (A) classical metal hydrides and (B) amino-hydrides.

2. Potential-dependent, Real-time Characterization of ORR Catalysts

2.1. Surface Enhanced Raman Spectroscopy (SERS)

In this area, we used *in situ* SERS to examine important but as yet poorly understood intermediates that mediate the ORR mechanism on both Cu and Pt surfaces. Detailed studies of peroxide reduction on the Cu surface – important because peroxide is an intermediate in the ORR and its reduction is problematic for many ORR catalysts undergoing a two-electron pathway – revealed the presence of a hydroxide intermediate at potentials just cathodic of the onset of peroxide reduction. SERS obtained from a polycrystalline Cu surface both in the presence and absence of peroxide shows that there are four new bands corresponding to peroxide. Three of these are associated with the presence of Cu-OH species on the electrode surface while the fourth band is the O-O stretch of peroxide, which diminishes in intensity as the potential is moved to more negative values. The presence of a surface hydroxide species during peroxide electroreduction is consistent with a large body of prior work from our group, establishing that a surface OH appears to be a general intermediate in this reactivity.

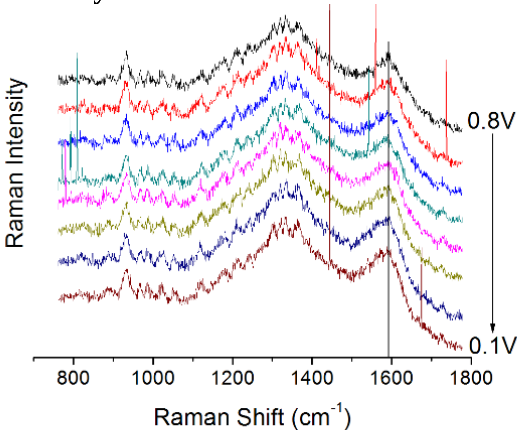

Figure 6. *In situ* SERS spectrum obtained from a Pt surface in a solution containing 0.1 M H_2SO_4 exposed to air. The broadened feature at 1560 cm^{-1} is associated with oxygen adsorption on Pt.

We also examined oxygen reduction on the technically more relevant Pt surface (Fig. 6). SERS measurements show the presence of a new band growing in at 1560 cm^{-1} at negative potentials, found only in the presence of oxygen. Deuteration studies show that this band is not associated with water and therefore is likely due to destabilization of the O-O bond upon O_2 association with the Pt surface. The critical point suggested here is that a sufficient population of non-dissociated O_2 is resident on the Pt catalyst surface even at potentials associated with significant reaction velocities for the ORR.

2.2. Analytical Electron Microscopy

We have brought to the program a state of the art characterization tool – Aberration Corrected Scanning Tunneling Electron Microscopy (C_s-STEM) – that is beginning to provide deep new understandings of electrocatalytic materials, including systems that hold great promise within the context of applications requiring useful ORR activities. Work to date has been described in a recent paper in *Analytical Chemistry*[21]. The representative C_s-STEM High Angle Annular Dark Field (HAADF) images illustrate highly ordered (single crystalline) nanostructural motifs in the PVP-capped Pt nanoparticles and more disordered nanomaterials (ones embedding and amplifying an apparent icosahedral core) for PVP-capped Pd nanoparticle materials (Fig. 7). Data of this type allow full characterization of the atomic speciation of clusters (as well as those of more complex compositions) via quantitative atom counting analysis and additionally establishes the nature of specific anisotropies in the habits produced along with the attributes of the facet systems and terminations they present. We have also utilized C_s-STEM HAADF microscopy in conjunction with new theoretical algorithms for quantitative image analysis to characterize the adsorption of the fundamental atomic bonding correlations of the ORR mediating metal center Cu-DAT on C electrocatalyst system. The data shows individual spots on the C surface that indicate individual Cu atoms coordinated to DAT. Analysis of distances between the spots yields a normalized pair distance frequency. Intriguingly, the most prominent pair distance is ca. 3.5 Å, which is the expected Cu-Cu distance in the Cu-DAT complex.

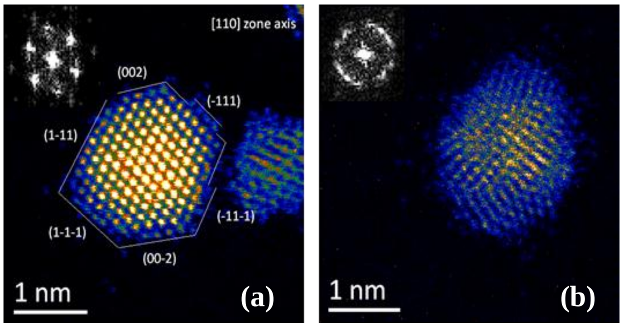

Figure 7. HAADF microscopy of PVP-capped (a) Pt and (b) Pd core-shell nanoparticles showing discrimination between core and shell elements (PVP = poly(*N*-vinyl-2-pyrrolidone)).

2.3. Catalyst Durability and Electrochemical Impedance Spectroscopy (EIS)

Another aspect of our catalyst durability studies involves examining Pt_3Co, Pt, and Pt_3Co/Mo catalyst durability using an accelerated degradation procedure. Under the aging protocol, the electrodes were exposed to acidic conditions and cycled over a range of potentials to simulate fuel cell operating conditions. Over the course of 10,000 cycles, a sharp deviation in fuel cell performance is observed. Pt_3Co/Mo demonstrates dramatically enhanced durability compared to Pt_3Co (Fig. 8). We used EIS to decouple the effects of cell resistance (R_{cell}) and charge transfer resistance (R_{ct}). Under acidic conditions, rapid hydrogen oxidation reaction kinetics lead to negligible anodic charge-transfer resistance thus the resistance of the sluggish ORR was isolated and quantified. R_{cell} of the aged Pt_3Co cathode shows fluctuations suggesting unstable transport processes within the electrode (including the catalyst layer) due to degradation. EIS data shows a greater increase in R_{ct} for the Pt_3Co cathode is compared to that for the Pt_3Co/Mo cathode, indicating a greater decrease in catalytic activity. Thus, dual effects of improved electrode stability and increased catalytic activity are responsible for the enhanced durability of the Pt_3Co/Mo cathode.

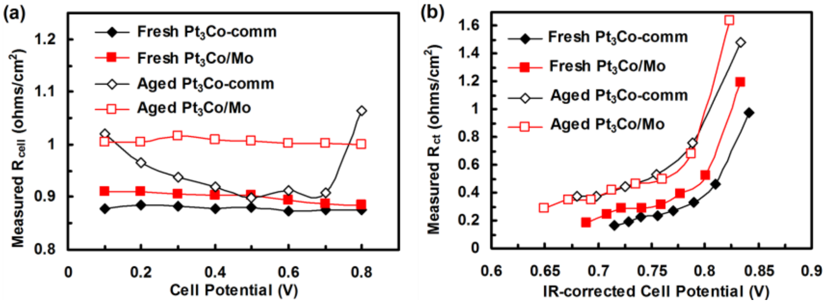

Figure 8. (a) Measured cell resistance (R_{cell}) as a function of cell potential and (b) measured charge-transfer resistance (R_{ct}) as a function of IR-corrected cell potential for fresh and aged Pt_3Co/Mo and Pt_3Co cathodes in an acidic microfluidic H_2/O_2 fuel cell.

2.4. X-ray Absorption Spectroscopy (XAS)

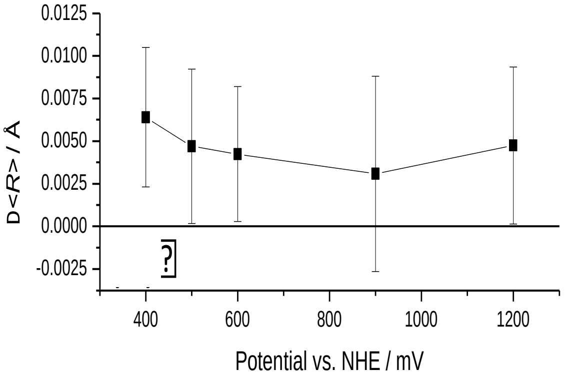

Figure 9: Potential dependence of the difference in EXAFS-determined Pt-Pt bond distances with and without O_2. The plot shows that Pt-Pt expansion occurs at all potentials, even those where the ORR rate is zero.

In the course of this collaborative program, we have further developed new methods for characterizing complex multimetallic structures at the most fundamental atomistic level by using XAS. We have developed new analytical protocols that allow the atomistic structures of the binuclear Pt-Ir cluster to be determined using XAS, an analysis that had not been possible at the level of detail achieved using our strategy due the close proximity of the absorption edges for these two element. Our procedure is an analytically robust and generalizable protocol that we feel will have broad impact on the XAS community. The data allow us to visualize the details of the atomistic structures of complex nanoscale systems allow for the characterization of segregation effects and the roles that adsorbates can play in restructuring them. These studies reveal a powerful new understanding for such nanoscale structures—that the nature of the atomic scale configurations is fluxional on fast temporal time scales, posing then a question as to how traditional static impressions of catalyst structure might underpin reactivity, ideas we believe have to be modified.

We also developed an *in situ* electrochemical X-ray absorption spectroscopy (XAS) with microfuel cells device that can be scaled down to the thickness of a few millimeters, and therefore is an ideal geometry for *in situ* electrochemical XAS characterization of the catalysts. The form factor of our device provides high diffusivity of oxygen through the elastomer membrane, supplying sufficient O_2 to the carbon-supported catalyst (as commonly used in PEM fuel cells) for reduction to occur even to very high (yet stable) current densities while X-ray absorption measurements are made. We monitored the Pt electrocatalyst during the ORR through the use of *in situ* electrochemical XAS. Our cell's novel poly(dimethylsiloxane) (PDMS) window provides high oxygen permeation to the working electrode, permitting heretofore unobserved monitoring of electrocatalyst evolution during ORR. Using this cell, we have produced the first comparison of Pt XAS data under N_2 sparged environment and during ORR electrocatalysis. The data suggest new understanding of the ORR mechanisms on this exemplary catalyst; specifically, oxygen adsorption occurs at every potential, even at 1.2 V where ORR current is not observed.[22] The present results shown in Fig. 9 conclusively demonstrate that the presence of O_2 in the electrochemical environment leads to a marked electronic d-band vacancy increase over a wide potential range (1.2 to 0.4 V vs normal hydrogen electrode).

2.5 *In situ* Surface Stress Measurement

One of the most stimulating – and problematic – aspects of the O_2 induced changes in the Pt-Pt distance is the relatively small (albeit still energetically significant) magnitude of the metal-metal bond strains induced. While error determination in extended X-ray absorption fine structure (EXAFS) is relatively mature, the changes in Pt-Pt distance with O_2 exposure are only slightly above zero, except possibly at 400 mV. We wanted another method to determine changes in Pt-Pt strains with potential and adsorbate association. We surmised that although the changes are small, the dynamical near-surface bond expansions found in the EXAFS should also give rise to consequential changes in the electrochemical surface stress.[23]

Fig. 10a shows electrochemical surface stress-thickness changes occurring on the cathodic sweep in the presence and absence of O_2. In general, increasing surface charge results in more attractive interactions between surface atoms, which cause tensile stress.[24-25] While surface stress-thickness curves from Ar and O_2 saturated solutions exhibit similar patterns, the curve from the O_2-exposed sample is displaced in a more compressive direction over the entire potential window interrogated. Fig. 10b shows the difference between the Ar and O_2 cases more directly, with the O_2 displacement between 0.05 and 0.2 N/m. Notably, the compressive displacement seen in the presence of O_2 is larger at more cathodic potentials, in qualitative agreement with the increased Pt-Pt bond expansion found in the EXAFS measurements reported above.

Intriguingly, we can use the Pt-Pt bond distance change determined from EXAFS to calculate a strain in the Pt adlayer. By using the Young’s modulus, the measured strain can be recast as a stress. Fig. 10b shows the stress calculated from the EXAFS-derived Pt-Pt bond length changes (blue) agrees well with the overlaid electrochemical stress measurement. The corroborating surface stress measurements may potentially yield a simpler method to examine metal-metal bond expansion during electrochemical processes. This is a new method to examine strains arising from electrochemical reactivity as a consequence of adsorbate association with the electrode.

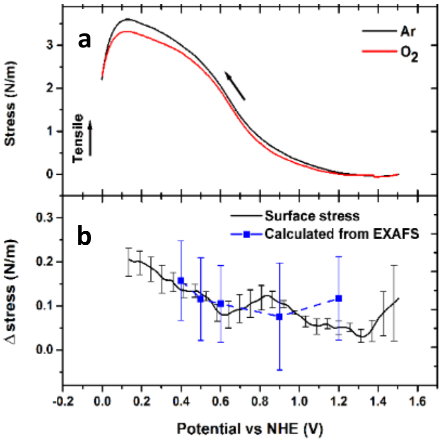

Figure 10. (a) Stress data of Pt/glass of both Ar and O_2 conditions, (b) The black line shows delta stress of Ar minus O_2 and the blue points indicate the expected delta stress based on the Pt-Pt bond strains obtained via EXAFS.

3. Controlling and Examining the Activity and Selectivity of ORR Catalysts using Proton Availability, Kinetic Isotope Effect Studies, and Temperature

We developed a new proton switch involving a hybrid bilayer membrane (HBM) in order to control the proton transfer event associated with the ORR. Our observation of a kinetic isotope effect (KIE) for the Cu complex raises a series of questions regarding the interplay of protons and electrons in the ORR for these and other related materials. We have an ongoing interest in other non-precious metal containing ORR catalysts, particularly those involving Fe, N, and C, an area seeing increased attention lately due to their superior performance in alkaline solutions. We are interested in demetalating these materials, using recently developed techniques, and also interrogating their high temperature and pressure ORR efficacy.

The overall effort in this section addresses the proton-coupled electron transfer (PCET) aspects of the ORR. PCET reactions are fundamental to many energy conversion processes including the four-electron four-proton ORR to water.[26] Much experimental and computational work examines the mechanism of the ORR in an effort to develop more efficient fuel cell cathodes.[27] Traditionally, the pH of bulk solution and covalently-bound proton relays are used to study PCET reactions. However, these studies give little information about the influence of proton flux on the mechanism of the ORR. Therefore, we have developed a electrochemical platform in which both the kinetics and thermodynamics of both the protons and electrons can be controlled in order to delineate the effects of these intricate processes.

3.1. Proton Availability Dictates Activity

Over the last few years, we developed a novel electrochemical platform to switch on and off proton transfer to a molecular oxygen reduction electrocatalyst. An HBM consists of a self-assembled monolayer (SAM) of thiols covered by a monolayer of lipid.[28-31] In this work we constructed an HBM containing a SAM of Cu triazole complex (CuBTT) (Fig. 11). In the absence of a lipid layer, CuBTT is a competent ORR catalyst at a wide pH range. Upon appending a lipid monolayer of 1,2-dimyristoyl-*sn*-glycero-3-phosphocholine (DMPC), proton transport to CuBTT is suppressed, thus resulting in inhibited ORR activity. By incorporating an alkyl phosphate proton carrier into the lipid layer, the ORR activity of CuBTT is enhanced compared to the lipid only case. Since the protonation state of the proton carrier depends on pH of the solution, proton delivery to CuBTT can be switched on and off by varying the pH.

Our initial results with the HBM PCET switch showed that by controlling the accessibility of protons to the ORR catalyst, we can control the rate of the ORR with qualities strongly mimetic of the dynamics exhibited in biological systems within in a tractable model catalyst assembly.[32] More recently, we discovered a new proton carrier and developed additional analytical techniques that have allowed us to quantify and modulate the rate of proton transport to an ORR catalyst. This work enabled us to interrogate and perturb the mechanism by which oxygen is reduced and control the ORR product distribution. Specifically, we discovered that incorporating an alkyl boronic acid into the lipid layer of the HBM revives the ORR current to almost the same values as observed in the absence of a lipid. By incorporating various amounts of alkyl boronic acid in the lipid, the rate of proton transfer to the CuBTT catalyst could be varied in a systematic and precise manner. We also showed that the HBM could be used to interrogate the rate of anion permeation of the bilayer.[33]

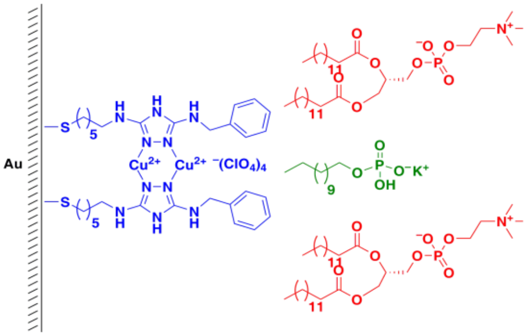

Figure 11. The HBM is composed of the Cu complex of BTT (blue), the 1,2-dimyristoyl-sn-glycero-3-phosphocholine (DMPC) lipid layer (red), and the alkyl phosphate proton carrier (green).

3.2. Kinetic Isotope Effect Studies

Based on our observation that Cu-based ORR activity could be gated by controlling the proton flux to the catalyst, we evaluated whether the catalyst would additionally exhibit a KIE. It is known that the ORR onset potential of NPM materials exhibits a strong dependence on bulk solution pH,[34-36] whereas the ORR onset of Pt is pH-insensitive. Spectroscopic studies of molecular catalysts and biological enzymes revealed that O-O bond cleavage of the bound O_2-adduct and the native intermediate is the RDS.[13, 37] This RDS is late in the catalytic cycle and is often promoted by coupling to protons—a classic example of a PCET process.[38-39]

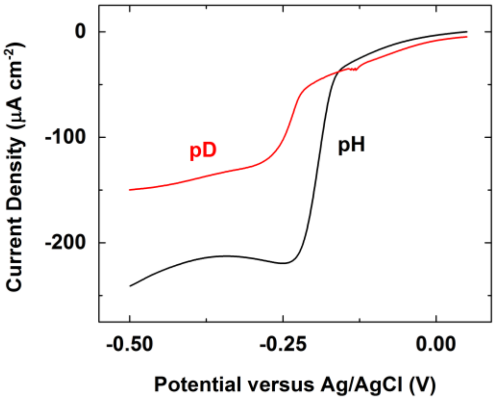

Figure 12. ORR LSVs of a SAM of CuBTT in O_2-saturated pH 5 (black) and pD 5 (red) phosphate buffer at a scan rate of 10 mV/s.

Fig. 12 shows two ORR LSVs of a SAM of CuBTT in H- and D-solutions. A SAM of CuBTT, which is an analogue of one of the best Cu-based ORR catalysts,[40-41] exhibits a substantial KIE, which is in contrast to the behavior demonstrated by Pt cathodes where no KIE is observed.[42] It is generally accepted that the RDS of Pt-catalyzed ORR is the first electron-transfer (ET) step.[43] Since no proton is involved during and/or before the RDS, no KIE is observed for Pt systems. The result from Fig. 12 confirms the involvement and importance of proton delivery to the overall ORR kinetics in the Cu-based systems, and calls for further effort in understanding and managing proton availability to other NPM ORR catalysts, especially those based on Fe or Co.

A KIE for Cu is expected because the RDS of ORR by CuBTT is the O-O bond breaking step which is coupled to protons or deuterons (Scheme 2, steps 4a and 4b). However, in the presence of a DMPC monolayer, no KIE is observed because protons or deuterons do not readily penetrate the hydrophobic lipid layer.[44] Therefore, we hypothesize that CuBTT reduces O_2 via a 1 e^- process to O_2^- inside lipid (Scheme 2, step 1a). More importantly, we also did not observe a KIE for ORR by CuBTT with DBA incorporated in the lipid layer at pH 5. This result suggests that the RDS in the presence of a proton carrier is a step slower than the O-O bond breaking event. Furthermore, according to rate law analysis, the lack of a KIE indicates that neither the RDS nor any steps prior to the RDS involve protons or deuterons. The only step in the mechanisms outlined in Scheme 2 that fit these criteria is the "flip-flop" diffusion of DBA across the lipid layer (step 2). This further suggests that it should be possible to isolate a O_2^- intermediate. Such intermediates have been found in non-aqueous oxygen reduction contexts with and without Cu.[45-49]

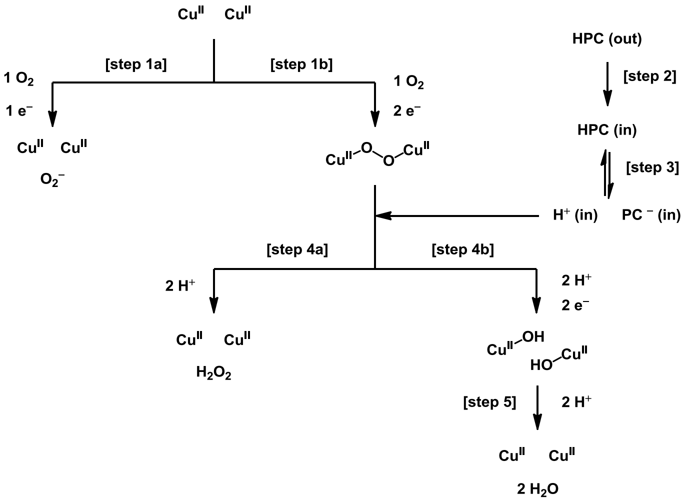

Scheme 2. Plausible O_2 reduction pathways in a HBM, PC = proton carrier.

3.3. Effect of Temperature and Pressure on the ORR Kinetics

Fundamental studies of the ORR in aqueous media at above 100 °C are limited due to the harsh experimental conditions. Interrogating the ORR on Pt at above 100 °C provides valuable kinetic information including the temperature dependences of Tafel slopes and transfer coefficients. Apart from enhancing the ORR kinetics, raising the temperature can enable efficient Pt-OH bond cleavage. Information on the strength of Pt-OH bonds at above 100 °C likely provides clues to lower the ORR overpotential on Pt. We recorded a striking improvement in the ORR kinetics by ca. 150 fold relative to 1 atm at 25 °C under an O_2 pressure of 3.4 MPa at 200 °C (Fig. 13) [50].We determined that the accurate knowledge of the temperature and pressure dependence of O_2 availability, transfer coefficient, and surface area is required to correctly account for the enhanced ORR kinetics.

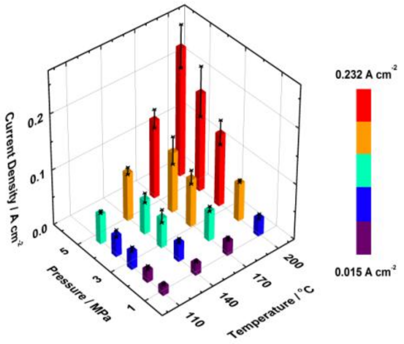

Figure 13. Temperature and pressure dependence of the ORR current density.

4. Development of a Theoretical Framework to Model Electrocatalytic Processes

A key difficulty in simulating electrochemical processes is the need to describe reactivity in the presence of potentials away from the potential of zero charge. In particular, both polarizability and charge transfer should be described in the context of bond formation and rearrangement. However, the typical system size required to represent an electrode accurately is much too demanding for direct solution of the quantum mechanical problem. In the context of electrochemistry problems, one must ensure that polarizability can be treated correctly in the region described by molecular mechanics. We have focused on a solution to this problem centered on achieving the ability to describe charge transfer, polarization, and bond rearrangement within the context of empirical force fields. To this end, the QTPIE (charge transfer with polarization current equalization) method has been developed.[51] The model we developed is merged with the QTPIE description to further describe polarizability and charge transfer.

4.1. Computational Methods to Examine Interfacial Electrode Processes

The QTPIE model enables large scale simulations including polarizability and charge transfer. Within QTPIE, every atom is described by its electronegativity and hardness. Hence, we represent an electrode surface at arbitrary chemical potential by introducing a single "site" with corresponding electronegativity. We have implemented this for the simple case of CO adsorbed to a Pt electrode, where extensive experimental information is available for comparison. The results are shown in Fig. 14. The good agreement with experiment[52] obtained from this simple model bodes well for future, more realistic applications taking into account the detailed atomistic structure of the electrode and surrounding solvent molecules.

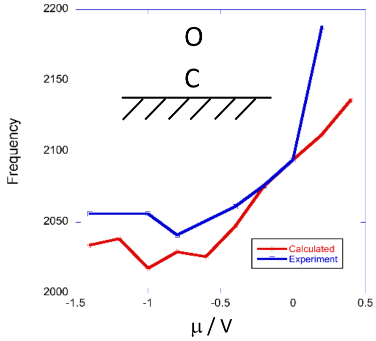

Figure 14. Comparison of experimental and predicted (Electrode-QTPIE) vibrational Stark shift of CO adsorbed on a metallic surface.

Accurate modeling of the electrified interface requires a realistic description of ions such as OH^- and H_3O^+.[53-54] We have introduced a new description of the OH^- ion that represents the lone pair electrons of the O atom by a negatively charged ring. This representation is very computationally inexpensive, but yields the correct behavior of the coordination shell in aqueous solution. The model is extended to include polarizability using QTPIE as described above.

5. Microfluidic Platforms for Catalyst Discovery and Fuel Cell Performance Assessment

We have developed a new form factor for an advanced fuel cell cathode, one that scales innately well for applications in both small and large power contexts. Two published works described the development of a prototype micro fuel cell based on this principle of operation – mass transfer via engineered patterns of passive permeation of reagent to fully immersed electrode assemblies – and subsequent developments have led to an ongoing study of this concept by a major industrial partner for use in large commercial/industrial power systems. A patent has been awarded on the design originating from this work.

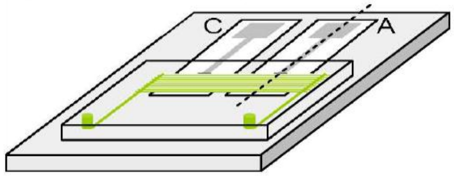

Figure 15. Schematic depiction and data showing the operation of a highly efficient micro fuel cell constructed using a passive permeation, fully immersed microfluidic anode and cathode.

Fig. 15 shows a schematic depiction of a fully integrated fuel cell based on this design form factor. Our studies show that this device form factor provides a capacity to generate enhancements in the diffusion limited current densities for the ORR by over an order of magnitude as compared to a similar electrode maintained in quiescent electrolyte. This surprising outcome reflects the spreading of the oxygen depletion zone into the polymer and the strong flow dynamics driven by the Faradaic current. We have developed a novel microfluidic hydrogen-oxygen (H_2/O_2) fuel cell that can function as both a rapid catalyst evaluation and an optimization tool, including for the ORR at the cathode.[55] Unlike polymer electrolyte membrane fuel cells (PEMFCs), in the present design a highly conductive liquid electrolyte stream flows between the anode and cathode.

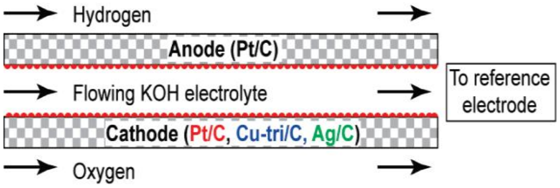

Figure 16. Schematic of microfluidic H_2/O_2 fuel cell with flowing alkaline electrolyte sandwiched by catalyst-coated gas diffusion electrodes.

We have further developed a pH-flexible microfluidic H_2/O_2 fuel cell with a flowing liquid electrolyte as a characterization tool for electrode-supported catalysts (Fig. 16). For analytical investigations, the flowing stream enables autonomous control of electrolyte parameters (*i.e.*, pH and composition), facilitates the removal and downstream analysis of reaction by-products, and allows for *in situ* monitoring of individual electrode characteristics via an external electrode. Thus, this platform is convenient for studying the performance and durability of novel catalysts integrated in gas diffusion electrodes (GDEs), closely resembling the way in which they will be employed in fuel cells. Over the past period, we have investigated the performance and durability of the CuDAT complex supported on carbon as a cathode catalyst for alkaline fuel cell applications using this microfluidic analytical platform. Part of this work has been published in the *Journal of the American Chemical Society*.[2]

An in-depth study of a radical new design for a PEM micro fuel cell has also been executed. This design advanced a planar device form factor that had been reported by us in earlier work and demonstrated effective separator free operation with fully passive water and reagent management for a formic acid PEMFC. The more important outcome of this work is the development of an important new tool that we feel will help bring revolutionary new understandings to the field, ones exploiting the unique *in situ* capacities of XAS to provide previously inaccessible insights into the atomic and electronic structures of electrocatalysts under *in operando* conditions and the responsivity of their structural dynamics to specific conditions of their operation.

We have successfully completed studies (i) to investigate alternate cathode catalysts; (ii) to investigate the effect of contaminants on ORR catalysis; and (iii) to develop a hydrogen-based laminar flow fuel cell platform.[56-57] In this fuel cell, the electrolyte is externally controlled by a syringe pump, allowing for versatile screening of multiple electrolytes.[58] The modular design facilitates rapid testing of different electrodes in the same setup without complex MEA fabrication steps.[58-60] A reference electrode can be placed in the outlet stream of the electrolyte, allowing for analysis of each electrode individually.[61-63] The fuel cell can be fueled with H_2 and O_2 as well as quiescent air, facilitating the study of cathode performance in both favorable and unfavorable conditions.[63-64]

6. List of Publications Attributable to the Grant in the Previous Period

6.1 Submitted

Tse, E. C. M.; Barile, C. J.; Kirchschlager, N. A.; Li, Y.; Gewargis, J. P.; Zimmerman, S. C.; Hosseini, A. and Gewirth, A. A., “Proton Transfer Kinetics Control the Mechanism of O_2 Reduction by a Non-Precious Metal Electrocatalyst,” *Nat. Mater.*, Submitted.

Varnell, J. A.; Tse, E. C. M.; Schulz, C. E.; Fister, T. T.; Haasch, R. T.; Timoshenko, J.; Frenkel, A. I. and Gewirth, A. A., “Isolation and Identification of Carbon-encapsulated Iron Nanoparticles as Active Catalytic Species for Oxygen Reduction,” *Nat. Energy*, Submitted.

Zhou, W. P.; Jayashree, R. S.; Brushett, F. R. and Kenis, P. J. A., "Characterization of Pt and Ag–Based Cathodes in an Alkaline Microfluidic H_2-O_2 Fuel Cell," *J. Electrochem. Soc.*, Submitted.

6.2 In preparation (manuscripts attached to the end of this pdf document)

Tse, E. C. M.; Hoang, T. T. H.; Varnell, J. A. and Gewirth, A. A., "Inverted and Normal Kinetic Isotope Effects in Oxygen Evolution and Oxygen Reduction Electrochemistry," Manuscript in preparation.

Tse, E. C. M.; Tregubov, A.; Zhou, X. Y.; Rauchfuss, T. B. and Gewirth, A. A., "Non-precious Metal Complexes of Pyrazolyl-, Imidazolyl-, and Triazolyl-based Ligands as Active Electrocatalysts for the Oxygen Reduction Reaction," Manuscript in preparation.

Tse, E. C. M.; Barile, C. J.; Kirchschlager, N. A.; Wu, H.-L. and Gewirth, A. A., "Physical and Electrochemical Characterization of a Cu-based Cathode Catalyst for the Oxygen Reduction Reaction Inside and Outside a Lipid Membrane," Manuscript in preparation.

Barile, C. J.; Tse, E. C. M.; Li, Y.; Hosseini, A.; Zimmerman, S. C. and Gewirth, A. A., "Proton Kinetics Dictates the Proton-coupled Electron Transfer Reaction Mechanism of Quinones at Lipid-modified Electrodes," Manuscript in preparation.

6.3 Published

Tse, E. C. M. and Gewirth, A. A., "Effect of Temperature and Pressure on the Kinetics of the Oxygen Reduction Reaction," *J. Phys. Chem. A,* **2015**, *119*, 1246–1255.

Tse, E. C. M.; Barile, C. J.; Gewargis, P.; Li, Y.; Zimmerman, S. C. and Gewirth, A. A., "Anion Transport through Lipids in a Hybrid Bilayer Membrane," *Anal. Chem.*, **2015**, *87*, 2403–2409.

Li, Y.; Tse, E. C. M.; Barile, C. J.; Gewirth, A. A. and Zimmerman, S. C., "Photoresponsive Molecular Switch for Regulating Transmembrane Proton-Transfer Kinetics," *J. Am. Chem. Soc.*, **2015**, *137*, 14059–14062.

Barile, C. J.; Tse, E. C. M.; Li, Y.; Sobyra, T. B.; Zimmerman, S. C.; Hosseini, A. and Gewirth, A. A., "Modulating Oxygen Reduction by a Hybrid Bilayer Membrane-embedded Dinuclear Copper Electrocatalyst using a Proton Switch," *Nat. Mater.*, **2014**, *13*, 619–623.

Erickson, E. M.; Oruc, E. M.; Wetzel, D. J.; Cason, M. W.; Hoang, T. T. H.; Small, M. W.; Li, D. Y.; Frenkel, A. I.; Gewirth, A. A. and Nuzzo, R. A., "A Comparison of Atomistic and Continuum Approaches to the Study of Bonding Dynamics in Electrocatalysis: Microcantilever

Stress and *in Situ* EXAFS Observations of Platinum Bond Expansion Due to Oxygen Adsorption during the Oxygen Reduction Reaction," *Anal. Chem.*, **2014**, *86*, 8368–8375.

Tse, E. C. M.; Schilter, D.; Gray, D. L.; Rauchfuss, T. B. and Gewirth, A. A., "Multicopper Models for the Laccase Active Site: Effect of Nuclearity on Electrocatalytic Oxygen Reduction," *Inorg. Chem.*, **2014**, *53*, 8505–8516.

Naughton, M. S.; Tornow, C. E.; Bonita, Y.; Jhong, H. R.; Brushett, F. R.; Gewirth, A. A. and Kenis, P. J. A., "*In-situ* Measurement of Ethanol Tolerance in an Operating Fuel Cell," *Int. J. Hydrogen Energy*, **2013**, *38*, 8980–8991.

Naughton, M. S.; Gu, G. H.; Moradia, A. A. and Kenis, P. J. A., "Tailoring Electrode Hydrophobicity to Improve Anode Performance in Alkaline Media," *J. Power Sources*, **2013**, *242*, 581–588.

Thorseth, M. A.; Letko, C. S.; Tse, E. C. M.; Rauchfuss, T. B. and Gewirth, A. A., "Ligand Effects on the Overpotential for Dioxygen Reduction by tris(2-Pyridylmethyl)amine Derivatives," *Inorg. Chem.*, **2013**, *52*, 628–634.

Oberst, J. L.; Thorum, M. S. and Gewirth, A. A., "Effect of pH on the Oxygen Reduction Reaction with a Pyrolyzed Fe Phthalocyanine Catalyst: Role of Azide," *J. Phys. Chem. C*, **2012**, *116*, 25257–25261.

Erickson, E. M.; Thorum, M. S.; Vasić, R.; Marinković, N. a. S.; Frenkel, A.; Gewirth, A. A. and Nuzzo, R. G., "In Situ Electrochemical X-ray Absorption Spectroscopy of Oxygen Reduction Electrocatalysis with High Oxygen Flux," *J. Am. Chem. Soc.*, **2012**, *134*, 197–200.

Brushett, F. R.; Naughton, M. S.; Ng, J. W. D.; Yin, L. and Kenis, P. J. A., "Analysis of Pt/C Electrode Performance in a Flowing Electrolyte Alkaline Fuel Cell," *J. Hydrogen Energy*, **2012**, *37*, 2559–2570.

Naughton, M. S.; Moradia, A. A. and Kenis, P. J. A., "Quantitative Analysis of Single-Electrode Plots to Understand In-Situ Behavior of Individual Electrodes," *J. Electrochem. Soc.*, **2012**, *159*, B761–769.

Letko, C. S.; Rauchfuss, T. B.; Zhou, X. Y. and Gray, D. L., "Influence of Second Coordination Sphere Hydroxyl Groups on the Reactivity of Copper(I) Complexes," *Inorg. Chem.*, **2012**, *51*, 4511–4520.

Jhong, H. M.; Brushett, F. R.; Yin, L.; Stevenson, D. M. and Kenis, P. J. A., "Combining Structural and Electrochemical Analysis of Electrodes Using Micro-Computed Tomography and a Microfluidic Fuel Cell," *J. Electrochem. Soc.*, **2012**, *159*, B292–B298.

Thorseth, M. A.; Letko, C. S.; Rauchfuss, T. B. and Gewirth, A. A., "Dioxygen and Hydrogen Peroxide Reduction with Hemocyanin Model Complexes," *Inorg. Chem.*, **2011**, *50*, 6158–6162.

Thorum, M. S.; Hankett, J. M. and Gewirth, A. A., "Poisoning the Oxygen Reduction Reaction on Carbon-Supported Fe and Cu Electrocatalysts: Evidence for Metal-Centered Activity," *J. Phys. Chem. Lett.*, **2011**, *2*, 295–298.

Erickson, E. M.; Mitrovski, S. M.; Gewirth, A. A. and Nuzzo, R. G., "Optimization of a Permeation-based Microfluidic Direct Formic Acid Fuel Cell (DFAFC)," *Electrophoresis*, **2011**, *32*, 947–956.

Gewirth, A. A. and Thorum, M. S., "Electroreduction of Dioxygen for Fuel-Cell Applications: Materials and Challenges," *Inorg. Chem.*, **2010**, *49*, 3557–3566.

Thorum, M. S.; Anderson, C. A.; Hatch, J. J.; Campbell, A. S.; Marshall, N. M.; Zimmerman, S. C.; Lu, Y. and Gewirth, A. A., "Direct, Electrocatalytic Oxygen Reduction by Laccase on Anthracene-2-methanethiol-Modified Gold," *J. Phys. Chem. Lett.*, **2010**, *1*, 2251–2254.

Brushett, F. R.; Thorum, M. S.; Lioutas, N. S.; Naughton, M. S.; Tornow, C.; Jhong, H. R.; Gewirth, A. A. and Kenis, P. J. A., "A Carbon-Supported Copper Complex of 3,5-Diamino-1,2,4-triazole as a Cathode Catalyst for Alkaline Fuel Cell Applications," *J. Am. Chem. Soc.*, **2010**, *132*, 12185–12187.

Brushett, F. R.; Duong, H. T.; Ng, J. W. D.; Behrens, R. L.; Wieckowski, A. and Kenis, P. J. A., "Investigation of Pt, Pt_3Co, and Pt_3Co/Mo Cathodes for the ORR in a Microfluidic H_2/O_2 Fuel Cell," *J. Electrochem. Soc.*, **2010**, *157*, B837–B845.

Brushett, F. R.; Kenis, P. J. A. and Wieckowski, A., "New Concepts in the Chemistry and Engineering of Low-Temperature Fuel Cells," In *Fuel Cell Science*; John Wiley & Sons, Inc., **2010**, 565–610.

Brushett, F. R.; Jayashree, R. S.; Zhou, W. P. and Kenis, P. J. A., "Investigation of Fuel and Media Flexible Laminar Flow-based Fuel Cells," *Electrochim. Acta*, **2009**, *54*, 7099–7105.

Brushett, F. R.; Hollinger, A. S.; Markoski, L. J. and Kenis, P. J. A., “Microfluidic Fuel Cells as Microscale Power Sources and Analytical Platforms,” *Proceedings of ASME 2009 2nd Micro/Nanoscale Heat & Mass Transfer International Conference*, **2009**.

Letko, C. S.; Heiden, Z. M. and Rauchfuss, T. B., “Activation and Deactivation of Cp*Ir(TsDPEN) Hydrogenation Catalysts in Water,” *Eur. J. Inorg. Chem.*, **2009**, *33*, 4927–4930.

Thorum, M. S.; Yadav, J. and Gewirth, A. A., “Oxygen Reduction Activity of a Copper Complex of 3,5-Diamino-1,2,4-triazole Supported on Carbon Black,” *Angew. Chem. Int. Ed.*, **2009**, *48*, 165–167.

Chen, J. and Martínez, T. J., “Charge Conservation in Electronegativity Equalization and Its Implications for the Electrostatic Properties of Fluctuating-Charge Models,” *J. Chem. Phys.*, **2009**, *131*, 044114.

Heiden, Z. M.; Gorecki, B. J. and Rauchfuss, T. B., “Lewis Base Adducts Derived from Transfer Hydrogenation Catalysts: Scope and Selectivity,” *Organometallics*, **2008**, *27*, 1542–1549.

Chen, J.; Hundertmark, D. and Martínez, T. J., “A Unified Theoretical Framework for Fluctuating-Charge Models in Atom-Space and in Bond-Space,” *J. Chem. Phys.*, **2008**, *129*, 214113.

Heiden, Z. M. and Rauchfuss, T. B., “Homogeneous Catalytic Reduction of Dioxygen Using Transfer Hydrogenation Catalysts,” *J. Am. Chem. Soc.*, **2007**, *129*, 14303–14310.

Ufimtsev, I. S.; Kalinichev, A. G.; Martínez, T. J. and Kirkpatrick, R. J., “A Charged Ring Model for Classical $OH^{-}_{(aq)}$ Simulations,” *Chem. Phys. Lett.*, **2007**, *442*, 128–133.

Chen, J. and Martínez, T. J., “QTPIE: Charge Transfer with Polarization Current Equalization. A Fluctuating Charge Model with Correct Asymptotics,” *Chem. Phys. Lett.*, **2007**, *438*, 315–320.

Kim, J. and Gewirth, A. A., “Electrocatalysis of Oxygen Reduction by Cu-containing Polymer Films on Glassy Carbon Electrodes,” *Bull. Korean Chem. Soc.*, **2007** *28*, 1322–1328.

Stewart, K. L. and Gewirth, A. A., “Mechanism of Electrochemical Reduction of Hydrogen Peroxide on Copper in Acidic Sulfate Solutions,” *Langmuir*, **2007**, *23*, 9911–9918.

Jayashree, R. S.; Mitchell, M.; Natarajan, D.; Markoski, L. J. and Kenis, P. J. A., “A Microfluidic Hydrogen Fuel Cell with a Liquid Electrolyte,” *Langmuir*, **2007**, *23*, 6871–6874.

Spendelow, J. S.; Goodpaster, J. D.; Kenis, P. J. A. and Wieckowski, A., “Methanol Dehydrogenation and Oxidation on Pt(111) in Alkaline Solutions,” *Langmuir*, **2006**, *22*, 10457–10464.

Spendelow, J. S.; Goodpaster, J. D.; Kenis, P. J. A. and Wieckowski, A., “Mechanism of CO Oxidation on Pt(111) in Alkaline Media,” *J. Phys. Chem. B.*, **2006**, *110*, 9545–9555.

Jayashree, R. S.; Egas, D.; Natarajan, D.; Spendelow, J. S.; Markoski, L. J. and Kenis, P. J. A., “Air-Breathing Laminar Flow-Based Direct Methanol Fuel Cell with Alkaline Electrolyte,” *Electrochem. Solid State Lett*., **2006**, *9*, A252–256.

Mitrovski, S. M. and Nuzzo, R. G., “A Passive Microfluidic Hydrogen-Air Fuel Cell with Exceptional Stability and High Performance,” *Lab on a Chip*, **2006**, *6*, 353–361.

Heiden, Z. M. and Rauchfuss, T. B., “Proton-Induced Lewis Acidity of Unsaturated Iridium Amides,” *J. Am. Chem. Soc.*, **2006**, *128*, 13048–13049.

Mitrovski, S. M. and Nuzzo, R. G., “An Electrochemically Driven Poly(dimethylsiloxane) Microfluidic Actuator: Oxygen Sensing and Programmable Flows and pH Gradients,” *Lab on a Chip*, **2005**, *5*, 634–645.

Mitrovski, S. M.; Elliott, L. C. C. and Nuzzo, R. G., “Microfluidic Devices for Energy Conversion: Planar Integration and Performance of a Passive, Fully Immersed H_2-O_2 Fuel Cell,” *Langmuir*, **2004**, *20*, 6974–6976.

7. Project Personnel with % Support from Grant

Fikile Brushett	100 %	Shiqi Fu	25 %
Dennis Butcher	50 %	Benjamin Garrett	25 %
Joseph Buthker	50 %	Jake Gold	25 %
Andrew Campbell	50 %	Brad Gorecki	50 %
Bryan Carlson	50 %	Geun Ho Gu	25 %
Michael Cason	50 %	Yeyoung Ha	50 %
Bryan Chan	100 %	Jeremy Hatch	50 %
Chi-Shian Chen	100 %	Zachariah Heiden	50 %
Jiahao Chen	50 %	Nicole Honesty	50 %
Joshua Day	25 %	Huei-Ru Jhong	50 %
Hung Duong	50 %	Byoungsu Kim	50 %
Ezra Eibergen	50 %	Clinton King	50 %
Evan Erickson	50 %	Christopher Letko	50 %

Tai Lin	100 %	David Schilter	100 %
Nicholas Lioutas	25 %	Karl Siil	25 %
Brandon Long	50 %	Matthew Thorseth	50 %
Sichao Ma	50 %	Matthew Thorum	50 %
Elizabeth Miller	50 %	Claire Tornow	50 %
Joyee Mitra	100 %	Andrey Tregubov	100 %
Svetlana Mitrovski	50 %	Chun Ming Edmund Tse	50 %
Matt Naughton	50 %	Sumit Verma	50 %
Justin Oberst	50 %	Fei Wang	50 %
Mitchell Ong	50 %	David Wetzel	50 %
Mark Ringenberg	50 %	Xiaoyuan Zhou	100 %

8. Unexpended Funds at the End of the Final Budget Period

The unexpended funds at the end of the final budget period was $1792, much less than 10% of the annual budget.

9. References Cited

1. Thorum, M. S.; Yadav, J.; Gewirth, A. A., Oxygen reduction activity of a copper complex of 3,5-diamino-1,2,4-triazole supported on carbon black. *Angew. Chem., Int. Ed.* **2009,** *48* (1), 165-167.
2. Brushett, F. R.; Thorum, M. S.; Lioutas, N. S.; Naughton, M. S.; Tornow, C.; Jhong, H. R.; Gewirth, A. A.; Kenis, P. J. A., A Carbon-Supported Copper Complex of 3,5-Diamino-1,2,4-triazole as a Cathode Catalyst for Alkaline Fuel Cell Applications. *J. Am. Chem. Soc.* **2010,** *132* (35), 12185-12187.
3. Barton, S. C.; Kim, H.-H.; Binyamin, G.; Zhang, Y.; Heller, A., Electroreduction of O_2 to Water on the "Wired" Laccase Cathode. *J. Phys. Chem. B* **2001,** *105* (47), 11917-11921.
4. Blanford, C. F.; Foster, C. E.; Heath, R. S.; Armstrong, F. A., Efficient electrocatalytic oxygen reduction by the 'blue' copper oxidase, laccase, directly attached to chemically modified carbons. *Faraday Discuss.* **2008,** *140*, 319-335.
5. Thorum, M. S.; Anderson, C. A.; Hatch, J. J.; Campbell, A. S.; Marshall, N. M.; Zimmerman, S. C.; Lu, Y.; Gewirth, A. A., Direct, Electrocatalytic Oxygen Reduction by Laccase on Anthracene-2-methanethiol-Modified Gold. *J. Phys. Chem. Lett.* **2010,** *1* (15), 2251-2254.
6. Kitajima, N.; Moro-oka, Y., Copper-Dioxygen Complexes. Inorganic and Bioinorganic Perspectives. *Chem. Rev.* **1994,** *94* (3), 737-757.
7. Kodera, M.; Katayama, K.; Tachi, Y.; Kano, K.; Hirota, S.; Fujinami, S.; Suzuki, M., Crystal Structure and Reversible O_2-Binding of a Room Temperature Stable μ-η^2:η^2-Peroxodicopper(II) Complex of a Sterically Hindered Hexapyridine Dinucleating Ligand. *J. Am. Chem. Soc.* **1999,** *121* (47), 11006-11007.

8. Kodera, M.; Kajita, Y.; Tachi, Y.; Kano, K., Structural Modulation of Cu(I) and Cu(II) Complexes of Sterically Hindered Tripyridine Ligands by the Bridgehead Alkyl Groups. *Inorg. Chem.* **2003,** *42* (4), 1193-1203.
9. Hatcher, L. Q.; Vance, M. A.; Narducci Sarjeant, A. A.; Solomon, E. I.; Karlin, K. D., Copper−Dioxygen Adducts and the Side-on Peroxo Dicopper(II)/Bis(μ-oxo) Dicopper(III) Equilibrium: Significant Ligand Electronic Effects. *Inorg. Chem.* **2006,** *45* (7), 3004-3013.
10. Karlin, K. D.; Tolman, W. B.; Kaderli, S.; Zuberbuehler, A. D., Kinetic and thermodynamic parameters of copper-dioxygen interaction with different oxygen binding modes. *J. Mol. Catal. A: Chem.* **1997,** *117* (1-3, Proceedings of the 6th International Symposium on the Activation of Dioxygen and Homogeneous Catalytic Oxidation, 1996), 215-222.
11. Jacobson, R. R.; Tyeklár, Z.; Farooq, A.; Karlin, K. D.; Liu, S.; Zubieta, J., A copper-oxygen (Cu_2-O_2) complex. Crystal structure and characterization of a reversible dioxygen binding system. *J. Am. Chem. Soc.* **1988,** *110*, 3690-3692.
12. Fukuzumi, S.; Kotani, H.; Lucas, H. R.; Doi, K.; Suenobu, T.; Peterson, R. L.; Karlin, K. D., Mononuclear Copper Complex-Catalyzed Four-Electron Reduction of Oxygen. *J. Am. Chem. Soc.* **2010,** *132* (20), 6874-6875.
13. Thorseth, M. A.; Letko, C. S.; Rauchfuss, T. B.; Gewirth, A. A., Dioxygen and Hydrogen Peroxide Reduction with Hemocyanin Model Complexes. *Inorg. Chem.* **2011,** *50* (13), 6158-6162.
14. Thorseth, M. A.; Letko, C. S.; Tse, E. C. M.; Rauchfuss, T. B.; Gewirth, A. A., Ligand Effects on the Overpotential for Dioxygen Reduction by Tris(2-pyridylmethyl)amine Derivatives. *Inorg. Chem.* **2013,** *52* (2), 628-634.
15. Thorum, M. S.; Yadav, J.; Gewirth, A. A., Oxygen reduction activity of a copper complex of 3,5-diamino-1,2,4-triazole supported on carbon black. *Angew. Chem. Int. Ed.* **2009,** *48* (1), 165-167.
16. Tornow, C. E.; Gray, D. L.; Gewirth, A. A., Effect of Cu-Cu Distance and Ligation on the Oxygen Reduction Reaction with Supported Cu Complexes. *Inorg. Chem.* **2014**, submitted.
17. Li, X.; Gewirth, A. A., Peroxide electroreduction on Bi-modified Au surfaces: Vibrational spectroscopy and density functional calculations. *J. Am. Chem. Soc.* **2003,** *125* (23), 7086-7099.
18. Kodera, M.; Katayama, K.; Tachi, Y.; Kano, K.; Hirota, S.; Fujinami, S.; Suzuki, M., Crystal Structure and Reversible O_2-Binding of a Room Temperature Stable μ-η^2:η^2-Peroxodicopper(II) Complex of a Sterically Hindered Hexapyridine Dinucleating Ligand. *J. Am. Chem. Soc.* **1999,** *121* (47), 11006-11007.
19. Kajita, Y.; Tanaka, S.; Kodera, M.; Kano, K., Reversible O_2-binding of μ-η^2:η^2-peroxodicopper(II) complexes: The O_2-affinity control with the distortion of the coordination geometry around Cu(II) ions. *J. Inorg. Biochem.* **2001,** *86* (1), 285-285.
20. Heiden, Z. M.; Rauchfuss, T. B., Proton-induced Lewis acidity of unsaturated iridium amides. *J. Am. Chem. Soc.* **2006,** *128* (40), 13048-13049.
21. Sanchez, S. I.; Small, M. W.; Sivaramakrishnan, S.; Wen, J.-g.; Zuo, J.-M.; Nuzzo, R. G., Visualizing Materials Chemistry at Atomic Resolution. *Anal. Chem.* **2010,** *82* (7), 2599-2607.

22. Erickson, E. M.; Thorum, M. S.; Vasic, R.; Marinkovic, N. S.; Frenkel, A. I.; Gewirth, A. A.; Nuzzo, R. G., In Situ Electrochemical X-ray Absorption Spectroscopy of Oxygen Reduction Electrocatalysis with High Oxygen Flux. *J. Am . Chem. Soc.* **2012,** *134* (1), 197-200.
23. Erickson, E. M.; Oruc, M. E.; Wetzel, D. J.; Cason, M. W.; Hoang, T. T. H.; Small, M. W.; Li, D. Y.; Frenkel, A. I.; Gewirth, A. A.; Nuzzo, R. G., A Comparison of Atomistic and Continuum Approaches to the Study of Bonding Dynamics in Electrocatalysis: Microcantilever Stress and in Situ EXAFS Observations of Platinum Bond Expansion Due to Oxygen Adsorption during the Oxygen Reduction Reaction. *Anal. Chem.* **2014,** *86* (16), 8368-8375.
24. Tavassol, H.; Chan, M. K. Y.; Catarello, M. G.; Greeley, J.; Cahill, D. G.; Gewirth, A. A., Surface Coverage and SEI Induced Electrochemical Surface Stress Changes during Li Deposition in a Model System for Li-Ion Battery Anodes. *J. Electrochem. Soc.* **2013,** *160* (6), A888-A896.
25. Puetter, R. C.; Gosnell, T. R.; Yahil, A., Digital Image Reconstruction: Deblurring and Denoising. *Annu. Rev. Astron. Astrophys.* **2005,** *43* (1), 139-194.
26. Gewirth, A. A.; Thorum, M. S., Electroreduction of Dioxygen for Fuel-Cell Applications: Materials and Challenges. *Inorg. Chem.* **2010,** *49* (8), 3557-3566.
27. Norskov, J. K.; Rossmeisl, J.; Logadottir, A.; Lindqvist, L.; Kitchin, J. R.; Bligaard, T.; Jonsson, H., Origin of the overpotential for oxygen reduction at a fuel-cell cathode. *J. Phys. Chem. B* **2004,** *108* (46), 17886-17892.
28. Robb, P. D.; Craven, A. J., Column ratio mapping: A processing technique for atomic resolution high-angle annular dark-field (HAADF) images. *Ultramicroscopy* **2008,** *109* (1), 61-69.
29. Srinivasan, K. S.; Ebenezer, D., A New Fast and Efficient Decision-Based Algorithm for Removal of High-Density Impulse Noises. *IEEE Signal Process Lett.* **2007,** *14* (3), 189-192.
30. Williams, D. B.; Carter, C. B., *Transmission Electron Microscopy: A Textbook for Materials Science 2nd edition ed.* Springer Science+Business Media, LLC: New York, NY, 2009.
31. Russell, A. E.; Rose, A., X-ray absorption Spectroscopy of low temperature fuel cell catalysts. *Chem. Rev.* **2004,** *104* (10), 4613-4635.
32. Barile, C. J.; Tse, E. C. M.; Li, Y.; Sobyra, T. B.; Zimmerman, S. C.; Hosseini, A.; Gewirth, A. A., Proton switch for modulating oxygen reduction by a copper electrocatalyst embedded in a hybrid bilayer membrane. *Nat. Mater.* **2014,** *13* (6), 619-623.
33. Tse, E. C. M.; Barile, C. J.; Gewargis, J. P.; Li, Y.; Zimmerman, S. C.; Gewirth, A. A., Anion Transport through Lipids in a Hybrid Bilayer Membrane. *Anal. Chem.* **2015**, *87* (4), 2403-2409.
34. Thorseth, M. A.; Tornow, C. E.; Tse, E. C. M.; Gewirth, A. A., Cu complexes that catalyze the oxygen reduction reaction. *Coord. Chem. Rev.* **2013,** *257* (1), 130-139.
35. Tse, E. C. M.; Schilter, D.; Gray, D. L.; Rauchfuss, T. B.; Gewirth, A. A., Multicopper Models for the Laccase Active Site: Effect of Nuclearity on Electrocatalytic Oxygen Reduction. *Inorg. Chem.* **2014,** *53* (16), 8505-8516.

36. Lee, M. H.; Wang, P. S.; Do, J. S., Effect of acid treatment of Co-richcore-Pt-rich shell/C electrocatalyst on oxygen reduction reaction. *J. Solid State Electrochem.* **2008,** *12* (7), 879-884.
37. Jones, S.; Solomon, E., Electron transfer and reaction mechanism of laccases. *Cell. Mol. Life Sci.* **2015**, 1-15.
38. Solis, B. H.; Hammes-Schiffer, S., Proton-Coupled Electron Transfer in Molecular Electrocatalysis: Theoretical Methods and Design Principles. *Inorg. Chem.* **2014,** *53* (13), 6427-6443.
39. Mayer, J. M., Proton-Coupled Electron Transfer: A Reaction Chemist's View. *Annu. Rev. Phys. Chem.* **2004,** *55* (1), 363-390.
40. Thorum, M. S.; Yadav, J.; Gewirth, A. A., Oxygen Reduction Activity of a Copper Complex of 3,5-Diamino-1,2,4-triazole Supported on Carbon Black. *Angew. Chem. Int. Ed.* **2009,** *48* (1), 165-167.
41. Barile, C. J.; Tse, E. C. M.; Li, Y.; Sobyra, T. B.; Zimmerman, S. C.; Hosseini, A.; Gewirth, A. A., Proton switch for modulating oxygen reduction by a copper electrocatalyst embedded in a hybrid bilayer membrane. *Nat. Mater.* **2014,** *13* (6), 619-623.
42. Ghoneim, M. M.; Clouser, S.; Yeager, E., Oxygen reduction kinetics in deuterated phosphoric acid. *J. Electrochem. Soc.* **1985,** *132* (5), 1160-1162.
43. Song, C.; Zhang, J., Electrocatalytic Oxygen Reduction Reaction. In *PEM Fuel Cell Electrocatalysts and Catalyst Layers*, Zhang, J., Ed. Springer London: **2008**; Chapter 2, 89-134.
44. Jain, M. K., *Introduction to biological membranes*. 2 ed.; Wiley: New York, **1988**.
45. Peterson, R. L.; Ginsbach, J. W.; Cowley, R. E.; Qayyum, M. F.; Himes, R. A.; Siegler, M. A.; Moore, C. D.; Hedman, B.; Hodgson, K. O.; Fukuzumi, S.; Solomon, E. I.; Karlin, K. D., Stepwise Protonation and Electron-Transfer Reduction of a Primary Copper-Dioxygen Adduct. *J. Am. Chem. Soc.* **2013,** *135* (44), 16454-16467.
46. Mandal, S.; De, A.; Mukherjee, R., Formation of $\{Cu_2(III)\ (\mu\text{-}O)(2)\}^{2+}$ core due to dioxygen reactivity of a copper(I) complex supported by a new hybrid tridentate ligand: Reaction with exogenous substrates. *Chem. Biodivers.* **2008,** *5* (8), 1594-1608.
47. Kieber-Emmons, M. T.; Ginsbach, J. W.; Wick, P. K.; Lucas, H. R.; Helton, M. E.; Lucchese, B.; Suzuki, M.; Zuberbuehler, A. D.; Karlin, K. D.; Solomon, E. I., Observation of a $Cu_2(II)(\mu\text{-}1,2\text{-peroxo})/Cu_2(III)(\mu\text{-oxo})(2)$ Equilibrium and its Implications for Copper-Dioxygen Reactivity. *Angew. Chem. Int. Ed.* **2014,** *53* (19), 4935-4939.
48. Gittleson, F. S.; Ryu, W.-H.; Taylor, A. D., Operando Observation of the Gold-Electrolyte Interface in LiO_2 Batteries. *ACS Appl. Mater. Interfaces* **2014,** *6* (21), 19017-19025.
49. Gittleson, F. S.; Sekol, R. C.; Doubek, G.; Linardi, M.; Taylor, A. D., Catalyst and electrolyte synergy in LiO_2 batteries. *Phys. Chem. Chem. Phys.* **2014,** *16* (7), 3230-3237.
50. Tse, E. C. M.; Gewirth, A. A., Effect of Temperature and Pressure on the Kinetics of the Oxygen Reduction Reaction. *J. Phys. Chem. A* **2015,** *119* (8), 1246-1255.
51. Chen, J.; Martinez, T. J., QTPIE: Charge Transfer with Polarization Current Equalization. A fluctuating charge model with correct asymptotics. *Chem. Phys. Lett.* **2007,** *438*, 315-320.

52. Tian, Z. Q.; Ren, B.; Mao, B. W., Extending Surface Raman Spectroscopy to Transition Metal Surfaces for Practical Applications. 1. Vibrational Properties of Thiocyanate and Carbon Monoxide Adsorbed on Electrochemically Activated Platinum Surfaces. *J. Phys. Chem. B* **1997,** *101* (8), 1338-1346.
53. Balbuena, P. B.; Johnston, K. P.; Rossky, P. J., Molecular Dynamics Simulation of Electrolyte Solutions in Ambient and Supercritical Water. 1. Ion Solvation. *J. Phys. Chem.* **1996,** *100*, 2706-2715.
54. Andaloro, G.; Palazzo, M. A.; Migliore, M.; Fornili, S. L., Hydration of the hydroxide ion: Ab initio claculations and monte carlo simulation. *Chem. Phys. Lett.* **1988,** *149*, 201-205.
55. Jayashree, R. S.; Mitchell, M.; Natarajan, D.; Markoski, L. J.; Kenis, P. J. A., Microfluidic hydrogen fuel cell with a liquid electrolyte. *Langmuir* **2007,** *23* (13), 6871-6874.
56. Sinnwell, S.; Inglis, A. J.; Stenzel, M. H.; Barner-Kowollik, C., Blocks, Stars and Combs: Complex Macromolecular Architecture Polymers via Click Chemistry. In *Click Chemistry for Biotechnology and Materials Science*, John Wiley & Sons, Ltd: **2009**, 89-117.
57. Brushett, F. R.; Zhou, W. P.; Jayashree, R. S.; Kenis, P. J. A., Alkaline Microfluidic Hydrogen-Oxygen Fuel Cell as a Cathode Characterization Platform. *J. Electrochem. Soc.* **2009,** *156* (5), B565-B571.
58. Jhong, H. R.; Brushett, F. R.; Kenis, P. J. A., The Effects of Catalyst Layer Deposition Methodology on Electrode Performance. *Adv. Energy Mater.* **2013,** *3* (5), 589-599.
59. Naughton, M. S.; Gu, G. H.; Moradia, A. A.; Kenis, P. J. A., Tailoring electrode hydrophobicity to improve anode performance in alkaline media. *J. Power Sources* **2013,** *242*, 581-588.
60. Brushett, F. R.; Duong, H. T.; Ng, J. W. D.; Behrens, R. L.; Wieckowski, A.; Kenis, P. J. A., Investigation of Pt, Pt_3Co, and Pt_3Co/Mo Cathodes for the ORR in a Microfluidic H-2/O-2 Fuel Cell. *J. Electrochem. Soc.* **2010,** *157* (6), B837-B845.
61. Dieterich, D. C.; Link, A. J., Click Chemistry in Protein Engineering, Design, Detection and Profiling. In *Click Chemistry for Biotechnology and Materials Science*, John Wiley & Sons, Ltd: **2009**, 309-325.
62. Nandivada, H.; Lahann, J., Copper-Catalyzed ‘Click’ Chemistry for Surface Engineering. In *Click Chemistry for Biotechnology and Materials Science,* John Wiley & Sons, Ltd: **2009**, 291-307.
63. Kitto, H. J.; Lauko, J.; Rutjes, F. P. J. T.; Rowan, A. E., Click Chemistry in the Preparation of Biohybrid Materials. In *Click Chemistry for Biotechnology and Materials Science,* John Wiley & Sons, Ltd: **2009**, 217-254.
64. Aznar, E.; Ferrer, S.; Borras, J.; Lloret, F.; Liu-Gonzalez, M.; Rodriguez-Prieto, H.; Garcia-Granda, S., Coordinative versatility of guanazole 3,5-diamino-1,2,4-triazole : Synthesis, crystal structure, EPR, and magnetic properties of a dinuclear and a linear trinuclear copper(II) complex containing small bridges and triazole ligands. *Eur. J. Inorg. Chem.* **2006,** (24), 5115-5125.

10. Appendix

Four manuscripts in preparation are attached.

Tse, E. C. M.; Hoang, T. T. H.; Varnell, J. A. and Gewirth, A. A., "Inverted and Normal Kinetic Isotope Effects in Oxygen Evolution and Oxygen Reduction Electrochemistry," Manuscript in preparation.

Tse, E. C. M.; Tregubov, A.; Zhou, X. Y.; Rauchfuss, T. B. and Gewirth, A. A., "Non-precious Metal Complexes of Pyrazolyl-, Imidazolyl-, and Triazolyl-based Ligands as Active Electrocatalysts for the Oxygen Reduction Reaction," Manuscript in preparation.

Tse, E. C. M.; Barile, C. J.; Kirchschlager, N. A.; Wu, H.-L. and Gewirth, A. A., "Physical and Electrochemical Characterization of a Cu-based Cathode Catalyst for the Oxygen Reduction Reaction Inside and Outside a Lipid Membrane," Manuscript in preparation.

Barile, C. J.; Tse, E. C. M.; Li, Y.; Hosseini, A.; Zimmerman, S. C. and Gewirth, A. A., "Proton Kinetics Dictates the Proton-coupled Electron Transfer Reaction Mechanism of Quinones at Lipid-modified Electrodes," Manuscript in preparation.

Inverted and Normal Kinetic Isotope Effects in Oxygen Evolution and Oxygen Reduction Electrochemistry

Edmund C. M. Tse,[1] Thao T. H. Hoang,[1] Jason A. Varnell,[1] and Andrew A. Gewirth[1,2*]

[1] Department of Chemistry, University of Illinois at Urbana–Champaign, Urbana, Illinois 61801, USA

[2] International Institute for Carbon Neutral Energy Research (WPI-I2CNER), Kyushu University, Fukuoka 812-8581, Japan

[*] Corresponding author. E-mail: agewirth@illinois.edu

Abstract

Earth-abundant and inexpensive catalysts with low overpotential and high durability are central to the development of efficient water splitting electrolyzers and high power density fuel cell systems. However, improvements in catalyst design and preparation are currently hampered by the lack of detailed understanding of the reaction mechanisms of both the oxygen reduction reaction (ORR) and oxygen evolution reaction (OER) facilitated by non-precious metal (NPM) catalysts. In this manuscript, we conducted a kinetic isotope effect (KIE) study in an effort to identify the rate-determining step (RDS) of these intricate electrocatalytic reactions involving multiple proton-coupled electron transfer (PCET) processes. We observed a KIE of about 2 for the ORR catalyzed by a NPM material, but no KIE was observed for Pt or Pd supported on carbon. We found an inverse KIE for OER catalyzed by Ni and Co electrodes. These results contribute to a more complete understanding of the ORR and OER mechanisms and allow for the future development of improved NPM catalysts.

1. Introduction

The ability to control the chemistry of oxygen represents a major step toward the utilization of sustainable energy from renewable energy sources.[1] To materialize this vision, facilitating the oxygen evolution reaction (OER, $4OH^- \rightarrow 2H_2O + 4e^- + O_2$ in alkaline or $2H_2O \rightarrow O_2 + 4H^+ + 4e^-$ in acid) and the oxygen reduction reaction (ORR, $2H_2O + 4e^- + O_2 \rightarrow 4OH^-$ in alkaline or $O_2 + 4e^- + 4H^+ \rightarrow 2H_2O$ in acid) at low overpotential is necessary to the widespread deployment of electrolyzers and fuel cells, respectively.[2] An electrolyzer is an energy conversion device that splits water into H_2 and O_2 via the following two half reactions: the anodic OER and the cathodic hydrogen evolution reaction (HER, $2H^+ + 2e^- \rightarrow H_2$).[3] In a fuel cell, the reverse of these two half reactions occurs.[4] In both devices, the performance is not limited by the reaction involving hydrogen, but is limited by the sluggish kinetics of the reaction involving oxygen.[1-4] Oxygen chemistry has thus attracted a tremendous amount of attention over the past fifty years to prepare robust, scalable and competent OER and ORR catalysts.[5-10] Despite the extensive effort expended in these areas, a complete understanding of the reaction mechanism has not been achieved.

The kinetic isotope effect (KIE) is a general method to study the reaction mechanism of many types of chemical transformations.[11,12] Specifically, the substitution of hydrogen with deuterium has been carried out extensively due to the large differences in reaction rates arising from the reduced mass differences between the isotopes.[13,14] For electrocatalysis involving protons, Conway et al. investigated KIE of the HER catalyzed by Pt and Yeager et al. conducted a similar KIE study on ORR catalyzed by Pt.[15-18] However, KIE studies are not prevalent in the field of electrochemistry. Therefore, we seek to expand the use of KIE studies to further understand the OER and ORR processes at the molecular level.

Current Understanding of ORR Mechanism

The ORR is central to the development of alternative energy conversion devices.[5,19] Currently, state-of-the-art fuel cells utilize Pt or one of its alloys to facilitate the ORR.[4] Unfortunately, these precious materials degrade or are poisoned during operation and despite being the best catalysts still exhibit overpotentials of about 300 mV. An alternate strategy to promote efficient O_2 reduction is to utilize low-cost and poison-resistant non-precious metal (NPM) catalysts.[5,20,21] State-of-the-art NPM ORR catalysts are prepared via pyrolysis of transition metal/N/C precursors,[6] which results in a highly heterogeneous surface structure. Due to the structural complexity of the catalyst material,[22] optimization of the ORR performance cannot be achieved using conventional structure-activity relationship approaches.[23] Apart from the incomplete structural information of the active site, the formation pathways of deleterious side products such as O_2^- and H_2O_2 that lead to degradation of fuel cell membranes and other components are also elusive.[24,25] A unified understanding of the ORR and degradation mechanism undoubtedly will benefit future catalyst design.

Understanding the ORR mechanism is instrumental to lowering the activation barrier of ORR. Over the past decade, there are few substantive attempts to elucidate the mechanism of ORR.[26] However, the relationship between the reaction pathway and catalytic performance remains poorly understood. The rate-determining step (RDS) of ORR catalyzed by Pt is generally accepted to be the first electron transfer step, as evidenced by a 120 mV/dec Tafel slope and supported by DFT calculations.[2] The onset potential of ORR by Pt is not pH-dependent,[27] further providing evidence that the RDS is not a proton-coupled electron transfer

(PCET) step. Yeager et al. demonstrated that Pt does not exhibit a KIE during ORR.[18] The absence of a KIE signifies that the steps at or before the RDS do not involve protons/deuterons.[18] One recent report found that Au(100) exhibits a substantial KIE during ORR at pH < 7, but no KIE at pH > 7.[28] This finding is suggestive of a change in proton-participation in the ORR mechanism upon pH changes. Recent studies of NPM catalysts have shown that the ORR onset potential is pH-dependent,[8,21,23] suggesting that protons are involved in the RDS. However, a comprehensive, comparative study of carbon-supported catalysts is lacking.

Current Understanding of OER Mechanism

Redox reactions involving multiple PCET steps are ubiquitous and have gathered a significant amount of interest over the past decades.[29,30] Using renewable sources to power water-splitting electrolyzers offers a promising scheme to generate H_2 with almost no carbon footprint.[31-33] The efficiency of the overall reaction is dictated by the OER overpotential at the anode and the stability of the anode material.[34,35] Ir and Ru are the anodes of choice in acidic electrolyte with low OER overpotentials.[36] However, their widespread application of Ir/Ru-based anodes is hindered by the prohibitive high cost and poor long-term stability of these precious metal catalysts.

Ni, Co, and their alloys are attractive OER electrocatalysts for OER in alkaline electrolyte, because these relatively inexpensive NPM materials are abundant and durable in basic condition.[37-39] However, OER overpotentials using Ni/Co-based materials range from ca. 50 to 150 mV relative to the thermoneutral potential of 1.48 V versus RHE.[31,40] Real-world thermodynamic efficiencies for water splitting are only ~75% with currently available Ni-based catalysts.[31] However, catalyst design to eliminate the high OER overpotential is still limited because insight into the OER mechanism is missing.[38]

Currently, tremendous effort is put in to elucidate the identity and surface structure of the bulk anode materials used to facilitate the OER.[39,41] Reports suggest that surface oxides and oxyhydroxides which are formed on the metal prior to the OER are the active catalytic species.[42] Compositional and morphological changes upon redox cycling of these porous thin film OER catalysts have been investigated using various techniques, including but not limited to voltammetric studies,[36,43,44] Raman spectroscopy,[45-48] X-ray photoelectron spectroscopy (XPS),[49-52] X-ray diffraction (XRD),[53,54] X-ray absorption spectroscopy (XAS),[55-57] scanning electron microscopy (SEM) and transmission electron microscopy (TEM),[54,58] scanning tunneling microscopy (STM),[59] ellipsometry,[60,61] atomic force microscopy (AFM),[62,63] electrochemical quartz crystal microbalance (EQCM),[64-67] and *in situ* stress measurement.[68]

In order to understand the OER mechanism on oxidized metals, it is important to interrogate the OER process at the molecular level. Density functional theory (DFT) calculations predicted that the binding energy of surface oxygen species such as $^*O$, $^*OH$, $^*OOH$ controls the OER activity.[32,38,42] This result sparks the following question: does the kinetics of deprotonation determine the overall OER rate? To the best of our knowledge, literature report on the KIE of the OER process is lacking.

KIE Studies of ORR and OER

Here, we launched comprehensive and comparative KIE studies of several precious and NPM ORR and OER catalysts to gain direct mechanistic insight into these intricate reactions involving multiple PCET steps. In particular, we examined the effect of deuteration on the ORR process in three different pH regimes: acidic condition that is relevant to proton-conducting polymer electrolyte membrane fuel cells, neutral condition that is found commonly in biological systems, and basic condition that is essential for alkaline fuel cell. We further interrogated the difference in OER response of NPM OER catalysts in the condition at which they are stable and active. We envision these results to provide unique information that will allow the development of next-generation, high-performance, durable, and affordable ORR and OER catalysts for practical energy conversion devices under operation conditions in the near future.

2. Experimental Section

Chemicals were obtained from commercial sources and used without further purification unless otherwise specified. All proteo and deutero aqueous solutions were prepared freshly each day using Milli-Q water (> 18 MΩ cm) and D_2O, respectively. For experiments at pH 0.3 and pD 0.3, H_2SO_4 (500 mM) and D_2SO_4 (500 mM) solutions were used, respectively. For experiments at pH 7 and pD 7, proteo potassium phosphate buffer solution (H-phos, 100 mM) and deutero potassium phosphate buffer solution (D-phos, 100 mM) were used, respectively. For experiments at pH 13 and pD 13, NaOH (100 mM) and NaOD (100 mM) solutions were used, respectively. For experiments at pH 14 and pD 14, NaOH (1 M) and NaOD (1 M) solutions were used, respectively. Solutions were sparged with Ar or O_2, both of which were dried using a drying tube, for 30 min prior to each experiment.

Electrochemical studies were carried out using a CH Instruments 760 D Electrochemical Workstation (Austin, TX) at room temperature (24 °C to 26 °C). ORR experiments were performed in a three-compartment cell with an aqueous “no leak” Ag/AgCl (3 M KCl, eDAQ, Inc.) reference electrode separated from the working electrode by a Luggin capillary. A deviation of ca. 1.3 mV in the electrode potential of the Ag/AgCl reference was expected due to a temperature deviation of 2 °C.[69] A carbon rod counter electrode was separated from the working electrode by a glass frit. OER experiments were performed in a sealed cell with a Pt mesh counter electrode and a "no leak" Ag/AgCl reference electrode. Electrochemical impedance spectra (EIS) for iR correction were collected using a SP-150 potentiostat (Bio-Logic). The resistance, R, was typically ca. 3 Ω, and iR correction was done following published procedures.[70-72] Unless otherwise stated, the scan rate was 10 mV/s. The measured potential by the Ag/AgCl reference electrode did not shift in proteo and deutero solutions, as confirmed by the peak position of the Fe(II/III) wave of $K_3Fe(CN)_6$.[73] Electrochemical potentials are reported relative to the reversible hydrogen electrode (RHE) the value of which was measured by sparging the solution with H_2 (1 atm) and monitoring the open circuit potential between the Ag/AgCl reference and a Pt wire introduced following the measurement.[23] All experiments performed were at least quadruplicated. Voltammograms shown are from representative trials. Error bars presented represent standard deviations of all trials.

For ORR studies, rotating disk electrode (RDE) experiments were performed using a glassy carbon (GC) disk electrode (0.196 cm^2, E5 series, Pine instruments) connected to a MSRX rotator (Pine Instruments). The GC working electrode was polished sequentially with 0.25 and 0.05 μm diameter diamond polish (Buehler), and sonicated in water after each stage. PANI-Fe-C was prepared according to published procedure.[6] Ink slurries were prepared using Nafion 117 solution (5 wt % in alcohols, Sigma-Aldrich) or solution made of Nafion powder (Sigma-Aldrich). To prepare the binder solution from Nafion powder, Nafion powder (5 mg) was dissolved in IPA or IPA-D8 (95 mg). After sonicating the mixture for 10 min and heating to 70 °C for 1 min, PEG200 (5 mg) was added. PANI-Fe-C (7.2 mg), Pt supported on Vulcan XC-72 (Pt/C, 7.2 mg, 20 wt. %, E-Tek Inc.), or Pd supported on Vulcan XC-72 (Pd/C, 7.2 mg, 20 wt. %, E-Tek Inc.) was dispersed in EtOH (500 μL) or EtOD (500 μL). After sonicating for 20 min, Nafion solution (10 μL) was added. For the binderless cases, the inks were prepared in analogous manner in the absence of Nafion solution. The resultant suspension was further sonicated for 20 min to afford an ink slurry, which was deposited onto a GC electrode and then dried under a stream of Ar.

For OER studies, Au substrates were fabricated from glass microscope coverslips (Gold Seal No. 1, 150 μm thick) modified on one side by electron beam deposition of 20 nm Ti followed by 200 nm Au. The geometric areas of the electrodes were typically ca. 1 cm^2. The Au electrodes were annealed with a H_2 flame prior to use. The Ni films (~ 300 nm) were electrodeposited onto Au cantilevers in an aqueous bath of $NiSO_4$ (0.5 M) and H_3BO_3 (0.4 M) adjusted to pH 3 using H_2SO_4 using a pulse deposition method: held at -4 mA cm^{-2} for 100 s followed by 10 s of resting time, and repeated for two more times. [68] For studies in deutero solutions, the bath was prepared using D_3BO_3 (0.4 M) in D_2O and adjusted to pD 3 using D_2SO_4. Co films (~ 300 nm) were prepared in an analogous manner using $CoSO_4$ (0.5 M) instead.

3. Results and Discussion

3.1 ORR in proteo and deutero solutions

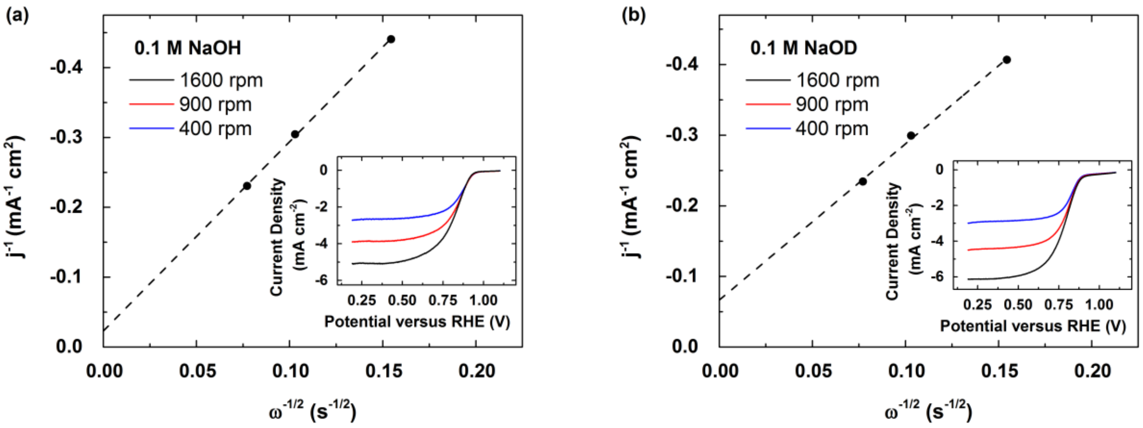

Figure 1. Koutecky-Levich plots and rotating disk electrode (RDE) voltammograms (insets) of PANI-Fe-C in (a) pH 13 and (b) pD 13 O_2-saturated solutions with a scan rate of 10 mV s^{-1} at 400 (blue), 900 (red), and 1600 (black) rpm.

To determine the role of protons in the RDS for the ORR, we carried out Koutecky-Levich analysis in proteo and deutero solutions. The voltammograms of O_2 reduction catalyzed by PANI-Fe-C, Pt/C, and Pd/C under various rotation regimes in acidic, neutral, and basic conditions and the corresponding Koutecky-Levich plots are shown in Figures 1 and S1-3. We note that in some cases the O_2-diffusion limited current densities observed in proteo solution are different from those found in deutero solution. However, the difference in the mass transport limited current density does not directly relate to the KIE (see S.I. note 1 for discussion on KIE determination). The KIE was determined from the voltammograms by comparing the kinetically limited current density (j_K) given by the Koutecky-Levich equation:

$$\frac{1}{j} = \frac{1}{j_K} + \frac{1}{j_{l,c}}$$

$$j_K = nFk_fC^*_{O_2}$$

where $j_{l,c}$ = limiting cathodic current density, n = number of electrons transferred, F = Faraday's constant, k_f = heterogeneous rate constant for reduction, and $C^*_{O_2}$ = the bulk concentration of O_2.

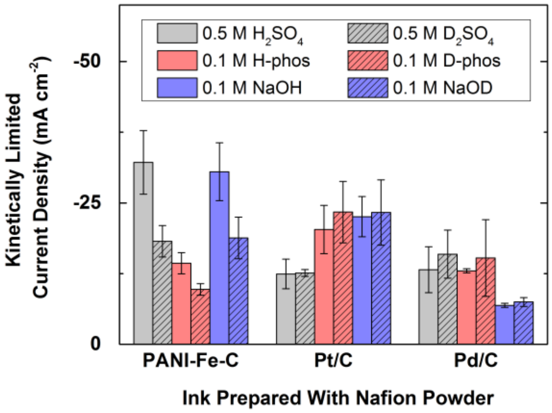

Figure 2. Bar graphs summarizing the kinetically limited current densities obtained from Koutecky-Levich analyses of O_2 reduction voltammograms for PANI-Fe-C, Pt/C and Pd/C with inks prepared with Nafion powder in O_2-saturated 0.5 M H_2SO_4 (gray), 0.5 M D_2SO_4 (gray with strips), 0.1 M pH 7 phosphate buffer (red), 0.1 M pD 7 phosphate buffer (red with strips), 0.1 M NaOH (blue), and 0.1 M NaOD (blue with strips) solutions.

In order to observe the kinetic effect of the replacement of hydrogen with deuterium, inks were prepared using Nafion powder to eliminate the effect of trapped protons in the catalyst film (see Figures S4-11 and Table S1-3 for further discussion). Figure 2 shows bar graphs that summarizes the kinetically limited current densities of PANI-Fe-C, Pt/C, and Pd/C in O_2-saturated acidic, neutral and basic solutions. The observed kinetically limited current densities are comparable to the values found for conventional heterogeneous ORR catalysts.[74-76] We observe a dramatic decrease in the ORR kinetically limited current density for the deutero case relative to the proteo case for PANI-Fe-C in all three pH regimes. By way of contrast, the ORR j_K for Pt/C and Pd/C exhibits only a slight dependence on whether the electrolyte is deuterated or not, which is attributed to the difference in bulk concentration of O_2 in proteo and deutero solvents (see S.I. note 1 for further discussion). By accounting for the differences in the value of

$C_{O_2}^*$ in the two solutions, the kinetic isotope effects for the ORR catalyzed by PANI-Fe-C, Pt/C and Pd/C can be calculated.

Table 1. Summary of the kinetic isotope effect of ORR catalyzed by PANI-Fe-C, Pt/C, and Pd/C in acidic (0.5 M sulfuric acid), neutral (0.1 M, pH 7 phosphate buffer) and basic (0.1 M NaOH/(D)) conditions.

Catalysts	PANI-Fe-C	Pt/C	Pd/C
Acidic	1.9 ± 0.5	1.1 ± 0.2	0.9 ± 0.4
Neutral	1.6 ± 0.3	1.0 ± 0.3	0.9 ± 0.4
Basic	1.8 ± 0.5	1.0 ± 0.3	1.0 ± 0.2

The majority of the decrease in the kinetically limited current density observed for the NPM catalyst is therefore attributed to a KIE. Table 1 shows the KIE corrected for the differences in $C_{O_2}^*$ in proteo and deutero solutions observed for PANI-Fe-C, Pt/C and Pd/C catalysts. For PANI-Fe-C, a KIE of approximately 2 was observed while for Pt/C a KIE of 1 was observed in all three pH regimes. The observed KIEs for the non-precious metal catalyst demonstrate the involvement of protons from solution at or before the RDS of the ORR. Pt/C exhibits a fairly low overpotential for the ORR, while that for PANI-Fe-C is somewhat higher. We wanted to test whether a higher overpotential for the ORR might be correlated with sensitivity to deuteration. Experiments using Pd/C, a catalyst that exhibits a higher overpotential for ORR than Pt/C, also show a KIE of 1, indicating that for these precious metal ORR catalysts (Pt/C and Pd/C) the RDS is a proton-independent electron transfer process.

3.2 Mechanistic insight of the ORR

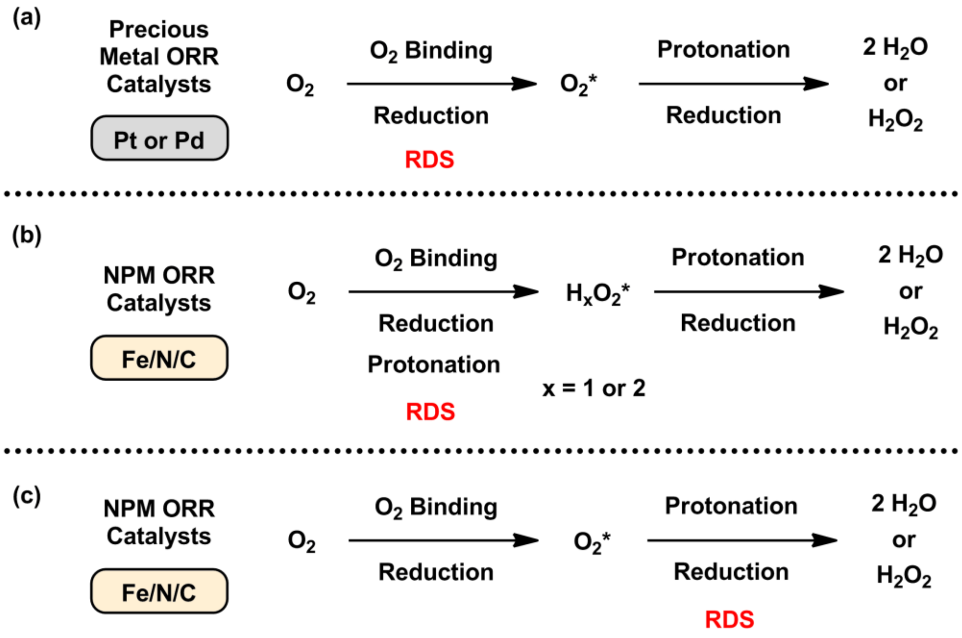

Figure 3. Possible mechanisms for the ORR on (a) precious metal and (b-c) non-precious metal materials. O_2^* and $H_xO_2^*$ represent surface-adsorbed, partially-reduced O_2 species without and with protonation, respectively. x = 1 or 2. RDS is shown in red.

Together, these findings suggest that the ORR proceeds by different mechanisms in the two classes of ORR catalysts investigated in this work. Figure 3 shows three possible mechanisms associated with the ORR catalyzed by either precious metals (Figure 3a) or a NPM ORR catalyst (Figure 3b and 3c). The lack of a KIE in the precious metal catalysts indicates that protons do not participate in the RDS of the ORR, confirming that the RDS of O_2 reduction by Pt and Pd is an electron transfer step (Figure 3a), at least in the high overpotential region.[18,27] The presence of an electron-transfer-limited RDS is fully consistent with the 120 mV dec^{-1} Tafel slope observed in the so-called Langmuir region of the ORR voltammetry.[2]

For the NPM ORR catalyst examined, the presence of a KIE ≈ 2 indicates that protons are involved at or before the RDS. Two possible general mechanisms are consistent with this insight. In the mechanism presented in Figure 3b, protons are associated with the initial reduction of O_2 during the RDS. Figure 3c displays a mechanism whereby protons likely interact with a bound partially-reduced O_2 species during the RDS. Unfortunately, our data cannot differentiate between the two proposed ORR pathways shown in Figures 3b and 3c for NPM catalysts. Previous work has shown that the ORR onset potential of NPM catalysts is pH-dependent,[8,21,23] further supporting the involvement of at least one protonation step at or before the RDS in the ORR mechanism. Our experiments using PANI-Fe-C as a model NPM catalyst show the presence of a KIE, consistent with the proposed mechanisms.

The direct evidence demonstrated by our KIE studies that different ORR catalysts achieve the same reaction via different mechanisms provides an important distinction when considering the design of new catalyst materials. An electron transfer RDS suggests that proton transfer plays a negligible role in determining the ORR kinetics on Pt. Therefore, methods to improve the ORR activity of Pt include alloying Pt with Ni and other transition metals to destabilize the surface OH poisons instead of enhancing proton transfer kinetics.[77-79] Alternatively, the presence of a KIE on the NPM catalyst examined here suggests that improvements in catalyst performance require specific attention to proton transfer during the RDS in addition to the electron transfer step(s).

3.3 Electrodeposited Ni and Co OER catalysts in proteo and deutero solutions

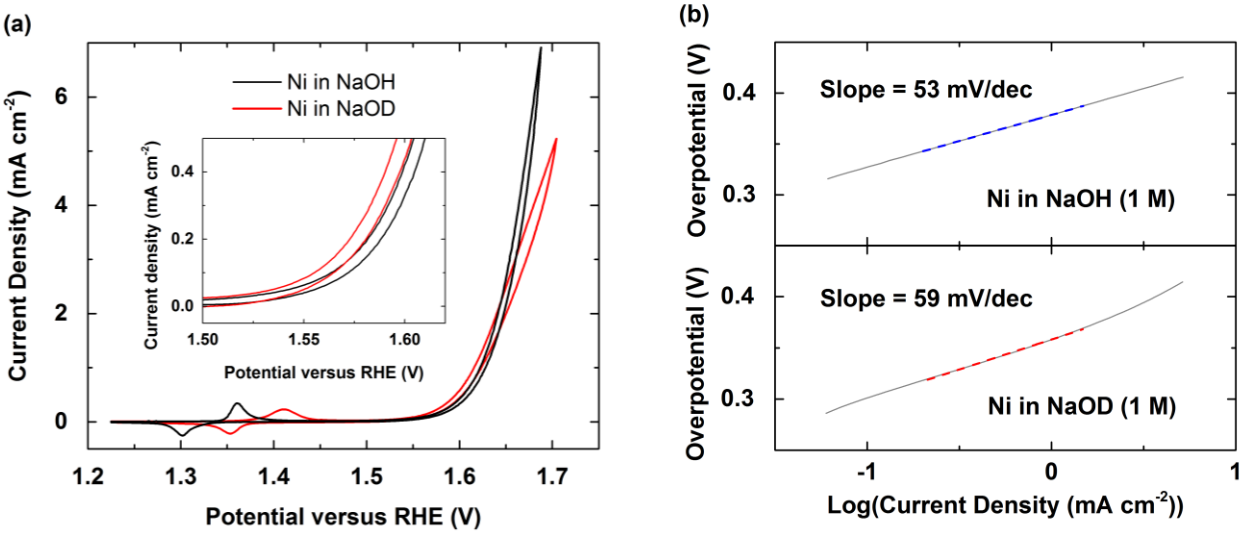

Figure 4. (a) IR-corrected CVs of Ni in NaOH (1 M) and NaOD (1 M) solutions. Inset displays the OER onset region. (b) Tafel plots of Ni in (top) 1 M NaOH and (bottom) 1 M NaOD solutions.

After examining proton involvement in the ORR, we next investigate the effect of protons on the OER. Figure 4a shows cyclic voltammograms (CVs) obtained from Ni in basic proteo and deutero solutions starting with the anodic sweep. Similar to previous reports in alkaline solutions,[33,80,81] Ni metal is spontaneously oxidized to Ni(II) hydroxide upon immersion,[53,82] and is then further oxidized to generate Ni(III) oxyhydroxide at 1.362 V. At 1.600 V, the electrodeposited Ni electrode delivers an OER current density of 0.5 mA cm^{-2}.

The black line in Figure 4a displays the $Ni(OH)_2$/NiOOH redox wave with a midpoint potential ($E_{1/2}$) of 1.333 V. The red line displays the $Ni(OD)_2$/NiOOD redox wave with a $E_{1/2}$ of 1.388 V. The position of the redox wave in deutero solution is ca. 55 mV more positive than that obtained in proteo solution, indicating that the oxidation of $Ni(OD)_2$ to NiOOD is thermodynamically more difficult than the oxidation of $Ni(OH)_2$ to NiOOH. Figure S12 summarizes other information related to the Ni(II/III) redox wave. To confirm the shift in the

Ni(II/III) wave with deuteration, we carried out similar experiments using Ni foil in proteo and deutero solutions and observed a 40 mV positive shift in deutero solution similar to the case using electrodeposited Ni (Figure S13). We note that these shifts in potential are not due to reference electrode effects, as confirmed by experiments with $K_3Fe(CN)_6$ which demonstrated identical potentials for the Fe(II/III) wave in both proteo and deutero media.[73]

Similar positive shifts upon deuteration have been observed for a variety of cationic transition metal complexes and are explained in two ways.[73,83,84] First, because the O-D bond is stronger than the O-H bond,[85] breaking the O-D bond is energetically more costly and the anodic wave shifts positive. Second, Ni(III) has a tighter solvation shell than Ni(II) and D_2O forms a stronger deuterium bonding network relative to the hydrogen bonding network of H_2O.[73] Therefore, there is a greater increase in entropy when the deuterated solvent structure relaxes during the reduction of Ni(III) to Ni(II).[83] Due to the more favorable change in entropy that occurs upon reducing Ni(III) to Ni(II) in deutero solutions, the cathodic wave shifts positive. Since both the anodic and cathodic waves shift positive, the $E_{1/2}$ shifts positive accordingly.

Figure S14 shows the CVs of Ni prepared in proteo solution and interrogated in deutero solution and CVs of Ni prepared in deutero solution and interrogated in proteo solutions. The CVs show that Ni metal film prepared in H solution and interrogated in D solution exhibit a Ni(II/III) redox wave more positive than that found using a Ni metal film prepared in D solution and interrogated in H solution. This result suggests that the shift in redox potential does not depend on the solution in which the film is prepared. Instead, the shift depends upon the solution in which the voltammetry is recorded, a condition analogous to the case presented in Figure 4. This “cross” experiment further demonstrates that preparing Ni metal film in H and D solution does not leave a detectable trace amount of H or D residual in the electrodeposited film.

Therefore, pulse deposition of Ni in pH- or pD-controlled solution likely leads to electrodeposits consisting of pure Ni metal films absent hydroxide, deuteroxide, oxyhydroxide, and/or oxydeuteroxide contamination.

The inset to Figure 4a shows a blowup of the OER onset region in both proteo and deutero solutions. Interestingly, the inset shows that the OER in D_2O exhibits a more negative onset and a lower overpotential at 0.5 mA cm^{-2} relative to the same system in H_2O. Figure 4b shows the Tafel slopes of OER catalyzed by Ni in proteo and deutero basic solutions. The Tafel slope found in NaOD at the low overpotential region (where η ranges between 0.3 and 0.4 V) is 59 mV dec^{-1} (Figure 4b, top), a value that is somewhat greater than the corresponding slope (53 mV dec^{-1}) found in NaOH (Figure 4b, bottom). Recent Tafel slope values for the OER in NaOH on Ni at the low overpotential range from 51 to 54 mV dec^{-1}.[86] At higher overpotentials, the NaOH and NaOD OER traces cross at 1.65 V versus RHE, likely due to the faster diffusion rate of H_2O relative to D_2O from bulk solution to the electrode surface where they interact with the oxide layers during OER.[87,88] The contribution of differential diffusion rates at low overpotential is insignificant because there are enough reactants between the oxide layers when the rate of OER is low. Therefore for the KIE analysis, we focus at the low overpotential region where the kinetics of the reaction is not dominated by the mass diffusion from reactants from the bulk solution to the catalytic site on the electrode surface.

Table 2. Summary of the overpotential at 0.5 mA cm^{-2}, Tafel slope and kinetic isotope effect of OER catalyzed by Ni and Co in 1 M NaOH and 1 M NaOD solutions.

Condition	Overpotential at 0.5 mA cm^{-2} (V)	Tafel Slope (mV dec^{-1})	k_H/k_D
Ni in 1 M NaOH	0.370 ± 0.006	53 ± 1	0.6 ± 0.1
Ni in 1 M NaOD	0.337 ± 0.006	59 ± 1	
Co in 1 M NaOH	0.330 ± 0.007	57 ± 1	0.5 ± 0.1
Co in 1 M NaOD	0.285 ± 0.002	63 ± 1	

Table 2 lists the OER activity of Ni found in Figure 4a, the OER Tafel slope obtained at the low overpotential region from Tafel analysis (Figure 4b), and k_H/k_D of Ni in proteo and deutero solutions. The KIE of OER was determined from the voltammograms using the Tafel equation:

$$\eta = \frac{R\,T}{\alpha\,n_a\,F} ln\,j_0 - \frac{R\,T}{\alpha\,n_a\,F} ln\,j$$

$$j_0 = nFk_0C^*$$

where η = overpotential, R = ideal das constant, T = temperature, α = transfer coefficient, n_a = number of electrons transferred during the rate-determining step, F = Faraday's constant, j_0 = exchange current density, j = current density, n = total number of electrons transferred, k_0 = standard heterogeneous rate constant, and C^* = bulk concentration of species (see S.I. note 2 for further information on KIE determination). Using the Tafel slopes found, the calculated KIE is 0.6. A k_H/k_D value of below 1 is indicative of an inverse KIE.[13,14]

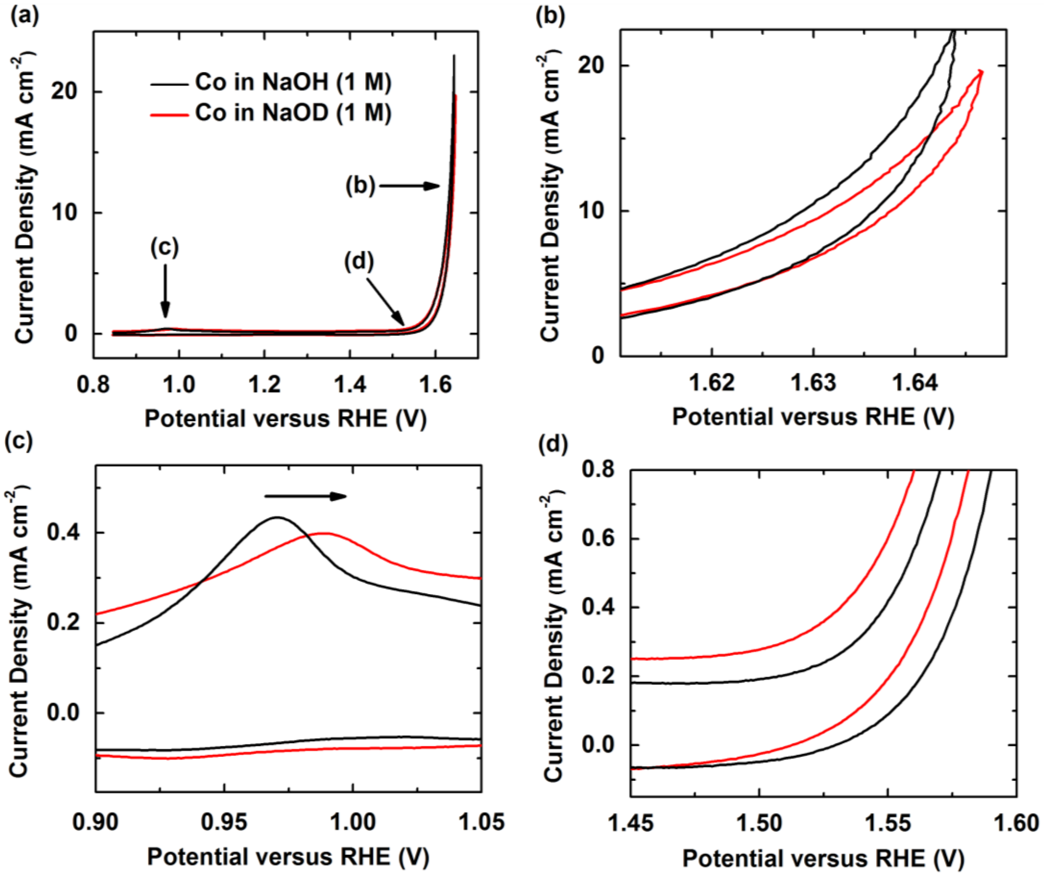

Figure 5. (a) IR-corrected CVs of Co in NaOH (1 M) and NaOD (1 M) solutions. (b), (c), and (d) display the blowups of the diffusion-controlled OER region, the Co(II/III) redox region, and the OER onset region, respectively.

To test the generality of the inverse KIE in alkaline OER catalysis, we next evaluate the effect of deuteration on the OER on Co electrodes. Figures 5a-d display the IR-corrected CVs of Co obtained in basic proteo and deutero solutions and Figure S15a-d shows the corresponding uncorrected data. Our Co OER results match with previous reports.[45] Figure 5c compares the anodic peak positions of the Co(II/III) wave in proteo and deutero basic solutions. Comparing to the Ni case (*vide supra*), the Co(II/III) anodic peak in 1 M NaOD is at 0.987 V versus RHE, which is slightly more positive relative to that found in 1 M NaOH (0.978 V versus RHE). The difference between the OER current densities measured at high overpotential between proteo and deutero solutions found for Co is less apparent as compared to the Ni case. Although Ni and Co exhibit the same qualitative trends, the dissimilarities in the magnitude observed is likely due to the fact that Co forms multiple types of oxides and hydroxides before and during OER,[35] while Ni only forms $Ni(OH)_2$ and NiOOH in alkaline.[39] Table 2 lists the OER overpotentials of Co at 0.5 mA cm^{-2} obtained in proteo and deutero basic solutions, which are similar to those found using Ni as the OER catalyst. Figure 6 shows the Tafel plots of Co at the low overpotential region. The calculated KIE is about 0.5 (Table 2), which is similar to the KIE value found for the Ni case.

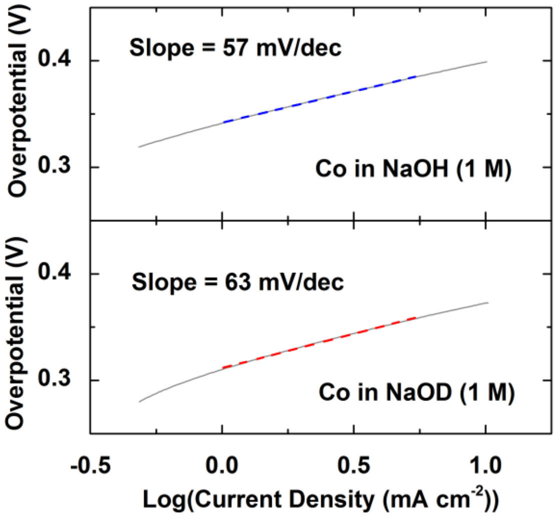

Figure 6. Tafel plots of Co in (a) 1 M NaOH and (b) 1 M NaOD solutions.

3.4 Origins of the inverted KIE during the OER

We next address the possible origins of the inverse KIE found for the OER on Ni and Co in basic solutions. First, inverse KIEs are usually associated with differences in the steric environment of the active site caused by deuteration during the RDS.[14] For example, interconversions of sterically-hindered biaryls typically exhibit inverse KIEs of ca. 0.8.[14,89-92] A comparison between the racemization rates of 2,2’-dibromo-4,4’-dicarboxybiphenyl and its 6,6’-dideutero derivative gives an inverse KIE of 0.85.[93-95] Another comparison of the inversion rates of 9,10-dihydroxy-4,5-dimethylphenanthrene and its derivative with the two methyl groups fully deuterated yields an inverse KIE of 0.86.[96,97] Translating this steric argument to the OER leads to a possible scenario shown in Figure 7a where surface crowding could lead to an inverse KIE. In this model, the O-D bond is stronger than the O-H bond.[85] This means that the O-D bond in MO(OD) is shorter than the O-H bond in MO(OH), where M = Ni or Co. The shorter O-D bond could lead to a less occluded active site, resulting in a less hindered pathway for reactants to diffuse to the MO(OD) surface as compared to the MO(OH) surface. As a result, the less bulky MO(OD) structure would exhibit faster OER kinetics. Our model shows a particular case in which a single metal center is the locus of reactivity, but this idea could easily be extended to a multi-metallic active site, as has been suggested in other work.[34,35,39,98-100]

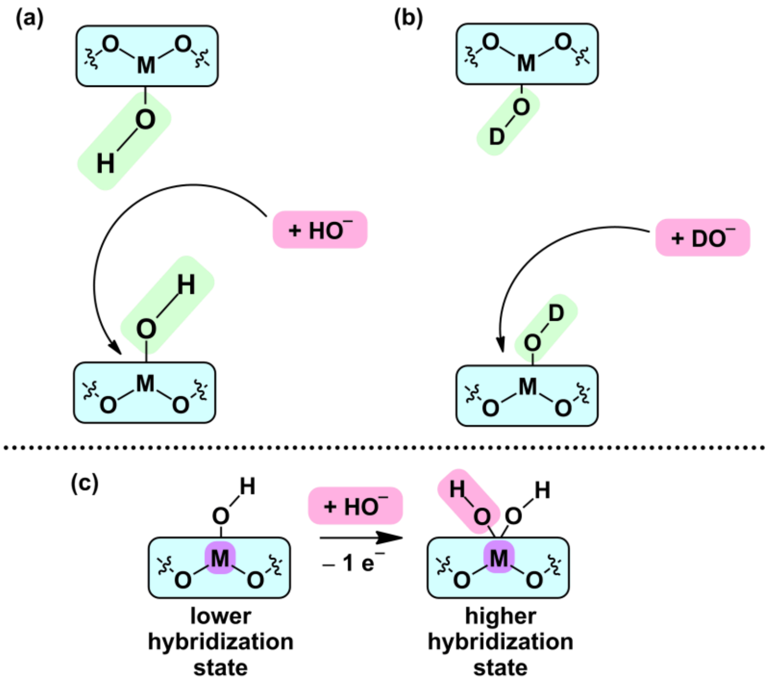

Figure 7. A possible scenario of the OER process catalyzed by M (Ni or Co) surface oxyhydroxides in which an inverse KIE can be observed highlighting (a) the hydroxide and (b)

deuteroxide (green) that impart KIE on the adjacent bond forming or breaking site, and (c) the change in coordination environment and the corresponding rehybridization of the metal center (violet) upon accommodating an incoming $^{-}$OH species (pink).

A second origin of an inverse KIE results from a change from a less hybridized state to a more hybridized state (e.g. sp^2 to sp^3) during the RDS.[14] The typical observed KIE relating to this type of rehybridization is about 0.9. For example, solvolyses of methyl esters containing iodide and their deuterated derivatives lead to inverse KIEs of ca. 0.87.[101] A change in the hybridization state during the RDS leads to a larger difference in the Δ zero point energy (ZPE) of the transition state than in the Δ ZPE in the ground state. Figure 7b displays a possible scenario where a change in the coordination environment of M (Ni or Co) could result in an inverse KIE. In this model, the MO(OH) changes hybridization state upon binding of a $^{-}$OH. Therefore, the Δ ZPE for the case involving $^{-}$OD as the incoming species may be larger than that for the $^{-}$OH case.

A third explanation for an inverse KIE invokes an electronic argument.[14] The magnitude of an inductive KIE is typically about 0.95, a less significant effect than the two types of inverse KIEs previously discussed.[14,102] Deuterium substitution at a position more remote than β to the reaction center along an alkyl chain yields an inverse KIE of 0.97.[103,104] D is more electropositive than H, meaning that D is more electron releasing.[105,106] Due to the difference in electron donating ability, $^{-}$OD is more polar than $^{-}$OH, resulting in a higher $^{-}$OD flux towards the positively charged metal centers.

At this point, it is not possible to distinguish between the different origins of the inverted KIE as it applies to the OER. The relatively large inverse KIEs found for the OER catalyzed by

Ni and Co may result from a combination of all three effects mentioned above, as has been suggested in other systems.[13,103]

3.5 Mechanistic Implications for the OER

We next evaluated OER mechanism in the context of the inverted KIE. Many OER mechanisms have been proposed.[100] Here, by utilizing the insight we obtained from the KIE experiments, we attempt to identify the plausible RDS in four OER mechanisms commonly discussed in literature. The lack of a primary normal KIE indicates that O-H or O-D bonds are not cleaved during the RDS of the OER. Instead, the observed inverse KIE suggests that the RDS involves forming or breaking of a bond which (1) does not directly involve H or D, (2) is adjacent to an OH or OD moiety, and/or (3) requires a change from a less to a more hybridized state on the metal or oxygen center.

$$^{-}\mathrm{OH} \longrightarrow (\mathrm{OH})_{ads} + e^{-} \qquad (1)$$

$$(\mathrm{OH})_{ads} + {}^{-}\mathrm{OH} \longrightarrow (\mathrm{O}^{-})_{ads} + \mathrm{H_2O} \qquad (2)$$

$$(\mathrm{O}^{-})_{ads} \longrightarrow (\mathrm{O})_{ads} + e^{-} \qquad (3)$$

$$2\,(\mathrm{O}^{-})_{ads} \longrightarrow \mathrm{O_2} \qquad (4)$$

Figure 8. An OER mechanism focusing on the adsorbed species.[86,87]

First, we consider the simplest case that emphasizes adsorbed species.[99,107] The mechanism presented in Figure 8 considers the adsorbed reactants only and discounts the role of the underlying metal oxides. $^{-}$OH adsorbs on the surface upon oxidation and generates adsorbed O^{-} species upon deprotonation (steps 1 and 2). Two O^{-} species react to give off $\mathrm{O_2}$ upon further oxidation (steps 3 and 4). Step 1 is not sterically hindered and step 2 contains direct O-H bond breaking. No protons are adjacent to the bond breaking/forming sites in steps 3 and 4. Since none of the steps in this mechanism fits any of the criteria that leads to an inverse kinetic isotope effect, our data does not support any of the steps shown in the mechanism presented in Figure 8 to be rate-limiting. Several other papers dismiss the mechanism in Figure 8 as a prevalent OER mechanism on metal oxide surfaces.[34,39] One of the reasons steps in Fig. 8 are not favored is the involvement of high energy species such as OH radicals and O atoms.[98]

$$\mathrm{M(OH)_2} + {}^{-}\mathrm{OH} \longrightarrow \mathrm{M(OH)(O)} + \mathrm{H_2O} + \mathrm{e^{-}} \tag{5}$$

$$\mathrm{M(OH)(O)} + {}^{-}\mathrm{OH} \longrightarrow \mathrm{M(OH)(OOH)} + \mathrm{e^{-}} \tag{6}$$

$$\mathrm{M(OH)(OOH)} + {}^{-}\mathrm{OH} \longrightarrow \mathrm{M(OH)(O_2)} + \mathrm{H_2O} + \mathrm{e^{-}} \tag{7}$$

$$\mathrm{M(OH)(O_2)} + {}^{-}\mathrm{OH} \longrightarrow \mathrm{M(OH)_2} + \mathrm{O_2} + \mathrm{e^{-}} \tag{8}$$

Figure 9. A mechanism of OER catalyzed by metal surfaces (M = Ni or Co) with neighboring bound OH species.[34,80] Plausible RDS are highlighted in red. Proton that imparts KIE on the adjacent bond forming or breaking site is highlighted in green.

Figure 9 displays an OER pathway that implicates adjacent OH species in the OER mechanism.[39,86] Steps 5 and 7 show the deprotonation of surface-bound OH and OOH species by aqueous $^{-}$OH. Since direct O-H bond cleavage exhibits a normal KIE,[13,14] steps 5 and 7 are likely not rate-limiting. Step 6 shows an attack of a bridging oxide or terminal oxo by $^{-}$OH with a neighboring surface-bound OH moiety, while step 8 displays an O_2 releasing step and a $^{-}$OH association step. Due to the heterogeneity of the metal surfaces and the ambiguity of the binding modes of the O, OOH and O_2 species,[45,68,108,109] the accurate assignment of the RDS in the case presented in Figure 9 is difficult. Since a sterically-hindering OH moiety is within the vicinity of the bond breaking or forming site with a possible rehybridization event occurring, we cannot exclude the possibility that either step 6 or 8 can be rate-limiting.

$$MO(OH) + {}^{-}OH \longrightarrow MO(OH)_2 + e^{-} \tag{9}$$

$$MO(OH)_2 + {}^{-}OH \longrightarrow MO(OOH) + H_2O + e^{-} \tag{10}$$

$$MO(OOH) + {}^{-}OH \longrightarrow MO(O_2) + H_2O + e^{-} \tag{11}$$

$$MO(O_2) + {}^{-}OH \longrightarrow MO(OH) + O_2 + e^{-} \tag{12}$$

Figure 10. An OER mechanism that involves metal oxides (M = Ni or Co).[34,98,110] A plausible RDS is denoted in red. A proton that imparts an inverse KIE on the adjacent bond forming or breaking site is denoted in green.

Figure 10 shows an OER mechanism that involves an addition of a $^{-}$OH to the metal center and changes the geometry and the coordination number of the metal center.[34,98,110] Step 9 is likely a RDS because it involves the formation of a M-O bond next to an existing OH moiety, which provides the steric crowding required for the observed inverse KIE.[14] Steps 10 and 11 are not rate-limiting because they contain deprotonation steps and direct cleavage of an O-H bond should give a measurable normal KIE.[13] Step 12 involves an O_2 dissociation step and a $^{-}$OH addition step. However, the reaction site is not occluded by bound OH moieties, suggesting that step 12 is not rate-limiting.

$$MO(OH) + {}^{-}OH \longrightarrow MO(OH)_2 + e^{-} \tag{13}$$

$$MO(OH)_2 \longrightarrow (MO)^{+} - H_2O_2 + e^{-} \tag{14}$$

$$(MO)^{+} - H_2O_2 + 2\,{}^{-}OH \longrightarrow MO(OH) - HO_2 + H_2O + e^{-} \tag{15}$$

$$MO(OH) - HO_2 + {}^{-}OH \longrightarrow MO(OH) + O_2 + H_2O + e^{-} \tag{16}$$

Figure 11. An OER mechanism that entails a H_2O_2 intermediate species.[29,88] Plausible RDS is represented in red. Proton that imparts KIE on the adjacent bond forming or breaking site is represented in green.

Figure 11 shows a pathway less frequently discussed in literature. Intriguingly, this pathway invokes the involvement and release of a H_2O_2 intermediate.[34,98] Identical to step 9 presented in Figure 10, step 13 in Figure 11 is a plausible RDS because the formation of a M-O bond close to an existing OH group fits the criteria required to yield an inverse KIE.[14] The release of H_2O_2 depicted in step 14 likely results in a change of the metal center from a more hybridized state to a less hybridized step, a change usually associated to a normal KIE.[13] Step 15 involves the addition of a ^{-}OH to M without neighboring OH functionalities. Steps 15 and 16 contain deprotonation steps of species not directly attached to the electrode surface. Therefore, the likelihood of steps 14-16 to be rate-limiting is low.

The goal of this section is not to disprove any mechanism proposed in the literature. Rather we intend to identify the plausible RDS in the many OER pathways suggested over the years. In Figures 8-11, we classify the many OER mechanisms previously proposed into four broad categories based on species involved in the process. Our observation of an inverse KIE for the OER suggest that the OER RDS likely involves breaking or forming a bond that (1) does not involve H or D directly, (2) occurs at an occluded site decorated by nearby OH or OD groups, and/or (3) requires a rehybridization of the reaction site to a more hybridized state. This observation provides constraints as to the nature of the RDS during the OER, constraints that must be addressed during the search for more competent OER catalysts.

Conclusion

In this report, we investigated the effect of deuteration on the ORR and the OER activities of both precious and NPM catalysts. For the ORR on the precious metal catalysts Pt and Pd, we found a KIE of 1, in agreement with previous studies. For the ORR on Fe-based

NPM catalysts, we found a KIE of 2 which demonstrates the involvement of protons at or before the RDS. For the OER on Ni and Co, we found an inverse KIE of 0.6 and 0.5, respectively. The OER results suggest that a rate-limiting bond breaking or forming event which does not involve the direct cleavage of an O-H bond, but likely occurs at an occluded site on the electrode surface with adjacent OH functionalities. The mechanistic insight gained from our KIE studies of the ORR and OER should be generally useful to the broad community that is interested in both the fundamental aspects of these PCET processes and the development of active, robust, and inexpensive catalysts for these energy-intensive reactions.

Associated Content

Supporting Information. Additional information including linear sweep and cyclic voltammograms, Koutecky-Levich analyses, notes and supplementary tables as discussed in the text. This material is available free of charge via the Internet at http://pubs.acs.org.

Author Information

Corresponding Author

[*] Tel: 217-333-8329. Fax: 217-244-3186. E-mail: agewirth@illinois.edu.

Notes: The authors declare no competing financial interest.

Acknowledgments

E.C.M.T. acknowledges a Croucher Foundation Scholarship. We thank the National Science Foundation (**grant #**) for support of this research. This work was carried out in part in the

Frederick Seitz Materials Research Laboratory Central Facilities, which are partially supported by the US Department of Energy (DE-FG02-07ER46453 and DE-FG02-07ER46471).

References

(1) Katsounaros, I.; Cherevko, S.; Zeradjanin, A. R.; Mayrhofer, K. J. J. *Angew. Chem. Int. Ed.* **2014**, *53*, 102-121.
(2) Zhang, J.; Xie, Z.; Zhang, J.; Tang, Y.; Song, C.; Navessin, T.; Shi, Z.; Song, D.; Wang, H.; Wilkinson, D. P.; Liu, Z.-S.; Holdcroft, S. *J. Power Sources* **2006**, *160*, 872-891.
(3) Carmo, M.; Fritz, D. L.; Mergel, J.; Stolten, D. *Int. J. Hydrogen Energy* **2013**, *38*, 4901-4934.
(4) Gewirth, A. A.; Thorum, M. S. *Inorg. Chem.* **2010**, *49*, 3557-3566.
(5) Jaouen, F.; Proietti, E.; Lefevre, M.; Chenitz, R.; Dodelet, J.-P.; Wu, G.; Chung, H. T.; Johnston, C. M.; Zelenay, P. *Energy Environ. Sci.* **2011**, *4*, 114-130.
(6) Wu, G.; More, K. L.; Johnston, C. M.; Zelenay, P. *Science* **2011**, *332*, 443-447.
(7) Bergmann, A.; Martinez-Moreno, E.; Teschner, D.; Chernev, P.; Gliech, M.; de Araujo, J. F.; Reier, T.; Dau, H.; Strasser, P. *Nat. Commun.* **2015**, *6*.
(8) Boulatov, R.; Collman, J. P.; Shiryaeva, I. M.; Sunderland, C. J. *J. Am. Chem. Soc.* **2002**, *124*, 11923-11935.
(9) Barile, C. J.; Tse, E. C. M.; Li, Y.; Sobyra, T. B.; Zimmerman, S. C.; Hosseini, A.; Gewirth, A. A. *Nat. Mater.* **2014**, *13*, 619-623.
(10) Das, D.; Lee, Y.-M.; Ohkubo, K.; Nam, W.; Karlin, K. D.; Fukuzumi, S. *J. Am. Chem. Soc.* **2013**, *135*, 4018-4026.
(11) Klinman, J. P. *FEBS Journal* **2014**, *281*, 489-497.
(12) Nelson, S. D.; Trager, W. F. *Drug Metab. Dispos.* **2003**, *31*, 1481-1497.
(13) Gómez-Gallego, M.; Sierra, M. A. *Chem. Rev.* **2011**, *111*, 4857-4963.
(14) Saunders, W. H.; Melander, L. R. *Reaction Rates of Isotopic Molecules*; Wiley: New York, 1980.
(15) Conway, B. E.; Salomon, M. *J. Chem. Phys.* **1964**, *41*, 3169-3177.
(16) Salomon, M.; Conway, B. E. *Ber. Bunsen-Ges. Phys. Chem.* **1965**, *69*, 669-674.
(17) Krishtalik, L. I. *Electrochim. Acta* **2001**, *46*, 2949-2960.
(18) Ghoneim, M. M.; Clouser, S.; Yeager, E. *J. Electrochem. Soc.* **1985**, *132*, 1160-1162.
(19) Mayer, J. M.; Rhile, I. J. *BBA-Bioenergetics* **2004**, *1655*, 51-58.
(20) Thorseth, M. A.; Tornow, C. E.; Tse, E. C. M.; Gewirth, A. A. *Coord. Chem. Rev.* **2013**, *257*, 130-139.
(21) Tse, E. C. M.; Schilter, D.; Gray, D. L.; Rauchfuss, T. B.; Gewirth, A. A. *Inorg. Chem.* **2014**, *53*, 8505-8516.
(22) Tylus, U.; Jia, Q.; Strickland, K.; Ramaswamy, N.; Serov, A.; Atanassov, P.; Mukerjee, S. *J. Phys. Chem. C* **2014**, *118*, 8999-9008.
(23) Thorseth, M. A.; Letko, C. S.; Tse, E. C. M.; Rauchfuss, T. B.; Gewirth, A. A. *Inorg. Chem.* **2012**, *52*, 628-634.
(24) Inaba, M.; Kinumoto, T.; Kiriake, M.; Umebayashi, R.; Tasaka, A.; Ogumi, Z. *Electrochim. Acta* **2006**, *51*, 5746-5753.

(25) Coms, F. D. *ECS Trans.* **2008**, *16*, 235-255.
(26) Nørskov, J. K.; Rossmeisl, J.; Logadottir, A.; Lindqvist, L.; Kitchin, J. R.; Bligaard, T.; Jónsson, H. *J. Phys. Chem. B* **2004**, *108*, 17886-17892.
(27) Li, M. F.; Liao, L. W.; Yuan, D. F.; Mei, D.; Chen, Y.-X. *Electrochim. Acta* **2013**, *110*, 780-789.
(28) Mei, D.; He, Z. D.; Zheng, Y. L.; Jiang, D. C.; Chen, Y.-X. *Phys. Chem. Chem. Phys.* **2014**, *16*, 13762-13773.
(29) Hammes-Schiffer, S.; Soudackov, A. V. *J. Phys. Chem. B* **2008**, *112*, 14108-14123.
(30) Weinberg, D. R.; Gagliardi, C. J.; Hull, J. F.; Murphy, C. F.; Kent, C. A.; Westlake, B. C.; Paul, A.; Ess, D. H.; McCafferty, D. G.; Meyer, T. J. *Chem. Rev.* **2012**, *112*, 4016-4093.
(31) Laguna-Bercero, M. A. *J. Power Sources* **2012**, *203*, 4-16.
(32) Man, I. C.; Su, H.-Y.; Calle-Vallejo, F.; Hansen, H. A.; Martínez, J. I.; Inoglu, N. G.; Kitchin, J.; Jaramillo, T. F.; Nørskov, J. K.; Rossmeisl, J. *ChemCatChem* **2011**, *3*, 1159-1165.
(33) Doyle, R. L.; Godwin, I. J.; Brandon, M. P.; Lyons, M. E. G. *Phys. Chem. Chem. Phys.* **2013**, *15*, 13737-13783.
(34) Lyons, M. E. G.; Brandon, M. P. *Int. J. Electrochem. Sci.* **2008**, *3*, 1386-1424.
(35) Lyons, M. E. G.; Brandon, M. P. *Int. J. Electrochem. Sci.* **2008**, *3*, 1425-1462.
(36) Reier, T.; Oezaslan, M.; Strasser, P. *ACS Catal.* **2012**, *2*, 1765-1772.
(37) Hall, D. E. *J. Electrochem. Soc.* **1985**, *132*, 41C-48C.
(38) Dau, H.; Limberg, C.; Reier, T.; Risch, M.; Roggan, S.; Strasser, P. *ChemCatChem* **2010**, *2*, 724-761.
(39) Lyons, M. E. G.; Brandon, M. P. *J. Electroanal. Chem.* **2010**, *641*, 119-130.
(40) Miles, M. H.; Kissel, G.; Lu, P. W. T.; Srinivasan, S. *J. Electrochem. Soc.* **1976**, *123*, 332-336.
(41) Godwin, I. J.; Lyons, M. E. G. *Electrochem. Commun.* **2013**, *32*, 39-42.
(42) Rossmeisl, J.; Logadottir, A.; Nørskov, J. K. *Chem. Phys.* **2005**, *319*, 178-184.
(43) Jaksic, M. M.; Johansen, B.; Tunold, R. *Int. J. Hydrogen Energy* **1994**, *19*, 321-335.
(44) Behl, W. K.; Toni, J. E. *J. Electroanal. Chem. Interfacial Electrochem.* **1971**, *31*, 63-75.
(45) Yeo, B. S.; Bell, A. T. *J. Phys. Chem. C* **2012**, *116*, 8394-8400.
(46) Melendres, C. A.; Xu, S. *J. Electrochem. Soc.* **1984**, *131*, 2239-2243.
(47) Desilvestro, J.; Corrigan, D. A.; Weaver, M. J. *J. Electrochem. Soc.* **1988**, *135*, 885-892.
(48) Bewick, A.; Gutiérrez, C.; Larramona, G. *J. Electroanal. Chem.* **1992**, *333*, 165-175.
(49) Ismail, K. M.; Badawy, W. A. *J. Appl. Electrochem.* **2000**, *30*, 1303-1311.
(50) Kötz, R.; Neff, H.; Stucki, S. *J. Electrochem. Soc.* **1984**, *131*, 72-77.
(51) Peuckert, M. *Electrochim. Acta* **1984**, *29*, 1315-1320.
(52) Foelske, A.; Strehblow, H.-H. *Surf. Interface Anal.* **2002**, *34*, 125-129.
(53) Medway, S. L.; Lucas, C. A.; Kowal, A.; Nichols, R. J.; Johnson, D. *J. Electroanal. Chem.* **2006**, *587*, 172-181.
(54) Pralong, V.; Delahaye-Vidal, A.; Beaudoin, B.; Gerand, B.; Tarascon, J. M. *J. Mater. Chem.* **1999**, *9*, 955-960.
(55) Hillman, A. R.; Skopek, M. A.; Gurman, S. J. *Phys. Chem. Chem. Phys.* **2011**, *13*, 5252-5263.
(56) Totir, D.; Mo, Y.; Kim, S.; Antonio, M. R.; Scherson, D. A. *J. Electrochem. Soc.* **2000**, *147*, 4594-4597.
(57) Mo, Y.; Stefan, I. C.; Cai, W.-B.; Dong, J.; Carey, P.; Scherson, D. A. *J. Phys. Chem. B* **2002**, *106*, 3681-3686.

(58) Li, X.; Walsh, F. C.; Pletcher, D. *Phys. Chem. Chem. Phys.* **2011**, *13*, 1162-1167.
(59) Yau, S.-L.; Fan, F.-R. F.; Moffat, T. P.; Bard, A. J. *J. Phys. Chem.* **1994**, *98*, 5493-5499.
(60) Kong, F.; Kostecki, R.; McLarnon, F.; Muller, R. H. *Thin Solid Films* **1998**, *313–314*, 775-780.
(61) Lu, P. W. T.; Srinivasan, S. *J. Electrochem. Soc.* **1978**, *125*, 1416-1422.
(62) Hu, Y.; Scherson, D. A. *J. Phys. Chem. B* **1997**, *101*, 5370-5376.
(63) Kowal, A.; Niewiara, R.; Perończyk, B.; Haber, J. *Langmuir* **1996**, *12*, 2332-2333.
(64) Mo, Y.; Hwang, E.; Scherson, D. A. *J. Electrochem. Soc.* **1996**, *143*, 37-43.
(65) Birss, V. I.; Elzanowska, H.; Gottesfeld, S. *J. Electroanal. Chem. Interfacial Electrochem.* **1991**, *318*, 327-333.
(66) Juodkazytė, J.; Šebeka, B.; Stalnionis, G.; Juodkazis, K. *Electroanalysis* **2005**, *17*, 1734-1739.
(67) Zhen, C.-H.; Sun, S.-G.; Fan, C.-J.; Chen, S.-P.; Mao, B.-W.; Fan, Y.-J. *Electrochim. Acta* **2004**, *49*, 1249-1255.
(68) Hoang, T. T. H.; Cohen, Y.; Gewirth, A. A. *Anal. Chem.* **2014**, *86*, 11290-11297.
(69) Bard, A. J.; Parson, R.; Jordan, J. *Standard Potentials in Aqueous Solution*; Marcel Dekker, Inc., 1985.
(70) Bard, A. J.; Faulkner, L. R. *Electrochemical Methods: Fundamentals and Applications, 2nd Edition*; Wiley Global Education, 2000.
(71) van der Vliet, D.; Strmcnik, D. S.; Wang, C.; Stamenkovic, V. R.; Markovic, N. M.; Koper, M. T. M. *J. Electroanal. Chem.* **2010**, *647*, 29-34.
(72) Tse, E. C. M.; Gewirth, A. A. *J. Phys. Chem. A* **2015**, *119*, 1246-1255.
(73) Weaver, M. J.; Nettles, S. M. *Inorg. Chem.* **1980**, *19*, 1641-1646.
(74) Ye, H.; Crooks, J. A.; Crooks, R. M. *Langmuir* **2007**, *23*, 11901-11906.
(75) Zurilla, R. W.; Sen, R. K.; Yeager, E. *J. Electrochem. Soc.* **1978**, *125*, 1103-1109.
(76) Ci, S.; Wu, Y.; Zou, J.; Tang, L.; Luo, S.; Li, J.; Wen, Z. *Chinese Sci. Bull.* **2012**, *57*, 3065-3070.
(77) Stamenkovic, V. R.; Fowler, B.; Mun, B. S.; Wang, G.; Ross, P. N.; Lucas, C. A.; Marković, N. M. *Science* **2007**, *315*, 493-497.
(78) Huang, X.; Zhao, Z.; Cao, L.; Chen, Y.; Zhu, E.; Lin, Z.; Li, M.; Yan, A.; Zettl, A.; Wang, Y. M.; Duan, X.; Mueller, T.; Huang, Y. *Science* **2015**, *348*, 1230-1234.
(79) Cao, L.; Mueller, T. *J. Phys. Chem. C* **2015**, *119*, 17735-17747.
(80) Lyons, M. E. G.; Doyle, R. L.; Godwin, I.; O'Brien, M.; Russell, L. *J. Electrochem. Soc.* **2012**, *159*, H932-H944.
(81) Trotochaud, L.; Ranney, J. K.; Williams, K. N.; Boettcher, S. W. *J. Am. Chem. Soc.* **2012**, *134*, 17253-17261.
(82) Pourbaix, M. *Atlas of electrochemical equilibria in aqueous solutions*; National Association of Corrosion Engineers, 1974.
(83) Weaver, M. J.; Tyma, P. D.; Nettles, S. M. *J. Electroanal. Chem.* **1980**, *114*, 53-72.
(84) Frank, H. S.; Wen, W.-Y. *Discuss. Faraday Soc.* **1957**, *24*, 133-140.
(85) Boyarkin, O. V.; Koshelev, M. A.; Aseev, O.; Maksyutenko, P.; Rizzo, T. R.; Zobov, N. F.; Lodi, L.; Tennyson, J.; Polyansky, O. L. *Chem. Phys. Lett.* **2013**, *568–569*, 14-20.
(86) Lyons, M. E. G.; Cakara, A.; O'Brien, P.; Godwin, I.; Doyle, R. L. *Int. J. Electrochem. Sci.* **2012**, *7*, 11768-11795.
(87) Franks, F. *The Physics and Physical Chemistry of Water*; Springer US, 2012.
(88) Liu, H.; Macedo, E. A. *J. Supercrit. Fluids* **1995**, *8*, 310-317.

(89) Carter, R. E.; Dahlgren, L. *Acta Chem. Scand.* **1969**, *23*, 504-514.
(90) Bartell, L. S. *J. Am. Chem. Soc.* **1961**, *83*, 3567-3571.
(91) Bartell, L. S. *Tetrahedron Lett.* **1960**, *1*, 13-16.
(92) Carter, R. E.; Dahlgren, L. *Acta Chem. Scand.* **1970**, *24*, 633-643.
(93) Melander, L.; Carter, R. E. *Acta Chem. Scand.* **1964**, *18*, 1138-1149.
(94) Westheimer, F. H. *J. Chem. Phys.* **1947**, *15*, 252-260.
(95) Westheimer, F. H.; Mayer, J. E. *J. Chem. Phys.* **1946**, *14*, 733-738.
(96) Mislow, K.; Graeve, R.; Gordon, A. J.; Wahl, G. H. *J. Am. Chem. Soc.* **1964**, *86*, 1733-1741.
(97) Mislow, K.; Graeve, R.; Gordon, A. J.; Wahl, G. H. *J. Am. Chem. Soc.* **1963**, *85*, 1199-1200.
(98) Juodkazis, K.; Juodkazytė, J.; Vilkauskaitė, R.; Jasulaitienė, V. *J. Solid State Electrochem.* **2008**, *12*, 1469-1479.
(99) Bocca, C.; Barbucci, A.; Cerisola, G. *Int. J. Hydrogen Energy* **1998**, *23*, 247-252.
(100) Mom, R. V.; Cheng, J.; Koper, M. T. M.; Sprik, M. *J. Phys. Chem. C* **2014**, *118*, 4095-4102.
(101) Llewellyn, J. A.; Robertson, R. E.; Scott, J. M. W. *Can. J. Chem.* **1960**, *38*, 222-232.
(102) Shiner, V. J.; Humphrey, J. S. *J. Am. Chem. Soc.* **1963**, *85*, 2416-2419.
(103) Collins, C. J.; Bowman, N. S. *Isotope effects in chemical reactions*; Van Nostrand Reinhold, 1971.
(104) Jewett, J. G.; Dunlap, R. P. *J. Am. Chem. Soc.* **1968**, *90*, 809-810.
(105) Clough, S. A.; Beers, Y.; Klein, G. P.; Rothman, L. S. *J. Chem. Phys.* **1973**, *59*, 2254-2259.
(106) Brittain, A. H.; Cox, A. P.; Duxbury, G.; Hersey, T. G.; Jones, R. G. *Mol. Phys.* **1972**, *24*, 843-851.
(107) Sadiek, I. M.; Mohammad, A. M.; El-Shakre, M. E.; El-Deab, M. S. *Int. J. Hydrogen Energy* **2012**, *37*, 68-77.
(108) Zhu, Y.; Li, H.; Koltypin, Y.; Gedanken, A. *J. Mater. Chem.* **2002**, *12*, 729-733.
(109) Schrebler Guzmán, R. S.; Vilche, J. R.; Arvía, A. J. *J. Electrochem. Soc.* **1978**, *125*, 1578-1587.
(110) Cibrev, D.; Jankulovska, M.; Lana-Villarreal, T.; Gómez, R. *Int. J. Hydrogen Energy* **2013**, *38*, 2746-2753.

Supporting Information for

Inverted and Normal Kinetic Isotope Effects in Oxygen Evolution and Oxygen Reduction Electrochemistry

Edmund C. M. Tse,[1] Thao T. H. Hoang,[1] Jason A. Varnell,[1] and Andrew A. Gewirth[1,2*]

[1] Department of Chemistry, University of Illinois at Urbana–Champaign, Urbana, Illinois 61801, USA

[2] International Institute for Carbon Neutral Energy Research (WPI-I2CNER), Kyushu University, Fukuoka 812-8581, Japan

[*] Corresponding author. E-mail: agewirth@illinois.edu

Table of Contents

Notes 1 & 2. Calculating kinetic isotope effect from Koutecky-Levich and Tafel slope analyses.

Figures S1-11 and Tables S1-3. Kinetic isotope effect of oxygen reduction reaction.

Figures S12-15. Kinetic isotope effect of oxygen evolution reaction.

Note 1. Calculating kinetic isotope effect from Koutecky-Levich analysis.[1]

$$\frac{1}{j} = \frac{1}{j_K} + \frac{1}{j_{l,c}}$$

$$limiting\ cathodic\ current\ density = j_{l,c} = 0.62nFD_{O_2}^{2/3}\omega^{1/2}v^{-1/6}C_{O_2}^{*}$$

$$kinetically\ limited\ current\ density = j_K = nFk_fC_{O_2}^{*}$$

Where j = current density, n = number of electrons transferred, F = Faraday's constant, D_{O_2} = diffusion coefficient of O_2, ω = electrode rotation rate, v = kinematic viscosity, $C_{O_2}^{*}$ = the bulk concentration of O_2, and $k_f = k_0\, e^{-\frac{\alpha F\eta}{RT}}$ = heterogeneous rate constant for reduction.

$j_{l,c}$ represents the current density obtained under totally mass-transfer-limited conditions and thus involves terms related to diffusion, bulk concentration, kinematic viscosity and rotation rate. j_K describes the current density measured under the kinetic limitation when the mass transfer is efficient enough to keep the concentration of reactants at the electrode surface equal to the bulk value. The current density absent any mass-transfer effects is a prerequisite to study kinetic isotope effect.

Plotting $y = \frac{1}{j}$ and $x = \frac{1}{\omega^{1/2}}$ gives:

$$slope = \frac{1}{0.62nFD_{O_2}^{2/3}v^{-1/6}C_{O_2}^{*}}$$

$$intercept = \frac{1}{j_K} = \frac{1}{nFk_fC_{O_2}^{*}}$$

Dividing j_K^H obtained in proteo solution by j_K^D obtained in deutero solution gives:

$$\frac{j_0^H}{j_0^D} = \frac{n^H k_f^H C_{O_2}^{*,H}}{n^D k_f^D C_{O_2}^{*,D}}$$

Following established methods,[2,3] the solvomolalities of O_2 in H_2O and D_2O at 298.15 K are converted to bulk concentrations of O_2 in H_2O ($C_{O_2}^{*,H}$) and in D_2O ($C_{O_2}^{*,D}$) to yield

$$\frac{C_{O_2}^{*,H}}{C_{O_2}^{*,D}} = 0.908$$

Calculating the KIE at constant overpotentials and assuming the total number of electrons transferred and the transfer coefficients to be similar yields:

$$\frac{k_0^H}{k_0^D} = \frac{j_0^H C_{O_2}^{*,D}}{j_0^D C_{O_2}^{*,H}} = \frac{j_0^H}{j_0^D}\,\frac{1}{0.908}$$

Changes in O_2 diffusion limited current is due to differences in O_2 diffusion coefficients, kinematic viscosity, and bulk O_2 concentration between H and D solutions. Similar changes in the peak current can be observed for the case without rotation.

Note 2. Calculating kinetic isotope effect from Tafel slope analysis.[4]

$$overpotential = \eta = \frac{R\,T}{\alpha\,n_a\,F}\ln j_0 - \frac{R\,T}{\alpha\,n_a\,F}\ln j$$

where R = ideal das constant, T = temperature, α = transfer coefficient, n_a = number of electrons transferred during the rate-determining step, F = Faraday's constant, and j = current density.

Plotting $y = \eta$ and $x = \ln j$ gives:

$$slope = -\frac{R\,T}{\alpha\,n_a\,F}$$

$$intercept = \frac{R\,T}{\alpha\,n_a\,F}\ln j_0$$

$$intercept = (-slope)\ln j_0$$

$$j_0 = e^{\frac{intercept}{-slope}}$$

Exchange current density (j_0) is described by the following equation:[1]

$$j_0 = nFk_0C^*$$

where n = total number of electrons transferred, k_0 = standard heterogeneous rate constant, and C^* = bulk concentration of species.

Dividing j_0^H obtained in proteo solution by j_0^D obtained in deutero solution gives:

$$\frac{j_0^H}{j_0^D} = \frac{n^H k_0^H C^{*,H}}{n^D k_0^D C^{*,D}}$$

$C^{*,H} = C^{*,D}$ because the experiments were conducted in pH 14 and pD 14 solutions, i.e. the hydroxide and deuteroxide concentrations are the same.

Assuming n remains unchanged in proteo and deutero solutions:

$$\frac{j_0^H}{j_0^D} = \frac{k_0^H}{k_0^D}$$

Using Tafel slope analysis to calculate kinetic isotope effect is not meaningful at high overpotential because the reaction is limited by mass transport. Therefore, to obtain meaningful interpretation of the kinetic isotope effect of OER catalyzed by Ni and Co, we utilize Tafel slope analysis at overpotentials less than 0.5 V where the reaction is not limited by mass transport.

Using the Gibbs formation energy of D_2O,[5] the formal reduction potential for the reaction $2 D_2 + O_2 \rightarrow 2 D_2O$ is calculated to be 1.26 V, which is 30 mV greater than H_2O (1.23 V). The standard potential of a hydrogen redox couple on Pt differs from that of a deuterium redox couple on Pt by 4.3 mV at 298 K.[6]

For maintaining consistency in Tafel slope analysis, Tafel slopes are obtained in the same potential window for both proteo and deutero solutions where the second derivatives of the CV traces are zero. The Tafel slopes measured for proteo solutions at both low and high overpotentials match with literature reported values. Recent Tafel slope values for the OER on Ni at high overpotential range from 126 to 132 mV dec^{-1}.[7] However, we focus our attention to the low overpotential region where the kinetics of the reaction is not plagued by mass diffusion from bulk solution to the electrode surface then through the layered-structure of the metal oxides/oxyhydroxides/hydroxides.

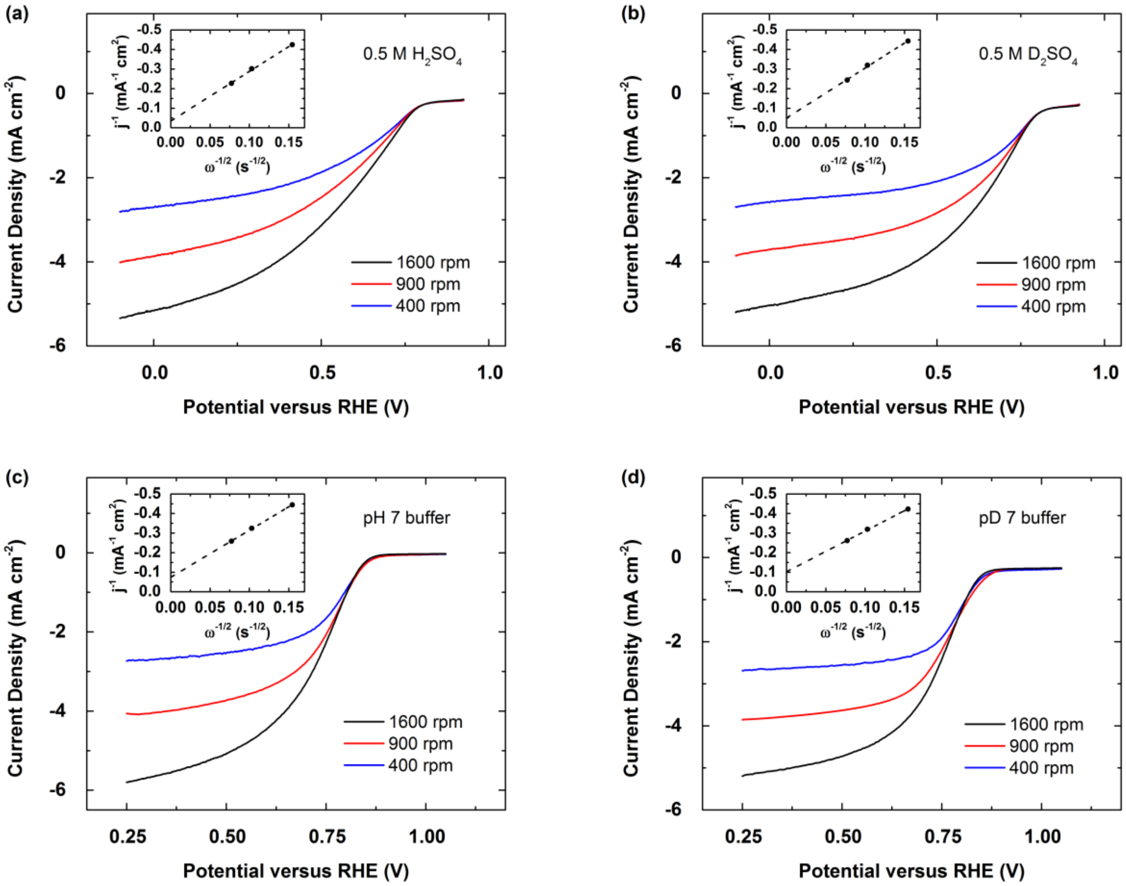

Figure S1. RDE voltammograms and Koutecky-Levich plots (insets) of PANI-Fe-C with inks prepared with Nafion powder in (a) pH 0.3, (b) pD 0.3, (c) pH 7, and (d) pD 7 O_2-saturated solutions with a scan rate of 10 mV/s at 400 (blue), 900 (red), and 1600 (black) rpm.

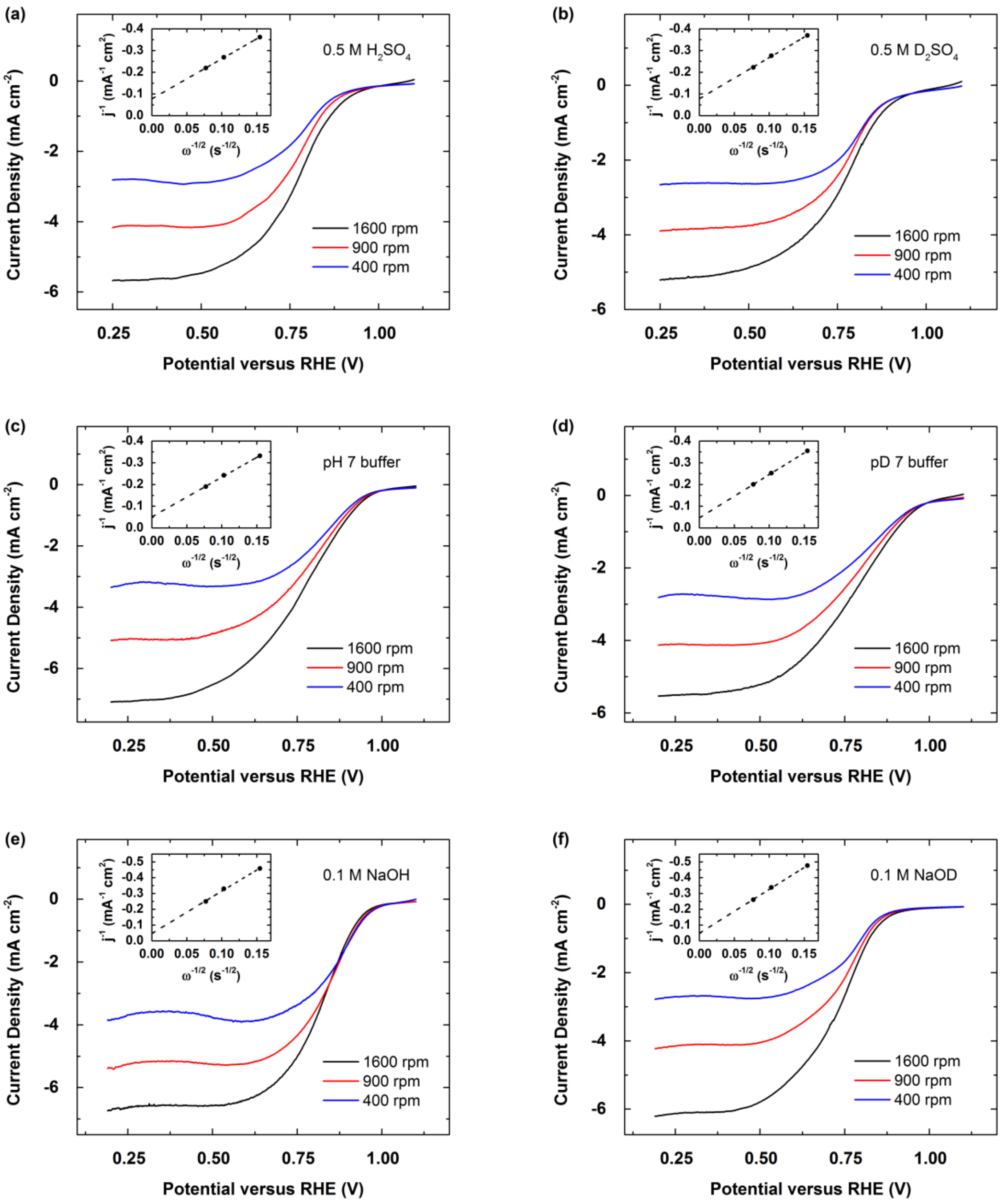

Figure S2. RDE voltammograms and Koutecky-Levich plots (insets) of 20 wt.% Pt supported on Vulcan XC-72 with inks prepared with Nafion powder in (a) pH 0.3, (b) pD 0.3, (c) pH 7, (d) pD 7, (e) pH 13, and (f) pD 13 O_2-saturated solutions with a scan rate of 10 mV/s at 400 (blue), 900 (red), and 1600 (black) rpm.

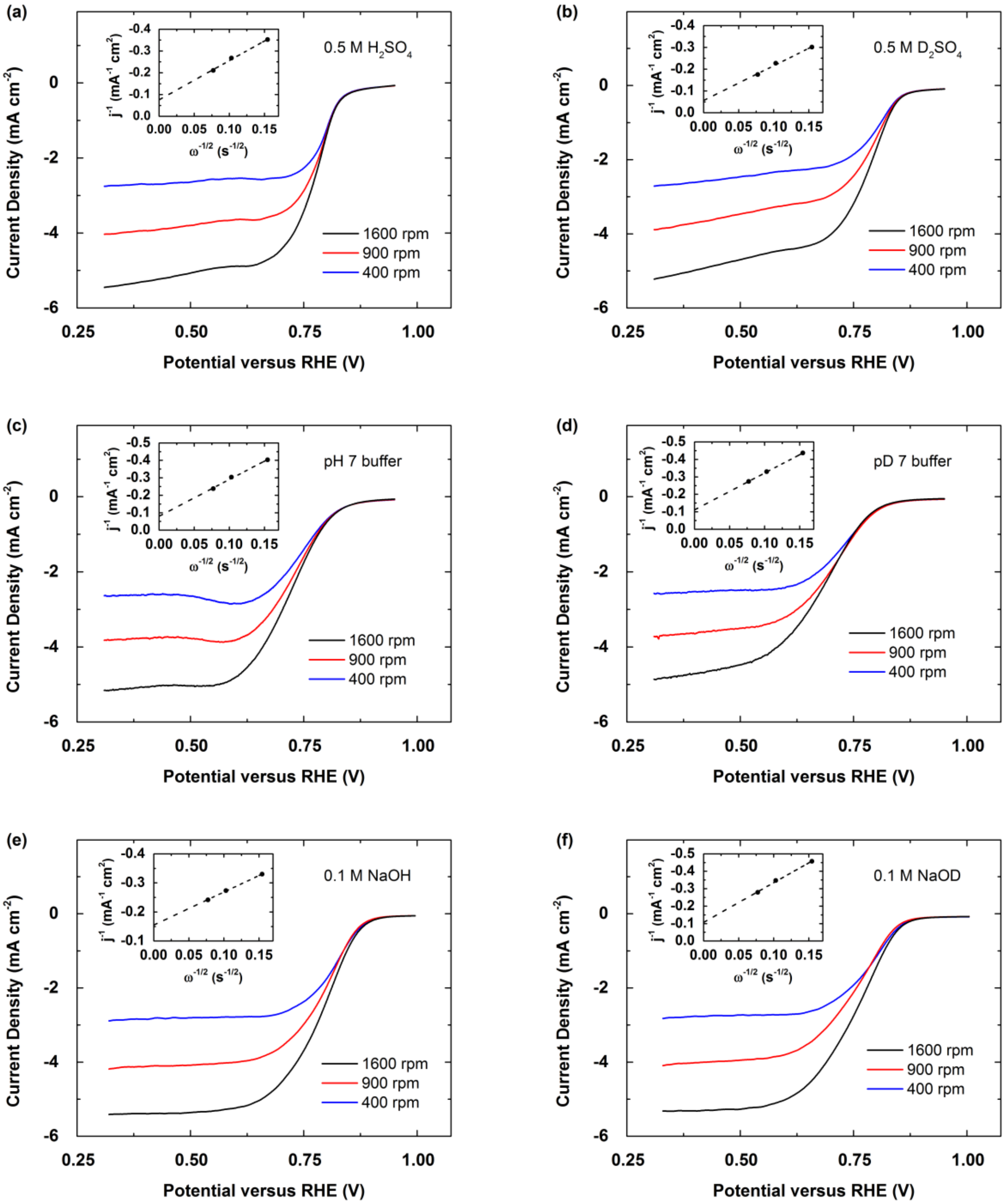

Figure S3. RDE voltammograms and Koutecky-Levich plots (insets) of 20 wt.% Pd supported on Vulcan XC-72 with inks prepared with Nafion powder in (a) pH 0.3, (b) pD 0.3, (c) pH 7, (d) pD 7, (e) pH 13, and (f) pD 13 O_2-saturated solutions with a scan rate of 10 mV/s at 400 (blue), 900 (red), and 1600 (black) rpm.

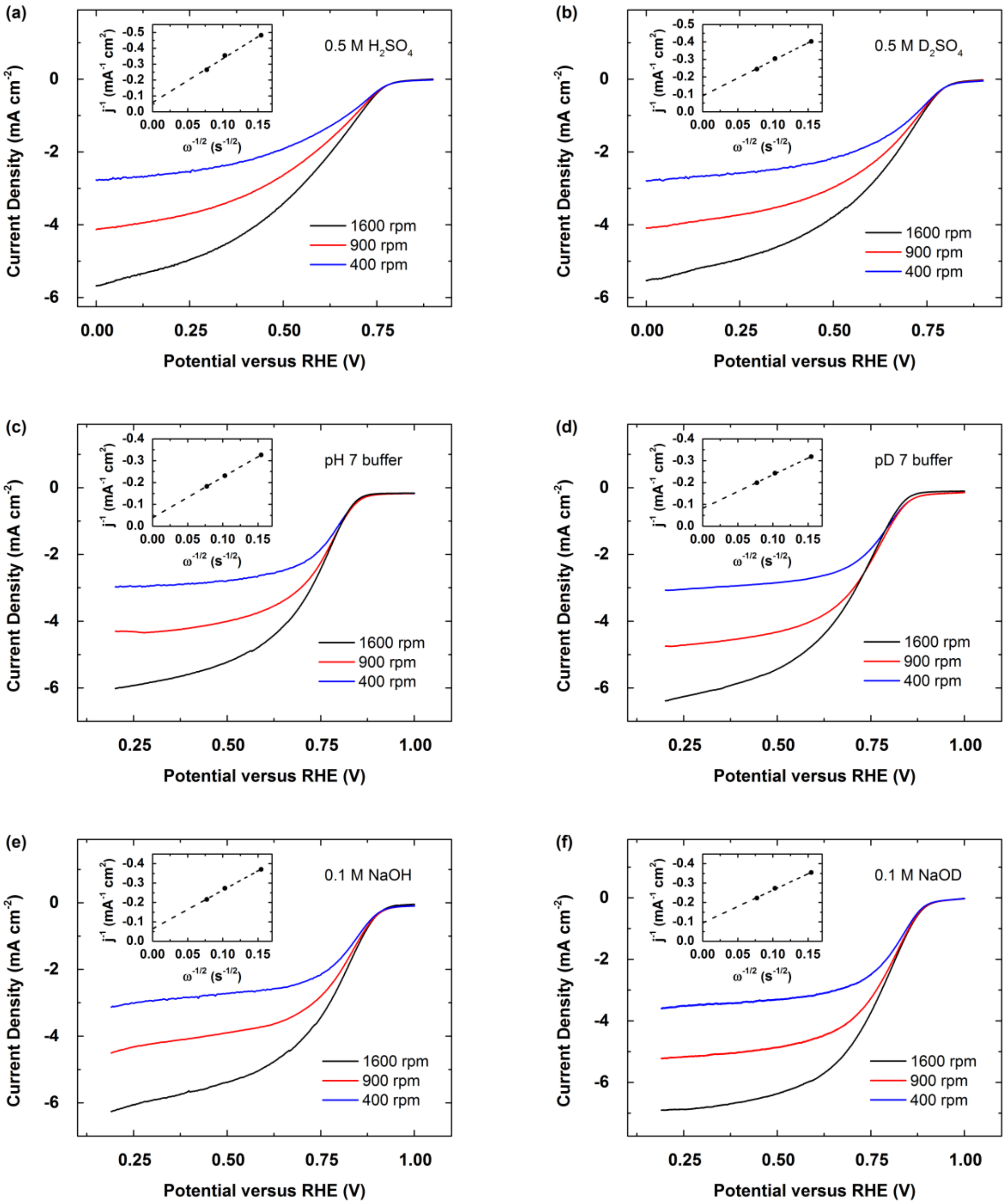

Figure S4. RDE voltammograms and Koutecky-Levich plots (insets) of PANI-Fe-C without binder in (a) pH 0.3, (b) pD 0.3, (c) pH 7, (d) pD 7, (e) pH 13, and (f) pD 13 O_2-saturated solutions with a scan rate of 10 mV/s at 400 (blue), 900 (red), and 1600 (black) rpm.

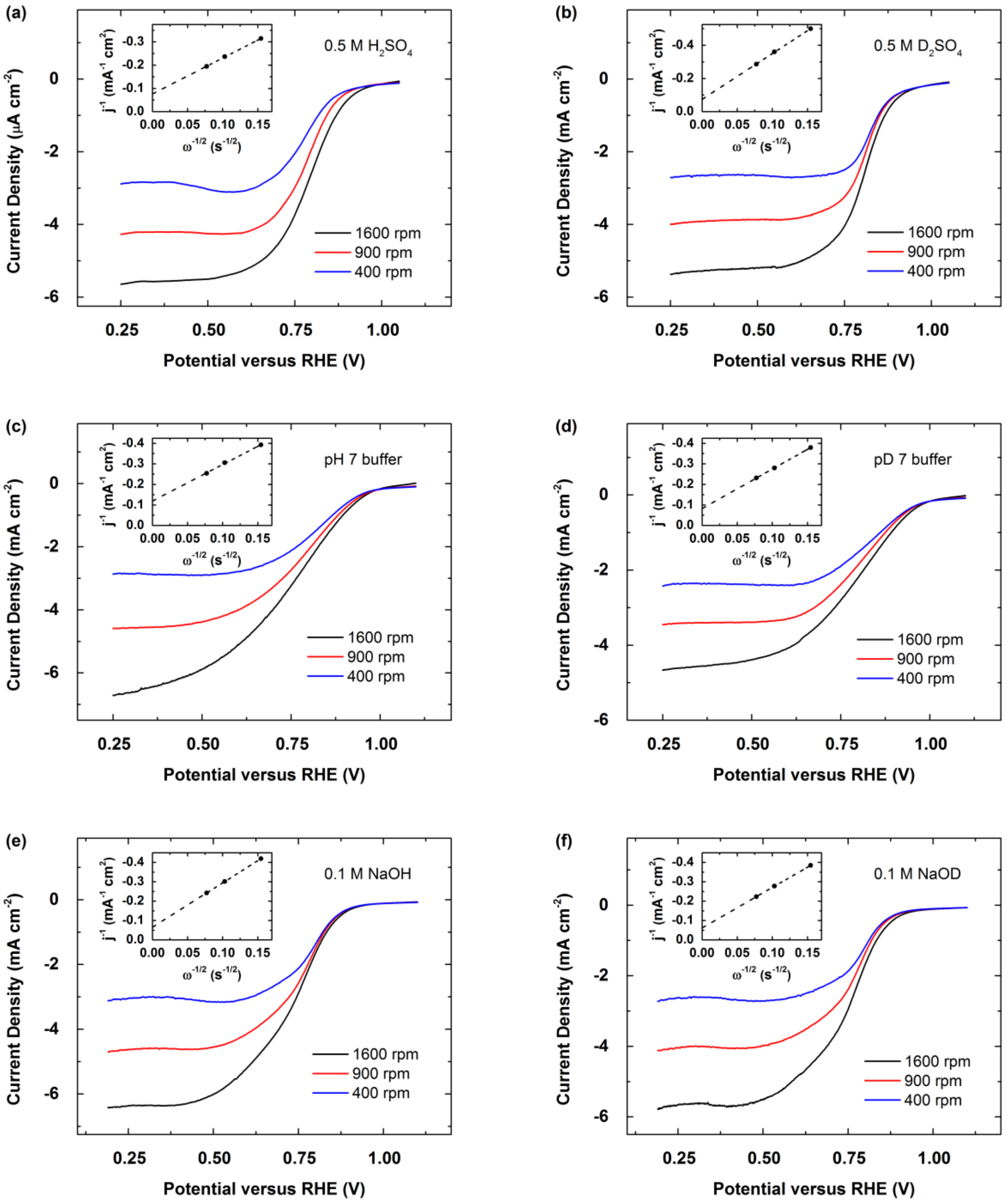

Figure S5. RDE voltammograms and Koutecky-Levich plots (insets) of 20 wt.% Pt supported on Vulcan XC-72 without binder in (a) pH 0.3, (b) pD 0.3, (c) pH 7, (d) pD 7, (e) pH 13, and (f) pD 13 O_2-saturated solutions with a scan rate of 10 mV/s at 400 (blue), 900 (red), and 1600 (black) rpm.

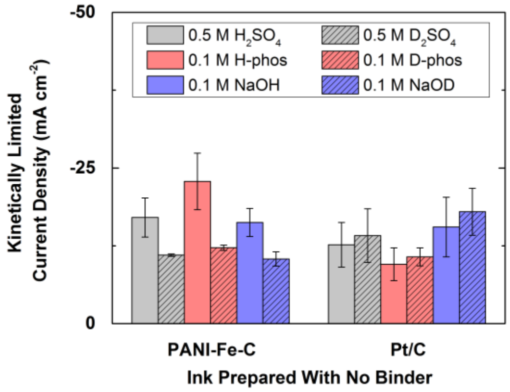

Figure S6. Bar graphs summarizing the kinetically limited current densities obtained from Koutecky-Levich analyses of O_2 reduction voltammograms for PANI-Fe-C, Pt/C and Pd/C with inks prepared with without binder in O_2-saturated 0.5 M H_2SO_4 (gray), 0.5 M D_2SO_4 (gray with stripes), 0.1 M pH 7 phosphate buffer (red), 0.1 M pD 7 phosphate buffer (red with stripes), 0.1 M NaOH (blue), and 0.1 M NaOD (blue with stripes) solutions.

In an effort to minimize the effect of binder on protons or deuterons delivery to the catalytic site during the ORR process, we study the ORR activity of PANI-Fe-C and Pt/C in proteo and deutero solutions using various ink preparation methods (Figure S4-11). Figure S6 compares the kinetically limited current densities calculated from Koutecky-Levich plots of PANI-Fe-C and Pt/C using inks without Nafion powder. We observe lower ORR kinetically limited current densities by PANI-Fe-C in deutero solutions as compared to proteo solutions. For Pt/C, the ORR kinetically limited current densities are similar in both deutero and proteo solutions. These results are similar to those obtained from inks prepared using Nafion powder as binders.

Table S1. Summary of the kinetic isotope effect of ORR catalyzed by PANI-Fe-C, Pt/C, and Pd/C with inks prepared without binder in acidic (0.5 M sulfuric acid), neutral (0.1 M, pH 7 phosphate buffer) and basic (0.1 M NaOH/(D)) conditions.

Catalysts	PANI-Fe-C	Pt/C
Acidic	1.7 ± 0.3	1.0 ± 0.4
Neutral	2.1 ± 0.4	1.0 ± 0.3

Basic	1.7 ± 0.3	0.9 ± 0.4

Table S1 displays the kinetic isotope effects calculated using values in Figure S6. In all three pH regimes, the kinetic isotope effects measured for PANI-Fe-C and Pt/C are ca. 2 and 1, respectively. The kinetic isotope effects are very similar for both inks with Nafion powder as binder and inks without binder, further confirming our conclusion above that protons are involved at or before the RDS of the ORR catalyzed by non-precious metal catalyst PANI-Fe-C but not for the case of Pt/C.

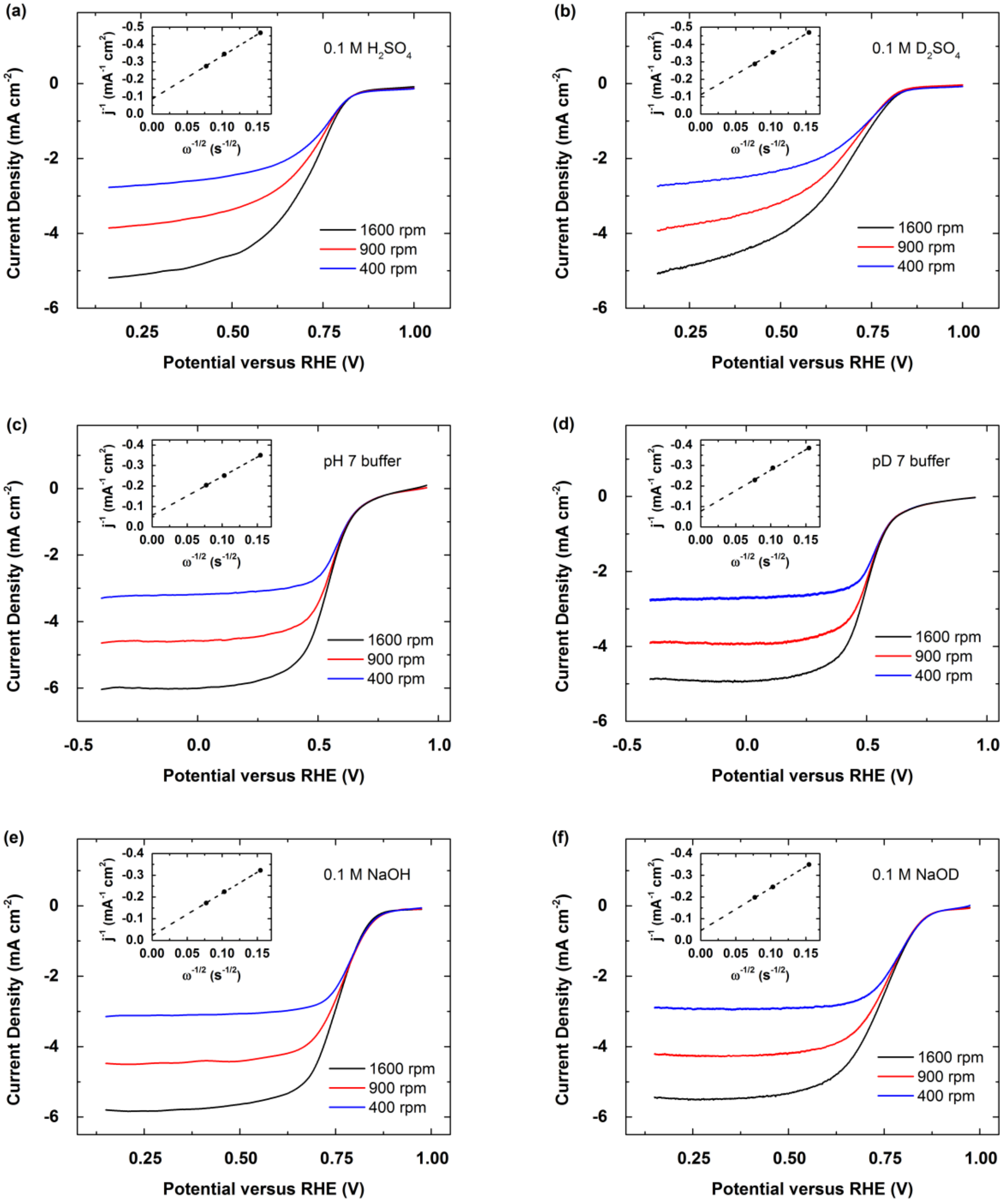

Figure S7. RDE voltammograms and Koutecky-Levich plots (insets) of PANI-Fe-C with inks prepared using Nafion 117 solution in EtOH in (a) pH 0.3, (b) pD 0.3, (c) pH 7, (d) pD 7, (e) pH 13, and (f) pD 13 O_2-saturated solutions with a scan rate of 10 mV/s at 400 (blue), 900 (red), and 1600 (black) rpm.

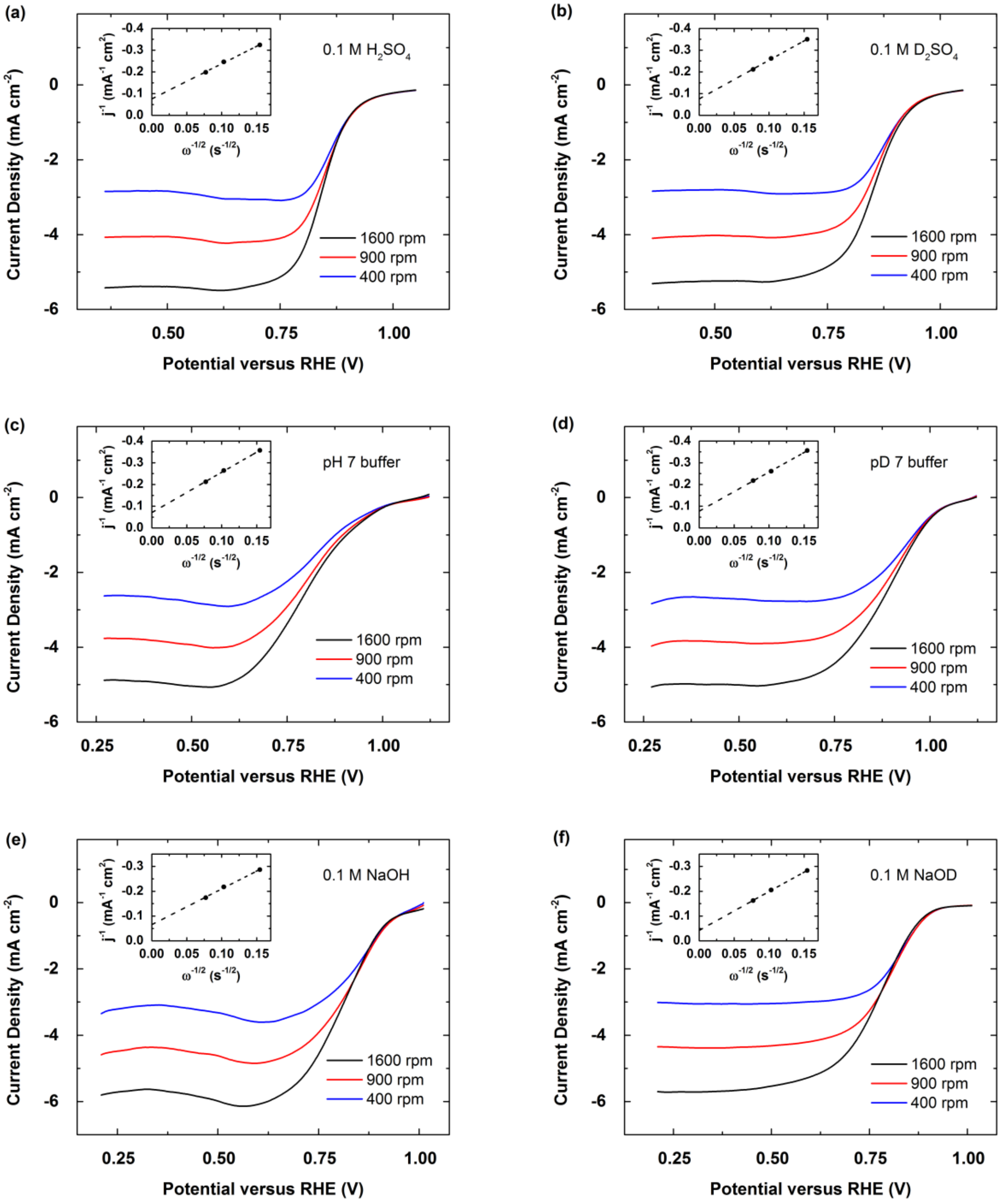

Figure S8. RDE voltammograms and Koutecky-Levich plots (insets) of 20 wt.% Pt supported on Vulcan XC-72 with inks prepared using Nafion 117 solution in EtOH in (a) pH 0.3, (b) pD 0.3, (c) pH 7, (d) pD 7, (e) pH 13, and (f) pD 13 O_2-saturated solutions with a scan rate of 10 mV/s at 400 (blue), 900 (red), and 1600 (black) rpm.

To further investigate the effect of trapped protons in binders, we formulate inks using Nafion 117 solution saturated with protons. Figures S7 and S8 display the ORR LSVs and Koutecky-Levich plots of PANI-Fe-C and Pt/C with inks saturated with protons. Using inks saturated with protons, we observed no change in the O_2 reduction voltammetries and the kinetically limited current densities.

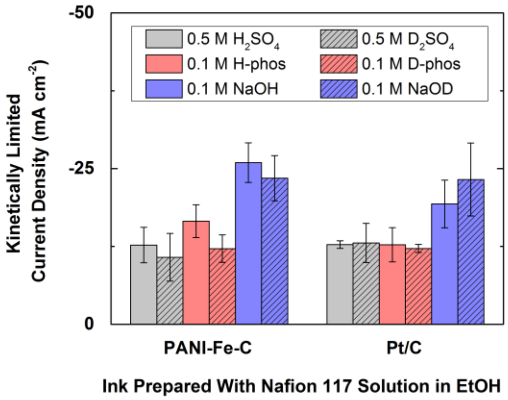

Figure S9. Bar graphs summarizing the kinetically limited current densities obtained from Koutecky-Levich analyses of O_2 reduction voltammograms for PANI-Fe-C and Pt/C with inks prepared using Nafion 117 solution in O_2-saturated 0.5 M H_2SO_4 (gray), 0.5 M D_2SO_4 (gray with stripes), 0.1 M pH 7 phosphate buffer (red), 0.1 M pD 7 phosphate buffer (red with stripes), 0.1 M NaOH (blue), and 0.1 M NaOD (blue with stripes) solutions.

Table S2. Summary of the kinetic isotope effect of ORR catalyzed by PANI-Fe-C and Pt/C with inks prepared using Nafion 117 solution in acidic (0.5 M sulfuric acid), neutral (0.1 M, pH 7 phosphate buffer) and basic (0.1 M NaOH/(D)) conditions.

Catalysts	**PANI-Fe-C**	**Pt/C**
Acidic	1.3 ± 0.5	1.1 ± 0.3
Neutral	1.5 ± 0.4	1.2 ± 0.3
Basic	1.2 ± 0.2	0.9 ± 0.3

Figure S9 shows the bar graphs summarizing the measured kinetically limited current densities of PANI-Fe-C and Pt/C with inks saturated with protons. Table S2 summaries the measured kinetically limited current densities and the calculated kinetic isotope effects of PANI-Fe-C and Pt/C with inks saturated with protons. Both PANI-Fe-C and Pt/C exhibit KIEs of ca. 1, suggesting that the presence of deuterons in bulk solution does not slow down nor speed up the ORR. These results suggest that by using inks prepared with the commercially available Nafion 117 solution, protons are trapped inevitably in the dried catalyst film on the electrode surface.

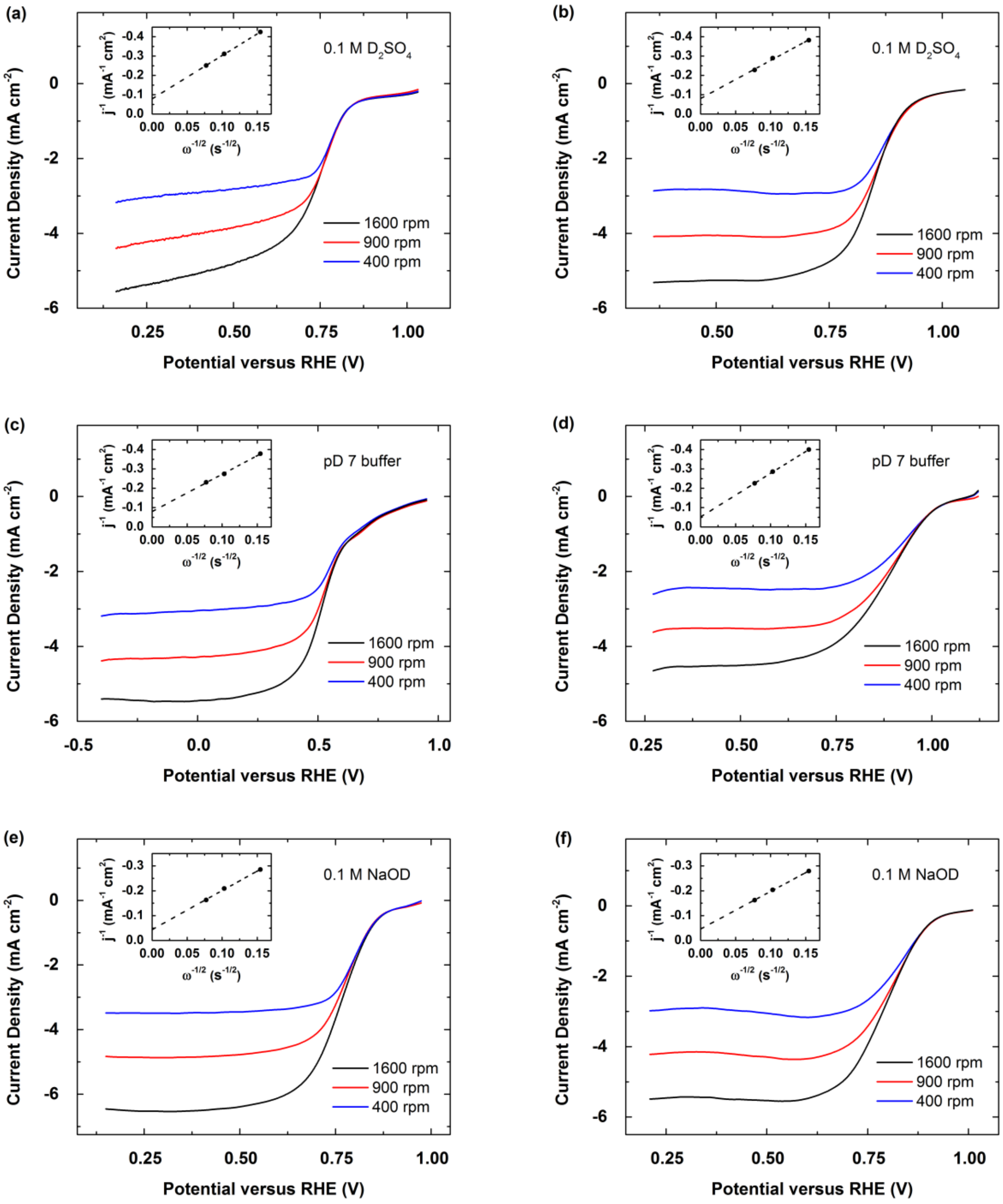

Figure S10. RDE voltammograms and Koutecky-Levich plots (insets) of PANI-Fe-C in (a) pD 0.3, (c) pD 7, and (e) pD 13 and 20 wt.% Pt supported on Vulcan XC-72 in (b) pD 0.3, (d) pD 7, and (f) pD 13 O_2-saturated solutions using inks prepared with Nafion 117 solution in EtOD with a scan rate of 10 mV/s at 400 (blue), 900 (red), and 1600 (black) rpm.

Since commercially available Nafion 117 solution results in trapped protons in the catalyst inks, we attempted to exchange out the trapped protons by using EtOD to prepare the inks. We also explored other methods to prepare the inks such as drying the Nafion 117 solution prior to preparing inks, but this method resulted in a translucent film that could not be redissolved upon addition of deuterated ethanol or isopropanol. Figure S10 compares the LSVs of an attempt to prepare deuterated inks using Nafion 117 solution diluted with EtOD. The corresponding bar graphs that summarize the kinetically limited current densities calculated from Koutecky-Levich plots are shown in Figure S11.

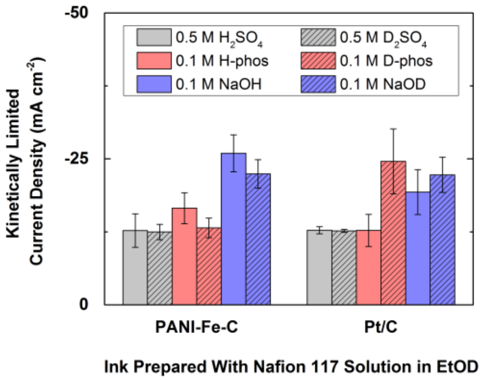

Figure S11. Bar graphs summarizing the kinetically limited current densities obtained from Koutecky-Levich analyses of O_2 reduction voltammograms for PANI-Fe-C and Pt/C with inks prepared using Nafion 117 solution in O_2-saturated 0.5 M H_2SO_4 (gray), 0.5 M D_2SO_4 (gray with stripes), 0.1 M pH 7 phosphate buffer (red), 0.1 M pD 7 phosphate buffer (red with stripes), 0.1 M NaOH (blue), and 0.1 M NaOD (blue with stripes) solutions.

Table S3. Summary of the kinetic isotope effect of ORR catalyzed by PANI-Fe-C and Pt/C with inks prepared using Nafion 117 solution with the deuterated inks containing EtOD in acidic (0.5 M sulfuric acid), neutral (0.1 M, pH 7 phosphate buffer) and basic (0.1 M NaOH/(D)) conditions.

Catalysts	**PANI-Fe-C**	**Pt/C**
Acidic	1.1 ± 0.3	1.1 ± 0.1
Neutral	1.4 ± 0.3	1.1 ± 0.2
Basic	1.3 ± 0.2	1.0 ± 0.2

Figure S11 shows the bar graphs summarizing the measured kinetically limited current densities of PANI-Fe-C and Pt/C with deuterated inks prepared using Nafion 117 solution diluted with EtOD. Table S3 summarizes the measured kinetically limited current densities and the calculated kinetic isotope effects of PANI-Fe-C and Pt/C with deuterated inks prepared using Nafion 117 solution diluted with EtOD. Both PANI-Fe-C and Pt/C exhibit KIEs of ca. 1, suggesting that the presence of deuterons in bulk solution does not slow down nor speed up the ORR. These results suggest that by using inks prepared with the Nafion 117 solution, protons are trapped in the dried catalyst film on the electrode surface irrespective to the solvent used to dilute the ink.

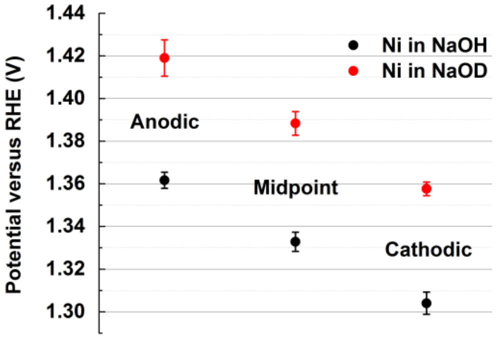

Figure S12a. Anodic, cathodic, and midpoint potentials of the $Ni(OH)_2/NiOOH$ wave in 1 M NaOH (black) and 1 M NaOD (red).

We note that the magnitudes of the isotope effects are less for the cases of surface catalysts, likely due to the planar geometry (as opposed to spherical geometry in the case for molecular compounds in solution) of the extended water network and solvation shell.[8-10]

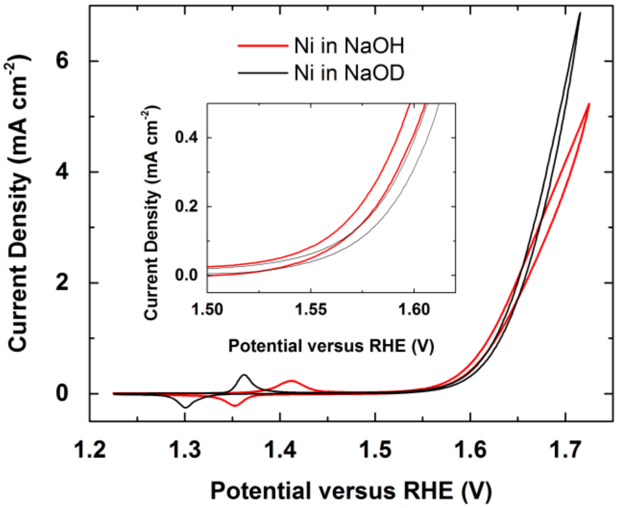

Figure S12b. IR-uncorrected CVs of Ni in NaOH (1 M) and NaOD (1 M) solutions. Inset displays the OER onset region.

Without IR-correction, we observe more OER current in proteo solution than deutero solution at potentials greater than 1.66 V for the case of Ni, likely because the diffusion coefficient of H_2O is larger than that of D_2O.[11,12] At potentials lower than 1.66 V, OER occurs at a slower rate and the interlayer $H(D)_2O$ inside the NiOOH(D) film is preferentially oxidized. At high potentials, interlayer $H(D)_2O$ is depleted and the gaps are replenished by bulk $H(D)_2O$. This bulk-to-interlayer diffusion process of $H(D)_2O$ likely limits the OER rates. We note that Co exhibits the same crossing behavior as Ni (*vide infra*), suggesting that this feature is likely not dependent on the identity of the OER catalysts, but rather a general phenomenon when running experiments in and comparing results between proteo and deutero solutions.

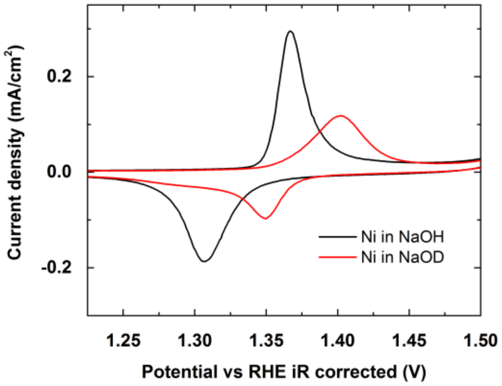

Figure S13. CVs of Ni foil in 1 M NaOH (black) and 1 M NaOD (red) solutions (zoomed into the Ni redox wave).

The difference in current observed in Figure S13 could be due to many reasons, one of which could be the difference in surface roughness of the Ni foil used. The Ni foil was polished with sand paper and dipped into H_2SO_4 or D_2SO_4 to expose fresh Ni surfaces prior to electrochemical studies, so the geometric area used to calculate current density does not reflect the actual electrochemical active surface area. We would like to stress that the point of this experiment is to check whether the Ni(II/III) peak shifts depending on the bulk solution content—in particular H versus D. This experiment clearly demonstrates that the Ni(II/III) peak in deutero solution is more positive than the case in proteo solution.

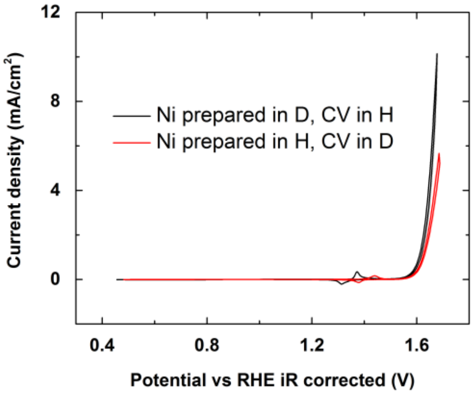

Figure S14. CVs of Ni prepared in proteo solution and ran CVs in NaOD (1 M) solution and prepared in deutero solution and ran in NaOH (1 M) solution.

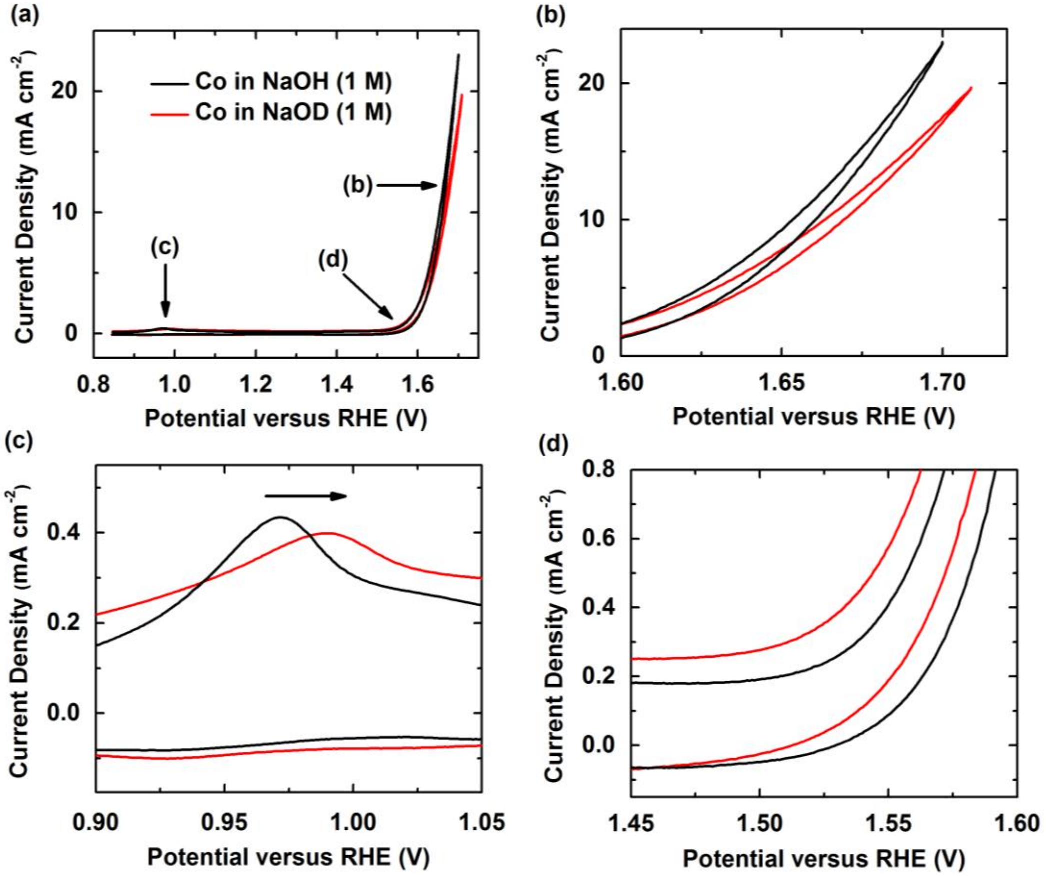

Figure S15. IR-uncorrected CVs of Co in NaOH (1 M) and NaOD (1 M) solutions. (b), (c), and (d) display the blowups of the diffusion-controlled OER region, the Co(II/III) redox region, and the OER onset region, respectively.

Without IR-correction, we observe more OER current in proteo solution than deutero solution at potentials greater than 1.63 V for the case of Co, likely because the diffusion coefficient of H_2O is larger than that of D_2O.[11,12] Qualitatively similar to the case of Ni, interlayer $H(D)_2O$ is depleted and the gaps are replenished by bulk $H(D)_2O$. This bulk-to-interlayer diffusion process of $H(D)_2O$ likely limits the OER rates at the high overpotential region. Since Co and Ni both exhibit the crossing behavior, we hypothesize that this feature is likely not dependent on the identity of the OER catalysts, but rather a common behavior when comparing results conducted in proteo and deutero solutions.

References

(1) Bard, A. J.; Faulkner, L. R. *Electrochemical Methods: Fundamentals and Applications, 2nd Edition*; Wiley Global Education, 2000.
(2) Ivanov, E. V.; Abrosimov, V. K. *Russ J Gen Chem* **2005**, *75*, 1851-1856.
(3) Battino, R.; Rettich, T. R.; Tominaga, T. *Journal of Physical and Chemical Reference Data* **1983**, *12*, 163-178.
(4) Shinagawa, T.; Garcia-Esparza, A. T.; Takanabe, K. *Scientific Reports* **2015**, *5*, 13801.
(5) Wagman, D. D. *The NBS Tables of Chemical Thermodynamic Properties: Selected Values for Inorganic and C1 and C2 Organic Substances in SI Units*; American Chemical Society and the American Institute of Physics for the National Bureau of Standards, 1982.
(6) Gary, R.; Bates, R. G.; Robinson, R. A. *The Journal of Physical Chemistry* **1964**, *68*, 1186-1190.
(7) Lyons, M. E. G.; Cakara, A.; O'Brien, P.; Godwin, I.; Doyle, R. L. *Int. J. Electrochem. Soc.* **2012**, *7*, 11768-11795.
(8) Weaver, M. J.; Tyma, P. D.; Nettles, S. M. *J. Electroanal. Chem.* **1980**, *114*, 53-72.
(9) Frank, H. S.; Wen, W.-Y. *Discuss. Faraday Soc.* **1957**, *24*, 133-140.
(10) Weaver, M. J.; Nettles, S. M. *Inorg. Chem.* **1980**, *19*, 1641-1646.
(11) Franks, F. *The Physics and Physical Chemistry of Water*; Springer US, 2012.
(12) Liu, H.; Macedo, E. A. *The Journal of Supercritical Fluids* **1995**, *8*, 310-317.

Non-precious Metal Complexes of Pyrazolyl-, Imidazolyl-, and Triazolyl-based Ligands as Active Electrocatalysts for the Oxygen Reduction Reaction

Edmund C. M. Tse,[1] Andrey Tregubov,[1] Xiaoyuan Zhou,[1] Thomas B. Rauchfuss,[1,2] and Andrew A. Gewirth[1,2*]

[1] Department of Chemistry, University of Illinois at Urbana−Champaign, 600 South Mathews Avenue, Urbana, Illinois 61801, United States

[2] International Institute for Carbon Neutral Energy Research (WPI-I2CNER), Kyushu University, Fukuoka 812-8581, Japan

* Author to whom correspondence should be addressed:

AAG: Tel: 217-333-8329, Fax: 217-244-3186, email: agewirth@illinois.edu

1. Abstract

Based on our previous successful attempt to use of Cu complex of 3,5-diamino-1,2,4-triazole (DAT) as an efficient oxygen reduction reaction (ORR) catalyst for fuel cell applications,[1] we spearheaded a follow-up study on utilizing Cu complexes of Schiff base derivatives of DAT as cathode catalysts (Figure 1). Our group also launched an investigation to use Cu complexes bound by pyridyl-based and alkyl-amine-based ligands as ORR catalysts (Figure 2). As an on-going effort, we further develop systems involving non-precious metal (NPM) complexes of ligands possessing pyrazole, imidazole, and triazole synthons (Figure 3).

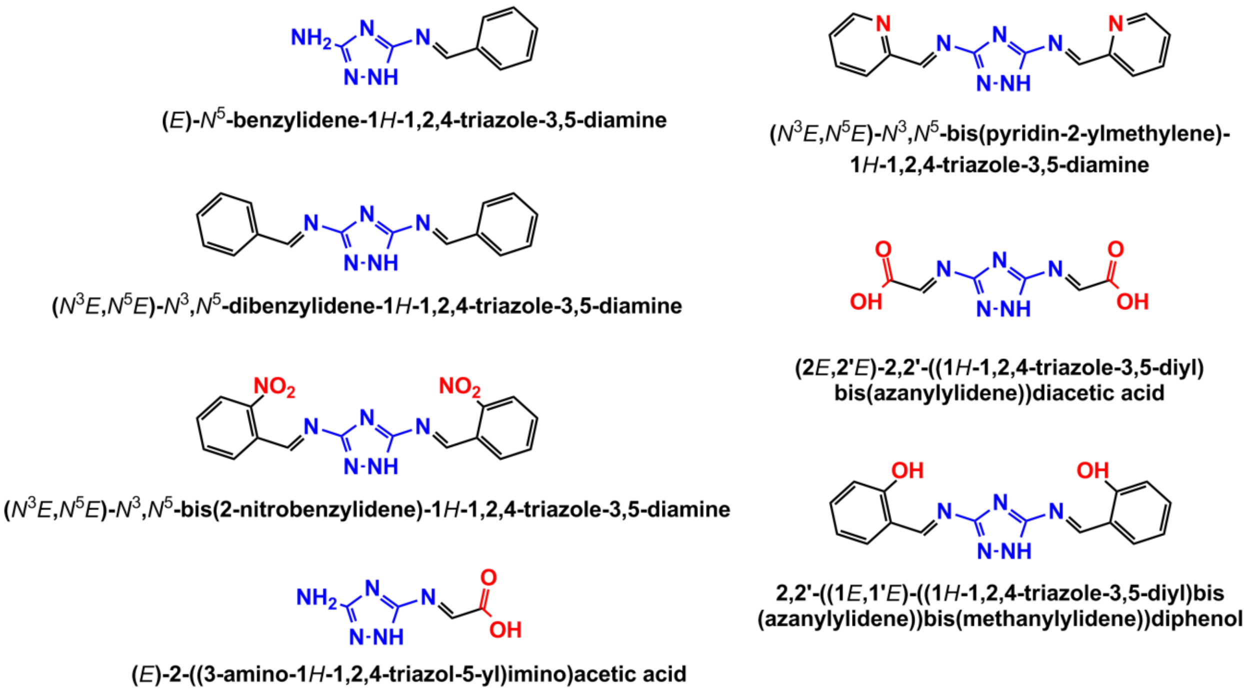

Figure 1. A selective list of triazolyl-based ligands used.

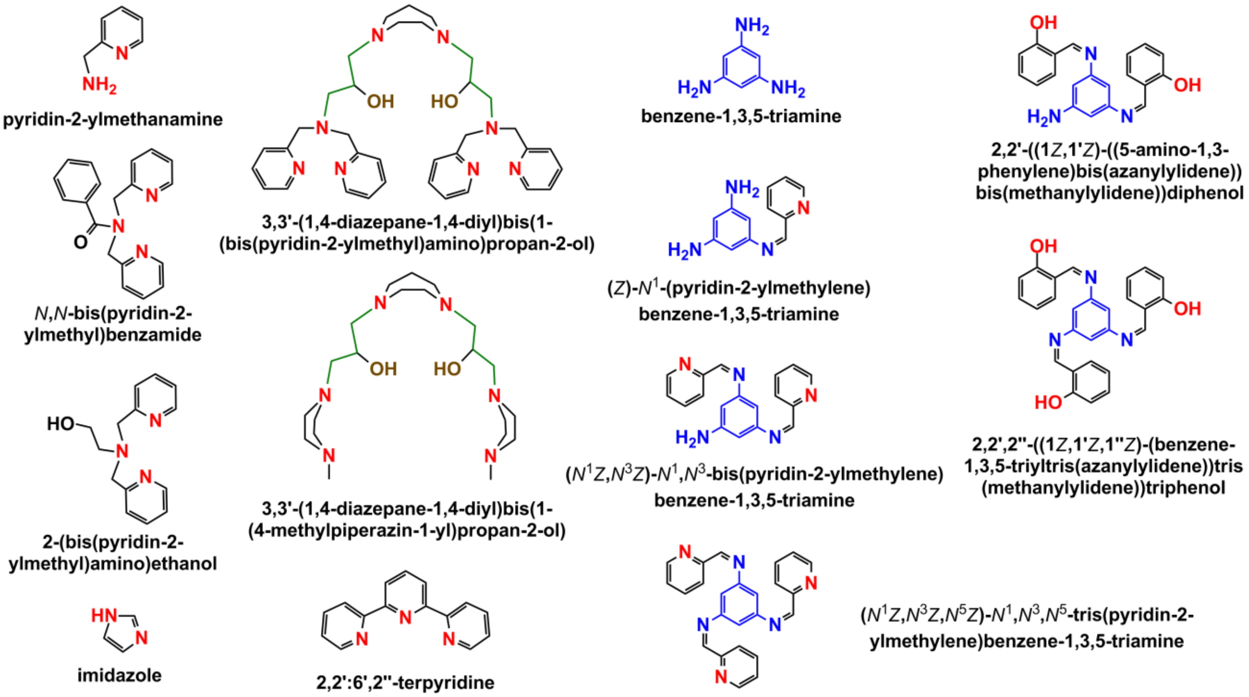

Figure 2. A selective list of pyridyl-, imidazolyl-, and alkyl-amine-based ligands used.

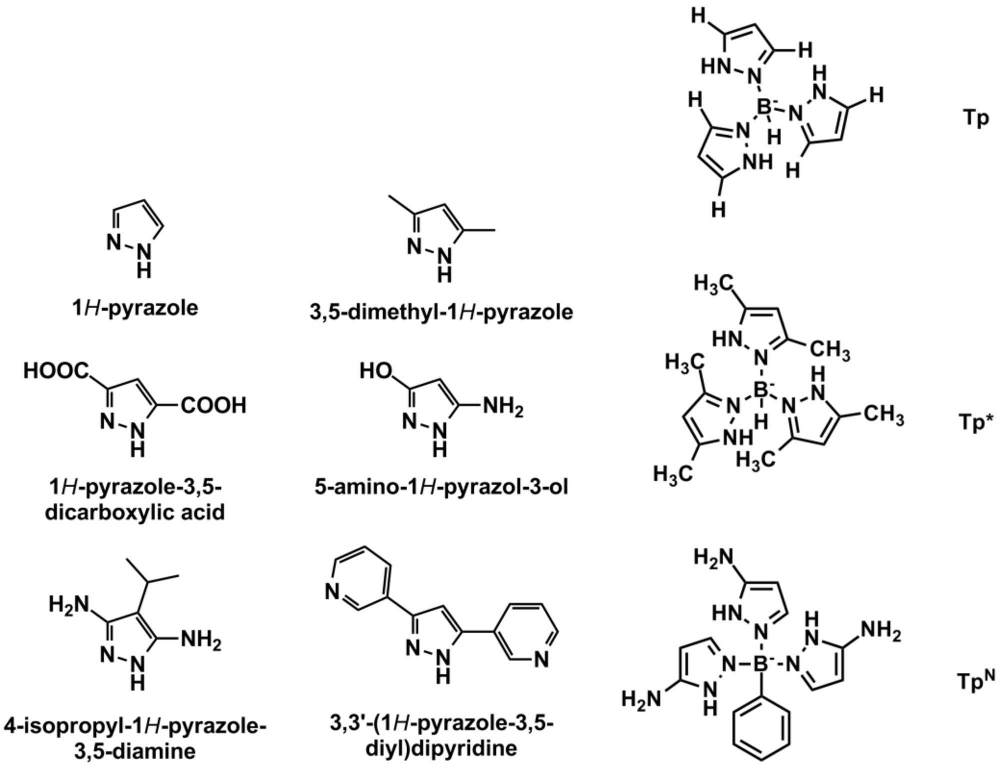

Figure 3. A selective list of pyrazole-based ligands used.

2. Introduction

The quest for renewable energy sources is one of the central research themes in the 21st century due to the detrimental environmental consequences of consuming fossil fuels, including but not limited to global warming,[2-4] rising sea level,[5] adverse climate change,[6] escalating greenhouse gas emissions,[7,8] food shortage,[9] and infectious disease threat.[10] One viable strategy to combat the rising energy demand and mitigate detrimental impacts on our ecosystem, public health, and economy is to utilize clean energy technology in the transportation and power generation sectors. Widespread adoption of alternative energy schemes, in principle, should lead to a sustainable energy economy, maintain food security, and reduce the dependence on foreign oil supplies in the future.[11] Fuel cells provide a feasible route to enable clean energy usage with minimal generation of undesired pollutants.

Fuel cells are electrochemical devices that convert chemical energy directly into electrical energy using an external fuel source.[12] Fuel cells are not heat engines, and therefore fuel cells are not limited by the Carnot cycle, which sets the upper boundary for the thermodynamic efficiency of internal combustion engines.[12] The theoretical efficiency of fuel cells can reach as high as 90 %.[12] With this superior efficiency and capacity, fuel cells are projected to be the energy conversion devices of choice for future transportation applications, provided that certain design problems can be solved.[13,14] These devices have utility in outer-space applications, but the costs remain too high for more conventional uses on Earth.[15]

Polymer electrolyte membrane fuel cells (PEMFCs) have a variety of potential portable applications, mainly in the transportation sector.[16] These relatively simple devices are comprised of a stack of ion-exchange membranes sandwiched between the cathode and anode, which are separated by a proton-conducting perfluoro-membrane commonly comprised of Nafion, with the catalysts deposited onto the electrode surfaces.[17,18] In addition to the attractive efficiency, PEMFCs also are environmentally friendly because water is the by-product. Despite their favorable qualities, PEMFCs are predominantly limited by fuel-crossover, a phenomenon that lowers the cell voltage, and sluggish oxygen reduction kinetics at the cathode, among other engineering issues.[19-25] The former impediment is being addressed by advances in the membrane material research but the kinetic issue remains largely unsolved. Therefore, at present the performance of PEMFCs is practically inhibited by the sluggish kinetics of the oxygen reduction reaction (ORR) at the cathode.

At present, no artificial catalyst is capable of facilitating the ORR at virtually no overpotential. The ORR is an intricate process that requires a lot of energy to break the particularly strong O=O double bond (498 kJ/mol) and involves multiple proton-coupled electron transfer (PCET) steps.[12] Apart from the large energy input required for O=O bond cleavage and the complicated reaction mechanism, most catalysts do not selectively reduce O_2 by 4 e^- to H_2O. Instead, these catalysts generate a substantial amount of H_2O_2 as a deleterious side product via a 2 e^- process that leads to membrane degradation and catalyst decomposition.[23-28] These limitations contribute to the lack of an active, selective, and cost-effective catalyst for the ORR which prevents the large-scale commercial use of low temperature PEMFCs.[29,30]

Catalysts are capable of lowering the kinetic barrier for the ORR, and precious metals such as Pt-group metals have long been used as an industrial standard to facilitate the ORR in fuel cells, especially those present in space shuttles and the international space station.[15] Current state-of-the-art fuel cells contain a high loading of Pt. However, the high cost and scarcity of Pt are two of the major impediments that have prohibited extensive commercialization of PEMFCs.[12] Another practical limitation of using Pt as the cathode catalyst is the 300 mV overpotential required to facilitate the ORR, a substantial energy loss that is higher than desired. In nature, a handful of naturally-occurring enzymes with well-defined active sites reduce O_2 more efficiently than Pt.[31,32] One attractive target is a class of enzymes called multicopper oxidases of which laccase is the most well-known example.[33] Laccase, a "blue oxidase" enzyme found in fungi, plants, and microorganisms, features a three-Cu active site where the ORR occurs.[34-39]

Laccase catalyzes the four-electron four-proton reduction of O_2 to H_2O, with minimal production of H_2O_2.[40-43] When immobilized onto gold surfaces using an anthracene-2-methanethiol linker, the enzyme functions as an efficient cathode catalyst at pH 7.[44] While commercial Pt catalysts exhibit a substantial overpotential of ~300 mV, the laccase-modified electrode shows a promising overpotential of merely ~70 mV.[45] However, the overall performance of the laccase-modified electrode is limited by the immense size of laccase (~60 kDa), which significantly decreases the current density and the power output. Furthermore, laccase is only stable in physiological pH solutions and is unable to withstand the harsh operating conditions of PEMFCs (typically temperatures 80–200 °C, pH <2).[12] Laccase activity is greatly inhibited under non-physiological conditions.[46] Taken together the enormous size, low chemical tolerance, and intrinsic thermal instability of the laccases studied, direct utilization of laccase as a cathode catalyst in PEMFCs is not practical.

Since the direct utilization of laccase is plagued with inherent shortcomings and cannot deliver the power density necessary for practical uses,[12] molecular models of the active site may yield a robust, yet efficient, catalyst.[47] It is desirable to develop new bio-inspired Cu complexes as fuel cell catalysts that supersede the activity of traditional materials at a substantially lower cost. Synthetic Cu complexes are well known to react with $O_{2,}$[12,48-51] although relatively few studies examine their ability to catalyze the reduction of O_2 to water. Recently, our group reported that the Cu complex of tris(2-pyridylmethyl)amine (TPA) catalyzes the ORR with an overpotential of 700 mV at pH 1, the lowest overpotential for a non-biological Cu complex at this pH.[52] Rational design of the ligand framework should allow further lowering of the ORR overpotential. By tuning the steric environment and electronic properties of the primary and secondary coordination spheres,[53-64] Cu complexes with O_2 in various binding modes have been isolated and characterized with concomitant changes to the thermodynamic reduction potentials of the metal centers.[65-69] The key to synthesizing fruitful biomimetic ORR catalysts based on laccase requires the *precise positioning* (spatial) of the *three copper centers* (chemical) of the *appropriate reducing power* (potential) at the *exact moment* (temporal). To ensure cooperativity comparable to that of metalloproteins, future catalysts require sophisticated ligand scaffolds.[70-73] Quantitative structure-activity relationship between ligand flexibility and ORR activity should assist in the identification of a molecular template that encourages intramolecular O_2 interaction by preorganizing the Cu units.

3. Results and Discussion

3.1. Cu complexes of Schiff base of DAT

Cu complexes of Schiff base of DAT essentially perform analogously to CuDAT, suggesting the addition of flanking electron-donating, electron-withdrawing, and proton-relay groups does not significantly perturb the dinuclear Cu core as the ORR reaction center. This is not the first example that ligand modification does not impact the electrocatalytic activity. For the tri- and di-pyridyl amine ligand scaffolds (TPA and DPA), tweaking the sterics, electronics, and contiguity of the framework has no effect on the ORR onset and diffusion-limited current achieved across a wide range of pH units (pH 1-13).[52,74,75] All these experiments strongly indicates that the electron transfer energetics is likely primarily dictated by the electrode potential at the glassy carbon surface and the proton transfer dynamics is predominantly controlled by the solution pH. Another possible explanation is the newly-installed functionality degrades during electrocatalytic activity assay to produce the unmodified parent Cu complex *in situ*.

3.2. Cu complex of pyrazolyl-based derivatives

In our continue effort to improve the performance of NPM catalysts for fuel cell technology, we prepared Cu complexes of pyrazole derivatives (substituents at the 3 and 5 positions) and trispyrazolylborate analogues (substituents at the 3 and 5 positions) shown in Figure 3. We further tested these earth-abundant catalysts on inexpensive carbon support as electrocatalysts for the ORR and compared their performance to that of the benchmark catalysts in this field (Tables 1 and 2).[76] The information in Table 1 came from detailed analyses of the raw data presented in Figure 4 to 9.

pH	Record	Onset	HO-py-NH_2	py-$(py)_2$	Tp^N
1	Cu-TPA	0.530 V			0.510 V
4	Cu-DAT	0.580 V			0.580 V
7	Cu-DAT	0.690 V	0.704 V	0.706 V	0.720 V
10	Cu-DAT	0.760 V			0.830 V
13	Cu-DAT	0.820 V			0.860 V

Table 1. ORR onsets of Cu complexes utilized in this study versus record holders in literature. ORR onsets are defined as the potential at which 5% of the i_{lim} is reached. See Table 2 for an extended list of reported ORR onsets of molecular ORR Cu electrocatalysts.[1,52]

Catalyst	ORR Onset (V vs. RHE)	pH, solution
$[Cu\text{-}Cu\text{-}2,9\text{-}Me_2\text{-}phen]^{2+}$	0.610	pH 5, Britton-Robinson
$[CuTPA](ClO4)_2$ and TPA-derivatives	0.690	pH 7, Britton-Robinson
$[Cu\text{-}hexaazamac]Cl_4$	0.670	pH 7.3, Borate Buffer

Table 2. An updated literature review on reported ORR onsets of non-heat-treated Cu catalysts.[75-77]

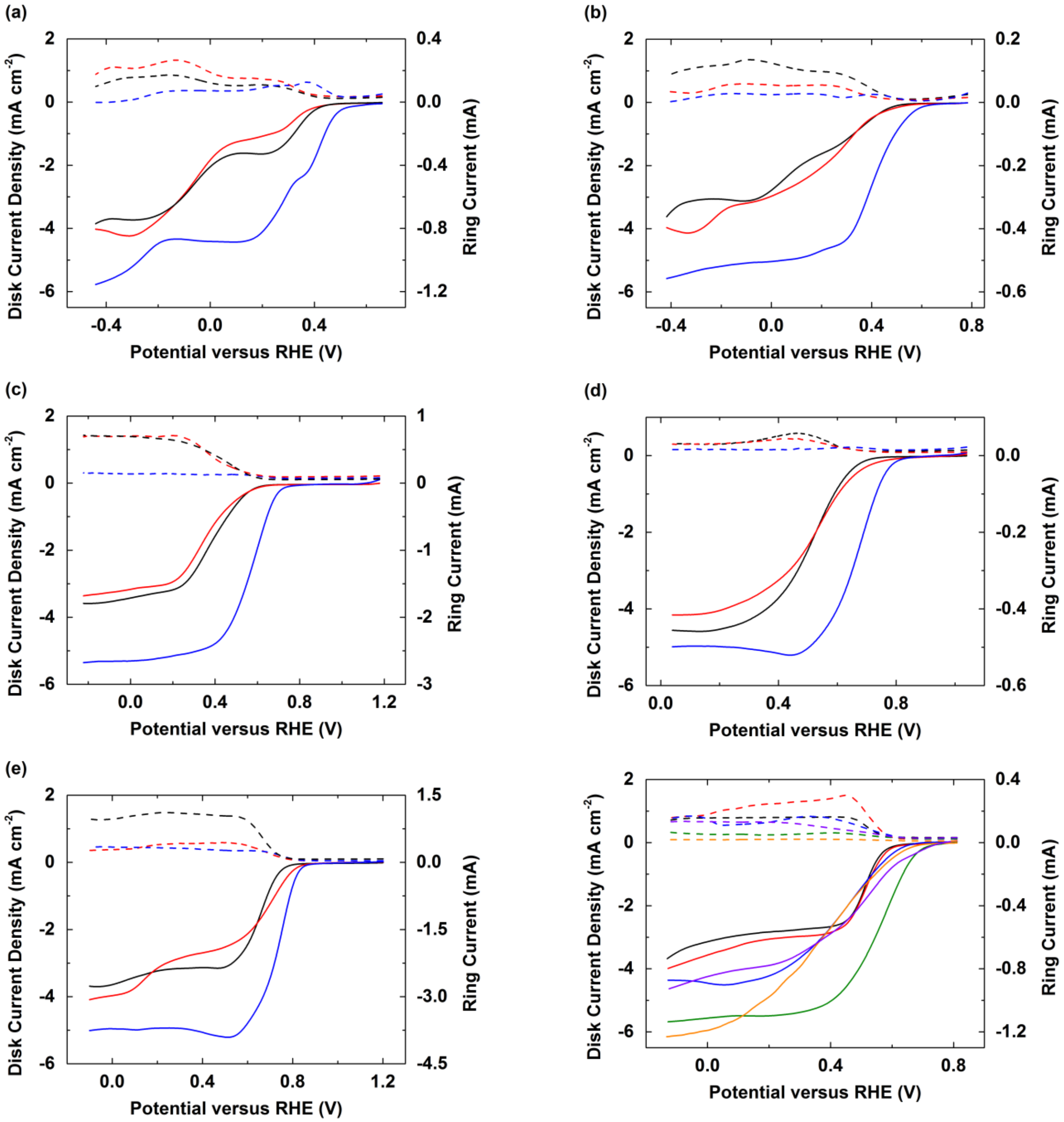

Figure 4. Linear sweep voltammograms (LSVs, solid lines) and ring currents (dashed lines) of $[Cu(Tp)]^{2+}$ (black), $[Cu(Tp^{*})]^{2+}$ (red), and $[Cu(TpN)]^{2+}$ (blue) supported on Vulcan XC-72 in (a) pH 1, (b) pH 4, (c) pH 7, (d) pH 10, and (e) pH 13 O_2-saturated Britton-Robinson buffer solutions with a scan rate of 10 mV/s at 1600 rpm. (f) LSVs (solid lines) and ring currents (dashed lines) of $[Cu(pr)]^{2+}$ (black), $[Cu(py\text{-}(CH_3)_2)]^{2+}$ (red), $[Cu(py\text{-}(COOH)_2)]^{2+}$ (blue), $[Cu(py\text{-}(NH_2)_2)]^{2+}$ (orange), $[Cu(py\text{-}(py)_2)]^{2+}$ (purple), and $[Cu(HO\text{-}py\text{-}NH_2)]^{2+}$ (green)

supported on Vulcan XC-72 in (a) pH 1, (b) pH 4, (c) pH 7, (d) pH 10, and (e) pH 13 O_2-saturated Britton-Robinson buffer solutions with a scan rate of 10 mV/s at 1600 rpm.

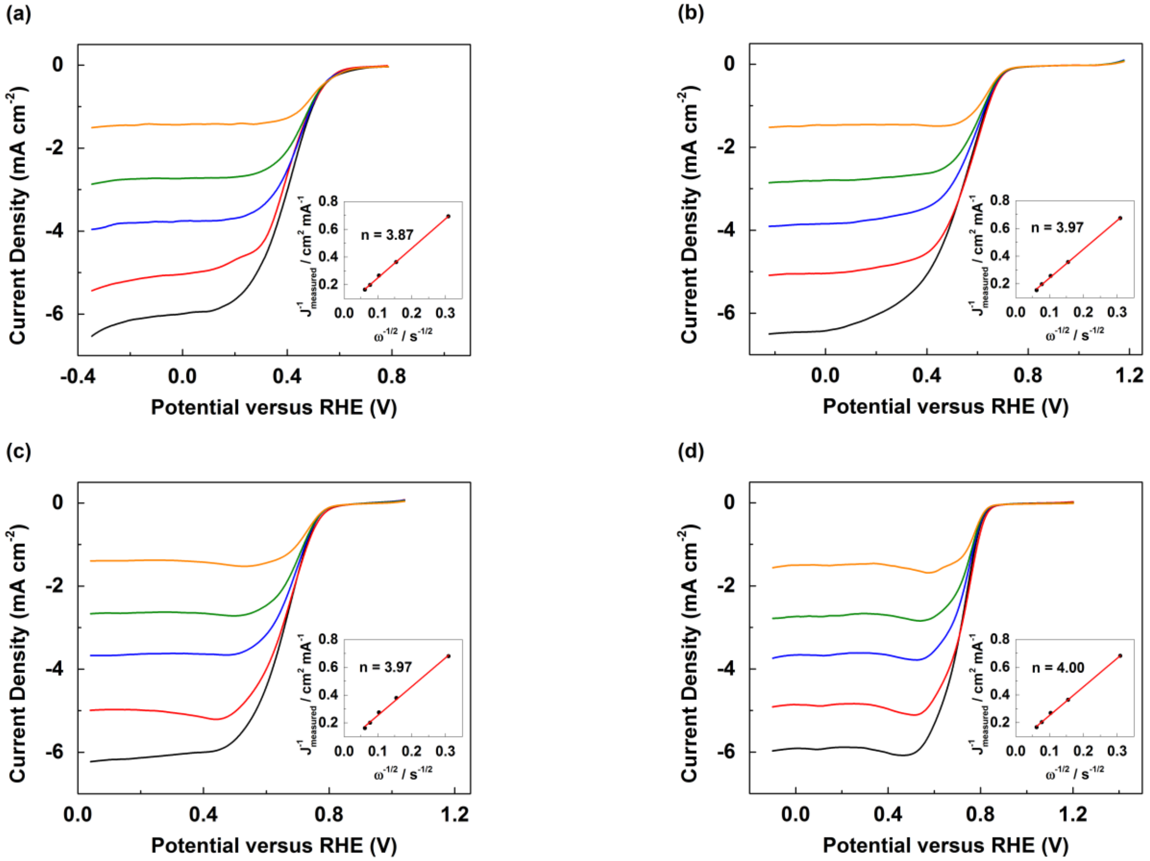

Figure 5. Rotating disk electrode (RDE) LSVs and Koutecky-Levich plots (inset) of $[Cu(TpN)]^{2+}$ supported on Vulcan XC-72 in (a) pH 4, (b) pH 7, (c) pH 10, and (d) pH 13 O_2-saturated solutions with a scan rate of 10 mV/s at 100 (red), 400 (blue), 900 (green), 1600 (violet), and 2500 rpm (orange).

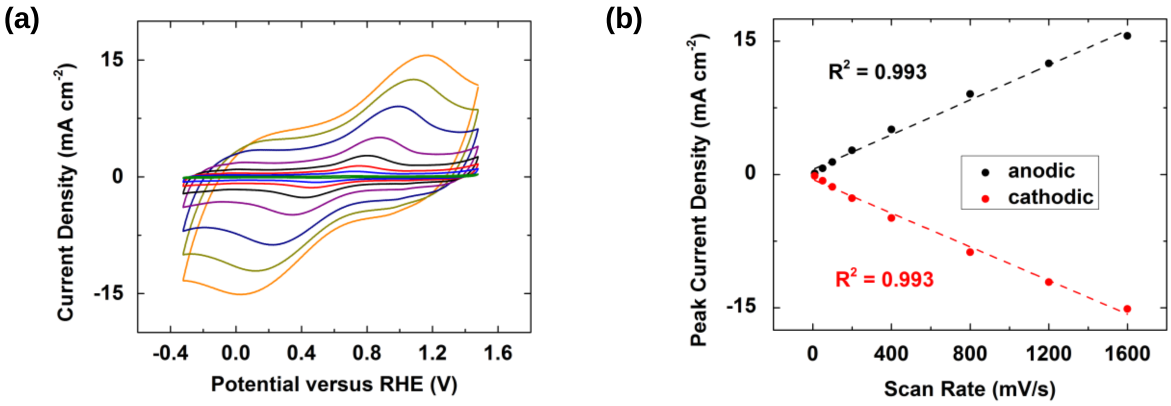

Figure 6. (a) Cyclic voltammograms (CVs) of $[Cu(TpN)]^{2+}$ with scan rates of 10 (green), 50 (blue), 100 (red), 200 (black), 400 (purple), 800 (navy), 1200 (yellow), and 1600 (orange) mV/s

in Ar-saturated pH 7 Britton-Robinson buffer solution. (b) Randles−Sevcik plot of $[Cu(TpN)]^{2+}$ obtained from the cathodic (red circles) and anodic (black circles) peak current densities.

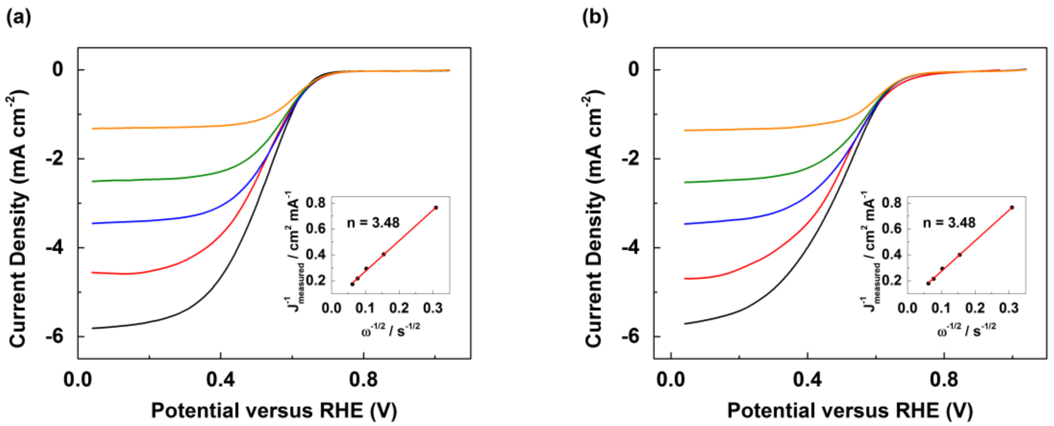

Figure 7. Rotating disk electrode (RDE) LSVs and Koutecky-Levich plots (inset) of (a) $[Cu(Tp)]^{2+}$ and (b) $[Cu(Tp^*)]^{2+}$ supported on Vulcan XC-72 in pH 10 O_2-saturated Britton-Robinson buffer solution with a scan rate of 10 mV/s at 100 (red), 400 (blue), 900 (green), 1600 (violet), and 2500 rpm (orange).

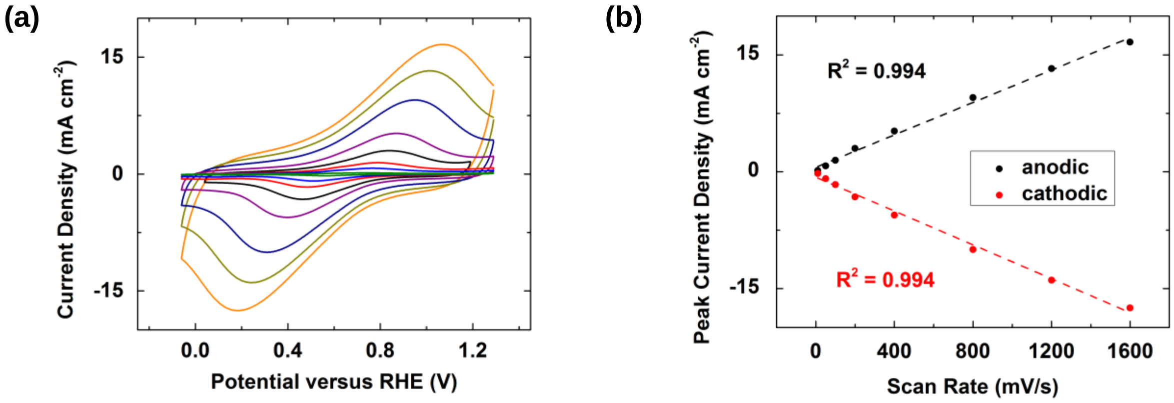

Figure 8. (a) CVs of $[Cu(TpN)]^{2+}$ with scan rates of 10 (green), 50 (blue), 100 (red), 200 (black), 400 (purple), 800 (navy), 1200 (yellow), and 1600 (orange) mV/s in Ar-saturated pH 10 Britton-Robinson buffer solution. (b) Randles−Sevcik plot of $[Cu(TpN)]^{2+}$ obtained from the cathodic (red circles) and anodic (black circles) peak current densities.

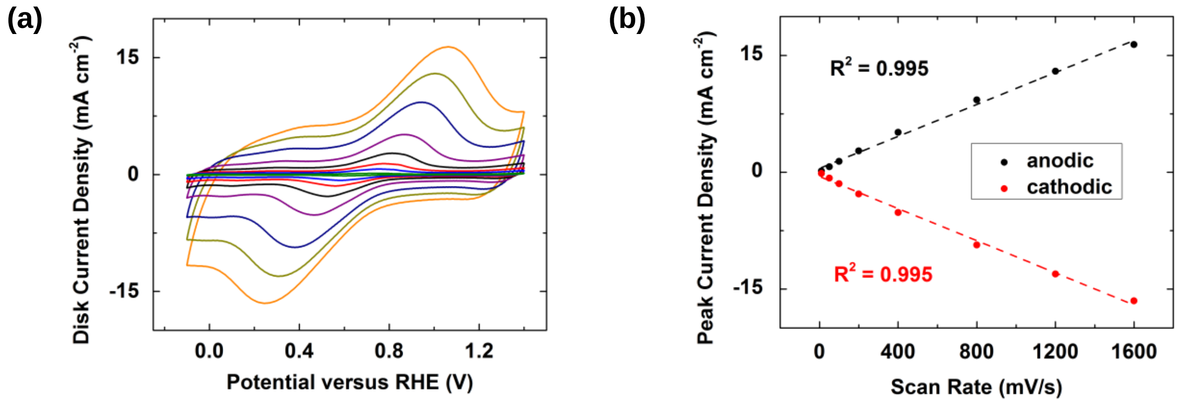

Figure 9. (a) CVs of $[Cu(TpN)]^{2+}$ with scan rates of 10 (green), 50 (blue), 100 (red), 200 (black), 400 (purple), 800 (navy), 1200 (yellow), and 1600 (orange) mV/s in Ar-saturated pH 13 Britton-Robinson buffer solution. (b) Randles−Sevcik plot of $[Cu(TpN)]^{2+}$ obtained from the cathodic (red circles) and anodic (black circles) peak current densities.

3.3. NPM catalysts that involve pyridyl-, imidazolyl-, and alkyl-amine-based ligands

Our preliminary screening tests corroborate that Cu complexes of melamine derivatives in general are ineffective ORR catalysts relative to other classes of Cu complexes, likely because the geometric constraints by melamine inhibited the formation of a multi-nuclear active site that enforces cooperativity among the three Cu ions. Alkyl-amine-based ligands are typically inactive electrocatalysts, likely due to the unfavorable electronic coupling between the resultant Cu complex and the graphitic-like electrode surface.[75] Although imidazole is structurally closest to histidine, the eight residues that assemble the three Cu in place in laccase, the basicity of pyridine resembles that of histidine more closely than imidazole.[78,79] In order to realize a functional analogue of laccase, we used pyridyl-based ligands as surrogates of histidines in hope to achieve more faithful mimicry. Building upon the T3-T2-T3 paradigm developed by our group using the Cu-DPA platform (Figure 10), we further investigated first-row transition metal complexes of these linked DPA ligands.

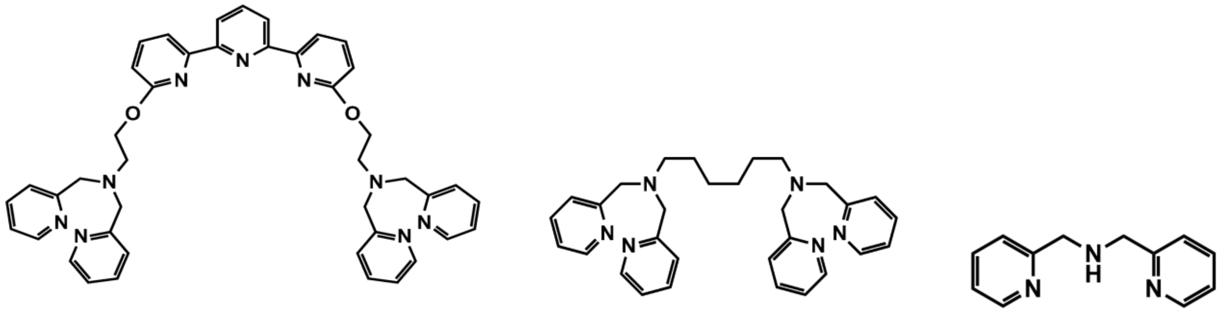
terpy-bis-DPA C6-bis-DPA DPA

Figure 10. A selective list of linked-DPA ligands used.

EA Results	**Weight %**				**Mole %**		**Ratio**	
C6-bis-DPA complex	**C**	**H**	**N**	**M**	**N**	**M**	**N:M**	**Lig:M**
$MnCl_2$	85.16	1.34	2.94	3.64	0.21	0.07	3.17	1.06
$FeCl_3$	89.52	0.92	2.00	1.94	0.14	0.03	4.11	1.37
$CoCl_2$	87.27	1.13	2.34	3.07	0.17	0.05	3.21	1.07
$NiCl_2$	88.04	0.97	1.86	2.36	0.13	0.04	3.30	1.10
$ZnCl_2$	81.31	1.73	3.80	5.98	0.27	0.09	2.97	0.99

Table 3. Elemental analysis of 1st row transition metal complexes of C6-bis-DPA.

Here, we prepared dinuclear complexes of Mn, Fe, Co, Ni, Cu, and Zn supported on Vulcan XC-72 carbon powder and characterized these earth-abundant materials using elemental analysis (EA) techniques (Table 3). We first investigated the redox response of the dinuclear complexes of C6-bis-DPA containing Mn, Fe, Co, Ni, Cu, and Zn in pH 7 buffer using CV and differential pulse voltammetry (DPV, for weak signal). Each of the di-Fe and di-Cu complexes of C6-bis-DPA shows a distinct redox peak (Figure 11a). The di-Co complex of C6-bis-DPA exhibits multiple redox waves, likely suggesting that several Co complexes are present or various Co redox states are accessible under these conditions. Multiple Co species were observed under similar conditions used for oxygen evolution reaction (OER) studies. However, we were not able to observe any redox response for the cases involving the dinuclear Mn, Ni, and Zn complexes using CV techniques. Therefore, we employed DPV in an effort to reveal weak redox signals. The orange line in Figure 11b reveals a weak redox wave of the di-Ni complex. However, the di-Zn and di-Mn complexes are redox silent under these conditions, consistent to previous reports of other Zn and Mn complexes.

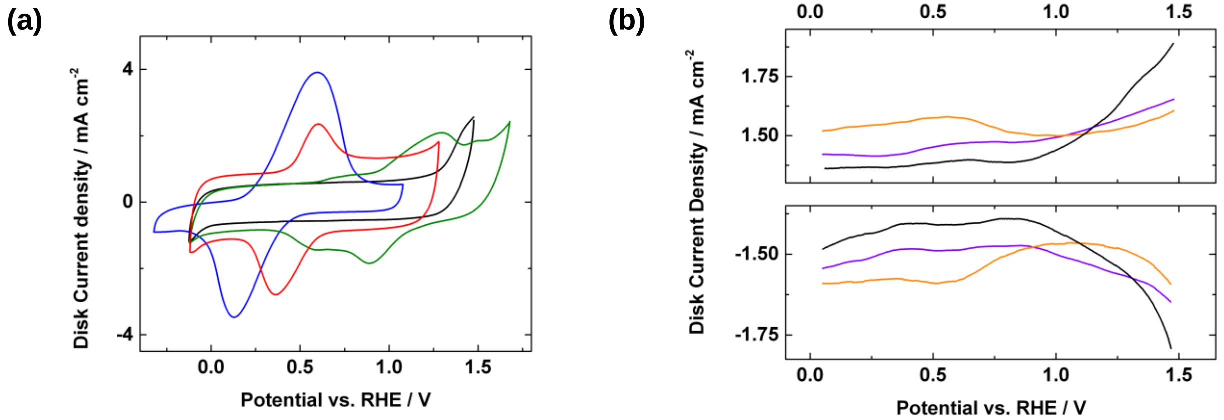

Figure 11a. CV of the Fe (red), Co (green), Cu (blue), and Zn (black) complexes of C6-bis-DPA in an Ar-sparged pH 7 Britton-Robinson buffer solution with a scan rate of 200 mV/s. Fig. 10 Differential pulse voltammograms of Ni (orange), Mn (purple), and Zn (black) complexes of C6-bis-DPA in an Ar-sparged pH 7 Britton-Robinson buffer solution.

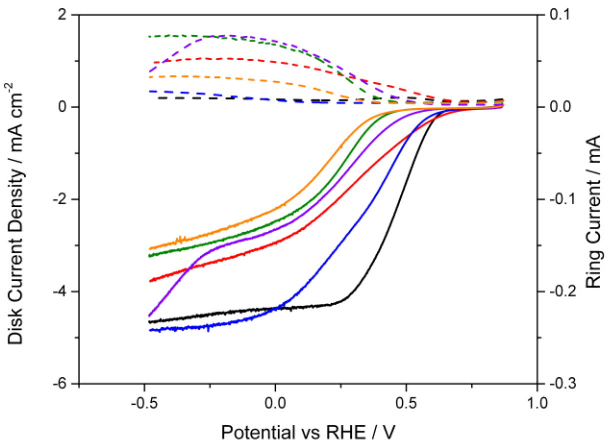

Figure 12. Rotating ring-disk electrode (RRDE) LSVs of [Cu_2(C6-bis-DPA)Cl_4] (black), [Co_2(C6-bis-DPA)$(H_2O)_2Cl_4$] (red), [Fe_2(C6-bis-DPA)Cl_6] (blue), [Ni_2(C6-bis-DPA)Cl_4] (green), [Zn_2(C6-bis-DPA)Cl_4] (violet), and [Mn_2(C6-bis-DPA)$(H_2O)_2Cl_4$] (orange) supported on Vulcan XC-72 in pH 7 O_2-saturated Britton-Robinson buffer solution at 1600 rpm.

The ORR activity of mononuclear first-row transition metal complexes of TPA was reported previously.[80] However, the use of dinuclear and trinuclear first-row transition metal complexes as ORR catalysts remains an uncharted area. Here, we investigated the ORR activity of these inexpensive carbon-supported catalysts in pH 7 solutions using rotating ring-disk electrode (RRDE) experiments (Figure 12). Table 4 summarizes the number of electrons transferred during the ORR process for the cases of the six dinuclear complexes using data from Figure 12. Results in Figure 12 and Table 4 demonstrate that only dinuclear complexes of C6-bis-DPA containing Fe and Cu reduce O_2 by almost 4 e^-. The di-Cu complex exhibits an onset potential more positive than the di-Fe complex, indicating the di-Cu complex is a better ORR catalyst candidate. The corresponding C6-bis-DPA complexes of Ni, Mn, Co, and Zn produce significant amounts of H_2O_2, as detected by the concentric Pt ring around the glassy carbon working electrode. The di-Co complex exhibits the lowest ORR onset potential, albeit undergoing a mixture of 2 e^- and 4 e^- process to reduce O_2. Experiments involving the trinuclear complexes of terpy-bis-DPA are underway.

Complexes supported on Vulcan XC-72	**Number of e^-**
$[Cu_2(C6\text{-bis-DPA})Cl_4]$	3.78
$[Co_2(C6\text{-bis-DPA})(H_2O)_2Cl_4]$	2.72
$[Fe_3(C6\text{-bis-DPA})Cl_6]$	3.76
$[Ni_2(C6\text{-bis-DPA})Cl_4]$	2.28
$[Zn_2(C6\text{-bis-DPA})Cl_4]$	2.98
$[Mn_2(C6\text{-bis-DPA})(H_2O)_2Cl_4]$	2.26

Table 4. Number of e^- transferred, calculated from the percent yield of H_2O_2 obtained from RRDE experiments presented in Figure 12, catalyzed by various 1st row transition metal complexes of C6-bis-DPA ligand.

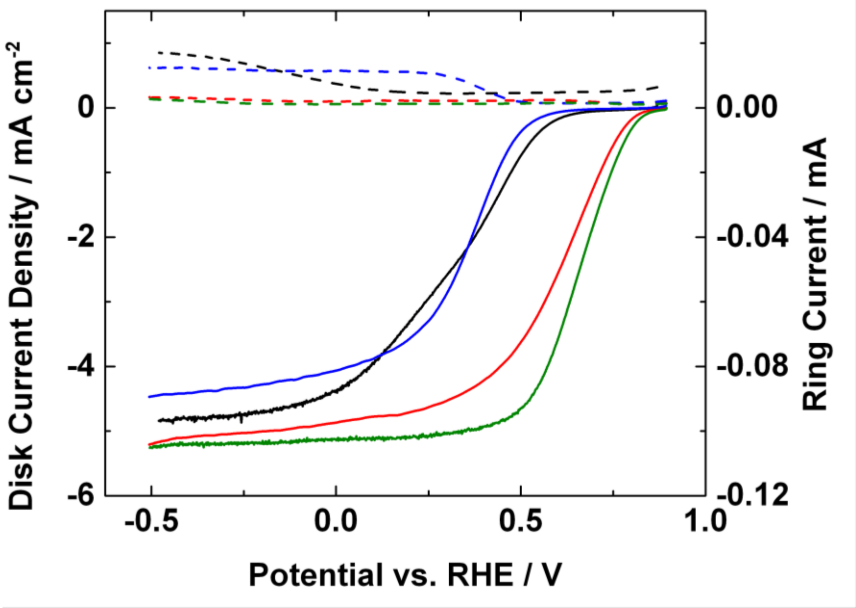

Figure 13. RRDE linear sweep voltammograms and ring currents of [Fe_2(C6-bis-DPA)Cl_6] (black), pyrolyzed [Fe_2(C6-bis-DPA)Cl_6] (red), [Fe_3(terpy-bis-DPA)Cl_6] (blue), and pyrolyzed [Fe_3(terpy-bis-DPA)Cl_6] (green) supported on Vulcan XC-72 in pH 7 O_2-saturated Britton-Robinson buffer solution at 1600 rpm.

Pyrolysis of first-row transition metal complexes commonly results in heterogeneous materials that exhibit enhanced ORR activity relative to that of the parent unpyrolyzed discrete small molecules.[81] In particular, pyrolyzed Fe materials are the most active among catalysts that contain first-row transition metals. Here, we prepared pyrolyzed materials using multi-nuclear Fe complexes of C6-bis-DPA and terpy-bis-DPA as starting materials. Figure 13 displays the RRDE results of pyrolyzed and unpyrolyzed Fe catalysts using DPA with C6 and terpy linker as the starting material. The unpyrolzyed di-Fe complex of C6-bis-DPA might feature a Fe_2-core resembling that of hemerythrin, a class of naturally-occurring non-heme iron proteins found in deep-ocean invertebrates that possesses rich O_2 chemistry.[82-99] Interestingly, the tri-Fe complex produces more H_2O_2 and exhibits a more negative ORR onset potential compared to the di-Fe complex. This empirical observation may stem from the terpy-bound Fe, a non DPA-bound Fe that contributes to the unfavorable effect observed. However, upon subjecting the di-Fe and tri-

Fe complexes to a pyrolysis treatment at 900 °C for 30 min, the amount of H_2O_2 detected decreases substantially and the ORR onset potential shifts positive by a significant amount, observations that are consistent with publish reports on using mononuclear Fe macrocycles and Fe-containing N-rich polymers as precursors. Taken together our preliminary results using di-Fe and tri-Fe as precursors and a vast library of published data, the active site of all these pyrolyzed materials likely does not resemble the precursors introduced prior to the pyrolysis step. In other words, the commonly-perceived Fe-N_4 core as the active site is highly likely a misconception due to the severe degree of heterogeneity as a result of the harsh condition utilized during the preparation step. Efforts to elucidate the active site are currently underway. Once we identify the structure and nature of the active site, we will construct the active site using a bottom-up method, tune the electronics and sterics of the site, and devise a simpler fabrication scheme in order to reduce the amount of waste during the preparation step.

4. Conclusions

In our continue effort to improve the performance of NPM catalysts for fuel cell technology, we prepared Fe, Co, and Cu complexes of pyrazolyl-, imidazolyl-, and triazolyl-based ligands as active electrocatalysts to facilitate the performance-limiting ORR. We found that for a given set of ligand under the same condition, molecular Cu complexes typically result in the most efficient NPM catalysts with the most positive onset potential for ORR and the least H_2O_2 yield. Upon high-temperature treatment, heterogeneous Fe materials general yield the most active NPM catalysts. Ligand modification serves as a general and effective strategy to enhance both the activity and selectivity of ORR catalysts.

5. References

(1) Thorum, M. S.; Yadav, J.; Gewirth, A. A. *Angew. Chem. Int. Ed.* **2009**, *48*, 165.

(2) Blois, J. L.; Zarnetske, P. L.; Fitzpatrick, M. C.; Finnegan, S. *Science* **2013**, *341*, 499.

(3) Moritz, C.; Agudo, R. *Science* **2013**, *341*, 504.

(4) Post, E.; Bhatt, U. S.; Bitz, C. M.; Brodie, J. F.; Fulton, T. L.; Hebblewhite, M.; Kerby, J.; Kutz, S. J.; Stirling, I.; Walker, D. A. *Science* **2013**, *341*, 519.

(5) Kintisch, E. *Science* **2013**, *341*, 480.

(6) Diffenbaugh, N. S.; Field, C. B. *Science* **2013**, *341*, 486.

(7) Appel, A. M.; Bercaw, J. E.; Bocarsly, A. B.; Dobbek, H.; DuBois, D. L.; Dupuis, M.; Ferry, J. G.; Fujita, E.; Hille, R.; Kenis, P. J. A.; Kerfeld, C. A.; Morris, R. H.; Peden, C. H. F.; Portis, A. R.; Ragsdale, S. W.; Rauchfuss, T. B.; Reek, J. N. H.; Seefeldt, L. C.; Thauer, R. K.; Waldrop, G. L. *Chem. Rev.* **2013**, *113*, 6621.

(8) Benson, E. E.; Kubiak, C. P.; Sathrum, A. J.; Smieja, J. M. *Chem. Soc. Rev.* **2009**, *38*, 89.

(9) Wheeler, T.; von Braun, J. *Science* **2013**, *341*, 508.

(10) Altizer, S.; Ostfeld, R. S.; Johnson, P. T. J.; Kutz, S.; Harvell, C. D. *Science* **2013**, *341*, 514.

(11) Chu, S.; Majumdar, A. *Nature* **2012**, *488*, 294.

(12) Gewirth, A. A.; Thorum, M. S. *Inorg. Chem.* **2010**, *49*, 3557.

(13) DeLuca, N. W.; Elabd, Y. A. *J. Polym. Sci., Part B: Polym. Phys.* **2006**, *44*, 2201.

(14) Carter, D.; Ryan, M.; Wing, J. *Fuel Cell Today* **2012**, 1.

(15) Chan, C. C. *Proc. IEEE* **2007**, *95*, 704.

(16) Sandy Thomas, C. E. *Int. J. Hydrogen Energ.* **2009**, *34*, 9279.

(17) Debe, M. K. *Nature* **2012**, *486*, 43.

(18) Wang, Y.; Chen, K. S.; Mishler, J.; Cho, S. C.; Adroher, X. C. *Applied Energy* **2011**, *88*, 981.

(19) Li, H.; Shi, Z.; Zhang, J. In *Encyclopedia of Electrochemical Power Sources*; Garche, J., Ed.; Elsevier: Amsterdam, 2009, p 941.

(20) Gervasio, D. In *Encyclopedia of Electrochemical Power Sources*; Garche, J., Ed.; Elsevier: Amsterdam, 2009, p 806.

(21) Srouji, A.-K.; Mench, M. M. In *Polymer Electrolyte Fuel Cell Degradation*; Veziroglu, M. M. M. C. K. N., Ed.; Academic Press: Boston, 2012, p 293.

(22) El-kharouf, A.; Pollet, B. G. In *Polymer Electrolyte Fuel Cell Degradation*; Veziroglu, M. M. M. C. K. N., Ed.; Academic Press: Boston, 2012, p 215.

(23) Wu, J.; Yuan, X. Z.; Martin, J. J.; Wang, H.; Zhang, J.; Shen, J.; Wu, S.; Merida, W. *J. Power Sources* **2008**, *184*, 104.

(24) Wu, J.; Yuan, X. Z.; Martin, J. J.; Wang, H. In *Encyclopedia of Electrochemical Power Sources*; Garche, J., Ed.; Elsevier: Amsterdam, 2009, p 848.

(25) Coms, F. D. *ECS Trans.* **2008**, *16*, 235.

(26) Cheng, X.; Shi, Z.; Glass, N.; Zhang, L.; Zhang, J.; Song, D.; Liu, Z.-S.; Wang, H.; Shen, J. *J. Power Sources* **2007**, *165*, 739.

(27) Jaouen, F.; Proietti, E.; Lefevre, M.; Chenitz, R.; Dodelet, J.-P.; Wu, G.; Chung, H. T.; Johnston, C. M.; Zelenay, P. *Energy Environ. Sci.* **2011**, *4*, 114.

(28) Higgins, D. C.; Chen, Z. *Can. J. Chem. Eng.* **2013**, *91*, 1881.

(29) Bezerra, C. W. B.; Zhang, L.; Liu, H.; Lee, K.; Marques, A. L. B.; Marques, E. P.; Wang, H.; Zhang, J. *J. Power Sources* **2007**, *173*, 891.

(30) Cao, D.; Sun, Y.; Wang, G. *J. Power Sources* **2007**, *167*, 250.

(31) Dagys, M.; Haberska, K.; Shleev, S.; Arnebrant, T.; Kulys, J.; Ruzgas, T. *Electrochem. Commun.* **2010**, *12*, 933.
(32) Blanford, C. F.; Heath, R. S.; Armstrong, F. A. *Chem. Commun.* **2007**, 1710.
(33) Yoon, J.; Fujii, S.; Solomon, E. I. *Proc. Natl. Acad. Sci. U.S.A.* **2009**, *106*, 6585.
(34) Solomon, E. I.; Augustine, A. J.; Yoon, J. *Dalton Trans.* **2008**, 3921.
(35) Solomon, E. I.; Randall, D. W.; Glaser, T. *Coor. Chem. Rev.* **2000**, *200*, 595.
(36) Solomon, E. I.; Sundaram, U. M.; Machonkin, T. E. *Chem. Rev.* **1996**, *96*, 2563.
(37) Solomon, E. I.; Kirk, M. L.; Gamelin, D. R.; Pulver, S. In *Biochemical Spectroscopy*; Academic Press Inc.: San Diego, CA, 1995; Vol. 246, p 71.
(38) Solomon, E. I.; Lowery, M. D.; Lacroix, L. B.; Root, D. E. *Metallobiochemistry, Part C* **1993**, *226*, 1.
(39) Solomon, E. I.; Hare, J. W.; Gray, H. B. *Proc. Natl. Acad. Sci. U.S.A.* **1976**, *73*, 1389.
(40) Silva, C. S.; Damas, J. M.; Chen, Z.; Brissos, V.; Martins, L. O.; Soares, C. M.; Lindley, P. F.; Bento, I. *Acta Crystallogr. D: Biol. Crystallogr.* **2012**, *68*, 186.
(41) Nogala, W.; Szot, K.; Burchardt, M.; Jönsson-Niedziolka, M.; Rogalski, J.; Wittstock, G.; Opallo, M. *Bioelectrochemistry* **2010**, *79*, 101.
(42) Bento, I.; Silva, C.; Chen, Z.; Martins, L.; Lindley, P.; Soares, C. *BMC Struct. Biol.* **2010**, *10*, 28.
(43) Blanford, C. F.; Foster, C. E.; Heath, R. S.; Armstrong, F. A. *Faraday Discuss.* **2009**, *140*, 319.
(44) Thorum, M. S.; Anderson, C. A.; Hatch, J. J.; Campbell, A. S.; Marshall, N. M.; Zimmerman, S. C.; Lu, Y.; Gewirth, A. A. *J. Phys. Chem. Lett.* **2010**, *1*, 2251.
(45) Schweiger, H.; Vayner, E.; Anderson, A. B. *Electrochem. Solid-State Lett.* **2005**, *8*, A585.
(46) Toledo-Núñez, C.; López-Cruz, J. I.; Hernández-Arana, A. *Biophys. Chem.* **2012**, *167*, 36.
(47) Spiccia, L.; Graham, B.; T. W. Hearn, M.; Lazarev, G.; Moubaraki, B.; S. Murray, K.; R. T. Tiekink, E. *Dalton Trans.* **1997**, 4089.
(48) Mirica, L. M.; Ottenwaelder, X.; Stack, T. D. P. *Chem. Rev.* **2004**, *104*, 1013.
(49) Lewis, E. A.; Tolman, W. B. *Chem. Rev.* **2004**, *104*, 1047.
(50) Hatcher, L. Q.; Karlin, K. D. In *Adv. Inorg. Chem.*; Eldik, R. v., Reedijk, J., Eds.; Academic Press: 2006; Vol. Volume 58, p 131.
(51) Hatcher, L. Q.; Karlin, K. D. *J Biol Inorg Chem* **2004**, *9*, 669.
(52) Thorseth, M. A.; Letko, C. S.; Rauchfuss, T. B.; Gewirth, A. A. *Inorg. Chem.* **2011**, *50*, 6158.
(53) Harata, M.; Hasegawa, K.; Jitsukawa, K.; Masuda, H.; Einaga, H. *Bull. Chem. Soc. Japan* **1998**, *71*, 1031.
(54) Schatz, M.; Becker, M.; Thaler, F.; Hampel, F.; Schindler, S.; Jacobson, R. R.; Tyeklár, Z.; Murthy, N. N.; Ghosh, P.; Chen, Q.; Zubieta, J.; Karlin, K. D. *Inorg. Chem.* **2001**, *40*, 2312.
(55) Jacobson, R. R.; Tyeklar, Z.; Farooq, A.; Karlin, K. D.; Liu, S.; Zubieta, J. *J. Am. Chem. Soc.* **1988**, *110*, 3690.
(56) Kitajima, N.; Fujisawa, K.; Morooka, Y.; Toriumi, K. *J. Am. Chem. Soc.* **1989**, *111*, 8975.
(57) Kitajima, N.; Moro-oka, Y. *Chem. Rev.* **1994**, *94*, 737.

(58) Maiti, D.; Fry, H. C.; Woertink, J. S.; Vance, M. A.; Solomon, E. I.; Karlin, K. D. *J. Am. Chem. Soc.* **2007**, *129*, 264.

(59) Maiti, D.; Woertink, J. S.; Narducci Sarjeant, A. A.; Solomon, E. I.; Karlin, K. D. *Inorg. Chem.* **2008**, *47*, 3787.

(60) Tyeklar, Z.; Jacobson, R. R.; Wei, N.; Murthy, N. N.; Zubieta, J.; Karlin, K. D. *J. Am. Chem. Soc.* **1993**, *115*, 2677.

(61) Thorseth, M. A.; Letko, C. S.; Tse, E. C. M.; Rauchfuss, T. B.; Gewirth, A. A. *Inorg. Chem.* **2012**, *52*, 628.

(62) Fujii, H. *J. Am. Chem. Soc.* **1993**, *115*, 4641.

(63) Kitajima, N.; Fujisawa, K.; Fujimoto, C.; Morooka, Y.; Hashimoto, S.; Kitagawa, T.; Toriumi, K.; Tatsumi, K.; Nakamura, A. *J. Am. Chem. Soc.* **1992**, *114*, 1277.

(64) Blackman, A. G.; Tolman, W. B. *Struct. Bonding* **2000**, *97*, 179.

(65) Nagao, H.; Komeda, N.; Mukaida, M.; Suzuki, M.; Tanaka, K. *Inorg. Chem.* **1996**, *35*, 6809.

(66) Blackman, A. G. *Euro. J. Inorg. Chem.* **2008**, *2008*, 2633.

(67) Chuang, C.-l.; Lim, K.; Chen, Q.; Zubieta, J.; Canary, J. W. *Inorg. Chem.* **1995**, *34*, 2562.

(68) Chuang, C.-L.; Lim, K.; Canary, J. W. *Supramol. Chem.* **1995**, *5*, 39.

(69) Sorrell, T. N.; Jameson, D. L. *Inorg. Chem.* **1982**, *21*, 1014.

(70) Maiti, D.; Woertink, J. S.; Ghiladi, R. A.; Solomon, E. I.; Karlin, K. D. *Inorg. Chem.* **2009**, *48*, 8342.

(71) Tsui, E. Y.; Kanady, J. S.; Day, M. W.; Agapie, T. *Chem. Commun.* **2011**, *47*, 4189.

(72) Tsui, E. Y.; Day, M. W.; Agapie, T. *Angew. Chem. Int. Ed.* **2011**, *50*, 1668.

(73) Lionetti, D.; Day, M. W.; Agapie, T. *Chem. Sci.* **2013**, *4*, 785.

(74) Tse, E. C. M.; Schilter, D.; Gray, D. L.; Rauchfuss, T. B.; Gewirth, A. A. *Inorg. Chem.* **2014**, *53*, 8505.

(75) Thorseth, M. A.; Letko, C. S.; Tse, E. C. M.; Rauchfuss, T. B.; Gewirth, A. A. *Inorg. Chem.* **2013**, *52*, 628.

(76) Thorseth, M. A.; Tornow, C. E.; Tse, E. C. M.; Gewirth, A. A. *Coor. Chem. Rev.* **2013**, *257*, 130.

(77) McCrory, C. C. L.; Ottenwaelder, X.; Stack, T. D. P.; Chidsey, C. E. D. *J. Phys. Chem. A* **2007**, *111*, 12641.

(78) Company, C. R. *CRC Handbook of Chemistry and Physics*; CRC Press, 1981.

(79) Sorrell, T. N. *Tetrahedron* **1989**, *45*, 3.

(80) Ward, A. L.; Elbaz, L.; Kerr, J. B.; Arnold, J. *Inorg. Chem.* **2012**, *51*, 4694.

(81) Chen, Z.; Higgins, D.; Yu, A.; Zhang, L.; Zhang, J. *Energy Environ. Sci.* **2011**, *4*, 3167.

(82) Wirstam, M.; Lippard, S. J.; Friesner, R. A. *J. Am. Chem. Soc.* **2003**, *125*, 3980.

(83) Sessler, J. L.; Sibert, J. W.; Lynch, V.; Markert, J. T.; Wooten, C. L. *Inorg. Chem.* **1993**, *32*, 621.

(84) Pulver, S.; Froland, W. A.; Fox, B. G.; Lipscomb, J. D.; Solomon, E. I. *J. Am. Chem. Soc.* **1993**, *115*, 12409.

(85) Plowman, J. E.; Loehr, T. M.; Schauer, C. K.; Anderson, O. P. *Inorg. Chem.* **1984**, *23*, 3553.

(86) Mizoguchi, T. J.; Lippard, S. J. *J. Am. Chem. Soc.* **1998**, *120*, 11022.

(87) Mizoguchi, T. J.; Kuzelka, J.; Spingler, B.; DuBois, J. L.; Davydov, R. M.; Hedman, B.; Hodgson, K. O.; Lippard, S. J. *Inorg. Chem.* **2001**, *40*, 4662.

(88) Mauerer, B.; Crane, J.; Schuler, J.; Wieghardt, K.; Nuber, B. *Angew. Chem. Int. Ed.* **1993**, *32*, 289.
(89) Mahapatra, S.; Kaderli, S.; Llobet, A.; Neuhold, Y. M.; Palanche, T.; Halfen, J. A.; Young, V. G.; Kaden, T. A.; Que, L.; Zuberbuhler, A. D.; Tolman, W. B. *Inorg. Chem.* **1997**, *36*, 6343.
(90) He, C.; Barrios, A. M.; Lee, D.; Kuzelka, J.; Davydov, R. M.; Lippard, S. J. *J. Am. Chem. Soc.* **2000**, *122*, 12683.
(91) Fernandes, C.; Neves, A.; Vencato, I.; Bortoluzzi, A. J.; Drago, V.; Weyhermuller, T.; Rentschler, E. *Chem. Lett.* **2000**, 540.
(92) Das, S.; Bhattacharyya, J.; Mukhopadhyay, S. *Dalton Trans.* **2008**, 6634.
(93) Brunold, T. C.; Solomon, E. I. *J. Am. Chem. Soc.* **1999**, *121*, 8277.
(94) Brunold, T. C.; Solomon, E. I. *J. Am. Chem. Soc.* **1999**, *121*, 8288.
(95) Brown, C. A.; Remar, G. J.; Musselman, R. L.; Solomon, E. I. *Inorg. Chem.* **1995**, *34*, 688.
(96) Bossek, U.; Hummel, H.; Weyhermuller, T.; Bill, E.; Wieghardt, K. *Angew. Chem. Int. Ed.* **1995**, *34*, 2642.
(97) Armstrong, W. H.; Lippard, S. J. *J. Am. Chem. Soc.* **1984**, *106*, 4632.
(98) Arii, H.; Nagatomo, S.; Kitagawa, T.; Miwa, T.; Jitsukawa, K.; Einaga, H.; Masuda, H. *J. Inorg. Biochem.* **2000**, *82*, 153.
(99) Arii, H.; Funahashi, Y.; Ozawa, T.; Jitsukawa, K.; Masuda, H. *J. Organomet. Chem.* **2007**, *692*, 343.

Physical and Electrochemical Characterization of a Cu-based Electrocatalyst Inside and Outside a Lipid Membrane

Edmund C. M. Tse,[1,†] Christopher J. Barile,[1,†] Nicholas A. Kirchschlager,[1] Heng-Liang Wu,[1] and Andrew A. Gewirth[1,2,*]

[1] Department of Chemistry, University of Illinois at Urbana−Champaign, 600 South Mathews Avenue, Urbana, Illinois 61801, United States

[2] International Institute for Carbon Neutral Energy Research (WPI-I2CNER), Kyushu University, Fukuoka 812-8581, Japan

[†] E. C. M. T. and C. J. B. contributed equally to this work.

[*] Corresponding author. E-mail: agewirth@illinois.edu

Abstract

In this manuscript, we analyze the electrochemical behavior of a self-assembled monolayer (SAM) of a Cu-based O_2 reduction catalyst. We construct a hybrid bilayer membrane (HBM) by appending a lipid monolayer on top of the SAM and control proton flux to the catalyst by incorporating an alkyl phosphate proton carrier in the lipid layer of the HBM. The HBM platform is interrogated using electrochemical impedance spectroscopy (EIS), atomic force microscopy (AFM), and X-ray photoelectron spectroscopy (XPS). Cyclic voltammetry (CV) experiments performed as a function of solution pH indicate that the Cu(I)/Cu(II) couple of the catalyst without lipid involves the transfer of one proton per electron. With lipid, however, the number of protons transferred per electron for the Cu(I)/Cu(II) decreases and varies with pH depending upon the structural integrity of the lipid layer. Upon adding the proton carrier to the lipid, both the number of protons transferred during the Cu(I)/Cu(II) redox event and the

integrity of the lipid layer increase. Furthermore, we report the pH dependence of the O_2 reduction reaction (ORR) as mediated by the Cu catalyst inside the HBM with proton carrier. Taken together, these results provide mechanistic insight into an electrochemical platform that is broadly useful in studying proton-coupled electron transfer (PCET) reactions.

1. Introduction

In a broad sense, proton-coupled electron transfer (PCET) refers to reactions that involve the addition or removal of both protons and electrons.[1-6] PECT reactions are ubiquitous in chemistry and biology and include N_2 fixation, CO_2 reduction, and H_2O oxidation.[7-11] One of the most studied PCET reactions is the O_2 reduction reaction (ORR),[12,13] which enables fuel cell catalysts and respiring enzymes such as cytochrome c oxidase.[14-17] Since the ORR to form H_2O involves the transfer of four electrons and four protons, there are many possible pathways by which this reaction can occur, making the ORR difficult to study.[18,19] Many different methods have been utilized to study ORR catalysts.[20-24] For example, by using a variety of spectroscopic techniques, multiple metal-O_2 binding motifs have been characterized.[25-28] Additionally, different derivatives in a class of catalysts have been synthesized in an effort to elucidate structure-activity relationships.[29-31] For example, the addition of pendant proton relays to ORR catalysts has been used to study the role of proton transfer in catalyst activity.[11,18,31-33] However, these modifications frequently perturb other aspects of the catalyst including the redox potential of the metal ions and the steric environment surrounding the O_2 binding site.[30,31,34,35]

We recently pioneered the use of a hybrid bilayer membrane (HBM) to study the effect of proton transfer kinetics on ORR catalysts without altering their molecular structure.[36,37] A HBM consists of a lipid monolayer appended on top of a self-assembled monolayer (SAM).[38,39] We previously utilized a SAM of a dinuclear Cu complex (CuBTT: Cu complex of 6-((3-(benzylamino)-1,2,4-triazol-5-yl)amino)hexane-1-thiol) and a monolayer of 1,2-dimyristoyl-*sn*-glycero-3-phosphocholine (DMPC) lipid to form a HBM containing an ORR catalyst.[36] While CuBTT exposed to bulk aqueous solution is an active ORR catalyst, appending a lipid layer on top of CuBTT significantly inhibits the ORR activity.[36] This inhibition results from the inability of hydrophilic protons to diffuse across the hydrophobic interior of the lipid membrane.[36,40]

We discovered that the activity of the CuBTT catalyst inside a HBM is revived by the presence of a proton carrier in the lipid layer.[36] Furthermore, we designed proton carriers that switch on and off the ORR activity of CuBTT by either light or a pH change.[36,41] The ability of these carriers to deliver protons across the lipid membrane of the HBM dictates the ORR activity of the underlying catalyst. Although the ORR switching behavior of these proton carriers has been demonstrated, the Cu(I)/Cu(II) couple of CuBTT that facilitates the ORR has not been studied in detail in this HBM framework. In this manuscript, we analyze the electrochemical behavior of BTT-modified electrodes inside and outside of lipid membranes under various pH regimes to gain mechanistic insight into this platform (Figure 1). We also further characterize the structure and composition of the HBM system using atomic force microscopy (AFM), electrochemical impedance spectroscopy (EIS), and X-ray photoelectron spectroscopy (XPS).

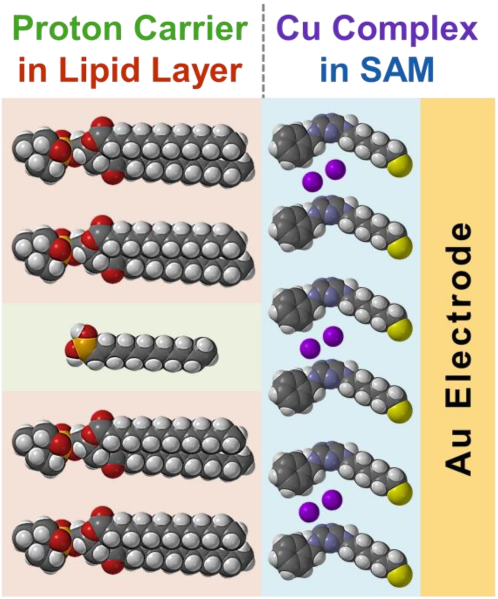

Figure 1. Schematic of the HBM electrochemical platform utilized in this study.

2. Experimental Section

Chemicals were obtained from commercial sources and used without further purification unless otherwise specified. For experiments from pH 3 to 11, potassium phosphate buffer solutions (100 mM) were prepared using Milli-Q water (> 18 MΩ cm) and adjusted to the desired pH using H_3PO_4 and KOH. For experiments at pH 1 and 13, $HClO_4$ (100 mM) and NaOH (100 mM) solutions were used, respectively. Solutions were sparged with Ar and O_2 for 30 min prior to each experiment.

Electrochemical studies were carried out using a CH Instruments 760 D Electrochemical Workstation (Austin, TX). For studies in aqueous solutions a three-electrode cell was used with a carbon counter electrode. Electrochemical potentials are measured and reported with respect to a “no-leak” Ag/AgCl (3 M KCl) reference electrode (eDAQ). Au working electrodes were deposited using an electron-beam vacuum deposition apparatus. A Ti adhesion layer (20 nm), followed by a Au layer (100 nm), was deposited on Pyrex glass slides. The electrodes were rinsed with water and EtOH prior to use.

All experiments were conducted at room temperature (26 ± 1) °C. For voltammetry collected under Ar and O_2, the scan rate was 100 and 10 mV/s, respectively. The thickness of the electrochemical platform was measured by electrochemical impedance spectroscopy (EIS) using a SP-150 potentiostat (Bio-Logic). EIS spectra were fitted to a Randles circuit commonly used for Au electrodes modified by thin organic layers shown in Figure 1,[42,43] and then the capacitance was calculated from the fit using the built-in EC-Lab® software V10.37 (Bio-Logic). For blocking experiments using $K_3Fe(CN)_6$, the scan rate was 50 mV/s.

Caution! Perchlorate salts are potentially explosive. Only small amounts of materials should be prepared.

Preparation of the HBM system was reported elsewhere.[36] In short, 6-((3-(benzylamino)-1,2,4-triazol-5-yl)amino)hexane-1-thiol (BTT) was synthesized and deposited as a SAM on a Au working electrode. Cu or Zn ions were incorporated into the BTT-modified Au surface using an ethanolic solution of $Cu(ClO_4)_2$ or $Zn(ClO_4)_2$, which was then embedded inside a monolayer of 1,2-dimyristoyl-*sn*-glycero-3-phosphocholine (DMPC) with and without 1 equivalent of mono-*N*-dodecylphosphate (MDP).[37,38]

The surface composition of the lipid-modified Au surfaces was analyzed by XPS using an AXIS Ultra spectrometer (Kratos Analytical) with a monochromatic Al Kα (1486.6eV) X-ray source. The surface morphology was characterized by contact-mode AFM using a Series 5500 multipurpose AFM/SPM probe and controller (Agilent Technologies). Au(111) evaporated onto freshly-cleaved mica substrate was utilized for AFM measurements (N9807A and N9805A, Keysight Technologies). Prior to use, the Au(111) substrates were annealed slightly using a H_2

flame (99.9999%, research grade, S. J. Smith Welding Supply). The SiN cantilever (DNP-S10, Bruker) with a spring constant of 0.35 N/m was used to acquire AFM images and force curves. While maintaining contact with the sample, the AFM tip with minimum force was applied on the surface during data collection to avoid any surface damage. All AFM images were recorded at 256 × 256 pixel resolution at a scan rate of 1 Hz. These images were flattened using PicoView 1.14 (Agilent Technologies). The cantilever deflection versus piezo-position curves were converted to force-distance curves. The cantilever deflection sensitivity was obtained according to published procedures by pressing the AFM tip against a glass substrate.[44] The AFM and force-distance curve measurements were carried out in pH 7 phosphate buffer solutions.

3. Results and Discussion

3.1. Characterization of the HBM Construct

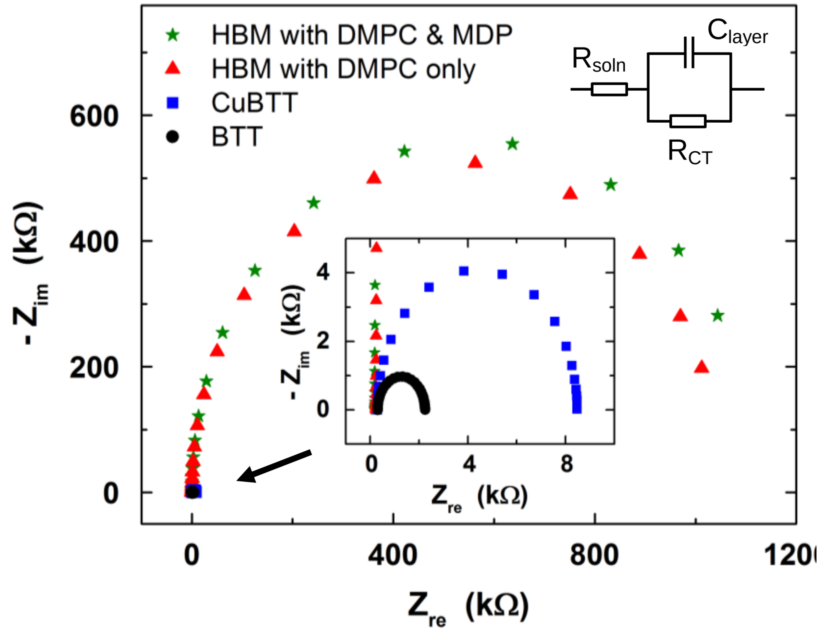

Figure 2. Nyquist plots of BTT on Au (inset, black circles), CuBTT on Au (inset, blue squares), HBM containing DMPC only (red triangles), and HBM containing DMPC with MDP added

(green stars) with the Randles circuit used provided to the top-right of Figure 1. R_{soln} = solution resistance, R_{CT} = charge transfer resistance, C_{layer} = capacitance of the layer of interest.

We first characterize the thickness of our electrochemical platform using EIS.[45-48] Figure 2 displays the Nyquist plots of the electrochemical systems utilized in this study. Using the Randles circuit presented in Figure 2, we obtained the capacitance of each of the system studied using published modeling protocols (Table 1).[42,43] The capacitance observed for a SAM of BTT is comparable to the values obtained using C9 or C10 alkanethiolate-modified Au electrode.[43,49] Table 1 also lists the thicknesses of the SAMs and HBMs calculated from the capacitance (C) using Eq. 1:

$$C = \frac{\varepsilon\,\varepsilon_0}{d} \qquad \text{Eq. 1}$$

where ε is the dielectric constant of the layer of interest, ε_0 is the dielectric constant of vacuum, and d is the thickness.

System	Capacitance (μF)	Thickness (nm)
A SAM of BTT on Au	1.6 ± 0.2	1.2 ± 0.2
A SAM of CuBTT on Au	0.9 ± 0.1	2.0 ± 0.3
A HBM containing DMPC only	0.6 ± 0.1	3.9 ± 0.4
A HBM containing DMPC and MDP	0.5 ± 0.1	4.1 ± 0.8

Table 1. The thicknesses of the systems examined in this study. The layer thickness is calculated using Eq. 1 from the capacitance measured by EIS. The dielectric constant (ε) of the SAM is taken to be equal to that of alkanethiol SAMs (2.1),[50,51] while the ε of lipid membranes is about 2.7 (ranges from 2.1 to 3.2).[52-57] Since the literature values of the lengths of BTT and DMPC are comparable,[36] we estimated the average ε for a HBM containing a lipid monolayer appended onto a SAM to be 2.4.

The thicknesses found for a SAM of BTT, a SAM of CuBTT, a HBM containing DMPC, and a HBM containing DMPC with MDP incorporated are similar to those found previously using ellipsometry (Figure 3).[36] We further verify these experimentally-measured thicknesses by computing the lengths of BTT and DMPC using Spartan'08 v.1.2.0 (Wavefunction Inc.). The calculated length of BTT is ca. 0.8 nm longer than the measured thickness, indicating that for the BTT-modified electrodes in aqueous environment, the benzyl arms of ca. 0.7 nm likely fold up to expose the hydrophilic N and maximize π-π stacking interactions. Upon the addition of Cu ions, the observed thickness (2.0 nm) of the CuBTT-modified system matches the length estimated computationally (2.0 nm). This result suggests that the benzyl arm unfolds to allow Cu coordination to the triazole rings to generate the dinuclear Cu electrocatalyst, which is the active site for O_2 reduction.[36,58] Upon appending a DMPC layer on top of CuBTT, the thickness almost doubles that of the CuBTT-only system. The increased thickness is 0.3 nm shorter than the literature reported length of DMPC with the discrepancy likely implying that either the lipid layer is formed at an angle or a small portion of the lipid tails overlaps with the benzyl arms of the CuBTT layer.[38] This finding indicates that the HBM consists of a SAM of CuBTT and a monolayer of DMPC appended on top. Upon incorporating MDP into the lipid monolayer, the thickness of the HBM remains relatively the same within error, signifying that MDP does not promote the formation of DMPC multilayers.

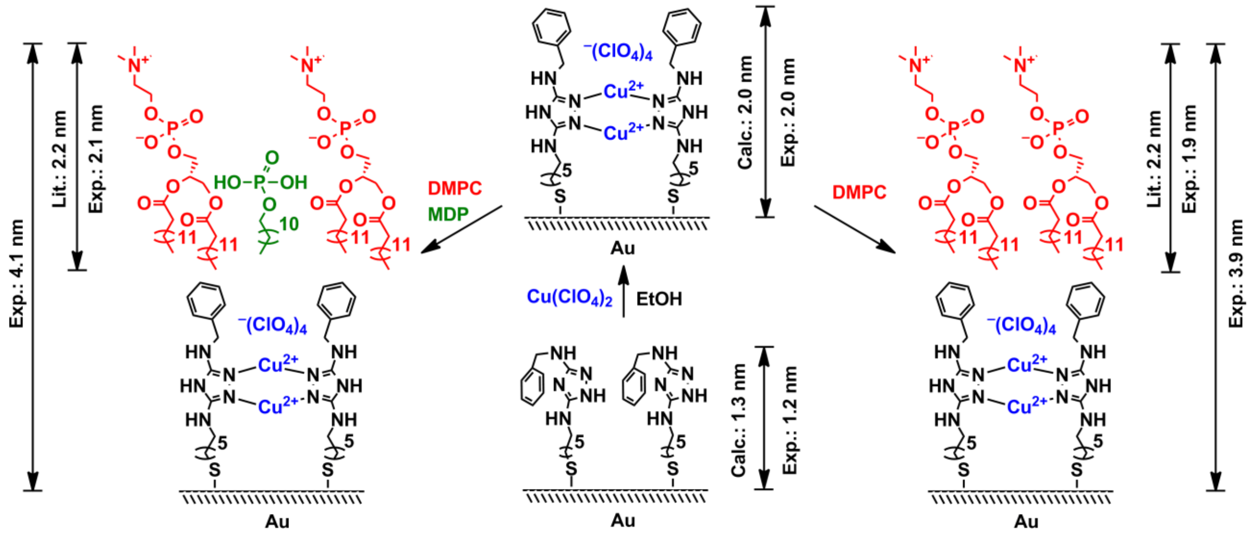

Figure 3. Calculated and measured thicknesses obtained from EIS of a SAM of BTT, a SAM of CuBTT, a HBM containing DMPC, and a HBM containing DMPC with MDP incorporated.

The surface morphology and surface roughness of a bare Au surface, a SAM of BTT, and a SAM of CuBTT have been previously determined using scanning tunneling microscopy (STM).[36] However, the lipid layer of a HBM system is electrically insulating, preventing the use of STM to probe the surface topology of a HBM containing a lipid monolayer. On the other hand, AFM is a well-established technique to interrogate supported lipid bilayers and HBMs.[59-65]

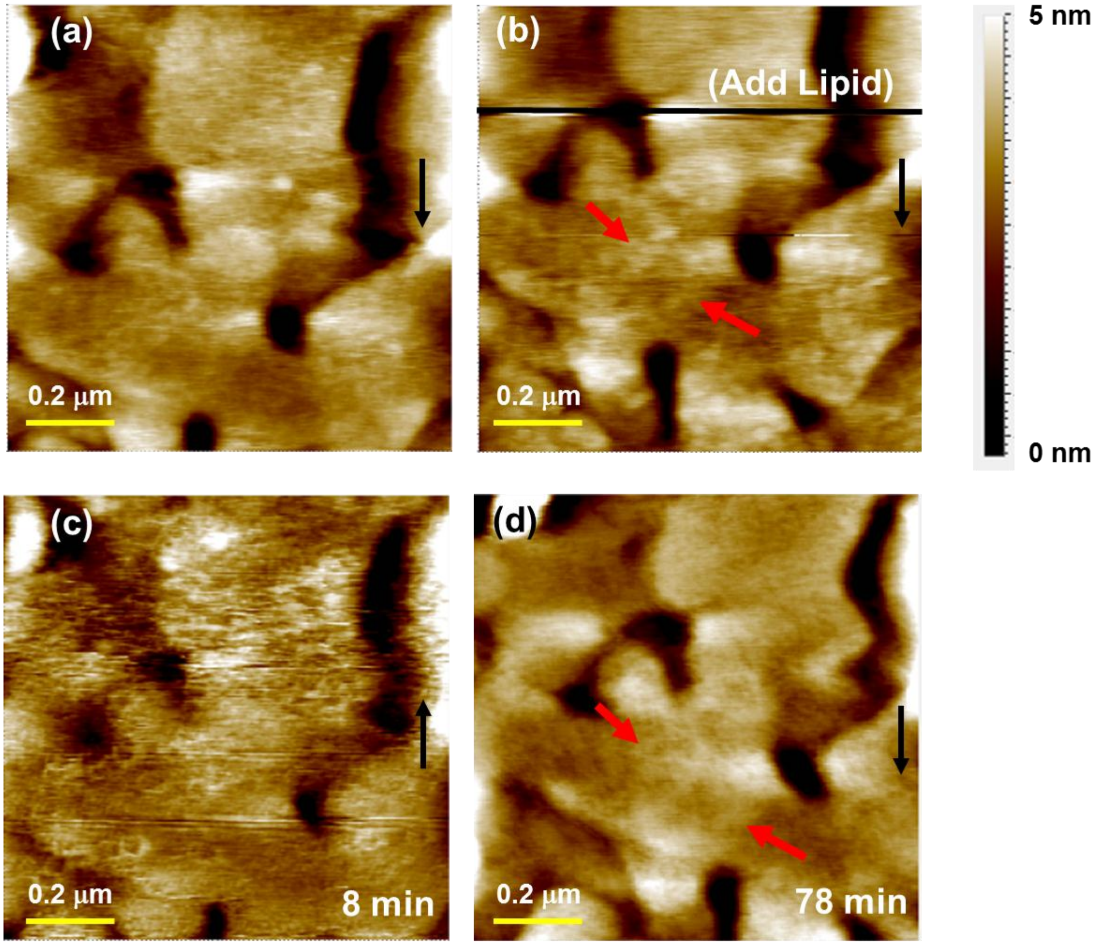

Figure 4. A set of sequential AFM images of the CuBTT SAM on Au acquired (a) before and (b)–(d) after the injection of DMPC vesicles at 3, 8, and 78 min. The black arrows indicate the scan direction, and the red arrows denote the spots of interest. The black line in (b) denotes the moment when the DMPC vesicles were injected. The scanned area of the AFM images was 1 µm × 1 µm.

Figure 4 displays a series of AFM images in chronological sequence recorded in pH 7 buffer solution with the black arrow showing the scan direction. Figure 4a shows the surface condition of the CuBTT SAM prior to lipid addition. The thick black line in Figure 4b indicates the time point at which a solution containing lipid vesicles is introduced to the AFM stage. Small patches grow on the surface in three minutes, as marked with red arrows, suggesting that the vesicle fusion process occurs on the surface rapidly. During the vesicle fusion process to generate a monolayer of lipid on top of the CuBTT SAM, the AFM image becomes blurry

(Figure 4c and lower part of Figure 4b). The blurred image is suggestive of a dynamic process that causes the AFM tip to be unstable. After the AFM tip stabilizes, we observed the formation of a lipid layer on top of the CuBTT SAM, which results in an AFM image that is less grainy (red arrows in Figure 4d) than those obtained from the CuBTT SAM without lipid (red arrows in Figure 4b). This smoothing of the AFM image is possibly caused by the fluid nature of the DMPC lipid layer at this temperature. A careful examination of the smooth surface of the HBM reveals that the DMPC monolayer in a HBM is different from the corrugated structure of the top layer in a supported DMPC bilayer on Au(111). The corrugated structure with periodicity and amplitude exists when the deformation of bilayer occurs, a process that introduces an elastic stress in a planar bilayer. This so-called "ripple-phase" structure usually occurs when the bottom leaflet interacts weakly with the underlying substrate.[66,67] In the HBM system, the strong Au-S linkage between CuBTT SAM and Au likely affects the spontaneous curvature of the DMPC monolayer appended on top. The smooth HBM surface persists for another hour, suggesting that the HBM is stable during AFM investigation.

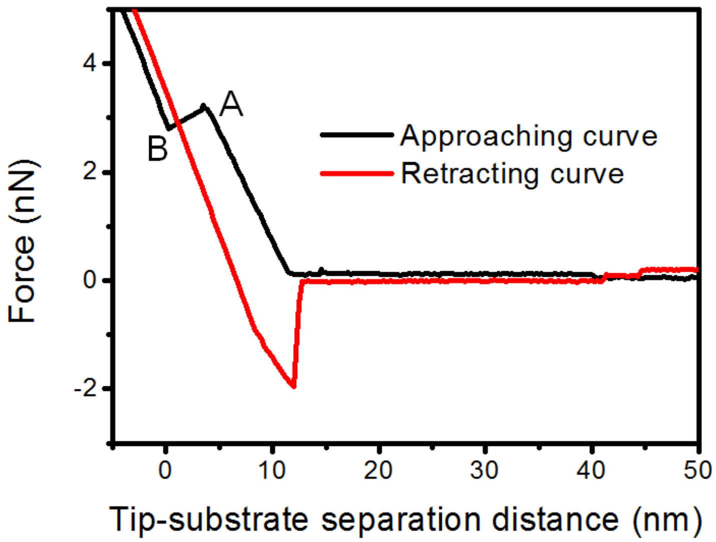

Figure 5. The approaching (black) and retracting (red) force-distance curve of the HBM containing the CuBTT SAM covered with a DMPC monolayer recorded immediately after the scan displayed in Figure 4d. Point A denotes the moment when the AFM tip breaks through the DMPC monolayer, and point B indicates the moment when the AFM tip makes contact with the underlying Au substrate.

Figure 5 shows the force curve obtained from the HBM-covered Au(111) surface shown in Figure 4d. A typical force-distance curve includes an approaching curve (black) and a retracting curve (red). We measured the thickness of the HBM system using the approaching trace of the force curve; the utility of this method to measure lipid bilayer thickness has been demonstrated previously.[44,67] The approaching curve displays a repulsive interaction between the tip and the HBM-covered surface at a tip-sample separation distance of about ca. 10 nm. The repulsive interaction increases further until the separation distance is ca. 3.5 nm when a discontinuity occurs in the force curve. This abrupt change in the force curve takes place when the tip punctures the HBM, indicating the breakthrough force of the HBM (point A in Figure 5). The repulsive interaction starts to increase at point B, suggesting the direct interaction between the AFM tip and the underlying Au substrate. Thus the tip-sample separation distance between points A and B in the force curve corresponds to the thickness of the HBM. The force-distance curve results indicate that the HBM thickness is (3.3 ± 0.5) nm, a value that matches our previously reported thickness using the EIS data presented (*vide supra*) and ellipsometry.[36] We further calculated the lateral lipid compressive force constant to be ~320 nN/m using the slope of the force-distance curve, a value consistent with published data on supported lipid bilayers.[68]

3.2. pH Dependence of SAMs Containing BTT

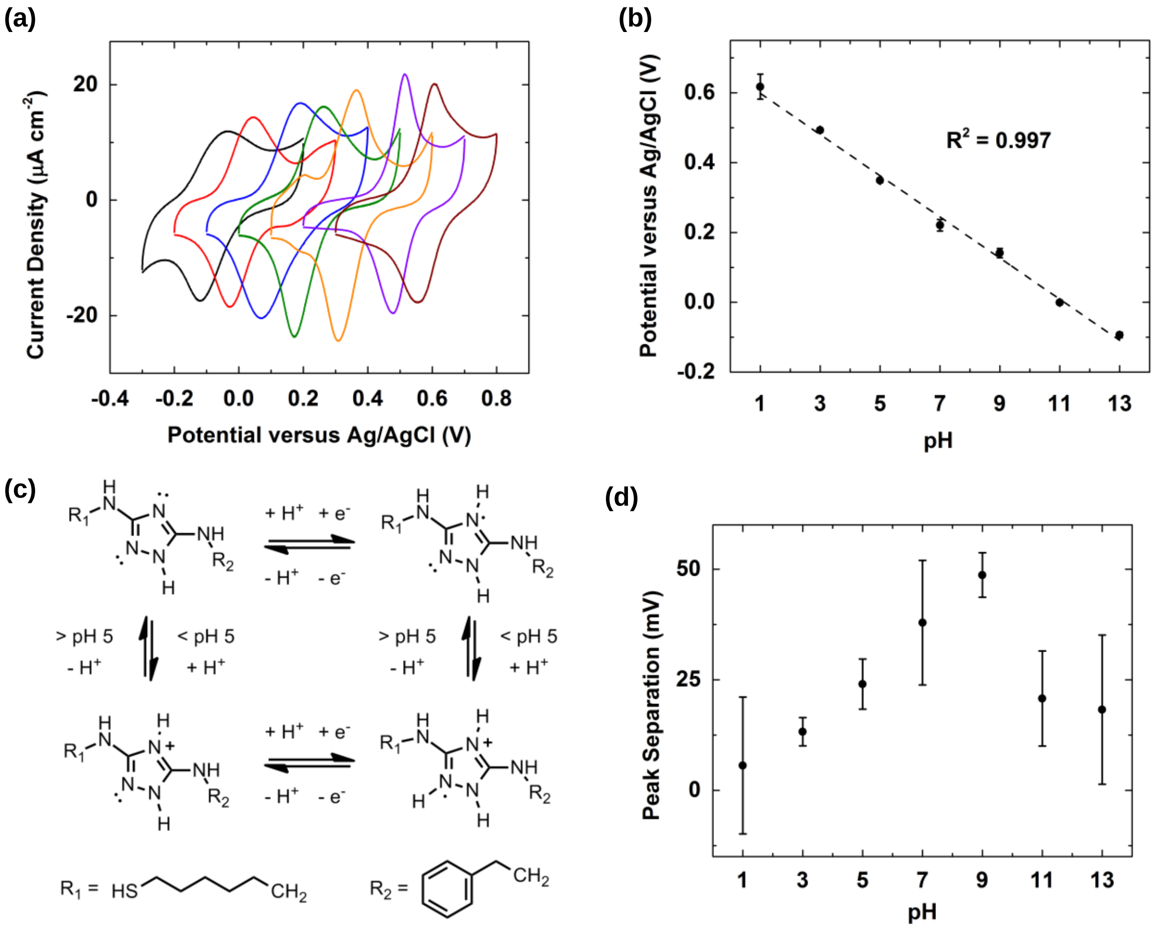

Figure 5. (a) Cyclic voltammograms (CVs) of SAMs of BTT on Au at pH 1 (brown), 3 (purple), 5 (orange), 7 (green), 9 (blue), 11 (red), and 13 (black) at a scan rate of 100 mV s^{-1}. (b) pH dependence of $E_{½}$ of the redox couple of a SAM of BTT on Au obtained from cyclic voltammograms at a scan rate of 100 mV/s. (c) Schematic of the BTT species involved in the redox process. (d) Peak separation of SAMs of BTT on Au as a function of solution pH.

After characterizing the structural attributes of the SAM and HBM systems, we investigated the pH-dependence of the voltammetry of a SAM of BTT. Figure 5a displays the cyclic voltammograms (CVs) of a SAM of BTT on Au in solutions ranging from pH 1 to 13. At all pH values, the ratio between the anodic and cathodic peak currents is approximately unity, indicating that BTT exhibits a reversible redox wave in acidic, neutral, and basic conditions. Figure 5b shows the pH dependence of the midpoint potentials ($E_{1/2}$) of a SAM of BTT on Au.

The midpoint potentials decrease by (59 ± 2) mV per pH unit, indicating that according to the Nernst equation, the redox event involves the transfer of H^+ and e^- in a 1:1 ratio from pH 1 to 13. Previous studies have demonstrated that triazoles undergo a reversible 1 e^- couple, and we previously showed that 3,5-diamino-1,2,4-triazole, a compound structurally related to BTT, also possesses a reversible redox couple.[36] Here, we add to this picture by demonstrating that 1 H^+ is also transferred in this process. Figure 5c shows a plausible schematic of the BTT species involved in this process based upon the pK_a of DAT.[69,70] We further note that in Figure 5a, the shape of the CVs changes as a function of pH. Figure 5d plots the peak separation values of BTT, which range from 0 to 50 mV, as a function of pH. The peaks separate more as the solution changes from pH 1 to pH 11, and separate less as the solution changes from pH 11 to pH 13. This inverted-V shaped behavior has been observed before by Finklea et al. using a SAM-bound galvinol system, which like BTT, undergoes a reversible 1 e^-:1 H^+ PCET process.[71]

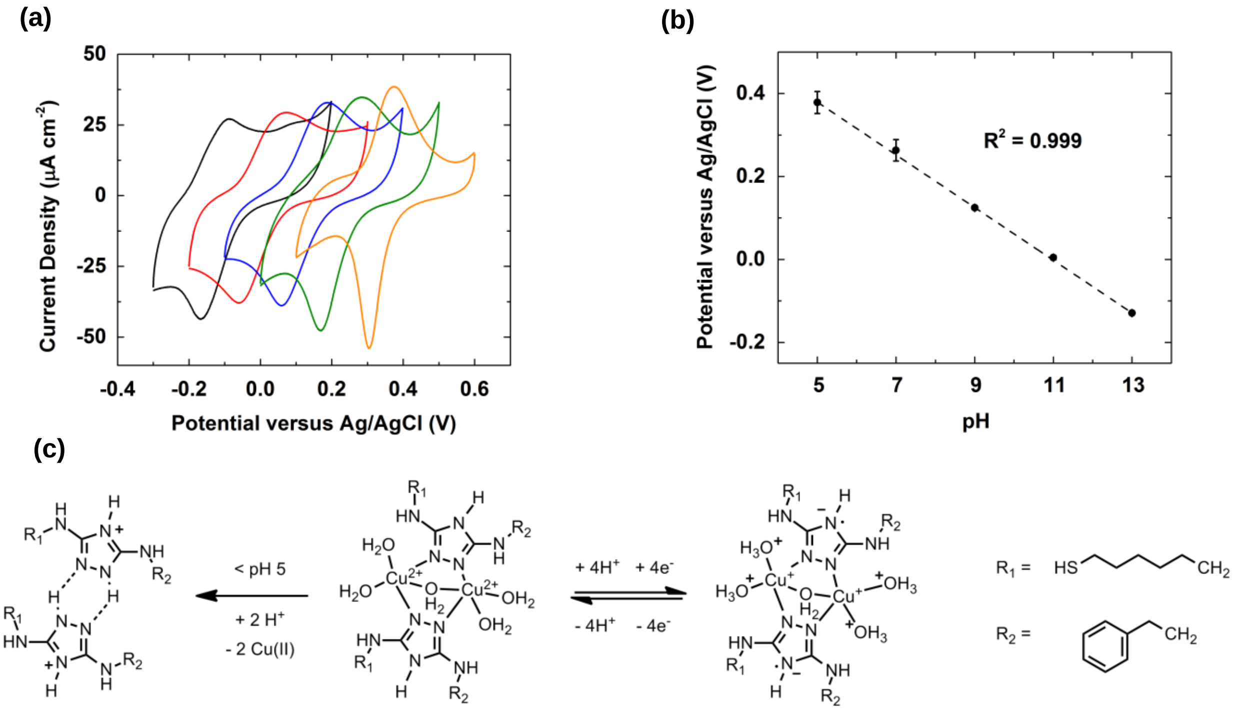

Figure 6. (a) CVs of SAMs of CuBTT on Au at pH 5 (orange), 7 (green), 9 (blue), 11 (red), and 13 (black) at a scan rate of 100 mV s^{-1}. (b) pH dependence of $E_{½}$ of the redox couple of a SAM of CuBTT on Au obtained from cyclic voltammograms at a scan rate of 100 mV/s. (c) Schematic of proton and electron transfer events of CuBTT.[72,73]

We next address the redox behavior of the BTT SAM after Cu incorporation to form the Cu(II) complex of BTT, CuBTT. Figure 6a displays CVs of CuBTT SAMs in solutions ranging from pH 5 to pH 13. Since the pK_a of the triazole ring in BTT is about 4.5, we find that Cu no longer binds to BTT below pH 5. Figure 6b displays the $E_{½}$ values of the redox couple of a SAM of CuBTT as a function of pH. The $E_{½}$ values decrease by (64 ± 0.5) mV per pH unit, a value close to the Nernstian prediction for a redox reaction involving H^+ and e^- in a 1:1 ratio. Upon addition of Cu, the integrated charge of the redox couple doubles,[36] signifying that the 1e$^-$ Cu(I)/Cu(II) redox couple coincides with the 1 e$^-$ redox couple of BTT. Here, we further understand the CuBTT system by establishing that equal number of protons and electrons are transferred in this process. Figure 6c describes the protonation and redox events for the CuBTT system we hypothesize occur using the information we gained from Figures 6a and b.

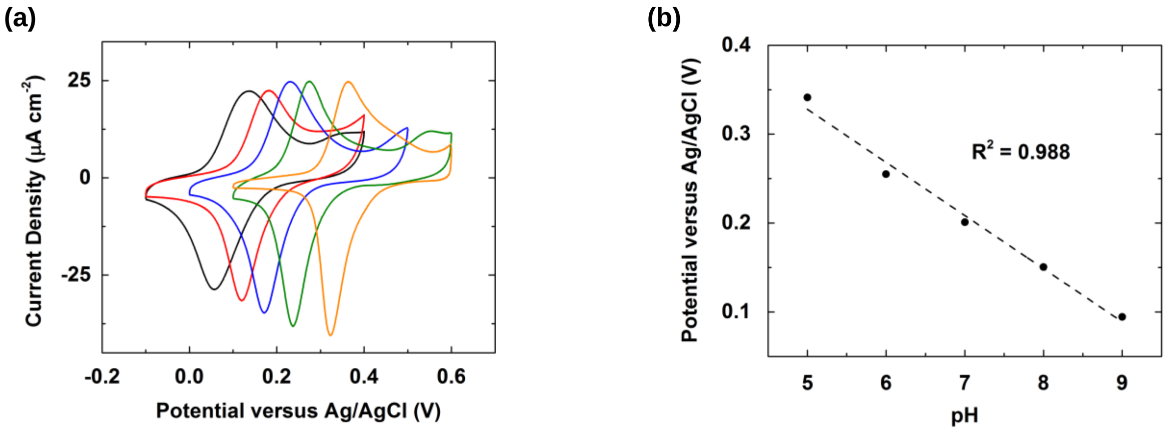

Figure 7. (a) CVs of SAMs of ZnBTT on Au at pH 5 (orange), 6 (green), 7 (blue), 8 (red), and 9 (black) at a scan rate of 100 mV s^{-1}. (b) pH dependence of the $E_{½}$ of the redox couple of a SAM of ZnBTT on Au obtained from cyclic voltammograms at a scan rate of 100 mV/s.

To verify that the BTT redox wave is not silenced upon complexation with a metal, we introduced Zn, a redox-inactive metal in the potential window used, to a BTT SAM. Figure 7a displays CVs of ZnBTT in solutions under varying pH regime. Figure 7b shows how the $E_{½}$ of the redox couple of a SAM of ZnBTT varies with pH. The $E_{½}$ decreases by (60 ± 4) mV per pH unit, which is expected for a process involving H^+ and e^- in a ratio of 1:1. Since Zn is redox-silent, the redox wave observed for ZnBTT must be due to the reduction of the triazole ring in BTT. In other words, metal binding to BTT does not suppress the BTT wave and does not affect the pH dependence of the BTT couple.

3.3. pH Dependence of HBMs Containing BTT SAMs

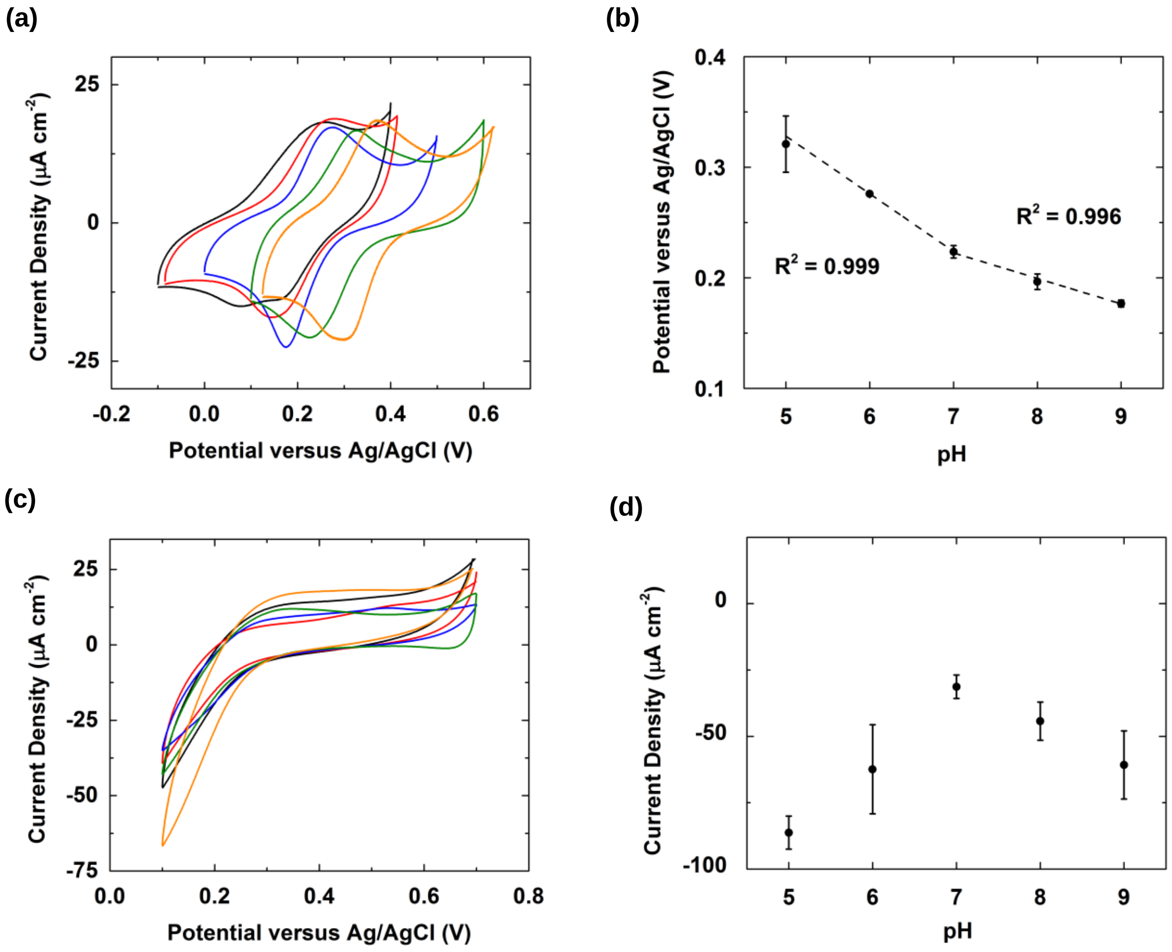

Figure 8. (a) CVs of SAMs of CuBTT covered by a monolayer of DMPC on Au at pH 5 (orange), 6 (green), 7 (blue), 8 (red), and 9 (black). (b) pH dependence of $E_{½}$ of a SAM of CuBTT covered by a monolayer of DMPC on Au obtained from cyclic voltammograms at a scan rate of 100 mV/s. (c) CVs of SAMs of CuBTT covered by a monolayer of DMPC on Au after running CVs at pH 5 (orange), 6 (green), 7 (blue), 8 (red), and 9 (black) in a solution of $K_3Fe(CN)_6$ (1 mM) and KCl (100 mM). (d) pH dependence of the maximum cathodic current densities of a SAM of CuBTT covered by a monolayer of DMPC on Au in a solution of $K_3Fe(CN)_6$ (1 mM) and KCl (100 mM).

To examine the effect of proton flux on PCET reactions, we utilized a HBM platform. This HBM platform consists of a BTT-modified electrode with a monolayer of DMPC appended on top through van der Waal's interactions between the hydrophobic lipid tails and the lipophilic benzyl arm on BTT. We first studied the case without proton carriers in the lipid layer to understand how a lipid layer affects the behavior of a HBM-buried redox couple. Figure 8a displays the CuBTT redox wave inside a HBM from pH 5 to pH 9, the range in which DMPC is stable.[74,75] Previously, we determined that the BTT wave is silent when covered by a lipid monolayer inside a HBM.[39] The redox wave of CuBTT inside a HBM observed in Figure 8a is therefore due solely to the Cu(I)/Cu(II) couple. Figure 8b shows the $E_{½}$ of a SAM of CuBTT covered by a monolayer of DMPC in solutions of varying pH values. $E_{½}$ decreases by (52 ± 2) mV per pH unit from pH 5 to 7, while $E_{½}$ decreases by (23 ± 2) mV per pH unit from pH 7 to 9. Interestingly, this result suggests that the ratio of protons to electrons transferred switches from 1:1 at pH 5 to 7 to 1:2 at pH 7 to 9 according to the Nernst equation.

In an effort to determine the origin of this change in the number of protons transferred to CuBTT inside a lipid, we interrogated the integrity of the DMPC lipid layer by using blocking experiments in which a redox probe is added to bulk solution.[36,39] Figure 8c displays CVs obtained for CuBTT covered by a monolayer of DMPC with $K_3Fe(CN)_6$ in the bulk solution. In the absence of a lipid layer, the reversible Fe(II)/Fe(III) redox couple is observed. However, upon appending a monolayer of DMPC, electron transfer from the electrode to $K_3Fe(CN)_6$ is impeded by the insulating nature of the lipid. Figure 8d demonstrates that from pH 5 to 9, the current density for the blocking experiment is the least at pH 7. This result indicates that the lipid layer is most well-formed at pH 7, which is expected since at this pH stable zwitterionic ionic lipid species predominant. If the lipid layer had completely blocked access of protons in the bulk solution to CuBTT from pH 5 to 9, then $E_{½}$ of CuBTT would not depend upon pH. However, upon increasing the pH from 7 to 9, the amount of current density obtained in the blocking experiment increases. This finding indicates that as the lipid layer becomes more anionic at higher pH values, it becomes more permeable to the redox probe and also protons in bulk solution. As a result, $E_{½}$ of CuBTT shifts negative with increasing pH, although to less of an extent as observed in the case of CuBTT without lipid. Upon decreasing the pH from 7 to 5, the amount of current density obtained in the blocking experiment increases more rapidly than from pH 7 to 9. This result indicates that the lipid layer becomes even more permeable to the redox probe and protons in bulk solution at pH 5. Correspondingly, $E_{½}$ of CuBTT is more sensitive to pH changes in the pH 5 to 7 range. In summary, the two different slopes observed in pH ranges 5-7 and 7-9 of the $E_{½}$ of CuBTT in Figure 8c correlate to the two slopes measured in the blocking experiments in Figure 8d.

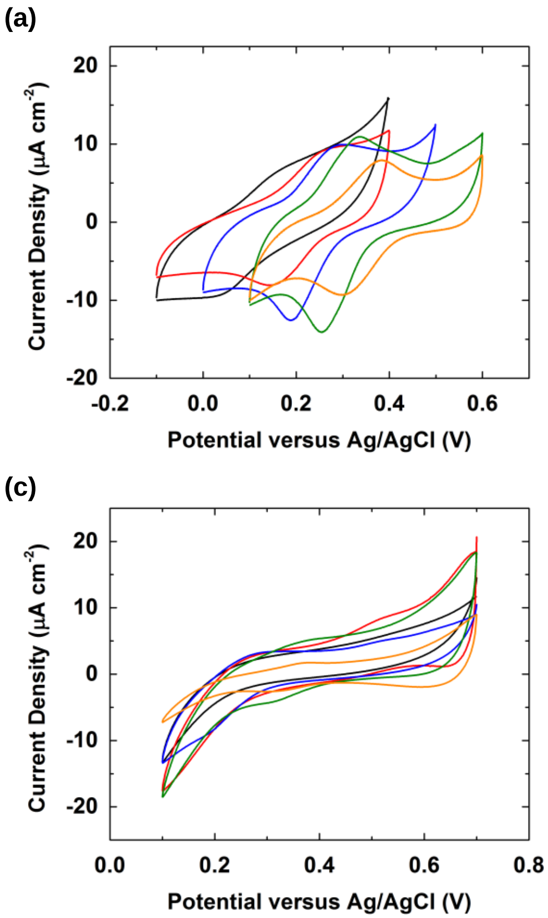

Figure 9. (a) CVs of SAMs of CuBTT covered by a monolayer of DMPC with 1 equivalent of MDP added to the lipid layer on Au at pH 5 (orange), 6 (green), 7 (blue), 8 (red), and 9 (black) at a scan rate of 100 mV s^{-1}. (b) pH dependence of $E_{½}$ of a SAM of CuBTT covered by a monolayer of DMPC with 1 equivalent of MDP added to the DMPC layer on Au obtained from cyclic voltammograms at a scan rate of 100 mV/s. (c) CVs of SAMs of CuBTT covered by a monolayer of DMPC with 1 equivalent of MDP added to the lipid layer on Au after running CVs at pH 5 (orange), 6 (green), 7 (blue), 8 (red), and 9 (black) in a solution of $K_3Fe(CN)_6$ (1 mM) and KCl (100 mM). (d) pH dependence of the maximum cathodic current densities of a SAM of CuBTT covered by a monolayer of DMPC with 1 equivalent of MDP added to the DMPC layer on Au in a solution of $K_3Fe(CN)_6$ (1 mM) and KCl (100 mM).

To probe the effect of assisted proton transport on PCET reactions in a HBM, we incorporated mono-*N*-dodecylphosphate (MDP), a proton carrier utilized previously by our group,[36] into the lipid layer of the HBM. Figure 9a displays the CuBTT redox wave inside a HBM system with MDP incorporated in the DMPC layer from pH 5 to pH 9. The redox wave presented is sensitive to the pH of the bulk solution. Figure 9b displays the $E_{½}$ of a SAM of CuBTT covered by a monolayer of DMPC with 1 equivalent of MDP added to the DMPC layer from pH 5 to 9. The $E_{½}$ of CuBTT decreases by (46 ± 4) mV per pH unit across the entire pH range. In contrast to the DMPC only case, we observe only one slope in Figure 9c for the case with MDP added to the lipid layer.

To understand the empirical difference between systems with and without MDP (Figure 9b vs. 8b), we conducted blocking experiments to the HBM with MDP added analogous to the case of lipid only. Figure 9c displays the CVs obtained for CuBTT covered by a MDP-DMPC layer with $K_3Fe(CN)_6$ in the bulk solution. Similar to the case of DMPC only, the absence of a reversible Fe(II)/Fe(III) redox couple signifies the formation of a complete lipid monolayer with MDP incorporated. Figure 9d shows the maximum amounts of current density obtained from the blocking experiments with CuBTT in a HBM containing MDP. Across the pH range studied, the magnitudes of the blocking current density at 0.1 V vs. Ag/AgCl remain relatively constant at about -25 μA cm^{-2}. These current densities are comparable to the value obtained for CuBTT in a HBM without MDP at pH 7, indicating that the lipid effectively blocks access of the $K_3Fe(CN)_6$ redox probe in bulk solution to CuBTT from pH 5 to 9 when MDP is incorporated in the HBM. These results suggest that the presence of MDP increases the stability of the DMPC at pH 5, 6, 8, and 9, possibly in a manner analogous to cholesterol incorporation in other HBM systems.[38] However, since the $E_{½}$ of the CuBTT redox process shifts with pH (Figure 9c), CuBTT must still have access to protons from the bulk solution. This finding suggests that MDP delivers protons across the lipid membrane to CuBTT during cycling of the Cu(I)/Cu(II) redox couple.

3.4. pH dependence of O_2 Reduction by CuBTT inside a HBM

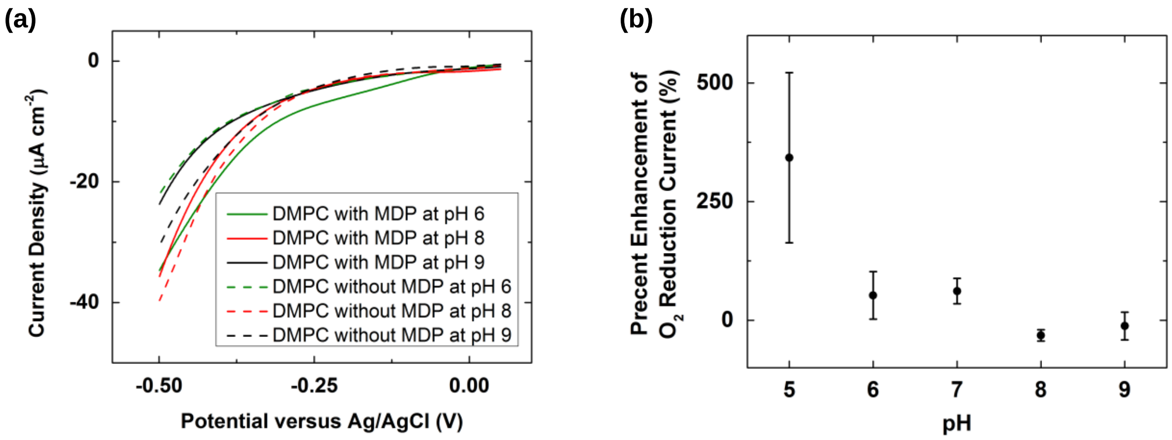

Figure 10. (a) Linear sweep voltammograms (LSVs) of SAMs of CuBTT covered by a monolayer of DMPC (dashed lines) with 1 equivalent of MDP added to the lipid layer (solid lines) on Au in O_2-saturated pH 6 (green), 8 (red), and 9 (black) buffer solutions. (b) Percent enhancement of O_2 reduction current by a SAM of CuBTT covered by a DMPC layer with 1 equivalent of MDP added to the lipid layer as compared to the lipid only case as a function of pH.

Having established that MDP delivers protons to CuBTT as it cycles between Cu(II) and Cu(I), we next studied the ability of CuBTT to catalyze the O_2 reduction reaction inside a HBM containing MDP as a function of pH. In prior work, we determined that a HBM containing MDP results in 130 μA of current at -0.5 V vs. Ag/AgCl,[36] about 300% more current than a HBM without MDP at pH 5. In contrast, at pH values greater than 5, the O_2 reduction current does not exceed 40 μA at similar overpotentials (Figure 10a), which means that at these pH values, there is very little to no enhancement of O_2 reduction current over the HBM case without proton carrier. Figure 10b shows the percent enhancement of O_2 reduction current by CuBTT-containing HBM with MDP added to the lipid layer compared to the lipid only case without MDP at various pH values. The ability of MDP to deliver protons changes based upon its protonation state. At pH 5, MDP exists primarily as $RHPO_4^-$ which can be protonated to RH_2PO_4. The neutral species RH_2PO_4 is hydrophobic enough to penetrate the hydrophobic lipid interior and deliver protons to CuBTT via flip-flop diffusion.[36] In contrast, from pH 6 to 9, the acid-base equilibrium of MDP shifts towards RPO_4^{2-}, which when protonated yields $RHPO_4^-$, a species too hydrophilic to undergo flip-flop diffusion across the lipid layer. The $RH_2PO_4/RHPO_4^-$ $/RPO_4^{2-}$ equilibrium of MDP thus explains the pH dependence of the enhancement of O_2 reduction current density by CuBTT in HBM.

Unlike the trend observed for O_2 reduction, the Cu(I)/Cu(II) couple of CuBTT in a HBM with MDP is not affected by the pH-controlled speciation of MDP (Figure 9a). This difference reflects the fact that during O_2 reduction, each MDP carrier delivers a catalytic amount of protons to CuBTT, whereas during the Cu(I)/Cu(II) redox event, MDP transports only a stoichiometric quantity of protons. In other words, MDP still delivers enough protons to facilitate the PCET Cu(I)/Cu(II) couple despite the fact that its acid-base equilibrium implies that it is predominantly speciated as RPO_4^{2-} at high pH.

3.5. XPS of HBMs before and after ORR

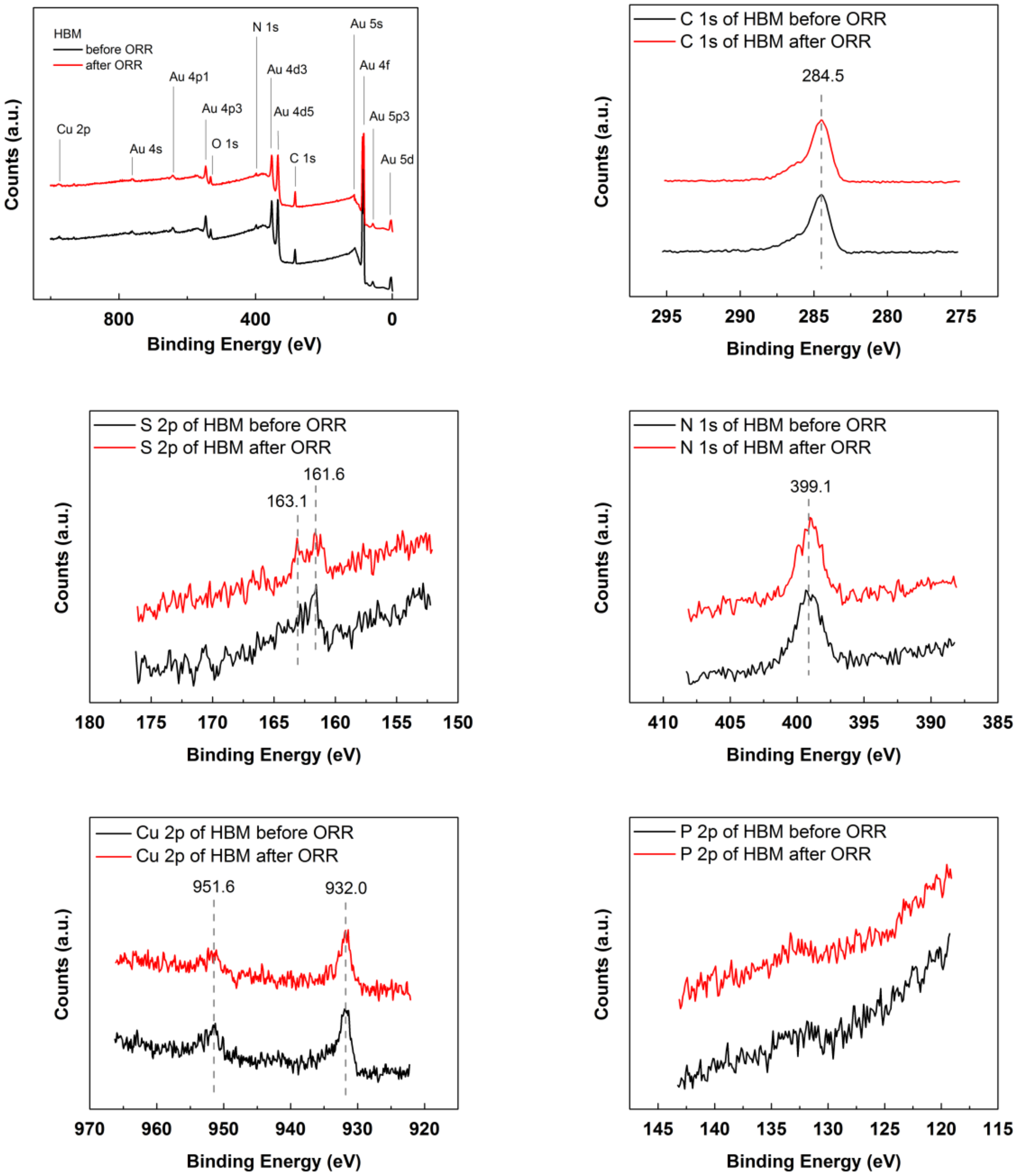

Figure 11. XPS (a) survey scan and high-resolution scans of (b) C 1s, (c) S 2p, (d) N 1s, (e) Cu 2p, and (f) P 2p obtained from HBMs before (black) and after (red) O_2 reduction.

To confirm that the integrity of the electrochemical platform is not compromised during O_2 reduction, we carried out post-mortem XPS measurements after ORR catalysis. Figure 11 compares the XPS spectra of HBMs before and after conducting electrocatalysis. The typical penetration depth using XPS is larger than 5 nm,[76] which is longer than the full thickness of a HBM, thus explaining the presence of Au peaks in the survey scan. All of the peaks observed in the high-resolution scans do not change or shift after O_2 reduction, suggesting that the surface species do not undergo chemical modifications during ORR. In particular, we do not observe any trace of Cu(0) signal, indicating that the formation of Cu metal or nanoparticles from Cu(II) ions does not occur in our HBM platform at these potentials.

4. Conclusions

In this report, we investigated the physical and electrochemical properties of a HBM electrochemical platform that is broadly useful to examine the role of proton transfer kinetics in PCET reactions. In particular, we probed the surface structure of the lipid monolayer of the HBM using AFM and characterized the pH-dependent redox behavior of the underlying Cu(I)/Cu(II) couple of the CuBTT SAM covered by the lipid layer. In addition to surface examination, we determined the number of electrons transferred for each of the redox waves observed in a BTT SAM, a CuBTT SAM, a HBM containing lipid only, and a HBM containing a lipid monolayer with an alkyl phosphate proton carrier incorporated. The pH dependence of the redox wave correlates to the amount of current passed in the blocking experiment, suggesting the redox event is related to the state of the lipid layer. XPS data of the HBM collected before and after catalysis corroborates that Cu(II) is responsible for the ORR activity and is not degraded by the ORR process.

5. References

(1) Soudackov, A.; Hammes-Schiffer, S. *J. Chem. Phys.* **2000**, *113*, 2385-2396.

(2) Horvath, S.; Fernandez, L. E.; Soudackov, A. V.; Hammes-Schiffer, S. *Proc. Natl. Acad. Sci. USA* **2012**, *109*, 15663-15668.

(3) Hammes-Schiffer, S. *Acc. Chem. Res.* **2009**, *42*, 1881-1889.

(4) Costentin, C.; Robert, M.; Savéant, J.-M. *Chem. Rev.* **2010**, *110*, PR1-PR40.

(5) Mayer, J. M.; Rhile, I. J. *BBA-Bioenergetics* **2004**, *1655*, 51-58.

(6) Mayer, J. M. *Annu. Rev. Phys. Chem.* **2004**, *55*, 363-390.

(7) Weinberg, D. R.; Gagliardi, C. J.; Hull, J. F.; Murphy, C. F.; Kent, C. A.; Westlake, B. C.; Paul, A.; Ess, D. H.; McCafferty, D. G.; Meyer, T. J. *Chem. Rev.* **2012**, *112*, 4016-4093.

(8) Fecenko, C. J.; Meyer, T. J.; Thorp, H. H. *J. Am. Chem. Soc.* **2006**, *128*, 11020-11021.

(9) Chen, Z.; Vannucci, A. K.; Concepcion, J. J.; Jurss, J. W.; Meyer, T. J. *Proc. Natl. Acad. Sci. USA* **2011**, *108*, E1461-E1469.

(10) Hammes-Schiffer, S.; Soudackov, A. V. *J. Phys. Chem. B* **2008**, *112*, 14108-14123.

(11) Wenger, O. S. *Acc. Chem. Res.* **2013**, *46*, 1517-1526.

(12) Zhang, J.; Xie, Z.; Zhang, J.; Tang, Y.; Song, C.; Navessin, T.; Shi, Z.; Song, D.; Wang, H.; Wilkinson, D. P.; Liu, Z.-S.; Holdcroft, S. *J. Power Sources* **2006**, *160,* 872-891.

(13) Jaouen, F.; Proietti, E.; Lefevre, M.; Chenitz, R.; Dodelet, J.-P.; Wu, G.; Chung, H. T.; Johnston, C. M.; Zelenay, P. *Energy Environ. Sci.* **2011**, *4*, 114-130.

(14) Collman, J. P.; Ghosh, S.; Dey, A.; Decréau, R. A.; Yang, Y. *J. Am. Chem. Soc.* **2009**, *131*, 5034-5035.

(15) Collman, J. P.; Devaraj, N. K.; Decréau, R. A.; Yang, Y.; Yan, Y.-L.; Ebina, W.; Eberspacher, T. A.; Chidsey, C. E. D. *Science* **2007**, *315*, 1565-1568.

(16) Collman, J. P.; Decréau, R. A.; Lin, H.; Hosseini, A.; Yang, Y.; Dey, A.; Eberspacher, T. A. *Proc. Natl. Acad. Sci. USA* **2009**, *106*, 7320-7323.

(17) Boulatov, R.; Collman, J. P.; Shiryaeva, I. M.; Sunderland, C. J. *J. Am. Chem. Soc.* **2002**, *124*, 11923-11935.

(18) Rosenthal, J.; Nocera, D. G. *Acc. Chem. Res.* **2007**, *40*, 543-553.

(19) Gewirth, A. A.; Thorum, M. S. *Inorg. Chem.* **2010**, *49*, 3557-3566.

(20) Kim, J.; Gewirth, A. A. *J. Phys. Chem. B* **2006**, *110*, 2565-2571.

(21) Erickson, E. M.; Thorum, M. S.; Vasić, R.; Marinković, N. S.; Frenkel, A. I.; Gewirth, A. A.; Nuzzo, R. G. *J. Am. Chem. Soc.* **2012**, *134*, 197-200.

(22) Erickson, E. M.; Oruc, M. E.; Wetzel, D. J.; Cason, M. W.; Hoang, T. T. H.; Small, M. W.; Li, D.; Frenkel, A. I.; Gewirth, A. A.; Nuzzo, R. G. *Anal. Chem.* **2014**, *86*, 8368-8375.

(23) Muramoto, K.; Ohta, K.; Shinzawa-Itoh, K.; Kanda, K.; Taniguchi, M.; Nabekura, H.; Yamashita, E.; Tsukihara, T.; Yoshikawa, S. *Proc. Natl. Acad. Sci. USA* **2010**, *107*, 7740-7745.

(24) Kieber-Emmons, M. T.; Qayyum, M. F.; Li, Y.; Halime, Z.; Hodgson, K. O.; Hedman, B.; Karlin, K. D.; Solomon, E. I. *Angew. Chem. Int. Ed.* **2012**, *51*, 168-172.

(25) Blackman, A.; Tolman, W. In *Metal-Oxo and Metal-Peroxo Species in Catalytic Oxidations*; Meunier, B., Ed.; Springer Berlin Heidelberg: 2000; Vol. 97, p 179-211.

(26) Karlin, K. D.; Gultneh, Y. In *Progress in Inorganic Chemistry*; John Wiley & Sons, Inc.: 2007, p 219-327.

(27) Solomon, E. I.; Heppner, D. E.; Johnston, E. M.; Ginsbach, J. W.; Cirera, J.; Qayyum, M.; Kieber-Emmons, M. T.; Kjaergaard, C. H.; Hadt, R. G.; Tian, L. *Chem. Rev.* **2014**, *114*, 3659-3853.

(28) Solomon, E. I.; Chen, P.; Metz, M.; Lee, S.-K.; Palmer, A. E. *Angew. Chem. Int. Ed.* **2001**, *40*, 4570-4590.
(29) Tse, E. C. M.; Schilter, D.; Gray, D. L.; Rauchfuss, T. B.; Gewirth, A. A. *Inorg. Chem.* **2014**, *53*, 8505-8516.
(30) Thorseth, M. A.; Tornow, C. E.; Tse, E. C. M.; Gewirth, A. A. *Coord. Chem. Rev.* **2013**, *257*, 130-139.
(31) Thorseth, M. A.; Letko, C. S.; Tse, E. C. M.; Rauchfuss, T. B.; Gewirth, A. A. *Inorg. Chem.* **2012**, *52*, 628-634.
(32) Sjödin, M.; Styring, S.; Wolpher, H.; Xu, Y.; Sun, L.; Hammarström, L. *J. Am. Chem. Soc.* **2005**, *127*, 3855-3863.
(33) Chng, L. L.; Chang, C. J.; Nocera, D. G. *Org. Lett.* **2003**, *5*, 2421-2424.
(34) Hatcher, L.; Karlin, K. *J Biol Inorg Chem* **2004**, *9*, 669-683.
(35) McCrory, C. C. L.; Ottenwaelder, X.; Stack, T. D. P.; Chidsey, C. E. D. *J. Phys. Chem. A* **2007**, *111*, 12641-12650.
(36) Barile, C. J.; Tse, E. C. M.; Li, Y.; Sobyra, T. B.; Zimmerman, S. C.; Hosseini, A.; Gewirth, A. A. *Nat. Mater.* **2014**, *13*, 619-623.
(37) Hosseini, A.; Barile, C. J.; Devadoss, A.; Eberspacher, T. A.; Decreau, R. A.; Collman, J. P. *J. Am. Chem. Soc.* **2011**, *133*, 11100-11102.
(38) Hosseini, A.; Collman, J. P.; Devadoss, A.; Williams, G. Y.; Barile, C. J.; Eberspacher, T. A. *Langmuir* **2010**, *26*, 17674-17678.
(39) Tse, E. C. M.; Barile, C. J.; Gewargis, J. P.; Li, Y.; Zimmerman, S. C.; Gewirth, A. A. *Anal. Chem.* **2015**, *87*, 2403-2409.
(40) Jain, M. K. *Introduction to Biological Membranes*; 2nd ed.; Wiley: New York, 1988.
(41) Li, Y.; Tse, E. C. M.; Barile, C. J.; Gewirth, A. A.; Zimmerman, S. C. *J. Am. Chem. Soc.* **2015**, *137*, 14059-14062.
(42) Ding, S.-J.; Chang, B.-W.; Wu, C.-C.; Lai, M.-F.; Chang, H.-C. *Anal. Chim. Acta* **2005**, *554*, 43-51.
(43) Agonafer, D. D.; Chainani, E.; Oruc, M. E.; Lee, K. S.; Shannon, M. A. *J. Nanotechnol. Eng. Med.* **2013**, *3*, 0310061-0310068.
(44) Garcia-Manyes, S.; Sanz, F. *BBA-Biomembranes* **2010**, *1798*, 741-749.
(45) Bard, A. J.; Faulkner, L. R. *Electrochemical Methods: Fundamentals and Applications*; Wiley, 2000.
(46) Long, Y.-T.; Li, C.-Z.; Kraatz, H.-B.; Lee, J. S. *Biophys. J.* **2003**, *84*, 3218-3225.
(47) Colonna, B.; Echegoyen, L. *Chem. Comm.* **2001**, 1104-1105.
(48) Kim, K.; Kwak, J. *J. Electroanal. Chem.* **2001**, *512*, 83-91.
(49) Boubour, E.; Lennox, R. B. *J. Phys. Chem. B* **2000**, *104*, 9004-9010.
(50) Damos, F. S.; Luz, R. C. S.; Kubota, L. T. *Langmuir* **2005**, *21*, 602-609.
(51) Slowinski, K.; Chamberlain, R. V.; Bilewicz, R.; Majda, M. *J. Am. Chem. Soc.* **1996**, *118*, 4709-4710.
(52) Gramse, G.; Dols-Perez, A.; Edwards, M. A.; Fumagalli, L.; Gomila, G. *Biophys. J.* **2013**, *104*, 1257-1262.
(53) Nymeyer, H.; Zhou, H.-X. *Biophys. J.* **2008**, *94*, 1185-1193.
(54) Dilger, J.; McLaughlin, S.; McIntosh, T.; Simon, S. *Science* **1979**, *206*, 1196-1198.
(55) Ohki, S. *J. Theor. Biol.* **1968**, *19*, 97-115.
(56) Huang, W.; Levitt, D. G. *Biophys. J.* **1977**, *17*, 111-128.
(57) Flewelling, R. F.; Hubbell, W. L. *Biophys. J.* **1986**, *49*, 541-552.

(58) Thorum, M. S.; Yadav, J.; Gewirth, A. A. *Angew. Chem. Int. Ed.* **2009**, *121*, 171-173.
(59) Garcia-Manyes, S.; Oncins, G.; Sanz, F. *Biophys. J.* **2005**, *89*, 4261-4274.
(60) Giocondi, M.-C.; Yamamoto, D.; Lesniewska, E.; Milhiet, P.-E.; Ando, T.; Le Grimellec, C. *BBA-Biomembranes* **2010**, *1798*, 703-718.
(61) El Kirat, K.; Morandat, S.; Dufrêne, Y. F. *BBA-Biomembranes* **2010**, *1798*, 750-765.
(62) Mingeot-Leclercq, M.-P.; Deleu, M.; Brasseur, R.; Dufrene, Y. F. *Nat. Protocols* **2008**, *3*, 1654-1659.
(63) Meuse, C. W.; Krueger, S.; Majkrzak, C. F.; Dura, J. A.; Fu, J.; Connor, J. T.; Plant, A. L. *Biophys. J.* **1998**, *74*, 1388-1398.
(64) Plant, A. L. *Langmuir* **1999**, *15*, 5128-5135.
(65) Twardowski, M.; Nuzzo, R. G. *Langmuir* **2003**, *19*, 9781-9791.
(66) Kaasgaard, T.; Leidy, C.; Crowe, J. H.; Mouritsen, O. G.; Jørgensen, K. *Biophysical Journal* **2003**, *85*, 350-360.
(67) Li, M.; Chen, M.; Sheepwash, E.; Brosseau, C. L.; Li, H.; Pettinger, B.; Gruler, H.; Lipkowski, J. *Langmuir* **2008**, *24*, 10313-10323.
(68) Waheed, Q.; Edholm, O. *Biophys. J.* **2009**, *97*, 2754-2760.
(69) Efimenko, I. A.; Shishilov, O. N. *Russ. J. Inorg. Chem.* **2012**, *57*, 1695-1722.
(70) Chernyshev, V. M.; Gaidukova, G. V.; Zemlyakov, N. D.; Taranushich, V. A. *Russ. J. Appl. Chem.* **2005**, *78*, 776-780.
(71) Finklea, H. O.; Haddox, R. M. *Phys. Chem. Chem. Phys.* **2001**, *3*, 3431-3436.
(72) Hernández-Gil, J.; Ferrer, S.; Castiñeiras, A.; Liu-González, M.; Lloret, F.; Ribes, Á.; Čoga, L.; Bernecker, A.; Mareque-Rivas, J. C. *Inorg. Chem.* **2014**, *53*, 578-593.
(73) Pankratov, A. N.; Borodulin, V. B.; Chaplygina, O. A. *Russ. J. Coord. Chem.* **2005**, *31*, 660-666.
(74) Guha, M.; Gantz, D. L.; Gursky, O. *J. Lipid Res.* **2008**, *49*, 1752-1761.
(75) Benjwal, S.; Jayaraman, S.; Gursky, O. *Biochemistry* **2005**, *44*, 10218-10226.
(76) Leng, Y. *Materials Characterization: Introduction to Microscopic and Spectroscopic Methods*; Wiley, 2013.

6. Author Information

Corresponding Author

*Tel: 217-333-8329. Fax: 217-244-3186. E-mail: agewirth@illinois.edu.

7. Acknowledgments

E.C.M.T. acknowledges a Croucher Foundation Scholarship. C.J.B. acknowledges a National Science Foundation Graduate Research Fellowship (NSF DGE-1144245) and a Springborn Fellowship. We thank the US Department of Energy (DE-FG02-95ER46260) for support of this research. This work was carried out in part in the Frederick Seitz Materials Research Laboratory Central Facilities, which are partially supported by the US Department of Energy (DE-FG02-07ER46453 and DE-FG02-07ER46471).

8. Competing Financial Interests

The authors declare no competing financial interests.

Proton Kinetics Dictates the Reaction Mechanism of Quinones at Lipid-modified Electrodes

Christopher J. Barile,[1†] Edmund C. M. Tse,[1†] Ying Li,[1] Ali Hosseini,[2] Steven C. Zimmerman,[1] and Andrew A. Gewirth[1,3*]

[1] Department of Chemistry, University of Illinois at Urbana−Champaign, 600 South Mathews Avenue, Urbana, Illinois 61801, United States

[2] Manufacturing Systems Ltd., Auckland 0632, New Zealand

[3] International Institute for Carbon Neutral Energy Research (WPI-I2CNER), Kyushu University, Fukuoka 812-8581, Japan

[†] C. J. B. and E. C. M. T. contributed equally to this work.

[*] Corresponding author. E-mail: agewirth@illinois.edu

Abstract

Proton-coupled electron transfer (PCET) reactions are ubiquitous in biochemistry and alternative energy schemes. Natural enzymes utilize ubiquinones in proton transfer chains and energy conversion processes. Here, we utilize a bio-inspired organic-inorganic hybrid bilayer membrane system to control the reaction mechanism of a quinone molecule covalently bound to an electrode surface. In particular, by impeding proton access to the quinone moiety, we change the reaction pathway from a PCET process to a pure electron transfer step. We further alter the reaction pathway to a stepwise PCET process by controlling the proton flux through the use of an alkyl proton carrier incorporated in the lipid membrane. We demonstrate that modulating proton kinetics dictates reaction pathway. This work provides unique insight into PCET reactions and a novel electrochemical platform for interrogating them.

1. Introduction

Proton-coupled electron transfer (PCET) reactions are ubiquitous in natural and artificial energy conversion schemes.[1,2] In particular, PCET reactions mediated by quinones are of particular importance in biological studies and the pharmaceutical industry.[3,4] Quinones enable both the cellular respiration and photosynthesis processes.[5] Quinones also serve as the structural basis of many potent anti-tumor chemotherapeutic compounds and anti-Alzheimer lead drug candidates.[6,7] Apart from their application and utility in medicinal chemistry, quinone-based redox mediators facilitate the oxygen reduction reaction (ORR) in implantable biofuel cells.[8-10]

Unsurprisingly, these important quinone-mediated PCET reactions are studied by a multitude of computational and experimental methods.[11,12] Based on the pioneering work of Laviron, Finklea et al. later incorporated ideas from Marcus theory to examine the potential- and pH-dependent apparent transfer coefficient (α) of PCET reactions involving quinones.[13] The proton and electron transfer steps can occur in sequential steps or concerted steps,[11,14,15] rendering these quinone systems difficult to study experimentally. While conventional studies of water-soluble quinones in buffered solutions provide insights into the PCET mechanism, surface-immobilized quinone systems result in cleaner electrochemical responses that allow for more accurate determination of apparent rate constants.[16,17] The PCET processes of quinones are now commonly described by a nine-membered square scheme (Figure 1).

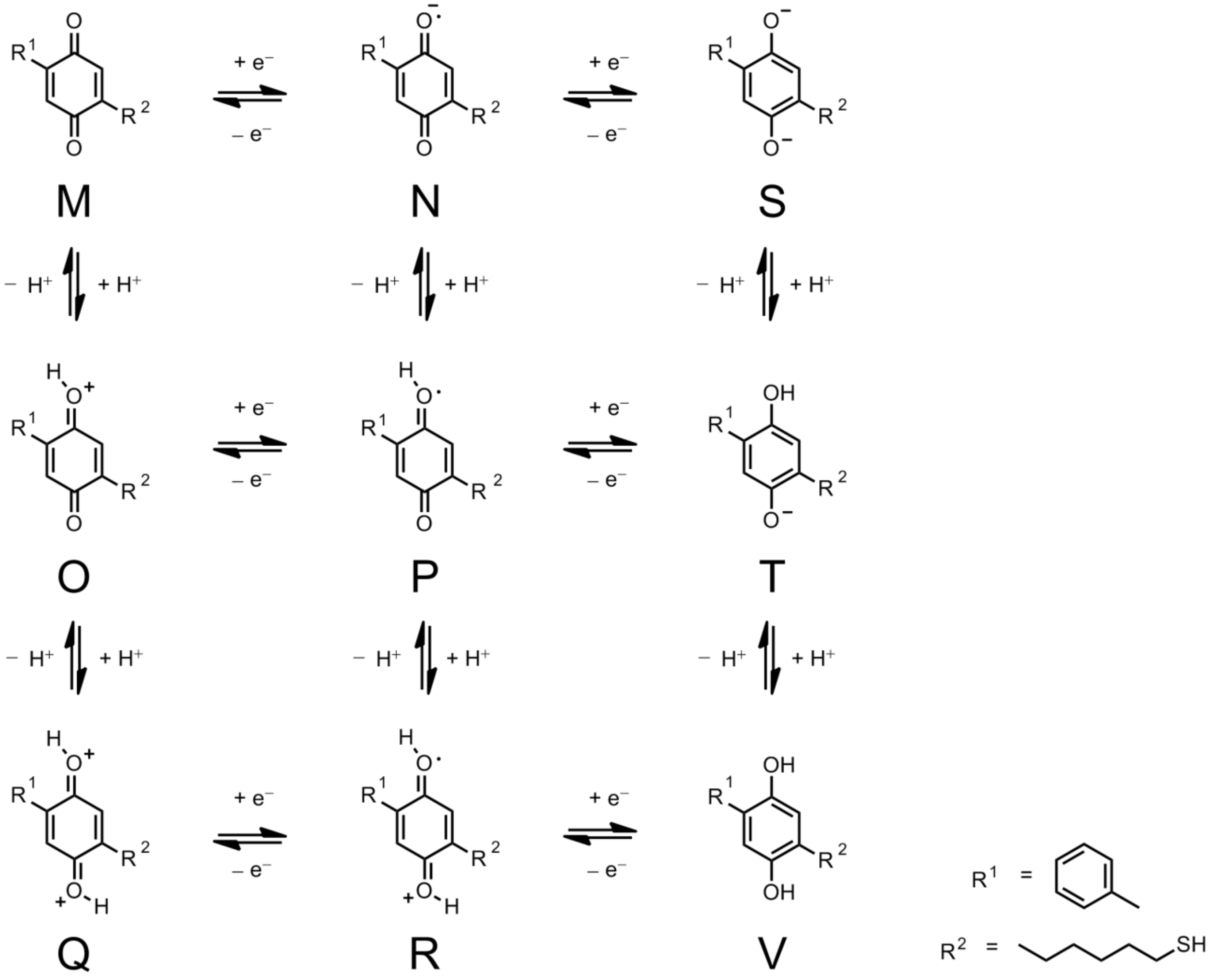

Figure 1. Nine-member square scheme for the quinone system. R_1 and R_2 functional groups are shown for 2-benzyl-5-(6-mercaptohexyl)hydroquinone (BHQ), one of the quinone molecules studied in this work.

The most common reaction pathway of simple quinones in aqueous solutions is the $2e^-$ $2H^+$ redox step that cycles between the fully-oxidized species “M” and the fully-reduced state “V,” as evidenced by a 59 mV/pH shift in the formal potential that follows Nernstian behavior. There are reports that suggest flanking amine functional groups induce a $2e^-$ $3H^+$ pathway at low pH.[18] While a tremendous amount of effort has been reported to measure and calculate the apparent rate constants and α and examine their dependencies on pH and potential, a significantly less amount of effort has been dedicated towards observing species other than “M” and “V” in the nine-membered square scheme.

There are two main impediments to accessing all nine species in the scheme. First, the relative energies of some of these species such as the dianion “S” and the doubly-protonated species “Q” are likely too high and thus are unstable and difficult to attain.[19] Second, the inability to independently control both electron transfer and proton transfer limits the chances to attain species when the ratio of electrons and protons transferred does not equal one. A self-assembled monolayer (SAM) on Au electrode is frequently used to tune the kinetics of electron transfer to a redox-reporter positioned at the SAM-solution interface.[20-28] However, proton thermodynamics and kinetics are much more difficult to modulate.[29-31]

A hybrid bilayer membrane (HBM) consists of a SAM covered by a lipid monolayer and can be used to delineate the effects of proton transfer from electron transfer.[32-34] Previously, we explored the pH-responsiveness of a lipid-bound proton carrier that reversibly turns on and off an embedded ORR catalyst.[35] We further utilized the HBM system to assess the lipid permeability of anions.[36] Here, we demonstrate that by tethering quinone moieties at the SAM-lipid interface with and without proton carrier added to the lipid monolayer, we access several species that are rarely observed for surface-confined quinone systems. We envision that the ability to modulate speciation across the nine-member square scheme will not only provide unique mechanistic insight into the intricate PCET pathway of quinones, but lay a foundation for new understanding of PCET reactions in both chemistry and biology.

2. Experimental

Chemicals were obtained from commercial sources and used without further purification unless otherwise specified. Britton-Robinson (BR) buffer solutions were prepared using H_3BO_3 (0.04 M, 99.999%, Sigma-Aldrich), CH_3COOH (0.04 M, 99.99%, Sigma-Aldrich), H_3PO_4 (0.04 M, 85 wt % in H_2O, 99.99%, Sigma-Aldrich), $NaClO_4$ (0.1 M, 99.9%, Sigma-Aldrich), and Milli-Q water (> 18 MΩ cm) and adjusted to desired pH using NaOH (10 M, analytical titration grade, Fisher Scientific). All experiments were conducted inside an Ar-filled glove box. Solutions were sparged with Ar overnight and stored in the glove box prior to each experiment.

Electrochemical studies were carried out using a CH Instruments 760 D Electrochemical Workstation (Austin, TX). For studies in aqueous solutions, a three-electrode cell was used with a Pt wire counter electrode. Electrochemical potentials were measured and are reported with respect to a 'no leak' Ag/AgCl (3 M KCl, eDAQ, Inc.) reference electrode. Au working electrodes were deposited using an electron-beam vacuum deposition apparatus. A Ti adhesion layer (20 nm), followed by a Au layer (100 nm), was deposited on Pyrex glass slides. The electrodes had a surface area of 0.219 cm^2 and were rinsed with water and EtOH prior to use.

The synthesis procedures for 2-benzyl-5-(6-mercaptohexyl)hydroquinone (BHQ) and 2-(benzyl(methyl)amino)-5-((6-mercaptohexyl)amino)hydroquinone (N_2-BHQ) are described in the Supplementary Information. A SAM of BHQ or N_2-BHQ was prepared by immersing a Au electrode in a solution of the desired quinone in EtOH (1 mM) for 2 h. The electrode was rinsed with EtOH and then with pH 7 BR buffer before further use. Preparation of the HBM system with and without MDP was reported elsewhere.[35]

Results and Discussion

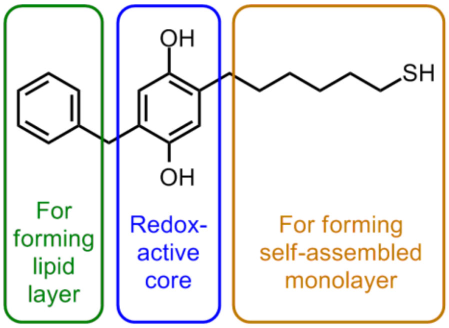

BHQ

Figure 2. Functional and structural features of BHQ.

Figure 2 displays the structure of 2-benzyl-5-(6-mercaptohexyl)hydroquinone (BHQ), one of the two quinone derivatives synthesized and utilized in this work. In addition to its redox-active core, the BHQ molecule features two important regions, both of which have a specific function. First, we equipped BHQ with a hexylthiol chain to allow for the formation of a well-packed SAM on Au electrodes. Electron transfer through this short-chained thiol is facile, thus ensuring that it is not the rate-determining step (RDS) in the quinone PCET reaction. Second, BHQ contains a terminal benzyl moiety. We previously determined that this group allows for a lipid monolayer to be appended to a SAM through van der Waals forces.[35]

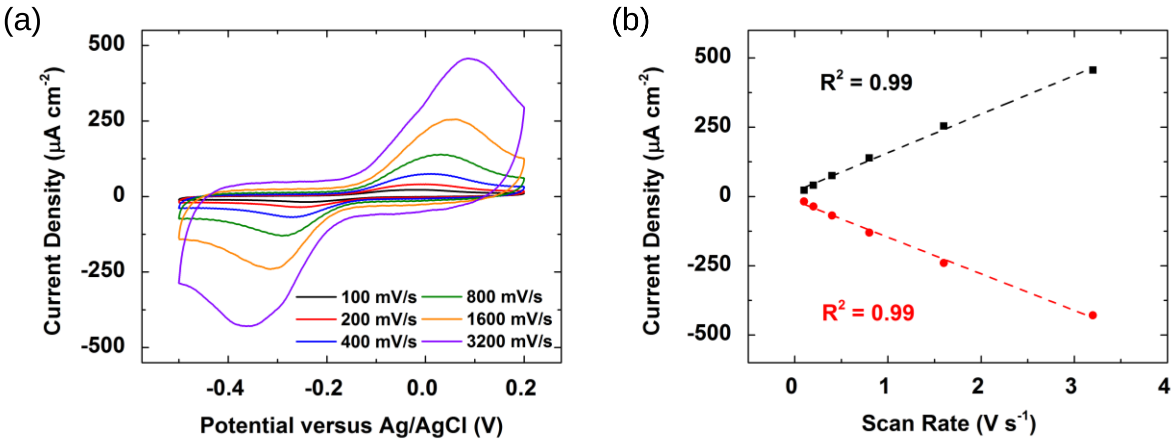

Figure 3. (a) CVs of a SAM of BHQ on Au in pH 7 Ar-saturated solution at scan rates of 100 (black), 200 (red), 400 (blue), 800 (green), 1600 (orange), and 3200 (purple) mV/s. (b) Randles-

Sevcik plot of the peak anodic (black) and cathodic (red) current densities of a SAM of BHQ versus scan rate.

Figure 3a shows representative cyclic voltammograms (CVs) of a SAM of BHQ at pH 7 at various scan rates. At all scan rates measured, the ratio between the anodic and cathodic peak currents is approximately unity, indicating that the redox system is reversible. Furthermore, both the peak anodic or cathodic currents increase linearly with increasing scan rate (Figure 3b), which is expected for a surface-confined redox species. Figures S1-3 show CVs of BHQ at various scan rates and the corresponding Randles-Sevcik plots in pH 3, 5, and 9 solutions. The results show that BHQ is bound to the surface at these pH values as well. However, in all cases, the peak-to-peak separation values (ΔE_p) of the voltammograms are large and non-zero, in contrast to what is observed for surface-confined redox species that demonstrate fast electron transfer such as simple ferrocene derivatives.[37] This finding indicates that the overall redox transformation of BHQ occurs relatively slowly likely due to the presence of multiple proton and electron transfer events. Indeed, we determined the apparent rate constants of the cathodic and anodic reactions to be (3.0 ± 1.0) s^{-1} and (3.9 ± 1.8) s^{-1}, respectively, using the Laviron equation.[38] Table S1 lists the apparent rate constants of the BHQ-containing systems used in this study. These values are similar to those obtained for SAMs of other quinones and metal complexes on carbon electrodes and are much less than those found for SAMs containing simple ferrocenes.[21,39]

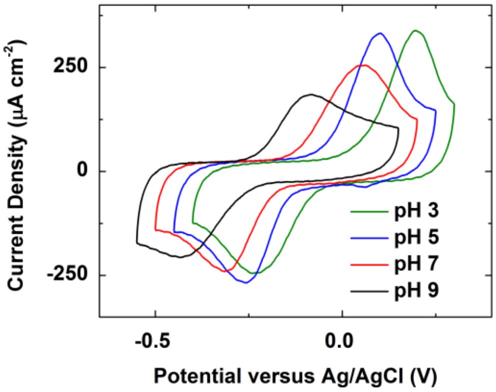

Figure 4. CVs of a SAM of BHQ on Au in pH 3 (green), 5 (blue), 7 (red), and 9 (black) Ar-saturated solutions at a scan rate of 1600 mV/s.

To probe the PCET process of the BHQ SAM, we obtained CVs of a SAM of BHQ from pH 3 to 9 (Figure 4). For the cathodic wave, the potential of the peak current (E_{pc}) shifts positive by an average of 32 mV per pH unit as the pH increases. This value is close to the 30 mV per pH unit predicted by the Nernst equation for a process involving the transfer of protons and electrons in a 1:2 ratio. Considering the nine-membered square scheme shown in Figure 1, we designate the cathodic process as converting the starting quinone, **M**, to a monodeprotonated hydroxyquinone species, **T**. In contrast to this finding, most quinone species are electrochemically reduced to their 2 H^+/2 e^- hydroquinone products. However, previous reports demonstrate that hydrophobic moieties on quinones can lead to reduction products in which fewer than two protons are transferred.[40] The data suggest that the phenyl groups of BHQ create a hydrophobic enough monolayer so that only one proton per BHQ is transferred upon reduction. For the anodic wave, the potential of the peak current (E_{pa}) shifts positive with increasing pH by 48 mV per pH unit. This number is in between the 59 mV/pH unit and 30 mV/pH unit values predicted by the Nernst equation for 2 H^+/2 e^- and 1 H^+/2 e^- processes, respectively.[41] We hypothesize that after reduction to **T** occurs, protons from bulk solution slowly diffuse into the hydrophobic interior of the SAM, resulting in the protonation of **T** to **Q**. Therefore, a mixture of **T** and **Q** is oxidized back to the starting quinone, **M**, explaining the intermediate value witnessed for the pH dependence of the anodic wave.

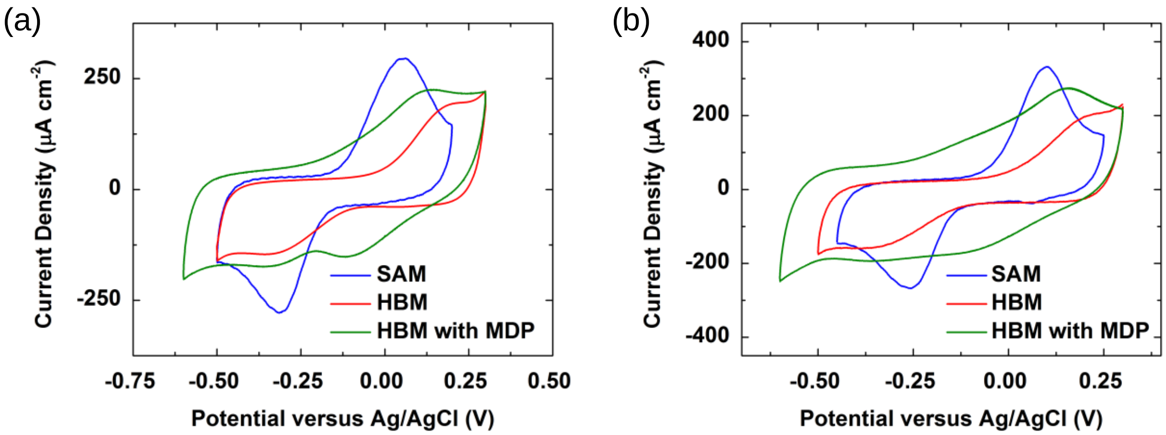

Figure 5. CVs of a SAM of BHQ (blue) covered by a monolayer of DMPC (red) with MDP added (green) in an Ar-saturated pH (a) 7 and (b) 5 solutions at a scan rate of 1600 mV/s.

Figure 5a shows CVs at pH 7 of a SAM of BHQ, a HBM containing BHQ and a DMPC lipid monolayer, and a HBM containing BHQ with the MDP proton carrier incorporated in the lipid layer. For the three cases, the voltammetric response of the quinone varies dramatically. Table S2 lists the integrated charges for the cathodic and anodic waves of each of the three voltammograms. For a SAM of BHQ, the cathodic and anodic waves have an average integrated charge of 33 and 31 μC cm^{-2}, respectively, and since it is known that quinone SAMs undergo 2 e^{-} reduction, this amounts to a BHQ surface coverage of about 180 pmole/cm^{2}. Our modeling of this surface coverage determines that the intermolecular diameter of the BHQ SAM is 10.8 Å, which compares well with other reported quinone systems.[42] Figures S4-7 display the CVs of BHQ covered by a DMPC monolayer with and without MDP at various scan rates and the corresponding Randles-Sevick plots. The results indicate that the quinone moiety is surface-bound in the presence of lipid with and without proton carrier. Figure S8 summarizes the quantitative analysis of the BHQ voltammetry in HBM systems.

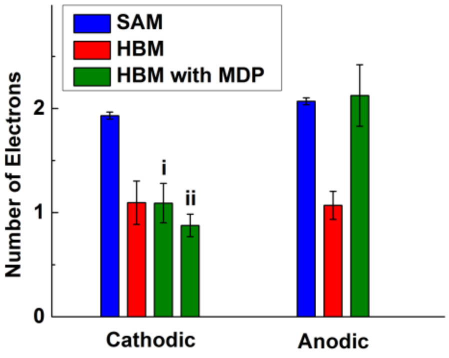

Figure 6. Bar graphs showing the number of electron transferred for the (a) cathodic and (b) anodic processes of BHQ in pH 7 Ar-saturated solution. Each graph has three sets of bars: open SAM (blue), HBM (red), and HBM with MDP (green). The cathodic process has two waves with the first wave (i) occurring at a more positive potential than the second (ii).

When the BHQ SAM is covered by a monolayer of lipid to form a HBM (Figure 5a, red line), the integrated charges for the cathodic and anodic processes decrease by approximately half (Figure 6, red bars). This result suggests that inside the lipid, the quinone undergoes a one electron reduction process. Figures S9 and S10 display the number of electrons transferred for the cathodic and anodic processes of a SAM of BHQ and BHQ-containing HBMs with and without MDP in various pH solutions. The red lines of Figures 5a and 5b display CVs of the HBM system with a SAM of BHQ covered by a monolayer of DMPC at pH 7 and 5, respectively. Unlike the open SAM case, the cathodic and anodic waves of the BHQ voltammetry increase an average of only 6 mV and 16 mV per pH unit, respectively (Figure 7, red bars), indicating that the redox activity of BHQ inside the lipid layer does not depend strongly on the concentration of protons in bulk solution. This finding is consistent with the observation that protons diffuse relatively slowly through lipid layers in biological systems.[43] Taken together, these results indicate that inside a HBM, BHQ (**M**) undergoes a 1 e^-/0 H^+ reduction process to give the free radical species, **N** (Figure 1). In other words, the mechanism of the BHQ redox event changes from a PCET reaction involving 2 e^-/1 H^+ to single electron transfer in the presence of a lipid layer. In a directly analogous manner, we previously determined that a SAM of an O_2 reduction catalyst switches its mechanism from primarily producing H_2O by a 4 H^+/4 e^- process to reducing O_2 by 1 e^- to O_2^- when it is covered by a lipid monolayer.(ref) Our findings demonstrate that in the proton-constrained environment created by the lipid layer, redox systems that proceed by PCET in bulk solution occur by single electron transfer. Multiple electron transfer, for example, to produce the dianionic species **S** in the case of BHQ, is too thermodynamically unfavorable to occur. The production of such a highly charged hydrophilic species is energetically too costly in the hydrophobic environment of the HBM.

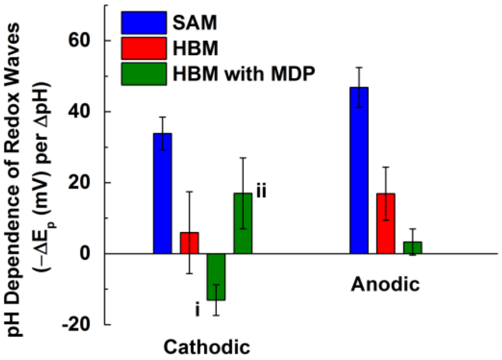

Figure 7. Bar graphs showing the average shifts in the cathodic and anodic peak positions of BHQ as the pH increases. Each graph has three sets of bars: open SAM (blue), HBM (red), HBM with MDP (green). The cathodic process has two waves with the first wave (i) occurring at a more positive potential than the second (ii).

Upon incorporation of the MDP proton carrier into the lipid layer of the HBM, the voltammetric response changes even further (Figures 5a and 5b, green lines). Strikingly, two cathodic peaks appear in the response, each with an amount of integrated charge corresponding to a 1 e^- process (Figure 6). One wave remains for the anodic process, but its integrated charge indicates a 2 e^- process. These findings demonstrate that in the presence of the HBM with the MDP proton carrier, BHQ is reduced stepwise to **P** and then to the final **Q** hydroquinone process. MDP only transfers one proton at a time and thus facilitates two individual 1 H^+/1 e^- PCET steps through flip-flop diffusion across the lipid membrane. Because flipping of the proton carrier is relatively slow,[44-47] it kinetically controls the cathodic response of the BHQ system in discrete steps and serves as the only source of protons to the quinone in the proton-restricted environment of the lipid. Figure S11 shows the CV of the HBM containing MDP with a potential window including the anodic and the first cathodic wave, but excluding the second cathodic wave. The redox wave integrates to about a 1 e^- process, further corroborating the formation of **P** in the presence of MDP. For O_2 reduction catalysts inside HBMs with lipid-bound proton carriers, we previously determined that O_2 reduction proceeds by a mixture of four- and two-electron reduction pathways depending on the proton transfer rate through the lipid layer.(ref) In a HBM absent a proton carrier, however, O_2 reduction occurs by single electron transfer to produce O_2^-. Similarly, the BHQ system switches from a single electron transfer mechanism inside a HBM to one involving 2 H^+/2 e^- PCET in the presence of a proton carrier in a HBM.

Figure 7 green bars, shows how the potential of the BHQ voltammetry inside a HBM with MDP changes as a function of increasing pH. Interestingly, the position of both the cathodic and anodic peak potentials do not shift significantly with pH, indicating that the thermodynamics of BHQ reduction does not depend strongly on the concentration of protons in bulk solution. Instead, MDP delivers protons to BHQ in a kinetically-controlled fashion via flip-flop diffusion across the lipid layer of the HBM. Therefore, the potential of the BHQ redox process is not very sensitive to the concentration of protons in bulk solution.

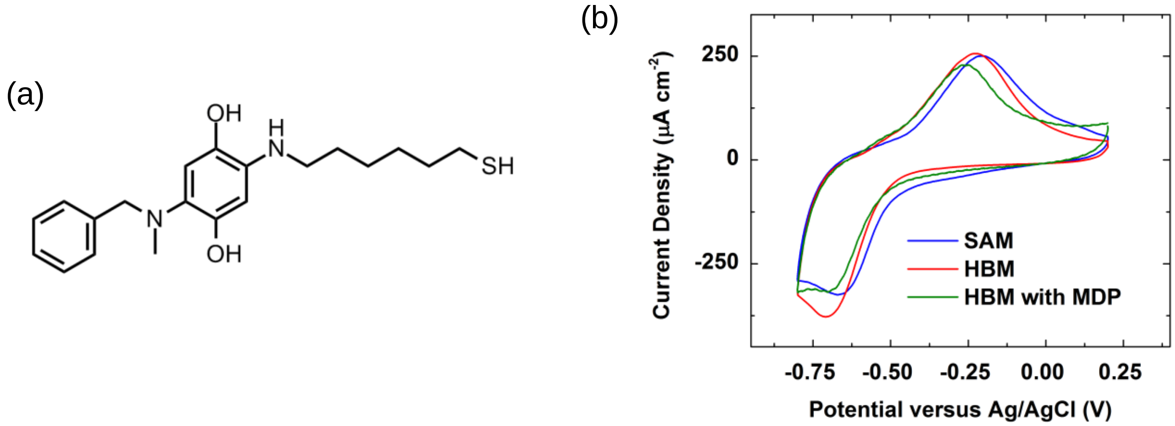

Figure 8. (a) Structure of N_2-BHQ and (b) CVs of a SAM of N_2-BHQ (blue) covered by a monolayer of DMPC (red) with MDP added (green) in an Ar-saturated pH 7 solutions at a scan rate of 1600 mV/s.

We further study 2-(benzyl(methyl)amino)-5-((6-mercaptohexyl)amino)hydroquinone (N_2-BHQ), a derivative of BHQ with two amines adjacent to the redox active core. Figure 8a displays the structure of N_2-BHQ, the synthesis and characterization data of which are presented in Section 1 of the S.I. Similar to BHQ, N_2-BHQ also features functional units to allow facile electron transfer, SAM formation, and favorable interaction with hydrocarbons on the lipid tail. We perform experiments on N_2-BHQ-modified Au surfaces in an analogous manner to the BHQ system. Figure S12 compares the redox waves of a SAM of BHQ and a SAM of N_2-BHQ. Due to the electron-donating nature of the amine groups, the midpoint potential of N_2-BHQ is ~300 mV more negative than that of BHQ, a similar phenomenon observed when comparing ferrocene to decamethyl-ferrocene.[48] Figure S13 displays the scan rate dependence and Randles-Sevcik plot of a SAM of N_2-BHQ. The results show that N_2-BHQ is indeed surface bound.

Figure 8b shows CVs of a SAM of N_2-BHQ, a N_2-BHQ-containing HBM, and the N_2-BHQ-HBM with MDP added to the lipid layer. Figure S14 summarizes the peak information of the redox waves of the three systems studied. In short, the three systems exhibit very similar voltammograms. To confirm the presence of a complete lipid layer on the SAM, we performed blocking experiments with $K_3Fe(CN)_6$ in the bulk solution. Figure S15 shows the results from the blocking experiments using the three systems. An absence of the Fe(II/III) wave and a decrease in the capacitance are indicative of a well-formed lipid layer, a phenomenon observed previously.[32,35,36,49]

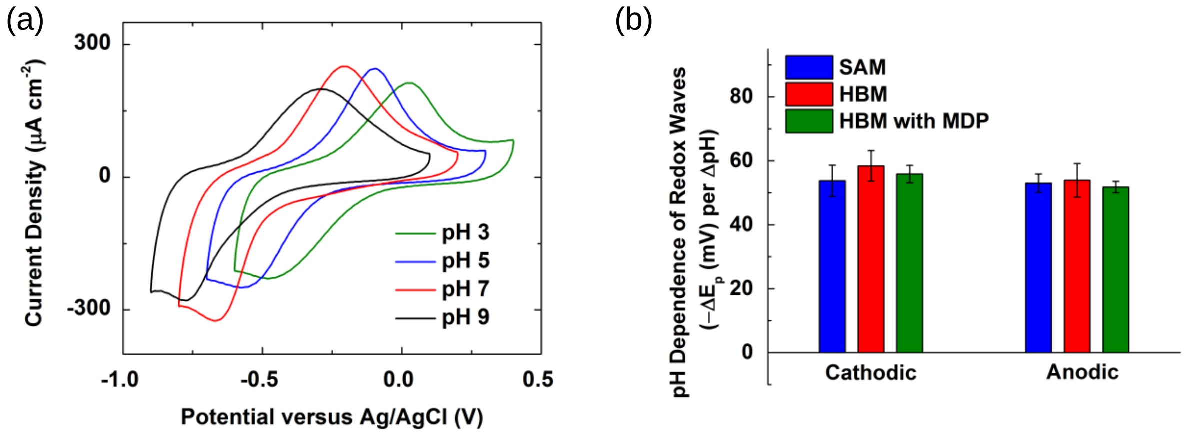

Figure 9. (a) CVs of a SAM of N_2-BHQ on Au in pH 3 (green), 5 (blue), 7 (red), and 9 (black) Ar-saturated solutions at a scan rate of 1600 mV/s. (b) Bar graphs showing the average shifts in the cathodic and anodic peak positions of N_2-BHQ as the pH increases. Each graph has three sets of bars: open SAM, HBM, and HBM with MDP.

To study the redox mechanism that the quinone moiety in N_2-BHQ undergoes, we varied the pH of the bulk solution in an analogous manner to the BHQ case. Figure 9a shows CVs of a SAM of N_2-BHQ in solutions of various pH, and Figure 9b summarizes the pH dependence of the SAM of N_2-BHQ, the N_2-BHQ-containing HBM, and the N_2-BHQ-HBM with MDP incorporated in the lipid layer. The results show that N_2-BHQ exhibits about 59 mV/pH shift in the three cases, suggesting that a $2H^+/2e^-$ pathway is operational in all three systems. Figure S16 displays a nine-member square scheme of N_2-BHQ. A $2H^+/2e^-$ pathway means that BHQ cycles between species **M** and **V** regardless of the presence of a lipid layer or the incorporation of a proton carrier in the lipid layer. Comparing the N_2-BHQ results to the BHQ results, we hypothesize that the amino groups flanking the redox core of N_2-BHQ serve as a proton relays that cause the redox response to be insensitive to changes in the surrounding environment. Indeed, the reactivity of quinone-terminated SAMs is affected by their surroundings.[50,51] The observation that a quinone-terminated SAM exhibiting a 59 mV/pH shift, as in the case of N_2-BHQ, is common.[52] In short, the lipid-modified electrodes behave similarly to the open SAM case in the presence of pendant proton relays. In the absence of the pendant amino groups (BHQ), however, we are able to observe several other species described in the nine-member square scheme.

Conclusions

In this work, we prepared quinone molecules that can self-assemble on a Au surface and allow a lipid monolayer to form on top. For BHQ, the addition of a hydrophobic lipid layer on top of the surface-bound quinone changes the reaction pathway from a PCET process to a pure electron transfer step. Upon incorporation of a proton carrier in the lipid layer, the mechanism of the quinone redox switches to stepwise PCET. The ability to control proton flux to a quinone moiety paves the way to a unified understanding of the interplay between the thermodynamics and kinetics of protons and electrons.

5. Associated Content

Supporting Information. Additional information including synthesis procedures and further electrochemical characterization data as discussed in the text. This material is available free of charge via the Internet at http://pubs.acs.org.

6. Author Information

Corresponding Author

*Tel: 217-333-8329. Fax: 217-244-3186. E-mail: agewirth@illinois.edu.

7. Acknowledgments

C.J.B. acknowledges a National Science Foundation Graduate Research Fellowship (NSF DGE-1144245) and a Springborn Fellowship. E.C.M.T. acknowledges a Croucher Foundation Scholarship. We thank the US Department of Energy (DE-FG02-95ER46260) for support of this research. This work was carried out in part in the Frederick Seitz Materials Research Laboratory Central Facilities, which are partially supported by the US Department of Energy (DE-FG02-07ER46453 and DE-FG02-07ER46471). We thank Professor Sharon Hammes-Schiffer, Dr. Soumya Ghosh, and Mioy T. Huynh for discussion on PCET theories.

8. Competing Financial Interests

The authors declare no competing financial interests.

9. References

(1) Warren, J. J.; Tronic, T. A.; Mayer, J. M. *Chem. Rev.* **2010**, *110*, 6961-7001.
(2) Hammes-Schiffer, S. *Acc. Chem. Res.* **2001**, *34*, 273-281.

(3) Nohl, H.; Jordan, W.; Youngman, R. J. *Adv. Free Radical Bio.* **1986**, *2*, 211-279.

(4) Santhamma, K. R.; Raj, R. K. *Biochem. Biophys. Res. Comm.* **1993**, *190*, 201-206.

(5) Coates, C. S.; Ziegler, J.; Manz, K.; Good, J.; Kang, B.; Milikisiyants, S.; Chatterjee, R.; Hao, S.; Golbeck, J. H.; Lakshmi, K. V. *J. Phys. Chem. B* **2013**, *117*, 7210-7220.

(6) Faig, M.; Bianchet, M. A.; Winski, S.; Hargreaves, R.; Moody, C. J.; Hudnott, A. R.; Ross, D.; Amzel, L. M. *Structure* **2001**, *9*, 659-667.

(7) Nepovimova, E.; Uliassi, E.; Korabecny, J.; Peña-Altamira, L. E.; Samez, S.; Pesaresi, A.; Garcia, G. E.; Bartolini, M.; Andrisano, V.; Bergamini, C.; Fato, R.; Lamba, D.; Roberti, M.; Kuca, K.; Monti, B.; Bolognesi, M. L. *J. Med. Chem.* **2014**, *57*, 8576-8589.

(8) Milton, R. D.; Hickey, D. P.; Abdellaoui, S.; Lim, K.; Wu, F.; Tan, B.; Minteer, S. D. *Chem. Sci.* **2015**, *6*, 4867-4875.

(9) Giroud, F.; Milton, R. D.; Tan, B.-X.; Minteer, S. D. *ACS Catal.* **2015**, *5*, 1240-1244.

(10) Cinquin, P.; Gondran, C.; Giroud, F.; Mazabrard, S.; Pellissier, A.; Boucher, F.; Alcaraz, J.-P.; Gorgy, K.; Lenouvel, F.; Mathé, S.; Porcu, P.; Cosnier, S. *PLoS ONE* **2010**, *5*, e10476.

(11) Costentin, C.; Robert, M.; Savéant, J.-M. *Chem. Rev.* **2010**, *110*, PR1-PR40.

(12) Weinberg, D. R.; Gagliardi, C. J.; Hull, J. F.; Murphy, C. F.; Kent, C. A.; Westlake, B. C.; Paul, A.; Ess, D. H.; McCafferty, D. G.; Meyer, T. J. *Chemical Reviews* **2012**, *112*, 4016-4093.

(13) Hammes-Schiffer, S.; Soudackov, A. V. *J. Phys. Chem. B* **2008**, *112*, 14108-14123.

(14) Mayer, J. M.; Rhile, I. J. *BBA-Bioenergetics* **2004**, *1655*, 51-58.

(15) Chen, Z.; Vannucci, A. K.; Concepcion, J. J.; Jurss, J. W.; Meyer, T. J. *Proc. Natl. Acad. Sci. U.S.A.* **2011**, *108*, E1461-E1469.

(16) Bouffier, L.; Lister, K. E.; Higgins, S. J.; Nichols, R. J.; Doneux, T. *Journal of Electroanalytical Chemistry* **2012**, *664*, 80-87.

(17) Haga, M.-a.; Hong, H.-G.; Shiozawa, Y.; Kawata, Y.; Monjushiro, H.; Fukuo, T.; Arakawa, R. *Inorganic Chemistry* **2000**, *39*, 4566-4573.

(18) Zhang, W.; Rosendahl, S. M.; Burgess, I. J. *The Journal of Physical Chemistry C* **2010**, *114*, 2738-2745.

(19) Staley, P. A.; Lopez, E. M.; Clare, L. A.; Smith, D. K. *The Journal of Physical Chemistry C* **2015**, *119*, 20319-20327.

(20) Chidsey, C. E. D. *Science* **1991**, *251*, 919-922.

(21) Smalley, J. F.; Feldberg, S. W.; Chidsey, C. E. D.; Linford, M. R.; Newton, M. D.; Liu, Y.-P. *J. Phys. Chem.* **1995**, *99*, 13141-13149.

(22) Collman, J. P.; Devaraj, N. K.; Decréau, R. A.; Yang, Y.; Yan, Y.-L.; Ebina, W.; Eberspacher, T. A.; Chidsey, C. E. D. *Science* **2007**, *315*, 1565-1568.

(23) Finklea, H. O.; Haddox, R. M. *Physical Chemistry Chemical Physics* **2001**, *3*, 3431-3436.

(24) Haddox, R. M.; Finklea, H. O. *Journal of Electroanalytical Chemistry* **2003**, *550–551*, 351-358.

(25) Haddox, R. M.; Finklea, H. O. *The Journal of Physical Chemistry B* **2004**, *108*, 1694-1700.

(26) Trammell, S. A.; Lebedev, N. *Journal of Electroanalytical Chemistry* **2009**, *632*, 127-132.

(27) Collman, J. P.; Devaraj, N. K.; Eberspacher, T. P. A.; Chidsey, C. E. D. *Langmuir* **2006**, *22*, 2457-2464.

(28) Henstridge, M. C.; Laborda, E.; Rees, N. V.; Compton, R. G. *Electrochimica Acta* **2012**, *84*, 12-20.

(29) Chang, C. J.; Chang, M. C. Y.; Damrauer, N. H.; Nocera, D. G. *Biochimica et Biophysica Acta (BBA) - Bioenergetics* **2004**, *1655*, 13-28.

(30) Irebo, T.; Reece, S. Y.; Sjödin, M.; Nocera, D. G.; Hammarström, L. *J. Am. Chem. Soc.* **2007**, *129*, 15462-15464.

(31) Bediako, D. K.; Solis, B. H.; Dogutan, D. K.; Roubelakis, M. M.; Maher, A. G.; Lee, C. H.; Chambers, M. B.; Hammes-Schiffer, S.; Nocera, D. G. *Proceedings of the National Academy of Sciences* **2014**, *111*, 15001-15006.

(32) Li, Y.; Tse, E. C. M.; Barile, C. J.; Gewirth, A. A.; Zimmerman, S. C. *J. Am. Chem. Soc.* **2015**, *137*, 14059-14062.

(33) Hosseini, A.; Barile, C. J.; Devadoss, A.; Eberspacher, T. A.; Decreau, R. A.; Collman, J. P. *J. Am. Chem. Soc.* **2011**, *133*, 11100-11102.

(34) Hosseini, A.; Collman, J. P.; Devadoss, A.; Williams, G. Y.; Barile, C. J.; Eberspacher, T. A. *Langmuir* **2010**, *26*, 17674-17678.

(35) Barile, C. J.; Tse, E. C. M.; Li, Y.; Sobyra, T. B.; Zimmerman, S. C.; Hosseini, A.; Gewirth, A. A. *Nat. Mater.* **2014**, *13*, 619-623.

(36) Tse, E. C. M.; Barile, C. J.; Gewargis, J. P.; Li, Y.; Zimmerman, S. C.; Gewirth, A. A. *Anal. Chem.* **2015**, *87*, 2403-2409.

(37) Eckermann, A. L.; Feld, D. J.; Shaw, J. A.; Meade, T. J. *Coord. Chem. Rev.* **2010**, *254*, 1769-1802.

(38) Laviron, E. *J. Electroanal. Chem. Interfacial Electrochem.* **1979**, *101*, 19-28.

(39) Tse, E. C. M.; Schilter, D.; Gray, D. L.; Rauchfuss, T. B.; Gewirth, A. A. *Inorg. Chem.* **2014**, *53*, 8505-8516.

(40) Kim, R. S.; Park, W.; Hong, H.; Chung, T. D.; Kim, S. *Electrochem. Commun.* **2014**, *41*, 39-43.

(41) Nagata, M.; Kondo, M.; Suemori, Y.; Ochiai, T.; Dewa, T.; Ohtsuka, T.; Nango, M. *Colloids and Surfaces B: Biointerfaces* **2008**, *64*, 16-21.

(42) Wieckowska, A.; Braunschweig, A. B.; Willner, I. *Chem. Comm.* **2007**, 3918-3920.

(43) Jain, M. K. *Introduction to Biological Membranes*; 2nd ed.; Wiley: New York, 1988.

(44) Schönfeld, P.; Schild, L.; Kunz, W. *BBA-Bioenergetics* **1989**, *977*, 266-272.

(45) Carley, A. N.; Kleinfeld, A. M. *Biochemistry* **2009**, *48*, 10437-10445.

(46) McConnell, H. M.; Kornberg, R. D. *Biochemistry* **1971**, *10*, 1111-1120.

(47) John, K.; Schreiber, S.; Kubelt, J.; Herrmann, A.; Müller, P. *Biophys. J.* **2002**, *83*, 3315-3323.

(48) Connelly, N. G.; Geiger, W. E. *Chem. Rev.* **1996**, *96*, 877-910.

(49) Han, X.; Wang, L.; Qi, B.; Yang, X.; Wang, E. *Analytical Chemistry* **2003**, *75*, 6566-6570.

(50) Kwon, Y.; Mrksich, M. *Journal of the American Chemical Society* **2002**, *124*, 806-812.

(51) Abhayawardhana, A. D.; Sutherland, T. C. *The Journal of Physical Chemistry C* **2009**, *113*, 4915-4924.

(52) Hong, H.-G.; Park, W. *Langmuir* **2001**, *17*, 2485-2492.

Supporting Information for

Proton Kinetics Dictates the Reaction Mechanism of Quinones at Lipid-modified Electrodes

Christopher J. Barile,[1†] Edmund C. M. Tse,[1†] Ying Li,[1] Ali Hosseini,[2]
Steven C. Zimmerman,[1] and Andrew A. Gewirth[1,3*]

[1] Department of Chemistry, University of Illinois at Urbana−Champaign, 600 South Mathews Avenue, Urbana, Illinois 61801, United States

[2] Manufacturing Systems Ltd., Auckland 0632, New Zealand

[3] International Institute for Carbon Neutral Energy Research (WPI-I2CNER), Kyushu University, Fukuoka 812-8581, Japan

[†] C. J. B. and E. C. M. T. contributed equally to this work.

[*] Corresponding author. E-mail: agewirth@illinois.edu

Table of Contents

1. General methods

All reactions were carried out under a dry N_2 atmosphere. Chemicals were purchased from commercial sources and used without further purification. Dry dichloromethane (DCM), tetrahydrofuran (THF), and dimethyl sulfoxide (DMSO) were used directly from a solvent delivery system just prior to use. Freshly purchased triethylamine (TEA) was dried and stored over 4 Å molecular sieves. All other solvents, like ethanol (EtOH), methanol (MeOH), ethyl acetate (EtOAc) and hexanes (Hx) were of reagent grade and used without further purification. Reported reaction temperatures refer to the temperature of the heating medium. The progress of reactions was monitored by silica gel thin layer chromatography (TLC) using 0.2 mm silica 60 coated, plastic plates with F254 indicator. Flash and gravity chromatography was performed using 230-400 mesh (40-63 μm) silica gel (SiO_2). Ratios of solvents for NMR solvents and flash chromatography are reported as volume ratios. NMR spectra were performed in $CDCl_3$ unless otherwise specified and acquired using a Varian Unity 500 MHz instrument (^1H, 500 MHz; ^{13}C, 125 MHz) in the VOICE laboratory, University of Illinois at Urbana-Champaign. Chemical shifts (δ) and coupling constants (J) are reported in parts per million (ppm) and hertz (Hz), respectively. For ^1H spectra, chemical shifts are referenced to the residual proton solvent peak: 7.26 ppm for $CDCl_3$. For ^{13}C spectra, chemical shifts are referenced to the solvent peak at 77.5 ppm in $CDCl_3$. Electrospray ionization mass spectrometry (ESI-MS) data were collected with a Quattro II instrument (Waters) at the University of Illinois at Urbana-Champaign.

2. Synthetic Procedures

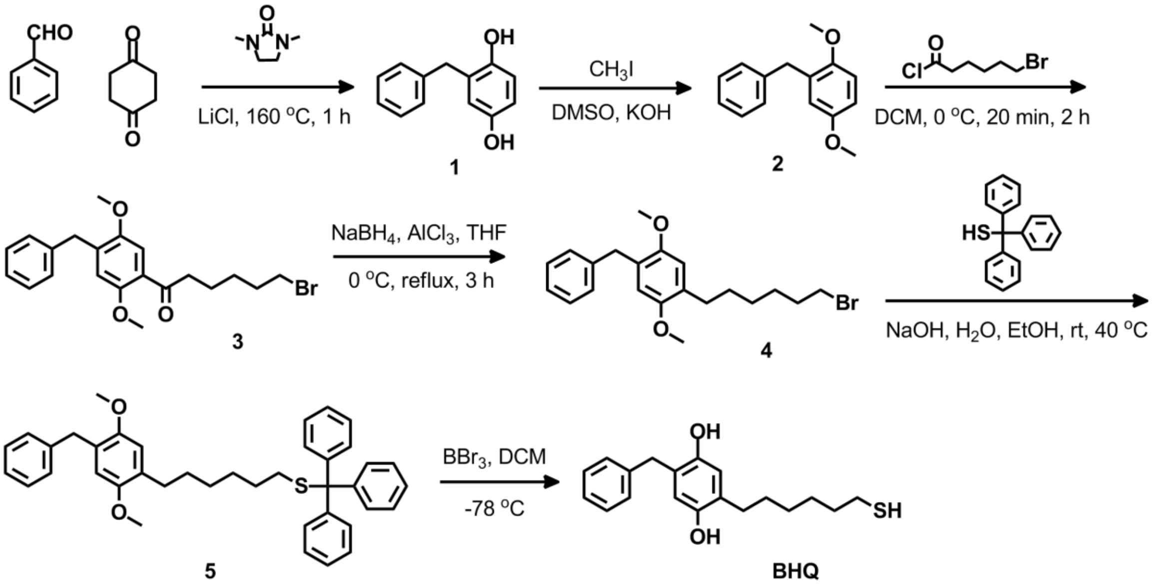

Compound 1. To a solution of 1,4-cyclohexanedione (2.8 g, 25 mmol) and benzaldehyde (2.65g, 25 mmol) in 10 mL of 1,3-dimethyl-2-imidazolidinone, lithium chloride (1.2 g, 28 mmol) was added. The mixture was heated to 160 °C for 1 h, cooled to room temperature, poured into 50 mL of water and extracted twice with 50 mL of diethyl ether. The organic layers were combined, dried with anhydrous Na_2SO_4 and concentrated down under reduced pressure. The crude product was purified by gradient column chromatography (EtOAc:hexanes = 1:4 to 1:1) to give a white solid (yield: 3.72 g, 82%). ^{1}H NMR δ 7.30 (m, 2H), 7.22 (m, 3H), 6.67 (m, 1H), 6.60 (m, 1H), 6.59 (s, 1H), 4.37 (b, 1H), 4.34 (b, 1H), 3.94 (s, 2H).

Compound 2. To 30 mL of DMSO, potassium hydroxide (6.4 g, 0.11 mol) was added. The mixture was stirred at room temperature for 10 min. To the suspension, **1** (3 g, 15 mmol) and methyl iodide (4 mL, 64 mmol) were added. The mixture was stirred at room temperature for 1 h, poured into 30 mL of water, and extracted twice with 50 mL of DCM. The organic layers were combined, dried with anhydrous Na_2SO_4, concentrated down under reduced pressure to give an off-white solid without further purification (yield: 3.2g, 93 %). ^{1}H NMR δ 7.27 (m, 2H), 7.19 (m, 3H), 6.80 (d, *J* = 8.5, 1H), 6.72 (dd, *J* = 8.5,3, 1H), 6.66 (d, *J* = 3, 1H), 3.95 (s, 2H), 3.78 (s, 3H), 3.72 (s, 3H).

Compound 3. A solution of **2** (1.7 g, 7.4 mmol) in 15 mL of DCM was cooled to 0 °C and $AlCl_3$ (1.34 g, 10 mmol) was added portion-wise over 20 min. To the mixture, 6-bromocaproyl chloride (1.12 mL, 7.3 mmol) was added dropwise and the suspension was stirred at 0 °C for 2 h. The reaction was quenched by adding 10 mL of aqueous HCl solution (0.1 M) and washed with 20 mL of saturated aqueous $NaHCO_3$ solution. The organic layer was dried with anhydrous Na_2SO_4 and concentrated down under reduced pressure. The crude product was purified by gradient column chromatography (EtOAc:hexanes = 1:10 to 1:4) to give an off-white solid (yield: 3.72 g, 82%). ^{1}H NMR δ 7.28 (m, 2H), 7.26 (s, 1H), 7.20 (m, 3H), 6.68 (s, 1H), 3.99 (s, 2H), 3.81 (s, 3H), 3.78 (s, 3H), 3.42 (t, *J* = 7, 2H), 2.98 (t, *J* = 7, 2H), 1.90 (m, 2H), 1.70 (m, 2H), 1.50 (m, 2H). ESI (*m/z*): $[M]^+$ calcd. for $C_{21}H_{25}BrO_3$, 404.1; found, 405.2 $[M+H]^+$.

Compound 4. To 6 mL of THF at 0 °C, $AlCl_3$ (4.3 g, 32 mmol) and $NaBH_4$ (1.3 g, 34 mmol) were added portion-wise. To this suspension, a solution of **3** (1.19 g, 2.9 mmol) in 3 mL of THF at 0 °C was added dropwise. The mixture was warmed to room temperature and heated to reflux for 3 h. The reaction was carefully quenched by 1 ml of acetone and 10 ml of ice water. The aqueous layer was extracted three times with 15 mL of ethyl acetate. The organic layers were combined, dried with anhydrous Na_2SO_4, and concentrated down under reduced pressure. The crude product was used without further purification. ^{1}H NMR δ 7.27 (m, 2H), 7.21 (M, 2H), 7.17 (m, 2H), 6.68 (s, 1H), 6.59 (S, 1H), 3.95 (s, 2H), 3.77 (s, 3H), 3.70 (s, 3H), 3.41 (t, *J* = 7, 2H), 2.57 (t, *J* = 7, 2H), 1.87 (m, 2H), 1.58 (m, 2H), 1.48 (m, 2H), 1.38 (m, 2H).

Compound 5. To a solution of triphenylmethanethiol (1.17 g, 4.2 mmol) in 10 mL of 95% EtOH, a solution of NaOH (0.6 g, 15 mmol) in 2 mL of water was added. The suspension was stirred at room temperature for 15 min and a solution of **4** (1.1g, 2.8 mmol) in 10 mL of ethanol was added. The mixture was vigorously stirred at 40 °C for 4 h and filtered. The solvent of the filtrate was evaporated under reduced pressure and the oily residue was combined with the filtered residue and dissolved in 20 mL DCM. The organic layer was washed with 20 mL of water, 20 mL of saturated brine solution, dried over anhydrous Na_2SO_4, and concentrated down under reduced pressure. The crude product was purified by gradient column chromatography (EtOAc:hexanes = 1:10 to 1:4) to give a white solid (yield: 1.2 g, 73%). ^{1}H NMR δ 7.45 (m, 6H), 7.31 (m, 8H), 7.25 (m, 4H), 7.21 (m, 2H), 6.70 (s, 1H), 6.62 (S, 1H), 3.99 (s, 2H), 3.79 (s, 3H), 3.72 (s, 3H), 32.56 (t, *J* = 8, 2H), 2.19 (t, *J* = 8, 2H), 1.53 (m, 2H), 1.45 (m, 2H), 1.34 (m, 2H), 1.27 (m, 2H). ^{13}C NMR δ 151.4, 151.3, 145.2, 144.1, 141.4, 130.3, 130.0, 129.8, 129.0, 128.4, 127.9, 127.5, 126.6, 125.9, 113.6, 113.5, 113.3, 113.2(5), 66.5, 56.4, 56.4, 56.3, 56.2, 36.0, 32.2, 30.2, 30.1, 29.3, 29.0(3), 29.0(1), 28.7.

Compound BHQ. To a solution of **5** (20 mg, 0.034 mmol) in 2 mL of DCM at -78 °C, BBr_3 (0.2 mL, 1 M solution in DCM) was added dropwise. The mixture was slowly warmed to room temperature and stirred for 2 h. The reaction was cooled to 0 °C and quenched with 0.2 mL of water. The organic layer was washed with 2 mL of saturated brine solution, dried over anhydrous Na_2SO_4, and concentrated down under reduced pressure. The crude product was purified by gradient column chromatography (MeOH:DCM = 1:99 to 5:95) to give a white oil (yield: 10 mg, 93%). ^{1}H NMR δ 7.29 (m, 3H), 7.22 (m, 2H), 6.57 (s, 1H), 6.49 (s, 1H), 4.30 (b, 1H), 3.91 (s, 2H), 3.40 (t, *J* = 7, 2H), 2.53 (t, *J* = 7.5, 2H), 1.86 (m, 2H), 1.60 (m, 2H), 1.47 (m, 2H), 1.40 (m, 2H).

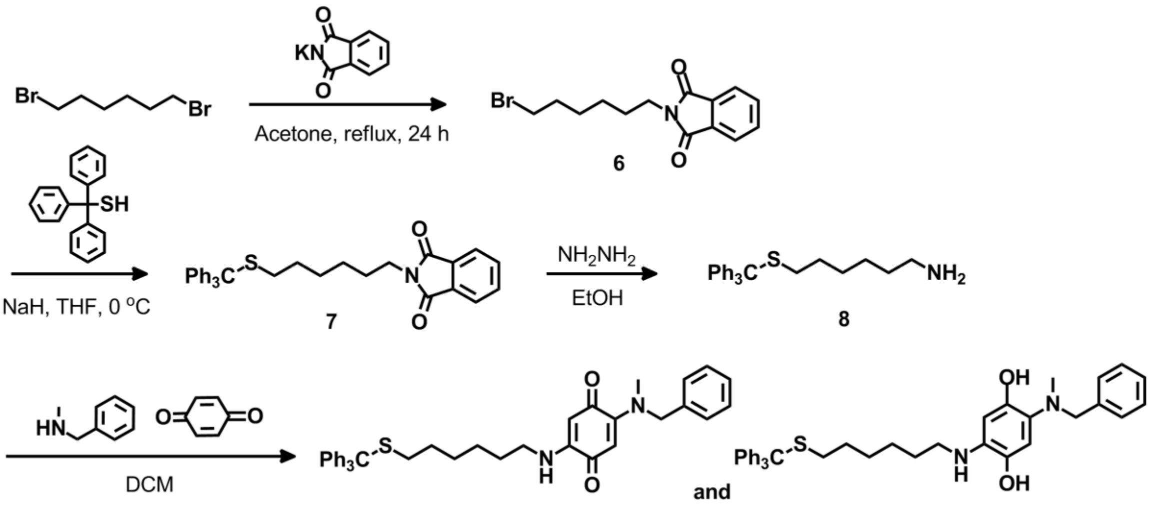

N_2-BHQ

Compound 6, **7**, and **8**. Products were obtained according to reported procedures.[1,2]

Compound N_2-BHQ: To a solution of benzylquinone (10.8 mg, 0.1 mmol) in 2 mL of DCM, *N*-methylbenzylamine (12.1 mg, 0.1 mmol) was added. The mixture was stirred at room temperature for 1 h and **4** (37.5 mg, 0.1 mmol) was added. The reaction was stirred at room temperature for 12 h. The organic layer was diluted with 10 mL of DCM, washed with 15 mL of saturated brine solution, dried over anhydrous Na_2SO_4, and concentrated down under reduced pressure. The crude product was purified by gradient column chromatography (silica, MeOH/DCM: 0/100 to 5/95) to give a red wax-like solid (yield: 26 mg, 43%, containing both the hydroquinone and benzylquinone forms, a mixture of products does not affect the electrochemical analysis because the molecules tethered to the surface are under potential-control upon redox cycling).

3. NMR spectra

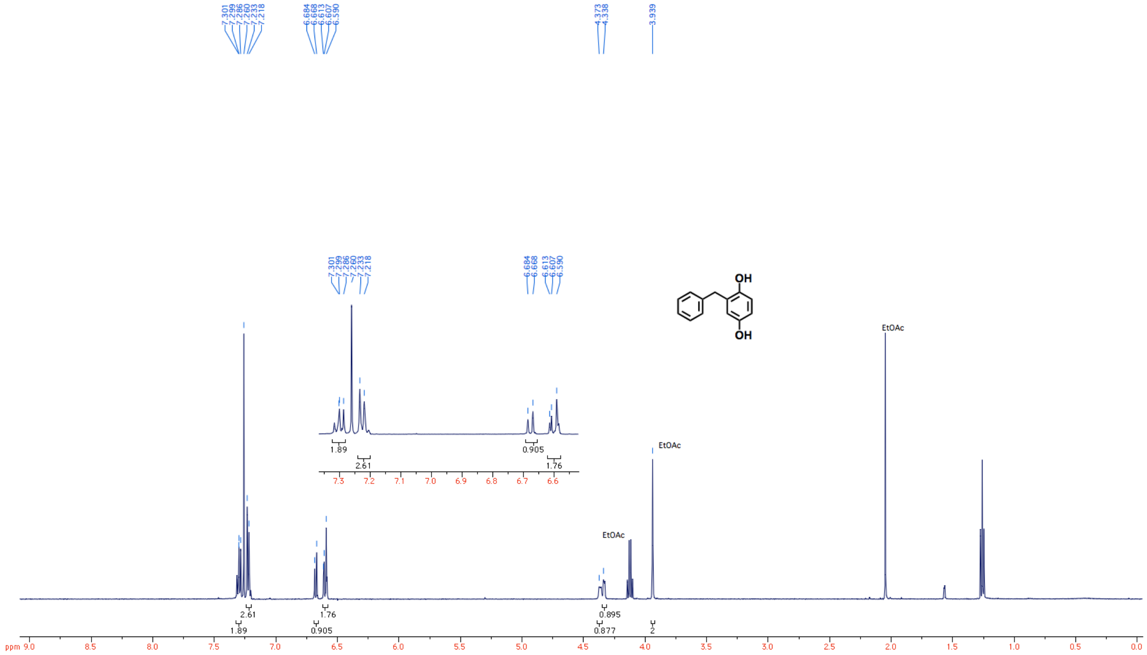

^{1}H NMR spectrum of **1**.

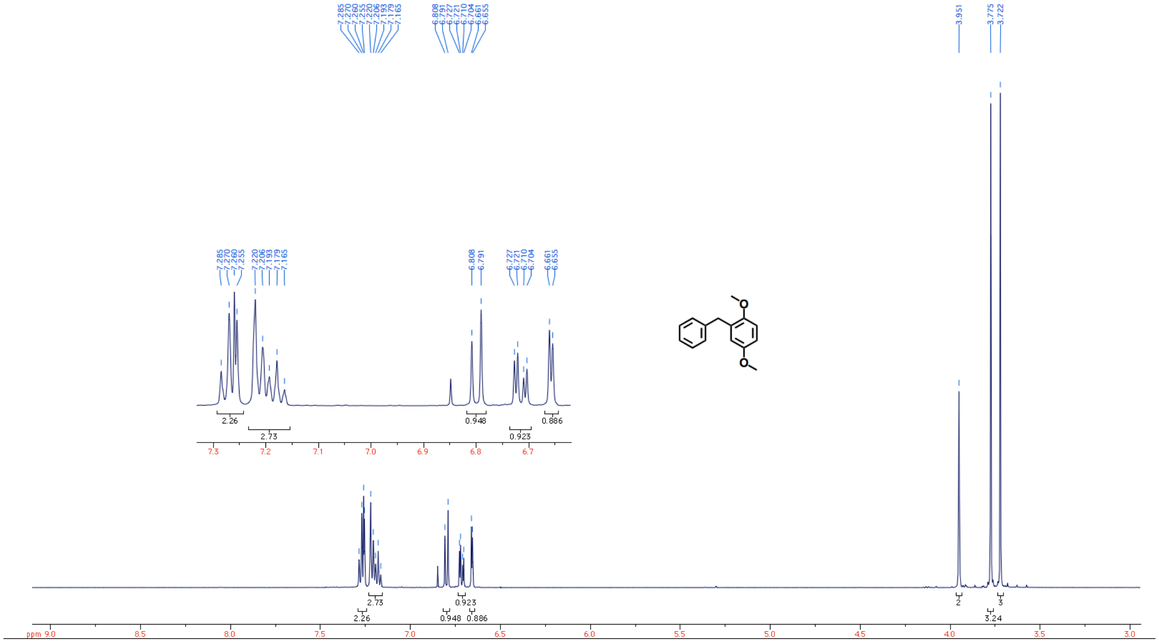

^{1}H NMR spectrum of **2**.

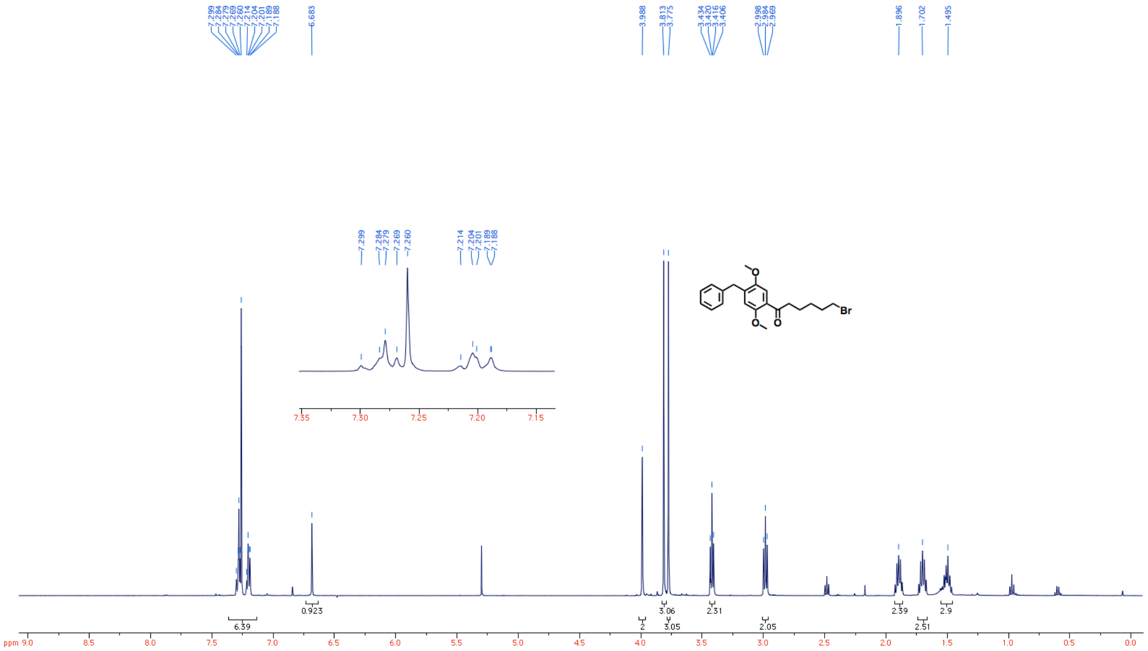

^{1}H NMR spectrum of **3**.

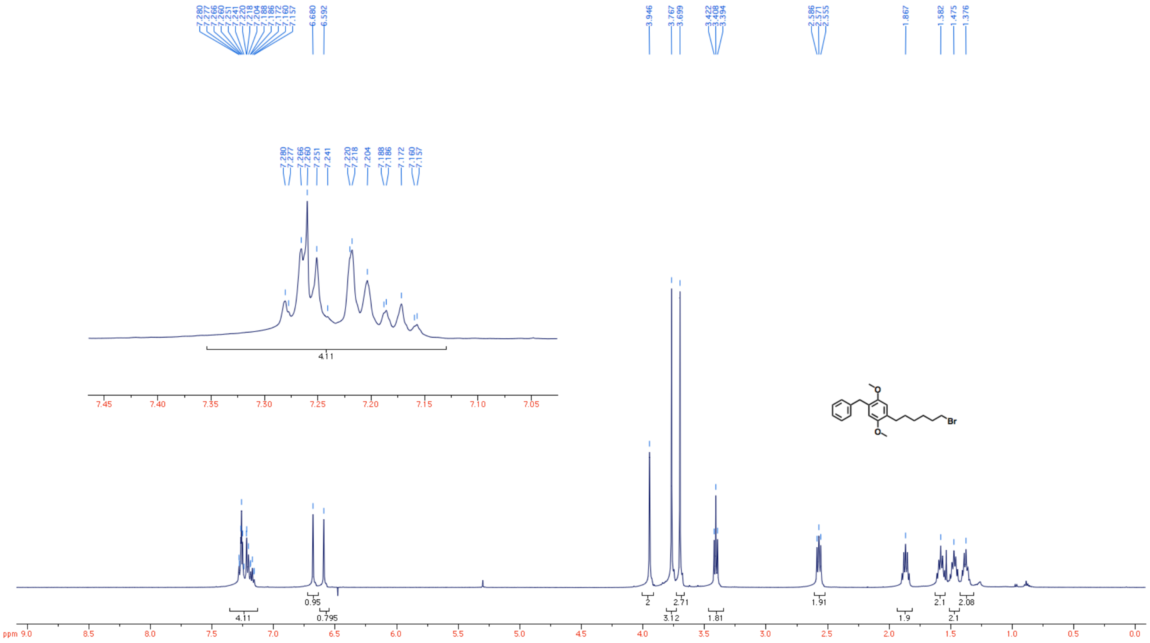

^{1}H NMR spectrum of **4**.

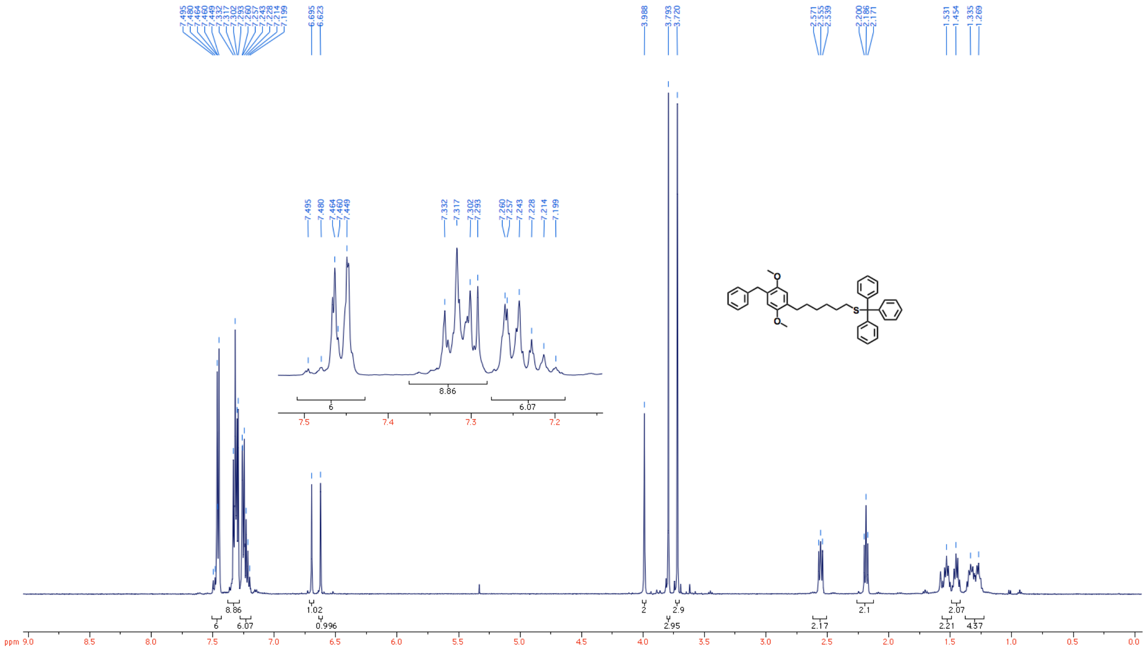

^{1}H NMR spectrum of **5**.

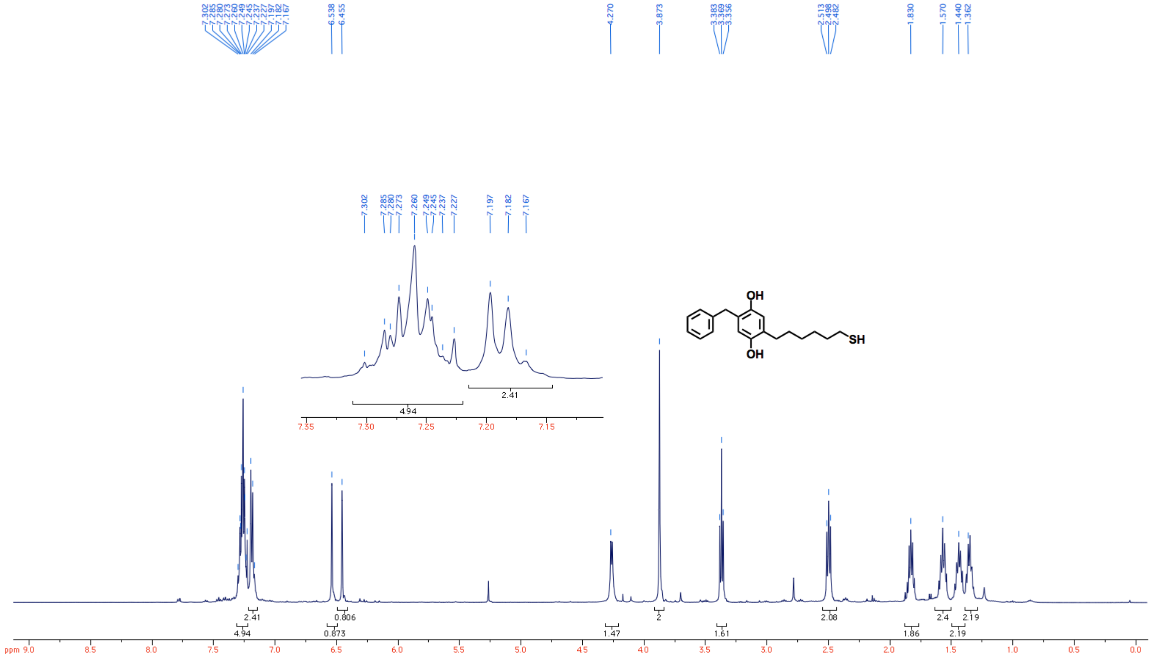

^{1}H NMR spectrum of **BHQ**.

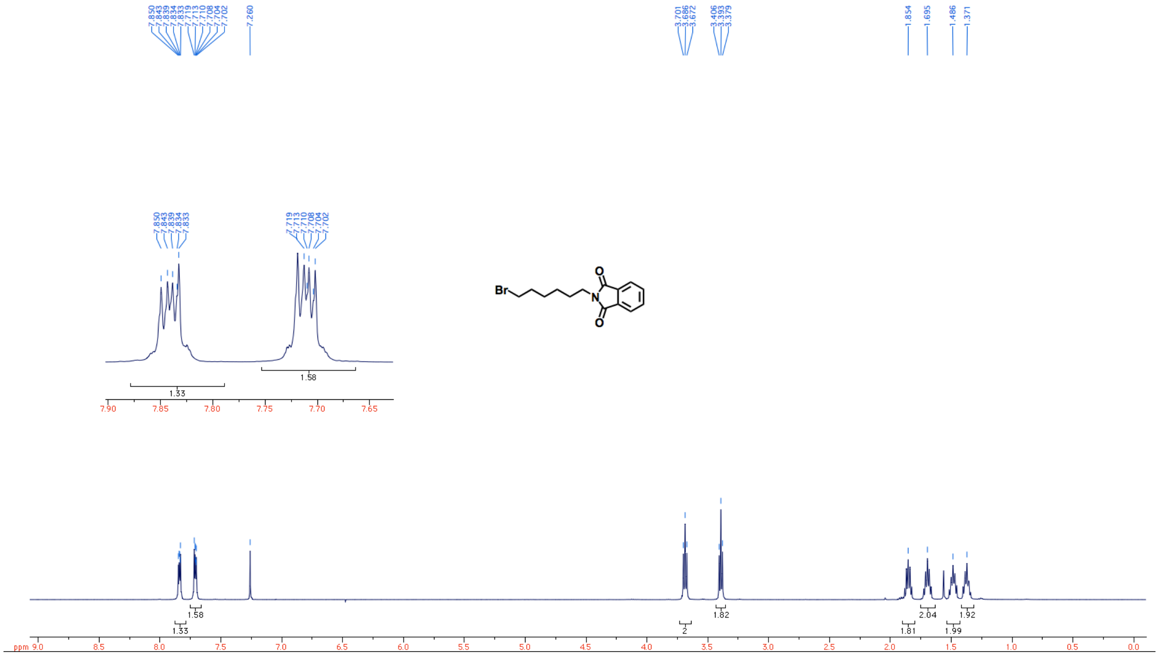

^{1}H NMR spectrum of **6**.

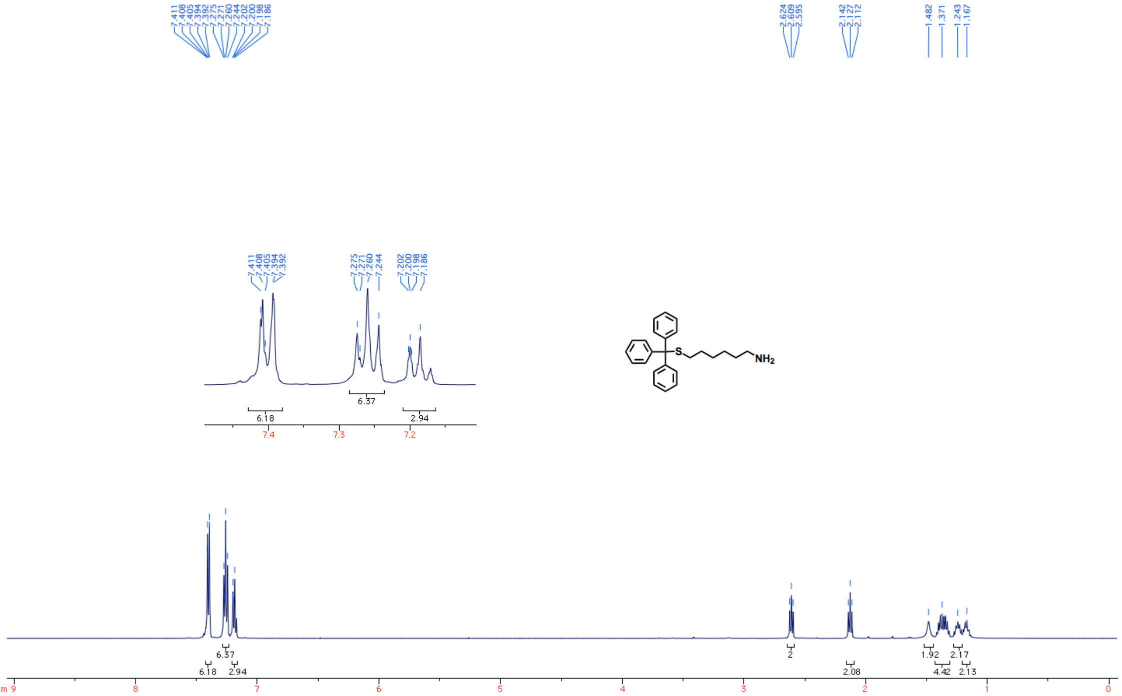

^{1}H NMR spectrum of **8**.

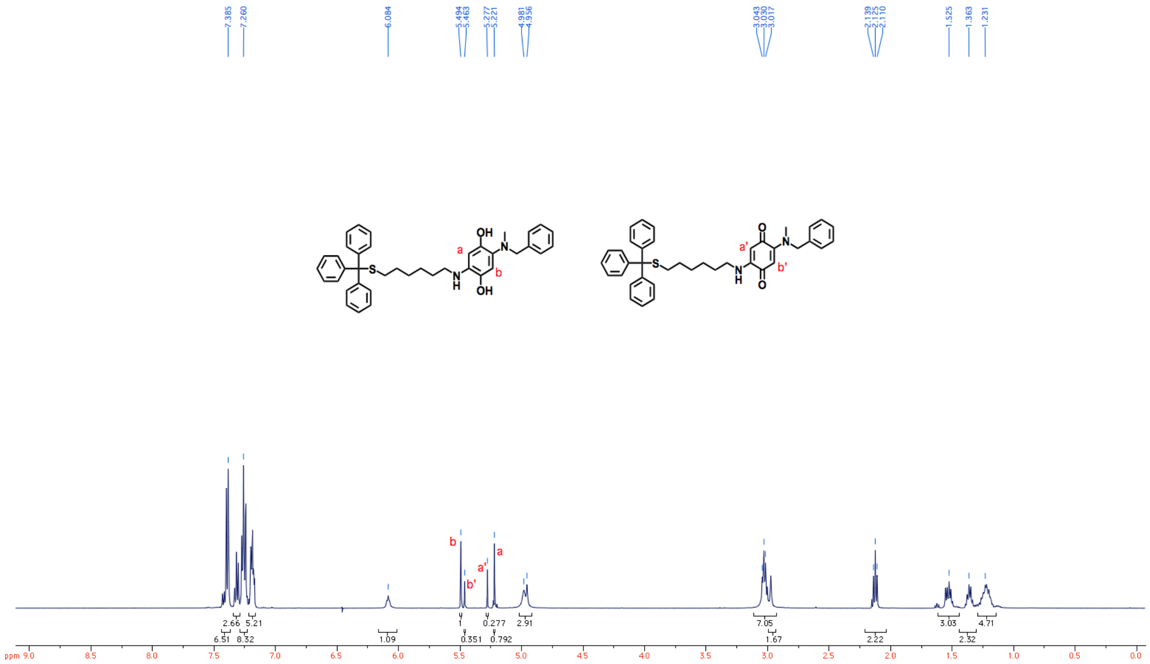

^{1}H NMR spectrum of N$_2$-**BHQ**.

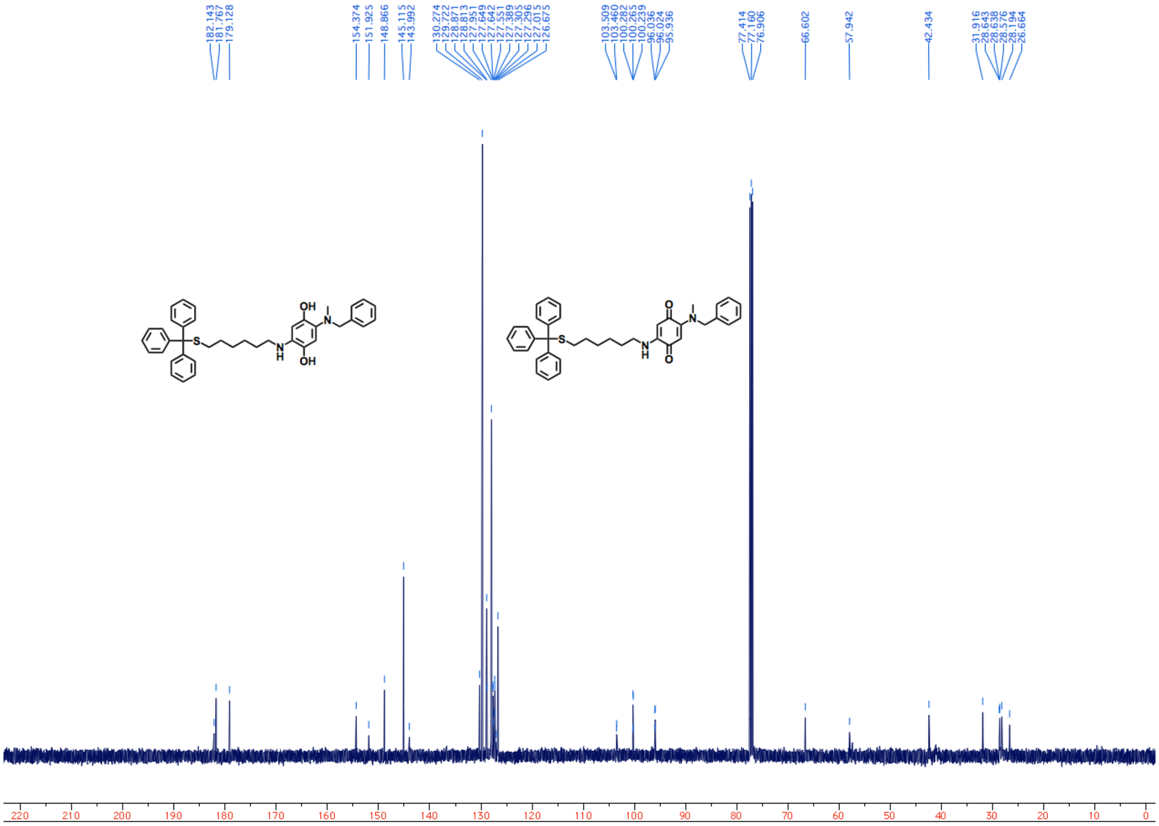

^{13}C NMR spectrum of N$_2$-**BHQ**.

4. Electrochemistry studies

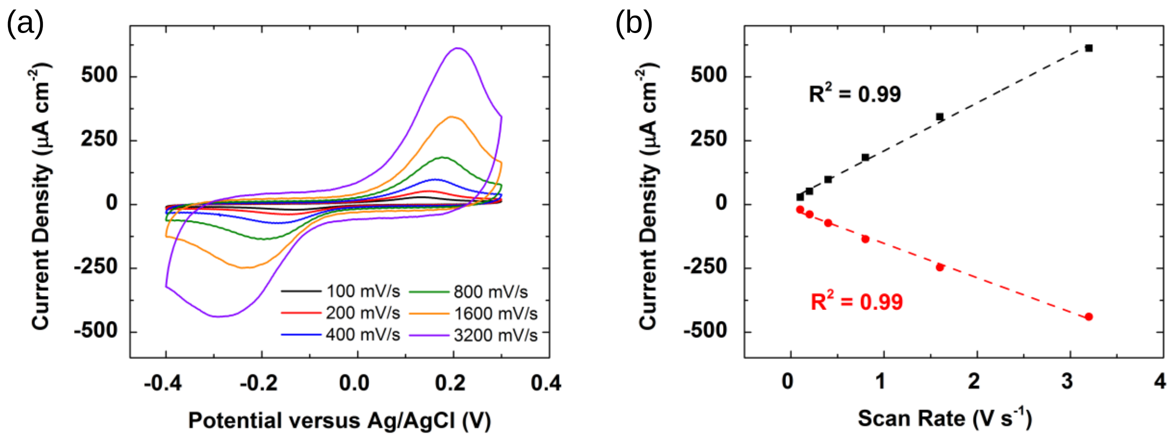

Figure S1. (a) CVs of a SAM of BHQ on Au in pH 3 Ar-saturated solution at scan rates of 100 (black), 200 (red), 400 (blue), 800 (green), 1600 (orange), and 3200 (purple) mV/s. (b) Randles-Sevcik plot of the peak anodic (black) and cathodic (red) current densities of a SAM of BHQ versus scan rate.

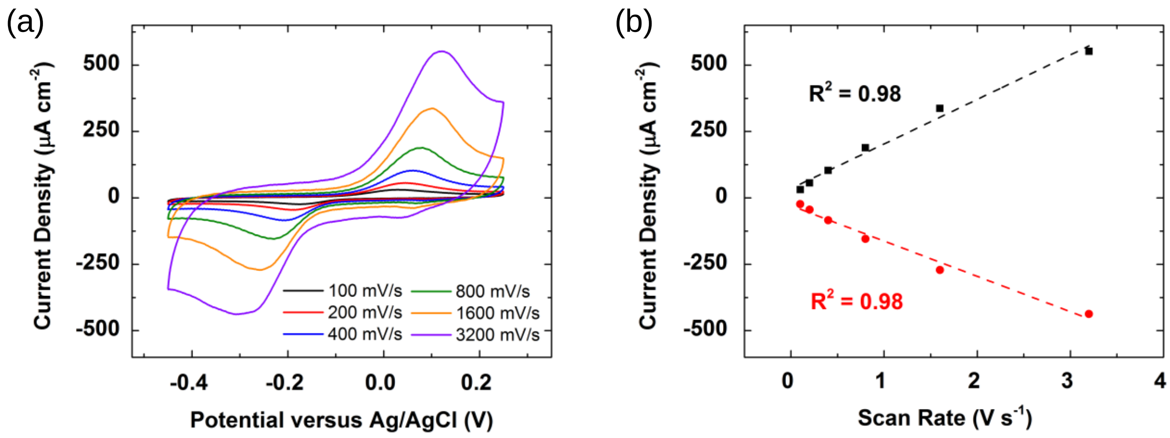

Figure S2. (a) CVs of a SAM of BHQ on Au in pH 5 Ar-saturated solution at scan rates of 100 (black), 200 (red), 400 (blue), 800 (green), 1600 (orange), and 3200 (purple) mV/s. (b) Randles-Sevcik plot of the peak anodic (black) and cathodic (red) current densities of a SAM of BHQ versus scan rate.

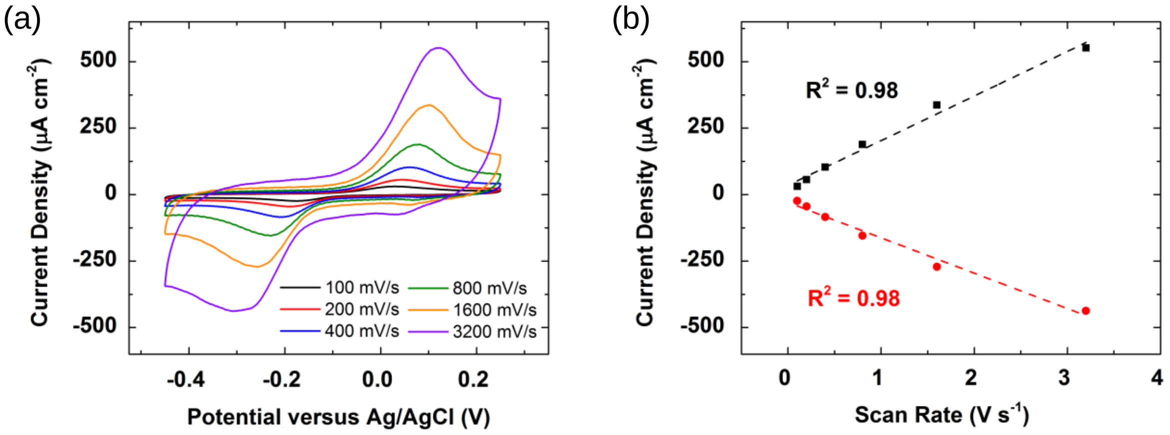

Figure S3. (a) CVs of a SAM of BHQ on Au in pH 9 Ar-saturated solution at scan rates of 100 (black), 200 (red), 400 (blue), 800 (green), 1600 (orange), and 3200 (purple) mV/s. (b) Randles-Sevcik plot of the peak anodic (black) and cathodic (red) current densities of a SAM of BHQ versus scan rate.

System	Cathodic Rate (s^{-1})	Anodic Rate (s^{-1})
BHQ SAM	3.0 ± 1.0	3.9 ± 1.8
BHQ covered by DMPC	3.0 ± 1.4	3.9 ± 1.0
BHQ covered by DMPC with MDP	3.7 ± 0.5	4.4 ± 1.6
N_2-BHQ SAM	2.2 ± 1.1	2.5 ± 0.5
N_2-BHQ covered by DMPC	2.0 ± 0.2	2.3 ± 0.9
N_2-BHQ covered by DMPC with MDP	1.2 ± 1.0	3.6 ± 1.9

Table S1. Apparent rate constants of a SAM of BHQ or N_2-BHQ and BHQ- or N_2-BHQ-containing HBMs with and without MDP.

	pH	Integrated Charges (μC cm^{-2})	
		Anodic	Cathodic
SAM	3	33 ± 3	33 ± 1
	5	36 ± 3	36 ± 2
	7	33 ± 3	31 ± 2
	9	28 ± 1	32 ± 1
HBM	5	18 ± 1	17 ± 1
	7	17 ± 1	17 ± 2
HBM with MDP	5	34 ± 8	35 ± 5
	7	34 ± 2	(i) 17 ± 2, (ii) 14 ± 3

Table S2. The integrated charges for the cathodic and anodic waves of a SAM of BHQ, the HBM containing BHQ, and the BHQ-HBM with MDP added to the lipid layer.

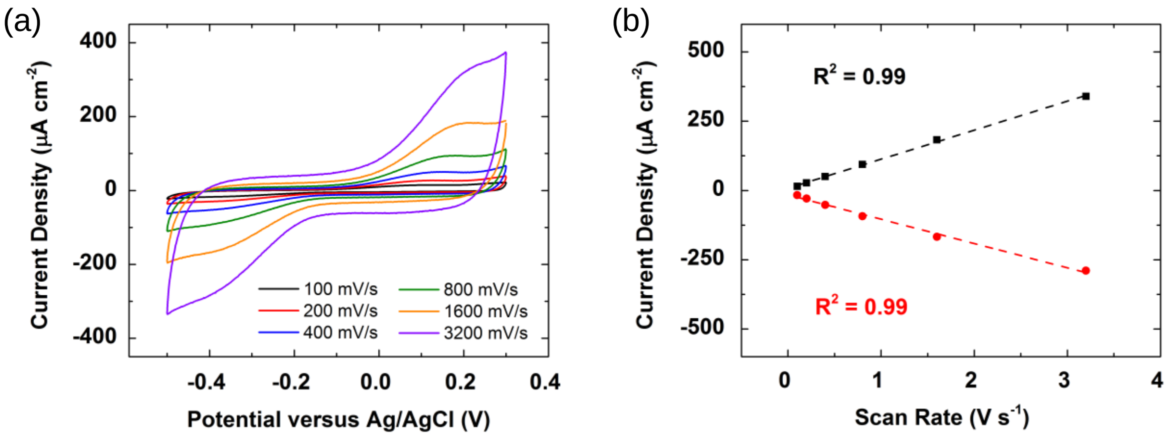

Figure S4. (a) CVs of a SAM of BHQ covered by a DMPC monolayer in pH 7 Ar-saturated solution at scan rates of 100 (black), 200 (red), 400 (blue), 800 (green), 1600 (orange), and 3200 (purple) mV/s. (b) Randles-Sevcik plot of the peak anodic (black) and cathodic (red) current densities of a SAM of BHQ covered by a DMPC monolayer versus scan rate.

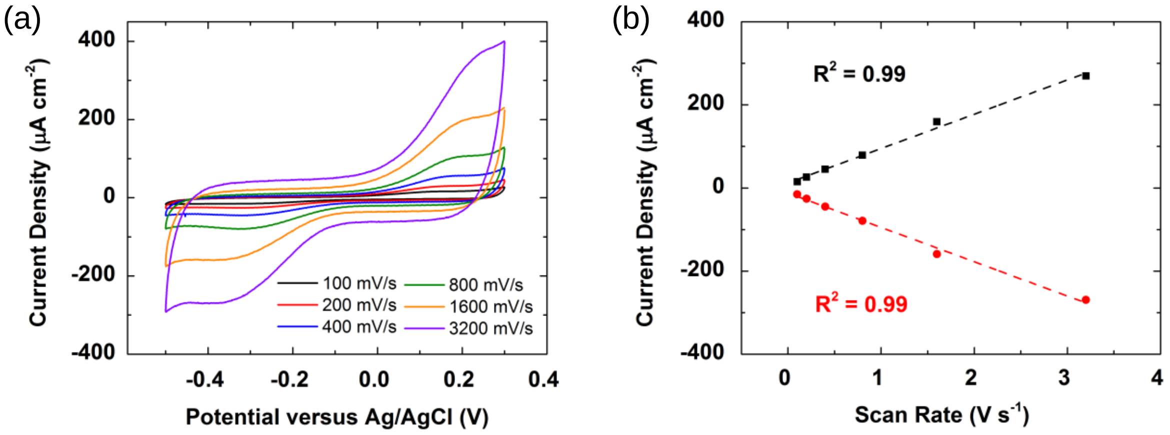

Figure S5. (a) CVs of a SAM of BHQ covered by a DMPC monolayer in pH 5 Ar-saturated solution at scan rates of 100 (black), 200 (red), 400 (blue), 800 (green), 1600 (orange), and 3200 (purple) mV/s. (b) Randles-Sevcik plot of the peak anodic (black) and cathodic (red) current densities of a SAM of BHQ covered by a DMPC monolayer versus scan rate.

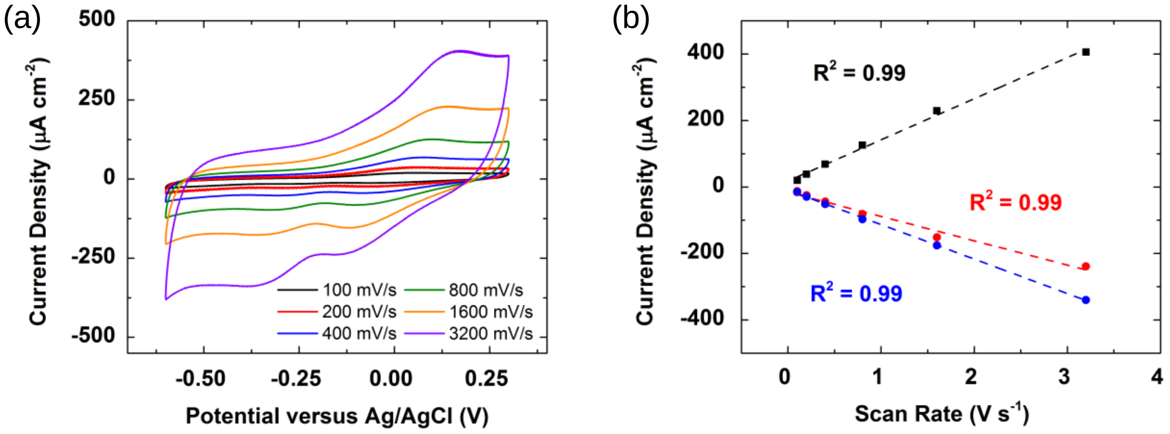

Figure S6. (a) CVs of a SAM of BHQ covered by a DMPC monolayer with MDP incorporated in the lipid layer in pH 7 Ar-saturated solution at scan rates of 100 (black), 200 (red), 400 (blue), 800 (green), 1600 (orange), and 3200 (purple) mV/s. (b) Randles-Sevcik plot of the peak anodic (black) and cathodic (red, blue) current densities of a SAM of BHQ covered by a DMPC monolayer with MDP incorporated in the lipid layer versus scan rate.

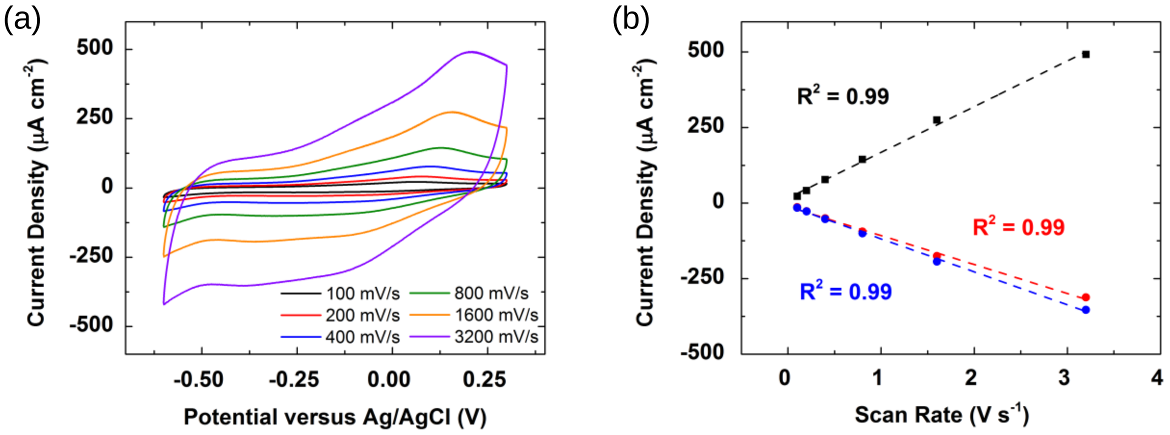

Figure S7. (a) CVs of a SAM of BHQ covered by a DMPC monolayer with MDP incorporated in the lipid layer in pH 5 Ar-saturated solution at scan rates of 100 (black), 200 (red), 400 (blue), 800 (green), 1600 (orange), and 3200 (purple) mV/s. (b) Randles-Sevcik plot of the peak anodic (black) and cathodic (red, blue) current densities of a SAM of BHQ covered by a DMPC monolayer with MDP incorporated in the lipid layer versus scan rate.

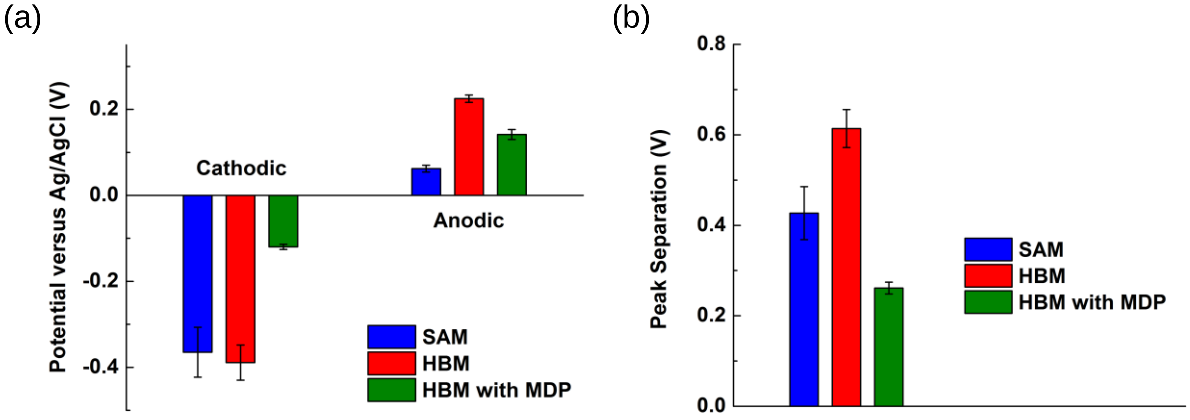

Figure S8. Bar graphs showing BHQ (a) cathodic and anodic peak positions and (b) peak separations at pH 7. Each graph has three sets of bars: open SAM, HBM, and HBM with MDP. For HBM with MDP, the cathodic peak position of the more negative cathodic wave is -0.374 ± 0.022 V versus Ag/AgCl. The cathodic process has two waves with the first wave (i) occurring at a more positive potential than the second (ii).

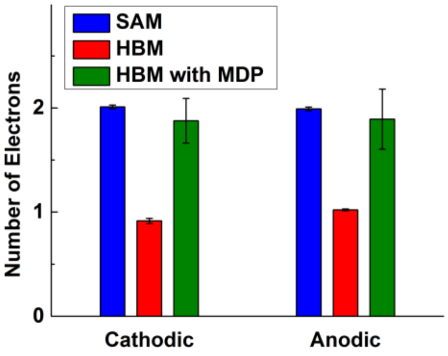

Figure S9. Bar graphs showing the number of electrons transferred for the cathodic and anodic processes of a SAM of BHQ (blue) covered by a monolayer of DMPC (red) with MDP incorporated in the lipid layer (green) in pH 5 Ar-saturated solution.

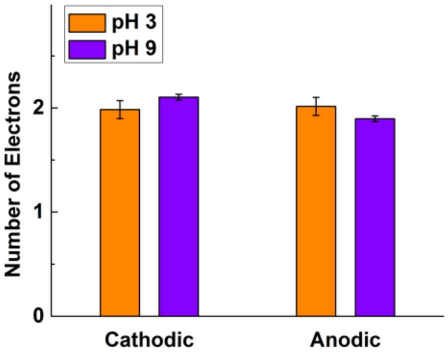

Figure S10. Bar graphs showing the number of electrons transferred for the cathodic and anodic processes of a SAM of BHQ in pH 3 (orange) and 9 (purple) Ar-saturated solutions.

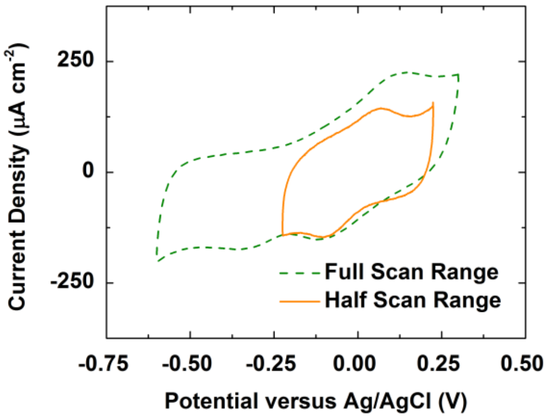

Figure S11. CVs of a SAM of BHQ covered by a monolayer of DMPC with MDP added scanning the full range (dashed green) and half range (solid orange) in an Ar-saturated pH 7 solution at a scan rate of 1600 mV/s.

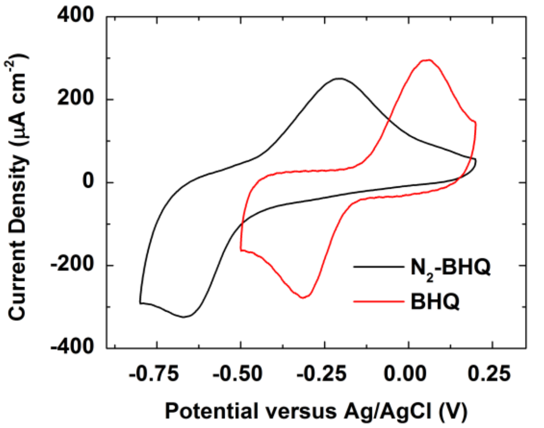

Figure S12. CVs of a SAM of BHQ (red) and a SAM of N_2-BHQ (black) on Au in pH 7 Ar-saturated solution at scan rates of 1600 mV/s.

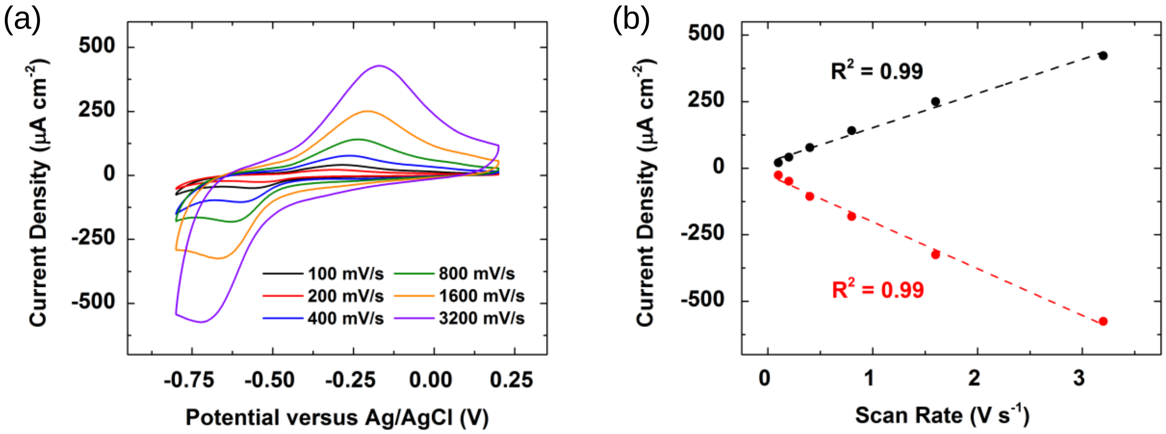

Figure S13. (a) CVs of a SAM of N_2-BHQ on Au in pH 7 Ar-saturated solution at scan rates of 100 (black), 200 (red), 400 (blue), 800 (green), 1600 (orange), and 3200 (purple) mV/s. (b) Randles-Sevcik plot of the peak anodic (black) and cathodic (red) current densities of a SAM of N_2-BHQ versus scan rate.

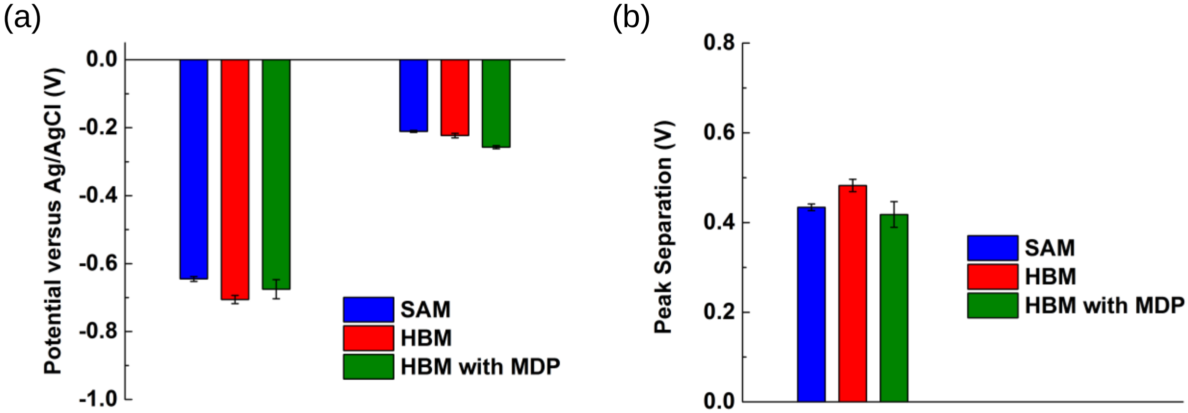

Figure S14. Bar graphs showing NQ (a) cathodic and anodic peak positions and (b) peak separations at pH 7. Each graph has three sets of bars: open SAM, HBM, and HBM with MDP.

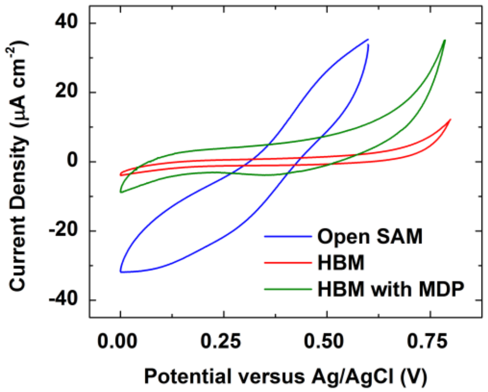

Figure S15. CVs of a SAM of N_2-BHQ (blue), the N_2-BHQ-containing HBM (red), and the N_2-BHQ-HBM with MDP incorporated in the lipid layer (green) in a solution of $K_3Fe(CN)_6$ (1 mM) with KCl (100 mM) at a scan rate of 50 mV/s.

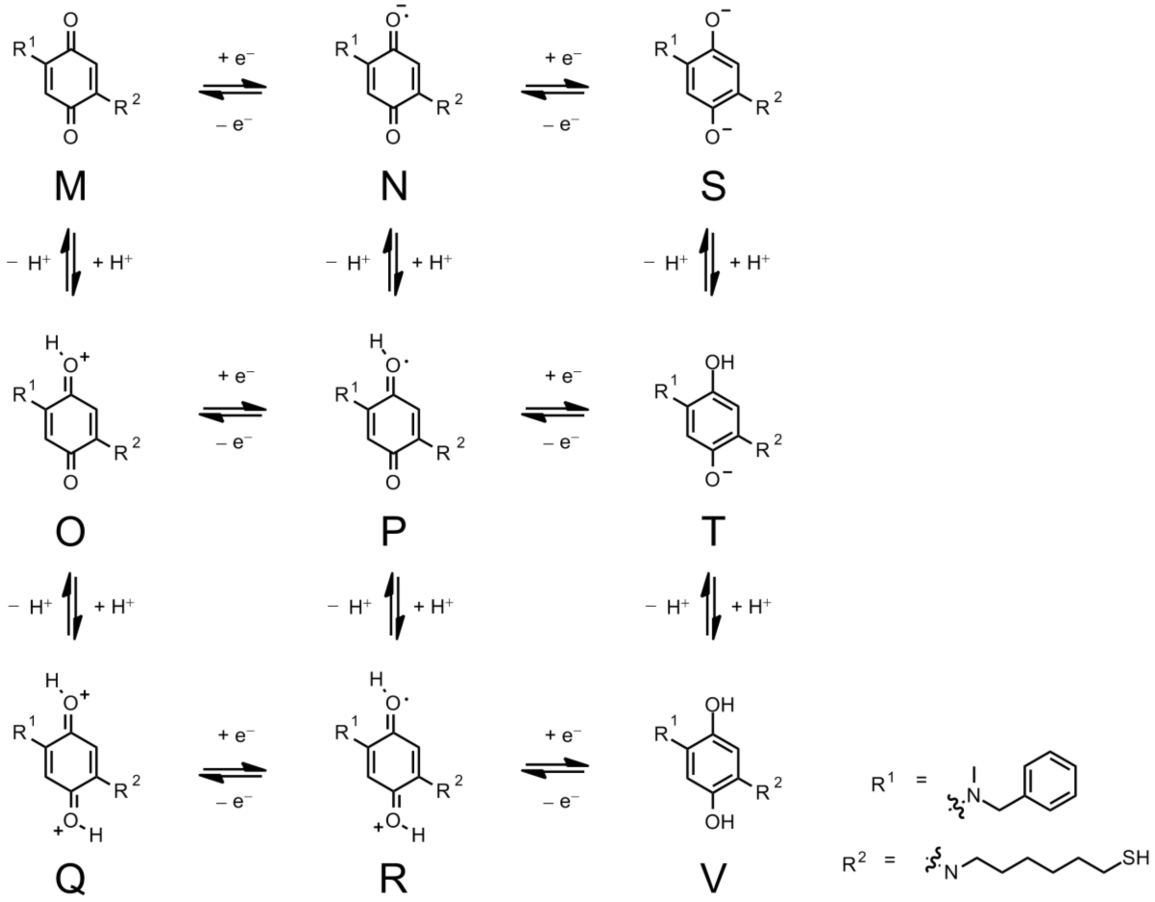

Figure S16. Nine-member square scheme for the N_2-BHQ system.

5. Reference

(1) Choi, K.; Mruk, R.; Moussa, A.; Jonas, A. M.; Zentel, R. *Macromolecules* **2005**, *38*, 9124-9134.
(2) Moreno, A. Y.; Mayorov, A. V.; Janda, K. D. *J. Am. Chem. Soc.* **2011**, *133*, 6587-6595.